Study of hadronic channels in the π^-+^{12}C reaction at 0.69 GeV/c with HADES

Fatima Hojeij

université PARIS-SACLAY

Study of hadronic channels in the $\pi^- + ^{12}C$ reaction at 0.69 GeV/c with HADES

Étude de canaux hadroniques dans la réaction $\pi^- + ^{12}C$ à 0.69 GeV/c avec HADES

Thèse de doctorat de l'université Paris-Saclay

École doctorale n° 576, Particules hadrons énergie et noyau : instrumentation, imagerie, cosmos et simulation (PHENIICS)
Spécialité de doctorat : Physique nucléaire
Graduate School : Physique. Référent : Faculté des sciences d'Orsay

Thèse préparée dans l'unité de recherche **IJCLab** (Université Paris-Saclay, CNRS), sous la direction de **Béatrice RAMSTEIN**, Directrice de recherche, et le co-encadrement d' **Izabela CIEPAŁ**, Professeure assistante

Thèse soutenue à Paris-Saclay, le 14 Novembre 2023, par

Fatima HOJEIJ

Composition du jury

Membres du jury avec voix délibérative

Jean-Christophe DAVID Directeur de recherche, CEA-Saclay DRF / IRFU / DPhN / LEARN, Université Paris-Saclay	Président
Christoph HARTNACK Maître assistant (HDR), IMT Atlantique et laboratoire SUBATECH, Nantes Université	Rapporteur & Examinateur
Jerzy ŁUKASIK Professeur associé (HDR), Institut de physique nucléaire, Académie polonaise des sciences	Rapporteur & Examinateur
Sara BOLOGNESI Ingénieure chercheuse, CEA-Saclay IRFU, Université Paris-Saclay	Examinatrice
Anna CORSI Ingénieure chercheuse, CEA-Saclay IRFU, Université Paris-Saclay	Examinatrice
Stefan TYPEL Directeur de recherche, Institut de physique nucléaire, Université technique de Darmstadt	Examinateur

THESE DE DOCTORAT
NNT : 2023UPASP155

université PARIS-SACLAY

ÉCOLE DOCTORALE
Particules, hadrons, énergie et noyau : instrumentation, imagerie, cosmos et simulation (PHENIICS)

Titre : Étude de canaux hadroniques dans la réaction $\pi^- + ^{12} C$ à 0.69 GeV/c avec HADES
Mots clés : physique nucléaire, physique hadronique, analyses de données, modèles de transport (simulations), pions (particules), détecteur HADES

Résumé : L'objectif de cette thèse est l'analyse des produits de la réaction $\pi^- + ^{12}$ C mesurée à une impulsion des pions incidents de 0.69 GeV/c par l'expérience HADES à GSI. Notre étude explore différents canaux hadroniques ($p\pi^-$, $p\pi^+$, $p\pi^-\pi^+$, $p\pi^-\pi^-$, $pp\pi^-$, pp, etc.) et s'intéresse à leur description par les modèles de transport tels que SMASH, RQMD.RMF, GiBUU, ainsi que le modèle de cascade intranucléaire INCL++. Dans ces modèles, les sections efficaces des réactions élémentaires pion-nucléon ou nucléon-nucléon et la description du noyau, avec en particulier la distribution spatiale et en impulsion des nucléons et le potentiel exercé sur chaque nucléon jouent un rôle de premier plan dans la dynamique de la réaction et la production des particules. La validation de ces modèles avec des données pion-noyau dans différents canaux de production de particules est très importante pour les études de matière hadronique et pour la physique des neutrinos, car la description précise des réactions noyau-noyau ou neutrino-noyau repose fortement sur la dynamique pion-nucléon. Or de telles données sont totalement absentes entre 500 et 900 MeV/c. Notre étude permet de fournir de telles mesures, avec non seulement des spectres inclusifs, mais aussi des corrélations pour différents types de particules émises. Dans ce domaine d'énergie, les rediffusions sont limitées, et la dynamique de la collision reste très sensible à l'interaction pion-nucléon élastique ou inélastique initiale. Ainsi, la comparaison de la distribution d'observables très variées avec les prédictions de modèles que nous présentons permet de tester sélectivement les différents processus (diffusion élastique, production de pions, rediffusions, absorption). Les simulations sont réalisées pour l'ensemble de l'angle solide, mais elles sont ensuite filtrées pour être cohérentes avec les données d'HADES, qui possède une acceptance angulaire entre $18°$ et $85°$ et un seuil en impulsion variable suivant le type de particules et leur angle polaire. Ce filtrage est effectué à l'aide du logiciel GEANT développé par le CERN, et les événements sont reconstruits en utilisant les mêmes méthodes que pour les données expérimentales. Les erreurs statistiques sont négligeables, tandis que les erreurs systématiques, principalement liées à l'efficacité du détecteur, sont estimées à environ 5%. Les résultats révèlent des disparités très importantes entre les modèles. Les modèles RQMD.RMF et SMASH surestiment la plupart des sections efficaces. Ces deux modèles semblent sous-estimer considérablement les rediffusions. Le modèle INCL++ se rapproche le plus des données observées, particulièrement en ce qui concerne les canaux de production des pions. Le modèle GiBUU donne des résultats similaires, sauf pour les canaux avec deux pions chargés pour lesquels des taux de production environ deux à trois fois trop faibles sont prédits. Parmi les réactions examinées, le processus quasi-élastique $\pi^- + ^{12}$ C $\rightarrow \pi^- + p + X$ revêt un intérêt particulier. Cette réaction permet d'explorer les effets des corrélations à courte portée (SRCs) en reconstituant l'impulsion du nucléon participant à la réaction. Une étude approfondie a été faite en utilisant une version récente du modèle INCL++ incluant les SRCs, dans le but d'isoler expérimentalement le processus quasi-élastique le plus efficacement possible, ce qui est une condition préalable pour observer les effets liés aux SRCs. Une analyse détaillée des simulations INCL++ permet d'identifier des régions cinématiques où les processus inélastiques et les effets de rediffusion peuvent être, d'après ce modèle, fortement réduits. Dans cette région, nos distributions expérimentales sont compatibles avec la présence de SRCs, mais ce résultat ne permet pas de conclure de façon définitive, d'autant plus que l'analyse des événements $pp\pi^-$ dans la même région cinématique pour la paire $p\pi^-$ montre des caractéristiques compatibles avec une émission séquentielle.

université PARIS-SACLAY

ÉCOLE DOCTORALE
Particules, hadrons, énergie et noyau : instrumentation, imagerie, cosmos et simulation (PHENIICS)

Title : Study of hadronic channels in the $\pi^- + ^{12}C$ reaction at 0.69 GeV/c with HADES
Keywords : nuclear physics, hadronic physics, data analysis, transport models (simulations), pions (particles), HADES detector

Abstract : The objective of this thesis is the analysis of products resulting from the reaction $\pi^- + ^{12}$C measured at a pion incident momentum of 0.69 GeV/c by the HADES experiment at GSI. Our study explores various hadronic channels ($p\pi^-$, $p\pi^+$, $p\pi^-\pi^+$, $p\pi^-\pi^-$, $pp\pi^-$, pp, etc.) and focuses on their description by transport models such as SMASH, RQMD.RMF, GiBUU, as well as the intranuclear cascade model INCL++. In these models, the cross-sections of elementary pion-nucleon or nucleon-nucleon reactions and the description of the nucleus, especially the spatial and momentum distributions of nucleons and the potential applied to each nucleon, play an important role in the dynamics of the reaction and particle production. The validation of these models with pion-nucleus data in different particle production channels is crucial for hadronic matter studies and neutrino physics, as the precise description of nucleus-nucleus or neutrino-nucleus reactions strongly relies on pion-nucleon dynamics. However, such data is entirely missing in the 500 to 900 MeV/c range. Our study provides such measurements, not only with inclusive spectra but also with correlations for different types of emitted particles. In this energy range, rescatterings are limited, and the collision dynamics remain highly sensitive to the initial elastic or inelastic pion-nucleon interaction. Thus, the comparison of diverse observable distributions with the models' predictions that we present allows for a selective testing of different processes (elastic scattering, pion production, rescattering, absorption). Simulations are performed over the full solid angle, but they are subsequently filtered to be consistent with HADES data, which has an angular acceptance between $18°$ and $85°$ and variable momentum thresholds depending on the particle type and polar angle. This filtering is done using the GEANT software developed by CERN, and events are reconstructed using the same methods as for experimental data. Statistical errors are negligible, while systematic errors, primarily related to the detector's efficiency, are estimated to be around 5%. The results reveal significant disparities between the models. The RQMD.RMF and SMASH models overestimate most of the cross-sections. These two models appear to significantly underestimate rescatterings. The INCL++ model comes closest to the observed data, especially in terms of pion production channels. The GiBUU model provides similar results, except for channels with two charged pions, for which production yields are predicted to be too low by a factor of two to three. Among the examined reactions, the quasi-elastic process $\pi^- + ^{12}\text{C} \rightarrow \pi^- + p + X$ is of particular interest. This reaction allows for exploring the effects of short-range correlations (SRCs) by reconstructing the momentum of the participant nucleon in the reaction. An in-depth study was conducted using a recent version of the INCL++ model that includes SRCs, with the aim of isolating the quasi-elastic process experimentally in the most efficient way, which is a prerequisite for observing the effects associated with SRCs. A detailed analysis of INCL++ simulations identifies kinematic regions where inelastic processes and rescattering effects can, according to this model, be strongly reduced. In this region, our experimental distributions are compatible with the presence of SRCs, but this result does not allow for a definitive conclusion, especially since the analysis of $pp\pi^-$ events in the same kinematic region for the $p\pi^-$ pair shows characteristics compatible with sequential emission.

Acknowledgements

The completion of this thesis was made possible by the invaluable support of several individuals listed below. Their contributions and encouragement have been crucial to this achievement, and for that, I extend my sincere appreciation.

First and foremost, I would like to express my profound appreciation for my dedicated supervisor, Béatrice. Her unwavering support has been instrumental throughout my three-year journey. Béatrice not only provided invaluable guidance but also served as a constant source of inspiration. Her extensive knowledge in physics and work methodologies significantly enriched my learning experience. What sets Béatrice apart is her exceptional patience and composure, even during the most challenging and stressful times. Her kindness and unwavering presence, always ready to offer assistance and guidance, testify to her contribution to my academic and personal development. This thesis would not have reached its completion without her supervision.

My co-supervisor, Izabela, deserves my deep admiration and appreciation. Her kindness, friendliness, and boundless energy have made our collaboration an absolute joy. Her support and guidance have been instrumental in my progress, and I felt comfortable working alongside her. Izabela's continuous support has driven my success, and I am truly grateful for her invaluable contributions to my academic journey.

I dedicate this success to my husband, Karim. He has been there for me since we first met during my early years at university, always caring, encouraging, and supporting me. His unwavering commitment was pivotal in my academic journey, from my bachelor's and master's studies to the third year of PhD. program. No matter what, he has always put me first in his life. During stressful times and tough moments, he stood by my side before anything, whether we were physically together or miles apart. His patience and constant support have been like a strong pillar, helping me stay resilient. I really appreciate how he's been a major force in helping me navigate this academic journey and succeed. His sacrifices and belief in me have been like a guiding light. I want to say a heartfelt thank you to him for being my biggest supporter. I couldn't have finished this thesis without you.

I also dedicate this success to my wonderful family, especially my parents. I want to say a big thank you. Your support and encouragement mean the world to me. When things got tough, you were always there cheering me on.

Your sacrifices and kind words kept me going. This success is as much yours as mine, reflecting the love, care, and strength you have infused into every step of my life's journey. I'm truly thankful for how much you've contributed to my education and personal growth.

I want to express my appreciation for my desk partner, Rayane, who shared my country's heritage, Lebanon, and made our time in the same bureau truly enjoyable. Rayane's company brought a sense of familiarity and camaraderie to our workspace, and I valued the moments we spent working together.

I sincerely thank Jack, a retired researcher at CNRS, for his invaluable support. Sharing the office with him has been a privilege. Jack, a constant mentor and supporter, brought a wealth of experience and insights. He also guided me through the theoretical aspects. Our discussions left a lasting impression, enriching my journey.

Finally, I would like to extend my gratitude to the HADES international collaborators, whose collaborative spirit has been instrumental in the success of this thesis. Working together has been an enriching experience. I appreciate their smooth cooperation, which broadened my horizons and greatly enriched my research experience.

Résumé en Français

L'expérience HADES, menée au sein de l'installation SIS18 au GSI, explore la région basse énergie du diagramme de phase de la QCD en utilisant des collisions d'ions lourds à des énergies dans le centre de masse ($\sqrt{s}_{NN}$) allant jusqu'à 2,6 GeV. La matière ainsi créée s'apparente à celle produite dans les collisions d'étoiles à neutrons, que l'on peut étudier, notamment grâce à la détection d'ondes gravitationnelles. L'expérience HADES fournit des informations sur les caractéristiques thermodynamiques et la composition microscopique de la matière avec une densité baryonique élevée, où les résonances baryoniques sont produites. Les réactions proton-noyau ou pion-noyau permettent d'étudier la matière nucléaire à faible énergie d'excitation. Enfin, l'étude des réactions élémentaires, proton-proton ou pion-proton fournissent une référence pour quantifier les effets de milieu. Ces réactions permettent par ailleurs de mesurer des canaux exclusifs hadroniques pour étudier les résonances baryoniques et les hypérons.

Les études de la résonance $\Delta(1232)$ ont pu être effectuées en mesurant la réaction proton-proton. Mais pour les résonances plus lourdes, dont les distrbutions en masse se chevauchent, la réaction pion-proton est plus appropriée. Les réactions pion-nucléon ont en effet historiquement constitué la principale source d'informations concernant le spectre des baryons. En effet, un baryon avec une masse ($\sqrt{s}_{\pi N}$) peut être directement excité dans de telles réactions. Cette approche offre un avantage significatif par rapport aux collisions NN. Un nouveau programme expérimental utilisant le faisceau de pions du GSI a donc été mis en place.

HADES a initié ce programme en explorant la deuxième région de résonance autour des masses des résonances N*(1520) et N*(1535), avec un accent particulier sur les canaux de production de deux pions et de paires e^+e^-. Cette expérience a été effectuée en été 2014 pendant 15 jours, en utilisant une cible en polyéthylène C_2H_4 et de carbone ^{12}C pour accéder, par soustraction, à la réaction π^-+p . Cette thèse se concentre principalement sur l'analyse des données relatives à la cible de carbone à une impulsion de faisceau de 0,685 GeV/c.

Les réactions pion-noyau sont nécessaires pour la description de la dynamique des collisions d'ions lourds. De nombreux pions sont produits durant ces réactions ($NN \rightarrow NN\pi$), puis ils excitent des résonances baryoniques ($\pi N \rightarrow N^*\Delta$). La dynamique des pions dans la matière nucléaire a été bien étudiée dans la région de la résonance $\Delta(1232)$, mais de telles informations ne sont pas disponibles pour les énergies plus élevées. Notre expérience

permet d'étudier la réponse du noyau de carbone dans la région des résonances N(1440),N(1520) et N(1535) . La dynamique des pions à ces énergies sera essentielle pour l'interprétation des réactions ions lourds sur le futur accélérateur FAIR à des énergies $2.6 < \sqrt{s}_{NN} < 5$ GeV.

Les modèles hadroniques théoriques sont des outils puissants pour étudier le comportement des hadrons dans la matière nucléaire et sont largement utilisés dans divers domaines, notamment la physique nucléaire, l'astrophysique et la cosmologie. Les modèles dynamiques permettent de décrire l'évolution des distributions de l'impulsion et de la position au cours du temps. Ce sont donc des outils bien adaptés pour l'étude de systèmes complexes tels que les collisions d'ions lourds. Bien que les modèles de cascade soient moins détaillés que les modèles de transport, ils demeurent pertinents pour décrire certains canaux hadroniques, notamment dans les réactions p+A ou π^-+A.

La validation de ces modèles avec des données pion-noyau dans différents canaux de production de particules est très importante pour les études de matière hadronique et pour la physique des neutrinos, car la description précise des réactions noyau-noyau ou neutrino-noyau repose fortement sur la dynamique pion-nucléon. Notre étude permet de fournir de telles mesures, avec non seulement des spectres inclusifs, mais aussi des corrélations pour différents types de particules émises. Dans ce domaine d'énergie, les rediffusions sont limitées, et la dynamique de la collision reste très sensible à l'interaction pion-nucléon élastique ou inélastique initiale. Ainsi, la comparaison de la distribution d'observables très variées avec les prédictions de modèles que nous présentons permet de tester sélectivement les différents processus (diffusion élastique, production de pions, rediffusions, absorption).

L'objectif de cette étude est de réaliser cette évaluation pour plusieurs modèles de transport, notamment SMASH, RQMD.RMF, GIBUU, ainsi que le modèle de cascade intranucléaire INCL++.

Le détecteur intègre un détecteur Cherenkov à Imagerie par Anneau (RICH) pour identifier les e^+e^- , un spectromètre magnétique des mini-chambres à dérive (MDC) pour analyser les trajectoires des particules chargées dans un champ magnétique toroïdal, des chambres à plaques résistives (RPC) et des détecteurs de temps de vol (ToF). L'acceptance du détecteur (divisé en six secteurs) couvre une grande partie de l'espace de phase, avec des angles azimutaux s'étendant sur 85% et des angles polaires allant de 18° à 85°.

Dans cette expérience, les pions ont été générés par un faisceau primaire de ^{14}N provenant du synchrotron SIS18, fonctionnant à 2A GeV avec une intensité moyenne d'environ 6 x 10^{10} ions par seconde frappant une cible de Beryllium. Une ligne magnétique longue de 33m et composée de deux dipôles et neuf quadrupôles permet de sélectionner les pions dans la gamme d'impulsions choisie. Le flux incident sur la cible d'HADES est d'environ 200 000 pions/s.

Les données brutes, provenant des divers détecteurs, sont enregistrées dans des fichiers spécifiques. La phase suivante consiste à calibrer les données et à reconstruire les trajectoires, transformant ainsi les informations en-

registrées en données physiques stockées dans des fichiers de résumé de données (DST). C'est là qu'intervient le système Hades pour la Réduction et l'Analyse des Données (HYDRA), qui permet de reconstruire les trajectoires des particules et de stocker des informations cruciales sur les données physiques. Ensuite, l'Analyse Post-DST se concentre sur l'exploration de coïncidences de particules spécifiques par l'application de critères d'identification de particules (PID).

Pour déterminer les impulsions des particules chargées, on se base sur les informations du système de trajectographie. Lorsque des particules chargées telles que les pions ou les protons se déplacent à travers un champ magnétique, la force de Lorentz provoque une courbure de leurs trajectoires. Cette courbure provoque un changement de direction de l'impulsion de la particule. L'identification des particules est réalisée en combinant les informations du système de trajectographie (l'impulsion) avec les données des détecteurs de temps de vol.

En ce qui concerne la normalisation des données, elle a été effectuée en utilisant la section efficace bien connue du processus élastique π^-+p $\rightarrow \pi^-$+p. La première étape a consisté à renormaliser les données du carbone sur celles du polyéthylène en raison de la différence de temps de collecte de données sur les deux cibles. Cela a été réalisé en étudiant la masse manquante au carré du processus quasi-élastique π^-+p $\rightarrow \pi^-$+p dans les deux cibles qui est très différente pour les réactions sur le proton et sur le carbone. On peut alors soustraire les événements provenant de l'interaction des pions avec le carbone. Ensuite, le spectre correspondant à l'interaction élastique avec les atomes d'hydrogène a été normalisée en utilisant la section efficace connue. Cette étape a été menée par un groupe polonais au sein de la collaboration.

Enfin, les erreurs systématiques sont principalement dues à l'efficacité du détecteur et à la normalisation.

Les modèles de simulation utilisés pour la comparaison avec les données se répartissent en modèles de transport et en modèles de cascade intranucléaire. Dans ces modèles, les sections efficaces des réactions élémentaires pion-nucléon ou nucléon-nucléon et la description du noyau, avec en particulier la distribution spatiale et en impulsion des nucléons et le potentiel exercé sur chaque nucléon jouent un rôle de premier plan dans la dynamique de la réaction et la production des particules. Bien qu'ils partagent de nombreuses similitudes, des différences notables existent entre eux. L'une des distinctions fondamentales entre les modèles GiBUU et SMASH par rapport à RQMD.RMF est que ce dernier considère les particules comme des paquets d'ondes, tandis que les deux premiers les traitent comme des particules ponctuelles.

En ce qui concerne la distribution en impulsion, tous les modèles de transport font appel au modèle local de Thomas-Fermi qui dépend de la densité locale des nucléons. Cette dernière est liée à la distribution spatiale de Saxon-Wood, à l'exception de RQMD.RMF, qui a une distribution gaussienne. D'autre part, INCL++ utilise le modèle du gaz de Fermi global.

En ce qui concerne les potentiels, INCL++ utilise un potentiel constant, ce qui signifie que les particules suivent

des trajectoires rectilignes. Cependant, dans les autres modèles, le potentiel varie en fonction de l'impulsion du noyau. SMASH utilise un potentiel nucléaire de Skyrme non relativiste. Ce dernier n'a d'impact que sur les baryons, et aucun potentiel coulombien ou dépendant de l'implusion n'est intégré, ce qui permet aux hadrons de suivre des trajectoires linéaires. GiBUU, quant à lui, permet de choisir entre ces deux types de potentiels (relativiste ou non relativiste), et RQMD.RMF comporte une composante relativiste.

Dans notre gamme d'énergie, la réaction procède par collisions successives sur différents nucléons. Nous avons d'abord étudié la cinématique des réactions élastiques et inélastiques pion-nucléon en utilisant le généarteur d'événements PLUTO, puis nous nous sommes intéressés à l'effet de l'impulsion du nucléon sur cette cinématique. L'analyse de données a été réalisée pour plusieurs canaux inclusifs (protons, pions, etc..) et exclusifs, notamment les réactions pπ^-quasi-élastiques et inélastiques p$\pi^-\pi^-$, p$\pi^-\pi^+$, ppπ^-, $\pi^-\pi^+$, pp, ppp, etc. Certains de ces canaux peuvent être produits en une seule collision (pπ^-quasi-élastiques) ou en plusieurs collisions avec des rediffusions (p$\pi^-\pi^-$, $\pi^-\pi^+$). Les autres canaux impliquent inévitablement plusieurs étapes. Notre étude nous a permis de différencier ces différents collisions en utilisant des variables cinématiques et des variables comme la masse manquante et la masse invariante des particules détectées. Les collisions qui comprennent la rediffusion des nucléons avec la production de pions occupent une petite partie de l'espace de phase. En plus, ces évenements sont hors de notre acceptance, car les pions sont émis à des angles polaires élevés, les plaçant hors de notre plage de détection.

Le modèle INCL++ a été privilégié par rapport aux autres modèles car il permet d'accéder à des informations qui ne sont pas accessibles dans l'expérience comme le nombre de collisions, la nature des processus... Une première investigation a été menée pour étudier avec INCL la probabilité des différentes catégories d'évenements qui se distinguent par le nombre de pions et de protons détectés. Nous avons aussi étudié la multiplicité des pions et des nucléons dans la réaction, ce qui a révélé que la production de π^-est la plus probable, par conséquent, l'accent a été mis sur l'étude des canaux impliquant des π^-, tandis que la production de 3 pions est pratiquement négligeable, justifiant ainsi son exclusion de l'étude.

Le processus quasi-élastique π^-+ ^{12}C $\rightarrow \pi^-$+ p + X a été sélectionné en fonction de la corrélation en impulsion du proton détecté et du π^-, en plus de la condition de coplanarité ($150^\circ < \Delta\Phi < 210^\circ$). Dans les évenements sélectionnés, on observe un ^{11}B peu excité, cependant, les simulations INCL++ montrent que dans de nombreux cas, une collision inélastique πN$\rightarrow \pi\pi$N suit la collision quasi-élastique. Nous avons aussi observé que les résultats dépendent peu du choix de l'impulsion de Fermi dans INCL++. De plus, nous avons testé l'impact d'un processus spécial utilisé dans INCL++ appelé "local E", qui consiste à corriger l'énergie des nucléons à la surface du noyau pour calculer la vraie section efficace de la réaction (car les nucléons ont des impulsions constantes qui doivent être compensées à la surface). Cette correction "local E" permet d'augmenter la section efficace et de mieux décrire la cinématique des particules. C'est donc un élement essentiel dans le code.

Le travail présenté dans cette thèse met en évidence des divergences significatives entre les modèles. En ce qui concerne le modèle RQMD.RMF, on observe une surestimation systématique des sections efficaces dans tous les canaux, parfois jusqu'à un facteur deux. La comparaison des distributions en masse manquante et impulsion manquante semble indiquer que l'impulsion moyenne des nucléons participant à la réaction quasi-élastique est trop faible. Cet effet est sans doute lié à la description de la densité nucléaire dans ce modèle, qui considère des paquets d'ondes alors que GIBUU et SMASH utilisent des particules individuelles. En effet, l'impulsion des nucléons dans le noyau est sensible à la densité, au travers de l'approximation de densité locale de Thomas-Fermi. De manière frappante, ce modèle présente une contribution fortement prononcée du processus quasi-libre (π^-n $\rightarrow$ p $\pi^-\pi^-$), ce qui est en désaccord avec les données expérimentales qui indiquent plus de rediffusions. Le même constat vaut pour les étapes élastiques séquentielles (quasi-élastique suivie de $pp \rightarrow pp$), qui sont peu présentes dans les données observées. Jusqu'à présent, ce modèle a été utilisé pour des énergies plus élevées et n'a probablement pas été ajusté à notre cas.

En comparaison avec RQMD.RMF et SMASH, le modèle GIBUU montre de meilleures performances. Il sous-estime la plupart les taux de production pour les processus inélastiques. Comme RQMD.RMF, GIBUU montre qu'une grande partie des événements p$\pi^-\pi^-$proviennent du processus quasi-libre (π^-n $\rightarrow$ p $\pi^-\pi^-$). La contribution de la résonance $\Delta(1232)$ est visible dans le canal pπ^+. GIBUU décrit assez bien les formes des distributions expérimentales et suit souvent les prédictions d'INCL.

SMASH surestime généralement les sections efficaces mesurées, surtout pour le canal quasi-elastique. En plus, il surestime la diffusion nucléon-nucléon dans le noyau après une étape quasi-élastique, comme dans le cas du RQMD.RMF. Nous avons pu aussi quantifier les effets du potentiel sur la simulation SMASH.

INCL++ offre une meilleure description que les autres modèles dans la plupart des distributions inclusives et exclusives étudiées, en particulier en ce qui concerne la production de pions, mais présente encore certaines limites. À des angles avant, il sous-estime les π^-et les protons dans le pic quasi-élastique et surestime la production de π^+.

Cependant, notre analyse n'a pas été sensible à l'absorption des pions, et des investigations supplémentaires, notamment avec la détection des neutrons, seraient nécessaires pour une compréhension plus approfondie de ce processus. L'évaluation de la description des canaux quasi-élastiques dans les réactions pion-noyau revêt une importance particulière pour la reconstruction de l'énergie des neutrinos.

Ayant à disposition des données sur la diffusion quasi-élastique, la question naturelle des effets SRC a été soulevée. Cela nous a donné l'opportunité de tester la version récente du code INCL++, incluant les paires SRC (pn). L'utilisation de ce code nous a permis d'étudier des zones cinématiques différentes afin de trouver des conditions qui éliminent les rediffusions. Cette étude montre que la région optimale est celle des impulsions de π^-les plus

élevées. Pour les impulsions manquantes très au-delà de l'impulsion de Fermi, les données sont en accord avec les prédictions de ce modèle incluant les SRCs. Nous avons également cherché un éventuel signal de paires SRC pp dans les événements ppπ^-, bien que les effets de paires SRC (pp) soient attendus bien plus faibles que ceux de paires SRC (pn). Nous n'avons observé aucun signal. En effet, les expériences avec des faisceaux de pions présentent des défis pour l'étude des corrélations à courte portée (SRC), car les pions interagissent plus souvent de manière élastique à la surface du noyau, où les SRC ne sont pas aussi importants qu'au centre du noyau. À l'avenir, la collaboration HADES prévoit des mesures spécifiques pour étudier les SRC en utilisant un faisceau de protons de haute intensité à 4,5 GeV avec différentes cibles. Ce travail de thèse a permis d'améliorer la compréhension des effets de rediffusions qui peuvent masquer les SRCs, ce qui sera utile pour l'analyse de ces futures expériences.

Dans un proche avenir, une expérience avec un faisceau de pions est prévue pour explorer la troisième région de résonances, à une énergie dans le centre de masse de 1.7 GeV/c. De nouvelles données sur la production de protons et de pions seront collectées, élargissant ainsi la base de données à plus haute énergie et permettant un test des modèles de transport et de cascade dans un nouveau domaine cinématique.

Pour les données dans la deuxième région de résonances, nos résultats révèlent des incohérences dans la capacité des modèles à décrire précisément les données. Nous espérons que ces différences seront prises en compte par les développeurs de modèles pour améliorer leurs performances. Cette recherche a également ouvert la voie à des collaborations futures pour l'utilisation des données de HADES dans des réactions induites par des pions pour la physique des neutrinos.

Contents

1 Introduction **15**

1.1 The strong interaction . . . 15

1.2 HADES and the QCD phase diagram . . . 16

1.3 Hades experiments . . . 18

1.3.1 Heavy-ion collisions . . . 18

1.3.2 Cold matter studies . . . 18

1.3.3 Nucleon-nucleon collisions . . . 18

1.3.4 Pion-nucleon collisions . . . 19

1.4 Transport and cascade models for data interpretation . . . 20

1.4.1 Dilepton emission in heavy-ion reactions . . . 20

1.4.2 Hadron production in Au+Au collisions with HADES . . . 21

1.4.3 Hadron production in p+Nb collisions at 3.5 GeV with HADES . . . 22

1.4.4 Hadron production in π^-+C and π^-+W collisions at 1.7 GeV/c with HADES . . . 22

1.4.5 Other applications of transport and cascade models . . . 24

1.5 Pion induced reactions in the second resonance region . . . 26

1.5.1 Pion-nucleon reactions . . . 27

1.5.2 $\pi\pi$ N channels . . . 31

1.5.3 Pion-nucleus reactions . . . 34

1.6 Summary . . . 36

2 The HADES experimental set-up **37**

2.1 Ring Imaging CHerenkov detector . . . 38

2.2 Tracking system . . . 39

2.2.1 The Superconducting Magnet . . . 39

2.2.2 The Multi-Wire Drift Chambers . . . 40

2.3 META Detectors . . . 42
2.3.1 TOF . . . 42
2.3.2 RPC . . . 43
2.3.3 Pre-shower . . . 44
2.4 Start detector . . . 45
2.5 Trigger and data acquisition system . . . 46
2.6 Target . . . 46
2.7 Pion beam line . . . 48

3 Experimental data analysis **51**
3.1 Data processing . . . 51
3.2 Track and momentum reconstruction . . . 53
3.2.1 Track path . . . 53
3.2.2 Momentum reconstruction . . . 55
3.2.3 META matching . . . 56
3.3 Charged Particle identification . . . 56
3.4 Data normalization . . . 58
3.5 Systematic errors estimation . . . 60

4 Transport and cascade models **63**
4.1 Transport models . . . 63
4.1.1 BUU and QMD approaches . . . 64
4.1.2 Nucleus description . . . 67
4.1.3 Collisions . . . 68
4.2 The Intranuclear Cascade Model (INCL++) . . . 71
4.3 The PLUTO event generator . . . 74

5 Simulation framework **77**
5.1 Full-scale simulations . . . 77
5.2 Filtered simulations . . . 78
5.3 Simulations Normalization . . . 82

6 Discussion of results **83**
6.1 Overview of the various exit channels . . . 83
6.1.1 Pion-Nucleon reactions . . . 83
6.1.2 Pion-Nucleus reactions . . . 86

6.1.3 Kinematics of the quasi-free reaction . . . 86
6.1.4 Multi-step processes . . . 88
6.1.5 Invariant and Missing masses . . . 89
6.1.6 Hadronic channels in INCL++ . . . 90
6.2 $p\pi^-$ channel . . . 93
6.3 $p\pi^-$ quasi-elastic . . . 94
6.3.1 Selection of quasi-elastic channel . . . 94
6.3.2 Comparison with models . . . 94
6.3.3 Tests of INCL parameters . . . 98
6.4 Discussion of experimental distributions of inelastic channels . . . 102
6.4.1 $p\pi^-$ and $p\pi^+$ channels . . . 103
6.4.2 $p\pi^-\pi^+$ and $p\pi^-\pi^-$ channels . . . 105
6.5 Comparison of inelastic channels with simulations . . . 105
6.5.1 channels: $p\pi^-$ & $p\pi^+$ . . . 105
6.5.2 channel: $p\pi^-\pi^+$ . . . 107
6.5.3 channel: $\pi^-\pi^+$ . . . 109
6.5.4 channel: $p\pi^-\pi^-$ . . . 110
6.5.5 channel : $pp\pi^-$ . . . 113
6.5.6 Pion absorption . . . 115
6.6 Cross section summary table . . . 116
6.7 SMASH potential test . . . 117
6.8 Inclusive analysis . . . 118
6.9 Summary . . . 120

7 Investigation of Short-Range Correlation effects **125**
7.1 Introduction on SRC . . . 125
7.1.1 Nucleon-nucleon interaction . . . 125
7.1.2 Limitations of the shell model . . . 126
7.1.3 Experimental observations . . . 126
7.1.4 Models for SRC description . . . 128
7.1.5 Implementation of SRC in INCL++ . . . 129
7.2 Missing momentum distribution . . . 133
7.3 Minimization of rescattering effects . . . 135
7.4 Comparison with INCL++ including SRC effects . . . 138

7.5 Search of SRC in ppπ^- events . . . 139
7.5.1 Selection of events . . . 140
7.5.2 Comparison with INCL++ simulations including SRC . . . 140

8 Conclusion and Outlook **145**

8.1 Conclusion . . . 145
8.2 Outlook . . . 147

List of Figures

1.1 Sketch of the QCD phase diagram (temperature versus baryochemical potential) showing the Hadron-Matter and Quark Gluon Plasma phases. 16

1.2 Evolution of average temperature (green), baryochemical potential (red) and density (blue) as a function of time in a Au+Au collision at an energy of 1.23A GeV in a coarse-grained approach based on the UrQMD transport model [1]. 16

1.3 Dilepton excess yield extracted by subtracting η contributions and NN reference after acceptance corrections. The yield is normalized to the number of neutral pions. Dashed curves: ρ ("vacuum" spectral function) contribution from HSD and from SMASH (dark blue) transport model calculations. Solid green curve: total HSD calculation. The blue, pink and dark blue curves show the results of three versions of coarse grained calculations using the modified ρ meson spectral function. See [2] for details. 20

1.4 Imaginary part of the ρ meson propagator (or spectral function) plotted for a constant momentum (q = 0.3 GeV/c) at different temperatures and baryon densities [3]. 20

1.5 Dilepton mass spectrum for pp collisions at 3.5 GeV. The hatched areas indicate the effects of the Δ form factor and baryon-resonance contributions to the ρ production, respectively. The total is shown (from bottom to top) with Δ form factor (left-hatched), ρ resonance contributions (right-hatched) and with both of these effects together [4]. 21

1.6 Dilepton mass spectrum for p+Nb at 3.5 GeV, showing all contributing channels with vacuum spectral functions. The hatched area indicates the effect of the Δ form factor [4]. 21

1.7 Pion multiplicities measured in Au+Au reaction at 1.25A GeV are compared to predictions from various transport models [5]. 22

1.8 Double differential cross sections for protons measured with HADES in the p+^{93}Nb reaction at 3.5 GeV (full circles). Cross sections are shown for three laboratory emission angles of $\theta = 25°$, $\theta = 55°$ (multiply by factor 10^{-1}) and $\theta = 80°$ (multiply by factor 10^{-2}). The experimental distributions are compared to the theoretical models: GiBUU (dash-dotted lines), UrQMD (dotted lines) and INCL++ (dashed lines). Figure adopted from [6]. 23

1.9 The same as in Fig. 1.8 but for π^+ (left plot) and π^- (right plot). 23

1.10 Double differential cross sections for deuterons (left plot) and tritons (right plot) measured with HADES in the p+^{93}Nb reaction at 3.5 GeV (full circles). Cross sections are shown for three laboratory emission angles of $\theta = 25°$, $\theta = 55°$ (multiply by factor 10^{-1}) and $\theta = 80°$ (multiply by factor 10^{-2}). The experimental distributions are compared to the INCL++ model (dashed lines). Figure adopted from [6]. 23

1.11 Upper panel: cross sections of Λ (orange), π^+ (green) and proton (red) as a function of rapidity in π^-+C (a) and π^-+W (b) reactions compared to the transport models, GiBUU (solid curve) and SMASH (dashed curve). Lower panel: deviations of the transport model simulations from the measured cross section as a function of rapidity. Figure adopted from [7]. 24

1.12 Comparison of the total (triangles) and inelastic (crosses) π^- differential cross sections as a function of rapidity with GiBUU (solid curves) and SMASH (dashed curves). Figure adopted from [7]. 25

1.13 Upper panel: double-differential cross sections for π^- as a function of the transverse momentum p_T in π^-+C (a) and π^-+W (b) reactions compared to GiBUU (solid curves) and SMASH (dashed curves) for various rapidity ranges (see legend). Lower panel: Relative deviations between experimental data and the two transport model calculations. Figure adopted from [7]. 25

1.14 The calculated pion mean free path (mfp) as a function of kinetic energy. The calculation of the mfp is $1/\rho_0\sigma_{tot}$, where ρ_0 is the central nuclear density and and σ_{tot} is the isospin-averaged pion total cross section at a given kinetic energy [8]. 27

1.15 Evolution of the cross section of different channels of the π^-p reaction as a function of the center-of-mass energy. The curves show the results of coupled-channel calculations [9]. 28

1.16 Total cross sections for the π^-p (dashed curves) and π^+p (full curves) reactions. The mass of the main baryon resonances are indicated [10]. 28

1.17 The data points show the existing measurements for cross sections for the elastic π^-+p $\rightarrow$ π^-+p (left), elastic π^+ p $\rightarrow$ π^+ p (equivalent to π^- n $\rightarrow$ π^- n) (middle) and charge exchange π^-+p$\rightarrow$ π^0 p (right) reactions in the range of incident pion momentum between 500 and 1000 MeV/c. The curves show the result of the SAID PWA. Crossed out data points are not considered in the SAID fits. Picture extracted from the SAID platform [11]. 29

1.18 π^-+p elastic-scattering angular distributions measured by the HADES collaboration at four pion beam momenta 0.650, 0.685, 0.733 and 0.786 GeV/c (red squares) are compared to the EPECUR data (blue dots) [12] available at the highest beam momentum and to other world data (open disks). The WI08 SAID solutions is shown as a black curve [13] 30

1.19 Same as Fig. 1.17 for differential cross sections as a function of the center-of-mass angle for the π^+p elastic scattering and π^-p $\rightarrow \pi^0$n charge exchange reaction. Data points measured for pion beam momenta p_{beam} between 670 and 710 MeV/c are shown. The curve shows the result of the SAID PWA for p_{beam}= 690 MeV/c. 30

1.20 Cross sections for the various channels of the π^-p $\rightarrow \pi\pi$ N (left) and π^+p$\rightarrow \pi\pi$ N (right) reactions. . . 31

1.21 Angular distributions measured in the center-of-mass for the reaction π^-+p$\rightarrow\pi^0\pi^-$+p at an incident energy E = 558 MeV at BNL [14] (left) and E = 573 MeV at Berkeley [15] (right). 31

1.22 Differential cross sections as a function of the center-of-mass angle of the $2\pi^0$ system produced in the reaction π^-+p$\rightarrow\pi^0\pi^0$ n at different π^-momenta [16]. 32

1.23 Differential cross sections as a function of the center-of-mass angle of the nucleons (left column) and pions (right column) in the CM frame for the π^-+p$\rightarrow$ n $\pi^+\pi^-$(upper row) and π^-+p$\rightarrow$ p$\pi^+\pi^0$(lower row) reaction channels for p_{beam}= 0.685 GeV/c. The curves display the contribution of the various partial waves in terms of spin and parity (dashed curves) and of angular momentum and isospin (full curves) in the Bonn-Gatchina PWA [13]. 33

1.24 Same as Fig. 1.23 for the invariant mass of the nucleon-π^- (left column) and two-pion (right column) systems. Here the curves display the contribution of the different decay channels [13]. 33

1.25 Results from ^{12}C(π^-,π^-) experiments at LAMPF. The data (open circles) is compared with two diferent intranuclear cascade calculations. The blue histograms are for the standard calculation. For the red ones, the time for $(\pi, 2\pi)$ reactions to occur is delayed by 2 fm/c. The dashed histograms indicate the portion of the respective INC calculations that are due to $(\pi, 2\pi)$ reactions [8]. 35

2.1 Side view of the HADES setup with the different sub-detectors. 37

2.2 Schematic layout of the RICH, with detail on the photon detector. 39

2.3 Photography of the HADES superconducting magnet during the mounting. 40

2.4 Left: Schematic view of a section of one sector including the RICH detector, four MDCs and coil of the superconducting magnet. Right: Arrangement of the HADES MDCs and the coils of the superconducting magnet. 41

2.5 (a) Schematic layout of the TOF detector with an example of the registration electron and positron. (b) Technical drawing of one sector. Taken from [17]. 43

2.6 Arrangement of the RPC cells within one module. 44

2.7 Internal layout of one RPC cell. On the left picture: 1 - Al electrodes, 2 - glass electrodes, 3 - pressure plate, 4 - kapton insulation and 5 - Al shielding. Taken from [17]. 44

2.8 The Pre-Shower detector is made up of three gas chambers (pre-, post1-, and post2-chamber) separated by lead converters. 45

2.9 Left: Top view of five and four diamond sensor plates with fourfold segmentation on the diamond support Printed Circuit Boards (PCBs). Right: The nine diamond sensor plates are mounted on two printed circuit boards of the Start detector. 45

2.10 Photo of the segmented high purity carbon target used during the pion beam time. 46

2.11 Schematic view of the polyethylene $(CH_2)n$ (left) and carbon (right) target systems. 47

2.12 Pion beam line facility at GSI [18]. 48

2.13 Pion beam momentum distribution measured with the in-beam tracking system CERBEROS [19, 18]. 48

3.1 Schematic diagram representing the event processing for the data and simulations. See text for details. 52

3.2 Schematic view of the four MDCs, each represented by only one of the six layers, and position of two projection planes, one between MDC-I and MDC-II and the other between MDC-III and MDC-IV. Also presented is kick plane between MDC-II and MDC-III [20]. 54

3.3 Illustration of procedure which utilizes the drift time to reduce the size of the projected area corresponding to a hit cell. The *drift distance shadow* can be compared to the *cell shadow*. The drift distance d_{dr} and the corresponding error, displayed as a green area are calculated from the measured time using GARFIELD simulations [20]. 54

3.4 Left: Projection of drift cells on x-y detector coordinate space for an event with four tracks. Right: 2-dimensional histogram with a peak at the location where the drift cell projections have maximum overlap. In this example, the z axis indicates the peak height, corresponding here to a track with 12 hit in layers in the inner drift chambers [20]. 55

3.5 Principle of the matching procedure between the track and META information [17]. 57

3.6 Particle identification of charged particles using beta vs. momentum$*$charge correlation and plotted after imposing graphical cuts. 57

3.7 Particle identification of hadrons using dE/dx energy loss in MDC vs. momentum$*$charge correlation. . 57

3.8 Squared $\pi^- p$ missing mass from the pion-proton system measured at 0.7 GeV/c after elastic-scattering selection. Black and red histograms present events from the polyethylene target and contribution of pion reactions on carbon nuclei in the polyethylene target, respectively. Their difference, hatched blue area, corresponds to $\pi^- p$ reactions. Simulations of the $\pi^- p$ elastic scattering are shown by the magenta histogram. 59

3.9 Comparison between distributions of θ polar angles plotted in the HADES acceptance with (black) and without (red) efficiency correction for protons (left plot) and π^- (right plot). 60

3.10 The count ratios for each sector with respect to the average count along θ, after applying efficiency correction using the INCL++ model. Left: protons. Right: π^-. Each sector is represented by a distinct color. 61

4.1 Schematic plot of various families of the transport codes and their evolution in time. 64

4.2 Proton-proton (a) and proton-neutron (b) cross sections from SMASH calculations compared to existing data. The contribution of single and double excitation of baryon resonances with isospin 1/2 (N*) and 3/2 (Δ) is shown [21]. 69

4.3 Proton-pion cross sections from SMASH calculations compared to existing data. 70

4.4 Cross sections for single pion production from proton-proton (left) and proton-neutron (right) collisions in the SMASH calculations compared to data [21]. 70

4.5 Nucleon momentum distributions in the carbon nucleus following various models: the Benhar-Fantoni 2D spectral function [22] (black), the Global Fermi model[23] (green), the Local-Thomas-Fermi gas model [24] (red) and the effective spectral function [25] (blue). 72

4.6 Kinetic energy and position correlations in the classical picture (top) and the fuzzy surface picture (bottom). The latter is used in INCL++ to describe the nucleus. 73

4.7 Momentum distributions measured in electron scattering on ^{12}C compared to shell-model calculations[26]. 74

5.1 Set of acceptance matrices for protons, π^+ and π^-. 80

5.2 Set of efficiency matrices for protons, π^+ and π^-. 81

5.3 Effect of the smearing procedure presented for the momentum distribution of protons. See text for details. 82

6.1 Correlation between the kinetic energy and the polar angle in the laboratory for the proton in the π N $\rightarrow \pi$ N process. 84

6.2 Same for the correlation between the proton and pion polar angles in the laboratory. 84

6.3 Center-of-mass momentum of pions and protons in the π N $\rightarrow \pi\pi$ N reaction at 0.69 GeV/c. 85

6.4 Correlation between proton and pion momenta in the laboratory in the π N $\rightarrow \pi\pi$ N reaction at 0.69 GeV/c. 86

6.5 Results of PLUTO simulations for the πN$\rightarrow \pi\pi$N reaction: $\pi\pi$ invariant mass distribution. 86

6.6 Comparison of the energy in the π^-p center-of-mass in the quasi-free π^-p reaction on ^{12}C (red) and in the free reaction (black) in PLUTO simulations. 89

6.7 Effective proton mass in the quasi-free π^-p reaction on ^{12}C in PLUTO simulations. 89

6.8 Predictions of INCL++ for the $\pi^- + C$ reaction at 0.685 GeV/c. 90
6.9 Predictions of INCL++ for the $\pi^- + C$ reaction at 0.685 GeV/c. Distribution of the multiplicities of π^+,π^-, $\pi^0$and of all pions. 91
6.10 Predictions of INCL++ for the $\pi^- + C$ reaction at 0.685 GeV/c. Distribution of the multiplicities of the protons, neutrons and all nucleons. 91
6.11 Distribution of the different categories of events, as predicted by INCL++ for the $\pi^- + C$ reaction at 0.685 GeV/c. The height of each bin is roughly proportional to the probability of the corresponding category. 92
6.12 Comparison of experimental results and theoretical predictions for the $\pi^- + {}^{12}C \rightarrow \pi^- + p + X$ reaction. The black line represents the theoretical center-of-mass momentum of the free elastic $\pi^- + p$ process = 0.432 GeV/c. 93
6.13 Left: Momentum correlation between the detected protons and negative pions showing two well-separated contributions (inelastic on the left and QE on the right). The black line corresponds to the momentum correlation for the free binary reaction $p + \pi^- \rightarrow p + \pi^-$. The red line shows the selections used for quasi-elastic and inelastic $p\pi^-$ events. Right: azimuthal angle difference between the detected proton and π^-, after applying the graphical cut shown on the left. 94
6.14 Angular distribution of the π^- for the quasi-elastic events. The distribution is shown in the center-of-mass frame of a $\pi^- + p$ reaction with a proton at rest. 95
6.15 Distribution of the missing mass M_{miss} for π^-+p events measured in the free π^-p reaction (cyan triangles), for selected quasi-elastic events measured on the carbon target (black dots) and for model calculations of the $\pi^- + C$ reaction using the same selection as data (colored curves). 96
6.16 Missing mass for the quasi-elastic process, calculated on the carbon target: $\pi^- + {}^{12}C \rightarrow \pi^- + p + X$. 97
6.17 Distribution of the missing momentum $\vec{P}$miss. The Black line represents the Fermi momentum (0.21 GeV/c) taken from [23]. 97
6.18 Impact of suppressing the multipion production in one step in INCL++ on the quasi-elastic observables. 99
6.19 Impact of using a mass-dependent Fermi momentum in INCL++ on the quasi-elastic observables. The default value in INCL++ for all nuclei is 270 MeV/c (blue). The mass-dependent value for Carbon is 210.632 MeV/c (magenta). 100
6.20 Impact of removing the local energy procedure in INCL++ on the quasi-elastic observables. 101
6.21 Comparison using INCL++, of protons momenta in the $p\pi^-$ channel, distinguishing between events where all protons are included (black curve) and events with only cascade protons (red colored area). Left: full solid angle (4π). Right: HADES acceptance. 102
6.22 p and π^+momentum correlation, for the pπ^+channel. The black line represents the elastic scattering p+π kinematics. 104

6.23 Analysis of the $\pi^- + C \rightarrow \pi^- + p + X$ reaction after selection of inelastic events: missing mass as a function of invariant mass. . . . 104

6.24 Analysis of the pπ^+ channel in the π^- + C $\rightarrow$ π^+ + p + X reaction: missing mass as a function of invariant mass. . . . 104

6.25 Analysis of the $\pi^- + C \rightarrow \pi^- + \pi^+ + p + X$ reaction. Top: missing mass as a function of invariant mass. Bottom: momentum as a function of the angle of the proton. . . . 106

6.26 Analysis of the $\pi^- + C \rightarrow \pi^- + \pi^- + p + X$ reaction. Top: missing mass as a function of invariant mass. Bottom: momentum as a function of the angle of the proton. . . . 106

6.27 Invariant mass (right) and missing mass distributions (left) for pπ^- events with the inelastic selection. . 107

6.28 Same Fig. 6.27 for the pπ^+ channel. . . . 107

6.29 Proton momentum in the CM for pπ^+events. . . . 108

6.30 Center-of-mass momenta of the π^-(left plot) and π^+(right plot) in the p$\pi^-\pi^+$channel. . . . 108

6.31 Missing mass and invariant mass of the π^-p $\rightarrow$ p $\pi^-\pi^+$+X channel. . . . 109

6.32 Invariant mass of the $\pi^-\pi^+$system in the $\pi^-\pi^+$channel. . . . 110

6.33 Invariant (right) and missing (left) masses for p$\pi^-\pi^-$channel. . . . 111

6.34 Center-of-mass momentum of the proton in the p$\pi^-\pi^-$channel. . . . 111

6.35 $\pi^-\pi^-$invariant mass in the p$\pi^-\pi^-$channel. . . . 112

6.36 $\pi^-\pi^-$ invariant mass distributions measured for $\pi^-\pi^-$(grey dots) and p$\pi^-\pi^-$events (red histogram) . 113

6.37 Invariant mass of the ppπ^-system in the ppπ^-channel. . . . 114

6.38 Center-of-mass momenta of the pion (left) and the proton (right) for the ppπ^-channel. . . . 115

6.39 Invariant mass and missing mass for the pp channel in INCL++, compared to the case of the pp channel where no pion is emitted (absorbed). . . . 116

6.40 Same as Fig.6.39, but for the center-of-mass distribution of the emitted proton. . . . 116

6.41 Comparison of the invariant mass of the two emitted proton in three channels: pp, pp$\pi^-$and ppp. . . . 116

6.42 Predictions of INCL++ for the pion absorption in the π^- + C reaction at 0.685 GeV/c. Distributions of the multiplicities of the protons, neutrons, and all nucleons. . . . 117

6.43 Comparison of the Proton momentum distribution for the quasi-elastic p$\pi^-\rightarrow$pπ^-channel, for SMASH simulation with and without nuclear potential. . . . 118

6.44 Same as in Fig.6.43, but for invariant mass of the ppπ^-in the ppπ^-channel. . . . 118

6.45 Same as in Fig.6.43, but for the invariant mass of the π^- + C $\rightarrow$ $\pi^-\pi^-$channel. . . . 118

6.46 Same as in Fig.6.43, but for invariant mass of the π^- + C $\rightarrow$ $\pi^-\pi^+$channel. . . . 118

6.47 Double differential cross sections of π^- (a), π^+(b) and protons (c): measured in HADES in π^-+^{12}C reaction at 0.7 GeV/c incident pion energy. The distributions measured at emission angles of 20°, 50° and 70° are shown. In order to facilitate the comparison each distribution at higher angle is multiplied by a factor of 10^{-2}. The experimental distributions are compared to the results of theoretical models: INCL++, RQMD.RMF, SMASH and GiBUU, see the legend for details. 121

6.48 Double differential cross sections of π^- (a), π^+(b), protons (c), deuterons(d) and tritons (e) : measured in HADES in π^-+^{12}C reaction at 0.7 GeV/c incident pion energy. The distributions measured at emission angles in the range $20^\circ - 80^\circ$ are shown. In order to facilitate the comparison, each distribution at higher angle is multiplied by a factor of 10^{-2}. The experimental distributions are compared to the results of the INCL++ model. 122

6.49 Double differential cross sections of π^- (a), π^+(b) and protons (c): measured in HADES in π^-+^{12}C reaction at 0.7 GeV/c incident pion energy. The distributions measured at emission angles in the range $20^\circ - 80^\circ$ are shown. In order to facilitate the comparison, each distribution at higher angle is multiplied by a factor of 10^{-2}. The experimental distributions are compared to the results of the SMASH model with and without nuclear potential. 123

7.1 The nucleon-nucleon potential. 126

7.2 The nucleon momentum n(k) distribution (solid lines) presented for ^{12}C and ^{56}Fe nuclei. The dotted lines show the low-momentum and single-particle part of n(k), i.e., when nucleon-nucleon correlations are switched off. The data points (squares) come from SLAC inclusive measurement A(e,e') [27]. The empty triangles represent the values of n_0(k) obtained from the exclusive experiments on various nuclear targets, e.g. [28, 29]. Figure adopted from [30]. 127

7.3 The experimental fractions of *np* (top) and *pp* (bottom) SRC pairs in nuclei. The green and yellow bands reflect 68% and 95% confidence levels, respectively. np-SRC pairs dominate over pp-SRC pairs in all measured nuclei. Figure adopted from [31]. 128

7.4 Constraints for the "extra momentum" generated by the SRCs. 130

7.5 Evolution of the fraction of high and low momentum neutrons to protons with the neutron excess. Taken from [32] 130

7.6 Evolution of the fraction of high to low momentum protons and neutrons with the neutron excess (N/Z). 131

7.7 Correlation between the proton and pion momentum for the ^{12}C(π^-, π^-pn) reaction simulated with the INCL+SRC cascade model at 0.7 GeV/c. Left panel: all the simulated events. Right panel: the simulated events but with conditions on the *number of collisions* and the *number of SRC collisions*, both equal to 1. 133

7.8 Experimental distribution of the missing momentum of the quasi-elastic pπ^-. The brown line represents the Fermi momentum value (221 MeV/c) which is taken from [23]. 133
7.9 P_{miss} resolution derived from INCL++ simulations. 134
7.10 Missing momentum for the quasi-elastic pπ^-channel. Simulations are normalized to the same area as the data. The distribution is represented in the logarithmic scale for the y-axis. 134
7.11 Missing mass distribution for the quasi-elastic graphical cut of the pπ^-events compared to total, pure quasi-elastic, and rescattering events in INCL++. 135
7.12 Missing momentum distribution for the quasi-elastic graphical cut of the pπ^-events compared to total, pure quasi-elastic, and rescattering events in INCL++. 135
7.13 Same as Fig.7.11 but in different bins in the proton momentum. 136
7.14 Same as Fig.7.11 but in different bins of pion momentum. 137
7.15 The missing momentum distribution for $P_{\pi-} > 600$ MeV/c. The different selections of pπ^-events in INCL++ are compared to the experimental data. QE means using the graphical cut shown in Fig.6.13. 137
7.16 Same as Fig.7.15, but using a logarithmic scale in the y-axis. 137
7.17 The missing momentum distribution for $P_{\pi-} > 600$ MeV/c compared between INCL++ simulations with/without SRCs with data. 139
7.18 Schematic drawing of the two proton knockout A(π, $\pi^{'}$pp) reaction, within the SRC model. 139
7.19 Correlation between the proton and pion momentum in the experimental data for the ^{12}C(π^-, π^-pp) reaction at 0.7 GeV/c. The correlations are plotted after deciding on which proton is a participant one and which is a spectator one. 140
7.20 Missing mass distributions obtained for the ^{12}C(π^-, π^-pp) reaction from the data (black line) and the INCL++ simulations (red line). Left plot presents normalized yields and the right plot shows arbitrary normalized distributions to compare their shapes. 142
7.21 Missing momentum distributions obtained for the ^{12}C(π^-, π^-pp) reaction from the data (black line) and the INCL++ simulations (red line). Left plot presents normalized yields and the right plot shows arbitrary normalized distributions to compare their shapes. 142
7.22 Distribution of the cosine of the angle between the recoil nucleon and missing momentum. Data measured by the BM@N collaboration for ^{12}C(p,pp)^{10}B reaction at 48 GeV/c of the ^{12}C beam are compared to GCF predictions (orange line) [33, 34]. 143
7.23 Distributions of cosine of the angle γ between the missing momentum p_{miss} and the momentum of the recoil proton p_{prot} for the ^{12}C(π^-, π^-pp) reaction obtained from the data (black line) and the INCL++ simulations (red line). Left plot presents normalized yields and the right plot shows arbitrary normalized distributions to compare their shapes. 143

List of Tables

2.1 Targets properties [35] 47

2.2 Summary of the collected statistics [35] in the pion beam experiment. 47

6.1 List of cross sections for various final states in π^-N collisions at $\sqrt{s_{\pi N}}$= 1490 MeV from the SAID analysis (solution WI08). 83

6.2 Table of different cross sections for experimental measurements of different hadronic exit channels consisting of two or three charged particles, compared with the models and calculated in the HADES acceptance. 117

Chapter 1

Introduction

Strong interaction is governing the microscopic structure of all known composite objects in the universe. Understanding the behavior of strongly interacting systems is therefore a challenging task, attracting interest from several scientific fields, as nuclear physics, hadronic physics and astrophysics. Both experimental and theoretical studies are needed, as progress can only be made by the comparison between model predictions and measured data. My PhD work focuses on hadronic systems resulting from the interactions of pions with carbon nuclei and presents a comparison between measurements and simulations based on existing models.
In this introductory chapter, our focus will be on highlighting the motivations behind studying the $\pi^- + ^{12} C$ reaction at 0.7 GeV/c. We will start from the general objectives of the HADES experiments conducted at the GSI facility and explain how these experiments provide valuable information for hadronic physics and baryon-dominated matter physics. We will also emphasize the importance of using transport models to effectively interpret the experimental data and the interest of pion beam experiments to validate these models. The motivation of our study will also be presented in a more general perspective, as it provides novel data, of fundamental interest for understanding the response of a nucleus to an excitation at energies above the $\Delta(1232)$ resonance. Lastly, we will dedicate a section of this chapter to reviewing the existing data obtained through pion beam experiments conducted within the energy range relevant to our research.

1.1 The strong interaction

Four types of interactions are known. While, in our daily experience, electromagnetic and gravity play the major role, the strong interaction is dominating at distances smaller than a few fm. The range of the weak interaction is even smaller by two orders of magnitude. This interaction is however crucial, e.g., to explain the nucleosynthesis in stars, but it does not play a role in binding the particles together. The structure of the matter at the nuclear scale is

therefore clearly due to the strong interaction.

At the most elementary level, the strong interaction is an interaction between quarks, antiquarks and gluons, described by a quantum field theory, the Quantum ChromoDynamics (QCD) [36]. One fundamental property of QCD is the confinement, i.e. quarks and gluons are bound in particles, called hadrons. Quarks can only be found in nature as groups of three quarks (baryons) or pairs of quarks and antiquarks (mesons), or rarely in some other combinations, but never isolated. The most common hadrons are the nucleons. In addition, in the low energy and non-strange sector, which is relevant for our study, the pions (π^-,π^+,π^0), η, $\rho(770)$ and $\omega(782)$ mesons and the $\Delta(1232)$, N(1440), N(1520) and N(1535) baryons are playing an important role.

At small distances or high energy interactions, the strong coupling constant α_S is small, and perturbative calculations directly based on QCD can be performed. However, most strong interaction processes occur at energy scales where α_S is large. An important effort is therefore needed to develop and test models able to describe QCD phenomena in the non-perturbative QCD range and test them by the confrontation with data for various systems and reaction types.

1.2 HADES and the QCD phase diagram

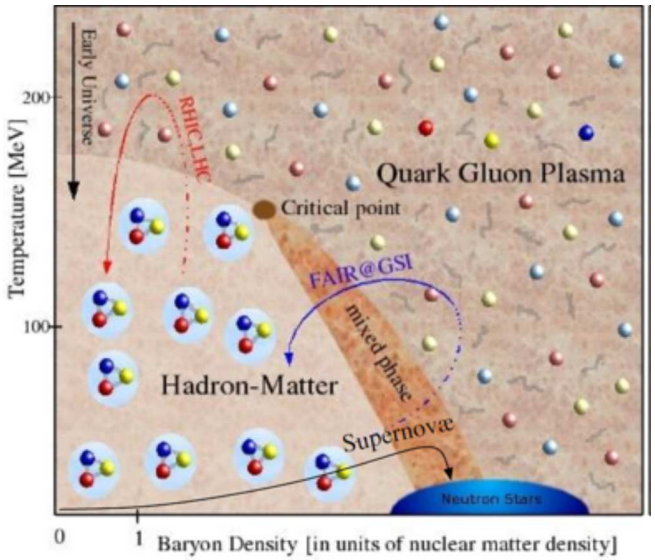

Figure 1.1: Sketch of the QCD phase diagram (temperature versus baryochemical potential) showing the Hadron-Matter and Quark Gluon Plasma phases.

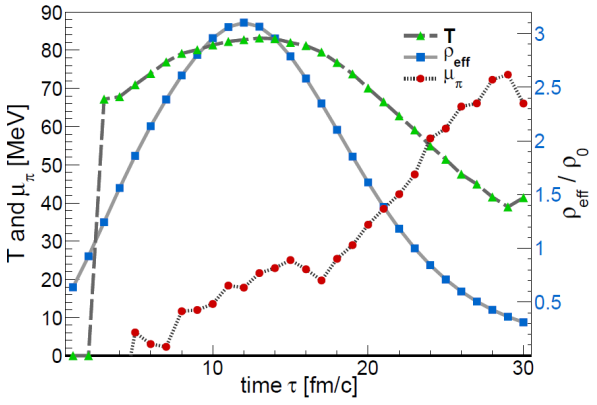

Figure 1.2: Evolution of average temperature (green), baryochemical potential (red) and density (blue) as a function of time in a Au+Au collision at an energy of 1.23A GeV in a coarse-grained approach based on the UrQMD transport model [1].

The most common form of matter around us is the atomic nucleus, made of bound neutrons and protons. Further in the universe, neutron stars are characterized by very high neutron densities ($\sim 5-10\rho_0$ and ρ_0= 0.17 nucleons/fm^3 is the normal nuclear density) and very low temperatures. Collisions of compact stellar objects were recently observed, in particular, thanks to the detection of gravitational waves [37], where lower densities ($\sim 2-3\rho_0$)

and higher temperatures (up to 70 MeV) can be reached [38]. Besides, in the early universe, a few μs after the BigBang, a deconfined phase of quarks and gluons (the Quark Gluon Plasma) existed, with large temperatures and essentially zero net baryonic density ($i.e$ the difference between baryon and antibaryon density). These different types of matter find their place in the QCD phase diagram of strongly interacting matter, which can be represented, using the baryonic chemical potential (μB) and the temperature (T) (Fig.1.1). The study of the QCD phase diagram can offer valuable insights into the fundamental properties of QCD, but it necessitates both theoretical modeling and experimental investigation to comprehend the properties and boundaries of the different regions. A challenging question is the equation of state (EOS) of hadronic matter (see [39] for a recent review). Theoretical approaches, such as lattice QCD and effective models are developed to describe the different phenomena, while experimental studies, such as those conducted at heavy-ion facilities like LHC, RHIC, and GSI deliver the data. To explore the different regions of the QCD phase diagram, experiments are conducted at various center-of-mass energies per nucleon $\sqrt{s_{NN}}$. At very large $\sqrt{s_{NN}}$, as reached at LHC or RHIC, the main objective of heavy-ion experiments is to produce a Quark Gluon Plasma and study its properties in detail. In this region, lattice QCD calculations can be performed to make predictions, which in particular, demonstrate that the transition between the hadronic and deconfined phase is a smooth transition, or cross-over. Such calculations can only be extended up to about μ_{B}=300 MeV [40]. At larger values of μ_{B}, the transition could be of the first order, which would then imply the existence of a critical point, marking the limit between the two regions. Experiments at RHIC with reduced energy (RHIC-BES), down to $\sqrt{s_{NN}}$=3 GeV are currently being performed in order to study hadronic matter at finite net baryon densities and to look for this critical point. Such studies require the measurement of various observables as a function of the energy to pin down discontinuities, which could signal the vicinity of the critical point. Versatile and large acceptance set-ups are therefore required for such studies. A major progress in the field is expected, in particular, from the results of the future experiments with the Compressed Baryonic Matter (CBM) set-up [41] at the FAIR facility under construction in Darmstadt [42]. The HADES experiment, operating at the SIS18 facility at GSI is exploring the low energy region of the QCD phase diagram, with heavy-ion experiments in the range of $\sqrt{s_{NN}}$ up to 2.6 GeV. In the search for the critical point, HADES serves as a low-energy reference and provides information on the microscopic structure of baryon-dominated matter, in particular its content in hadronic resonances and strangeness. Studies of the hadronic matter in the SIS18 region recently attracted a lot of interest, as it exhibits conditions as close as possible to the ones observed in neutron star mergers. However, the access to the EOS is only possible via models, which need to be validated in conditions where they are not sensitive to the EOS. At SIS18 energies, the strongly interacting matter is substantially compressed and collective kinetic energy is converted into intrinsic degrees of freedom. As a result, nucleons are excited to baryonic resonances which can propagate and regenerate due to their short lifetime compared to the long life-time of the dense phase in these collisions (typically of the order of 1.5 and 15 fm/c). As shown in Fig. 1.2, the baryonic density (blue curve) reaches values close to three times the normal nuclear density and the maximum temperature is close to 80 MeV in the Au+Au reaction at 1.23A GeV. A large fraction of

these baryons are baryonic resonances. The excitation of baryonic resonances governs the production of mesons, via their hadronic decays (R→NM, where R is a baryonic resonance, M is a meson and N a nucleon). But it is also a major source of electromagnetic radiation, via the Dalitz decay processes (R→ N e^+e^-). Up to 2 GeV/nucleon, the $\Delta(1232)$ is dominating, but for higher energies, higher lying resonances become important. In this energy range, the production of pions via the excitation of baryon resonances is the dominant contribution to inelastic nucleon-nucleon reactions. The dynamics of the heavy-ion reactions is therefore driven by the succession of nucleon-nucleon and pion-nucleon reactions, which distributes the initial global kinetic energy of the incident nucleus into many participant nucleons and produced mesons. This process may lead to the thermalization of the nucleus, where an equilibrium can be reached, at least locally and the ”memory” of the initial nucleon-nucleon collisions is lost.

1.3 Hades experiments

1.3.1 Heavy-ion collisions

The main mission of the HADES experiment is to study the hot and dense phase in heavy-ion collisions at a few GeV per nucleon, i.e., in conditions close to neutron stars. Several systems have been measured: C+C at 1 and 2A GeV [43], Ar+KCl at 1.65A GeV[44], Au+Au at 1.25 AGeV [2] and more recently, Ag+Ag at 1.65A GeV. Although HADES was designed for dilepton detection, which carries undisturbed information about all stages of the collision [45], many other observables are measured to characterize the properties of the hadronic medium, as meson production [46], sub-threshold strangeness production [44], baryonic resonance excitation [47], light cluster formation, fluctuations of proton number, etc.

1.3.2 Cold matter studies

The study of proton-nucleus and pion-nucleus reactions allows to investigate effects at normal nuclear densities, i.e., in better controlled conditions than in heavy-ion collisions. HADES has measured the reaction p+Nb at 3.5 GeV, where both dilepton and hadronic final states were studied [48]. The pion beam (see Sec. 2.7) has also been used to study π+A reactions (π^- + W and C at 1.7 GeV/c), but only hadronic channels could have been measured, due to the lack of beam time. This thesis is devoted to the study of hadronic systems.

1.3.3 Nucleon-nucleon collisions

To fully understand the in-medium e^+e^- radiation, measurements of the dilepton spectrum from elementary collisions (pp or np via dp) are needed. They provide an important reference for the interpretation of heavy-ion results since they can be used directly to constrain dilepton sources from the initial stages of the reaction. Exclusive chan-

nels as pp→ppe$^+$e$^-$ allow us to study Dalitz decays of N* or Δ resonances ($R \rightarrow Ne + e-$) and investigate the time-like electromagnetic transition form factors of these baryons. For example, detailed studies of the $\Delta^+ \rightarrow pe+e-$ Dalitz decay have been performed in proton-proton (p+p) collisions at 1.25 GeV, resulting in the extraction of the corresponding branching ratio [49]. Measurements of dielectron production in p+p collisions at 3.5 GeV revealed the importance of higher mass resonances and demonstrated the strong influence of their couplings to the ρ meson (R→Nρ → Ne$^+$e$^-$). Such results have an important impact on in-medium dilepton emission. Indeed, the ρ meson spectral functions are expected to be strongly modified in the hot and dense medium. In addition, HADES experiments in nucleon-nucleon collisions can provide elementary cross sections for meson, hyperon, or baryonic resonance production, which are necessary ingredients for the interpretation of heavy-ion or p+A collisions. The analyses of data measured in nucleon-nucleon reactions exploited the complementarity between hadronic and electromagnetic channels. Reaction mechanisms and in particular baryon resonance production can indeed be more easily constrained in the meson production channels, which present larger statistics. These constraints are then used for the study of the Dalitz decay of baryons, which is a rare process.

1.3.4 Pion-nucleon collisions

The study of baryon resonances higher than $\Delta(1232)$ in proton-proton reactions is however complicated due to the overlap between resonances of different masses. This motivated a new experimental program using the GSI pion beam. In π-N reactions baryon resonances are produced with a fixed mass M in the s-channel $M = \sqrt{s_{\pi N}}$, which is a big advantage with respect to NN collisions. HADES has started from the exploration of the second resonance region with an energy scan around the N*(1520) and N*(1535) resonance mass with a focus on two pion [13] and dielectron production channels [50]. This measurement has been performed using a C_2H_4 polyethylene target and a pion beam at four pion beam momenta 0.650, 0.685, 0.733, and 0.786 GeV/c. The motivation for the beam energy scan was the study of two-pion production channels using a Partial Wave analysis (see Sec. 1.5.2). The largest fraction of the beam time period was devoted to the pion beam setting at 0.685 GeV/c, to study the time-like electromagnetic structure of baryons in the second resonance region using the e^+e^- radiation [13, 51]. Simultaneously, measurements with a carbon target were also performed in order to subtract interactions with carbon nuclei from the polyethylene target. This PhD work is focused on the analysis of the data recorded on the carbon target at a beam momentum of 0.685 GeV/c.

1.4 Transport and cascade models for data interpretation

Transport models are unavoidable tools for the interpretation of data obtained from heavy-ion collisions over a wide range of energies. Although they involve less detailed physics processes than transport models, cascade models are also relevant for the description of some hadronic channels, in particular for p+A or π+A reactions. In chapter 4, more details about these models will be given. Here we show some examples of comparisons of transport model predictions to HADES data.

1.4.1 Dilepton emission in heavy-ion reactions

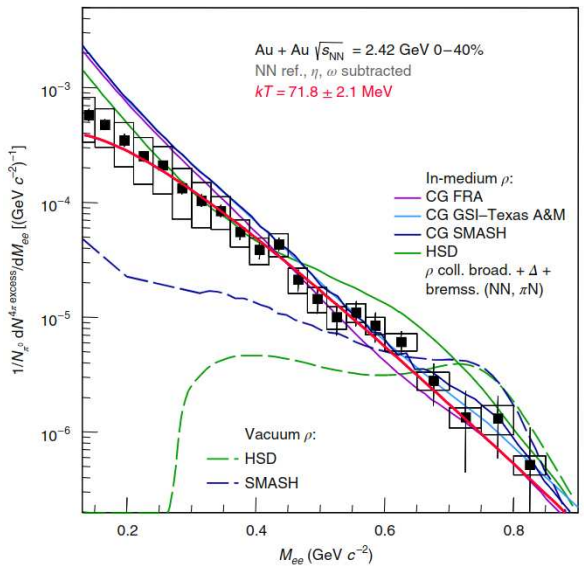

Figure 1.3: Dilepton excess yield extracted by subtracting η contributions and NN reference after acceptance corrections. The yield is normalized to the number of neutral pions. Dashed curves: ρ ("vacuum" spectral function) contribution from HSD and from SMASH (dark blue) transport model calculations. Solid green curve: total HSD calculation. The blue, pink and dark blue curves show the results of three versions of coarse grained calculations using the modified ρ meson spectral function. See [2] for details.

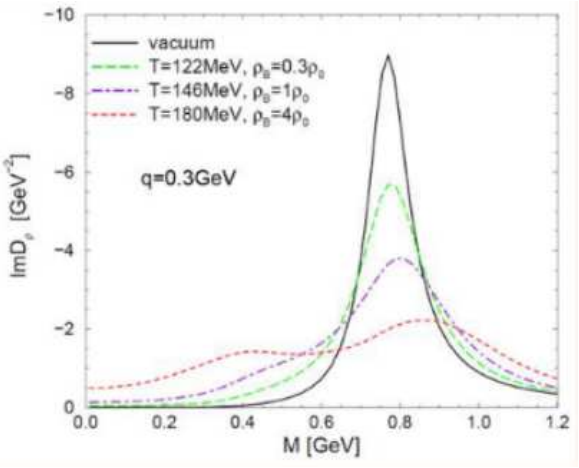

Figure 1.4: Imaginary part of the ρ meson propagator (or spectral function) plotted for a constant momentum (q = 0.3 GeV/c) at different temperatures and baryon densities [3].

Fig. 1.3 shows the invariant mass spectrum for the e^+e^- emission from Au+Au at 1.25A GeV [2] obtained after subtraction of the reference measured in pp and pn reactions. It can be observed that no clear structure is present in the data for invariant masses around $M_{ee} = 0.7 GeV/c^2$. The data therefore favor calculations including, a modified ρ meson spectral function. These modifications are implemented in the HSD (Hadron String Dynamics) transport model by increasing the ρ meson width to take into account its interactions with the medium (collisional broadening). On the other hand, in coarse-grained approaches (noted as CG), a spectral function calculated in many-body approaches is used, as shown in Fig. 1.4. During the collision, at each step in time, the temperature and the density are calculated. The latter determines the exact shape of the spectral function, which is then used by the model to estimate the e^+e^- distributions. In both approaches, the distortions of the e^+e^- spectrum due to the

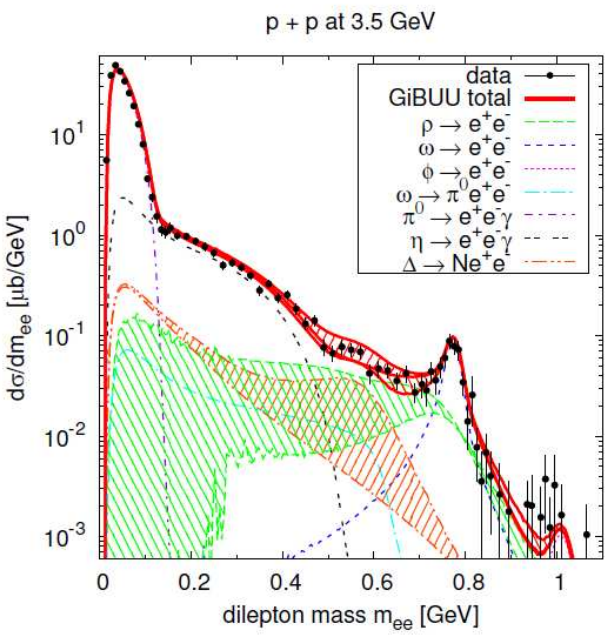

Figure 1.5: Dilepton mass spectrum for pp collisions at 3.5 GeV. The hatched areas indicate the effects of the Δ form factor and baryon-resonance contributions to the ρ production, respectively. The total is shown (from bottom to top) with Δ form factor (left-hatched), ρ resonance contributions (right-hatched) and with both of these effects together [4].

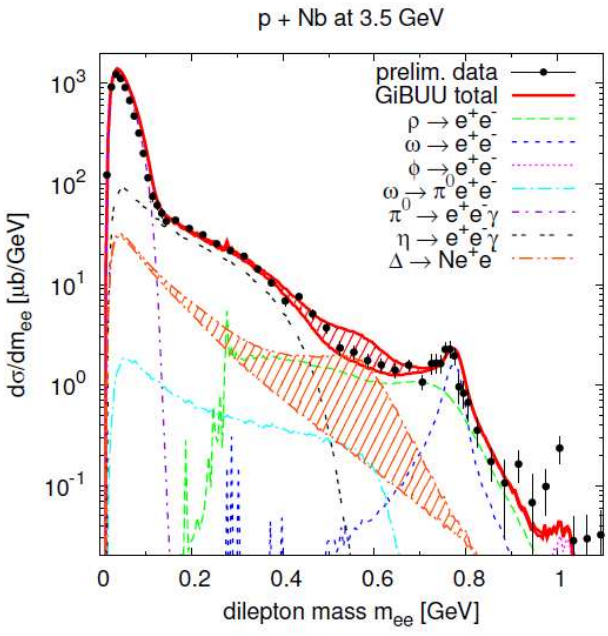

Figure 1.6: Dilepton mass spectrum for p+Nb at 3.5 GeV, showing all contributing channels with vacuum spectral functions. The hatched area indicates the effect of the Δ form factor [4].

ρ meson propagation in the medium are very sensitive to the dynamics of the reaction, which, as explained above, is strongly influenced in the SIS18 energy range by pion-nucleon interactions.

The confrontation of transport model predictions to dilepton spectra measured in proton-proton reactions allows to check that the elementary sources of dilepton production (vector meson decays, scalar mesons, and baryon resonance Dalitz decays, etc.) are correctly treated, while the measurements in proton-nucleus are sensitive to secondary reactions mainly due to pion-nucleon collisions. Results are shown in Fig. 1.5 and 1.6 for the GiBUU transport code.

1.4.2 Hadron production in Au+Au collisions with HADES

However, significant discrepancies are observed for pion multiplicities measured for the Au+Au system at 1.25A GeV [5]. This is shown in Fig. 1.7, where state-of-the-art transport models, including PHSD, IQMD, PHQMD, GiBUU, and SMASH, were compared to experimental results. This indicates that the current transport models face challenges in accurately describing all the aspects of such heavy-ion reactions.

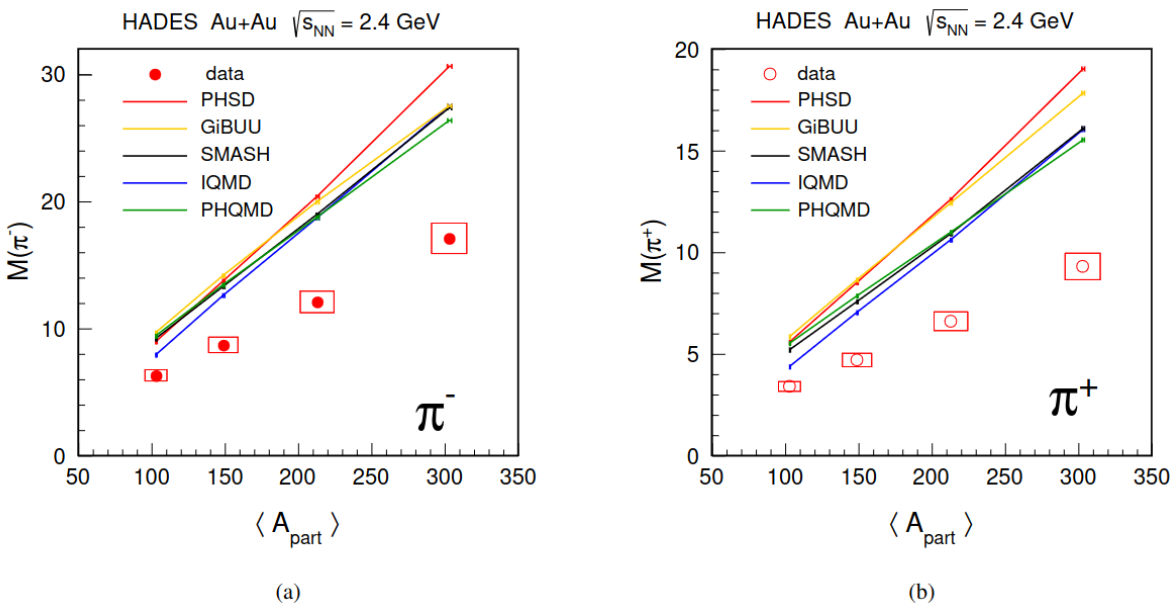

Figure 1.7: Pion multiplicities measured in Au+Au reaction at 1.25A GeV are compared to predictions from various transport models [5].

1.4.3 Hadron production in p+Nb collisions at 3.5 GeV with HADES

Another example is given by the recent studies of the p+Nb reaction at 3.5 GeV. In this case, the matter is probed in quite different conditions than in the Au+Au reaction at 1.25 GeV. The higher energy favors inelastic reactions which excitation of higher lying resonances or hyperons and the production of heavier mesons. One can then mostly assume that these products travel in normal nuclear matter at zero temperature. The study of hydrogen isotope (*p*, *d*, *t*) and charged pion (π^+, π^-) production in this system revealed deficiencies of the data description by GiBUU (Giessen Boltzmann-Uehling-Uhlenbeck) and UrQMD (Ultra-relativistic Quantum Molecular Dynamics) transport calculations and the INCL++ cascade model [6, 52]. In general, these models are able to reproduce the data only within a factor of ~ 2. The best description of the angular and energy dependent distributions of protons (see Fig. 1.8) and charged pions (see Fig. 1.9) is provided by the GiBUU model. In the case of the composite particles production (*d*, *t*) the INCL++ model describes very well the differential production cross sections for tritons, while it overestimates the data in the case of the deuterons, see Fig. 1.10.

1.4.4 Hadron production in π^-+C and π^-+W collisions at 1.7 GeV/c with HADES

The inclusive strange (Λ, K^0_s, $K^\pm$) and non-strange (p, π^+, π^-) hadrons production have also been studied with the pion beam experiment at 1.7 GeV/c with carbon and tungsten targets [7]. The main goal of this measurement was to study K^- and ϕ mesons absorption in nuclear matter [53]. The inclusive spectra have been compared to the transport model calculations SMASH and GiBUU. The transport models have also been compared to the inclusive proton and charged pion cross sections as a function of the rapidity, see Figs. 1.11, 1.12.

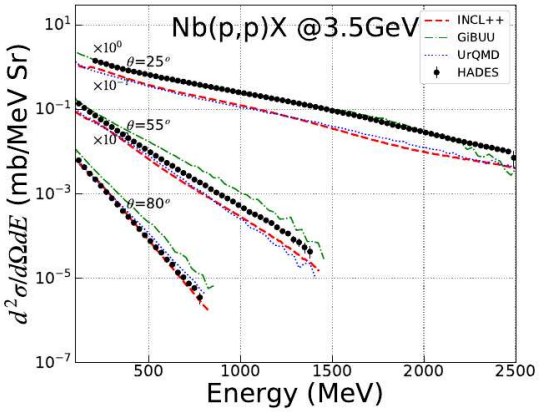

Figure 1.8: Double differential cross sections for protons measured with HADES in the p+^{93}Nb reaction at 3.5 GeV (full circles). Cross sections are shown for three laboratory emission angles of $\theta = 25°$, $\theta = 55°$ (multiply by factor 10^{-1}) and $\theta = 80°$ (multiply by factor 10^{-2}). The experimental distributions are compared to the theoretical models: GiBUU (dash-dotted lines), UrQMD (dotted lines) and INCL++ (dashed lines). Figure adopted from [6].

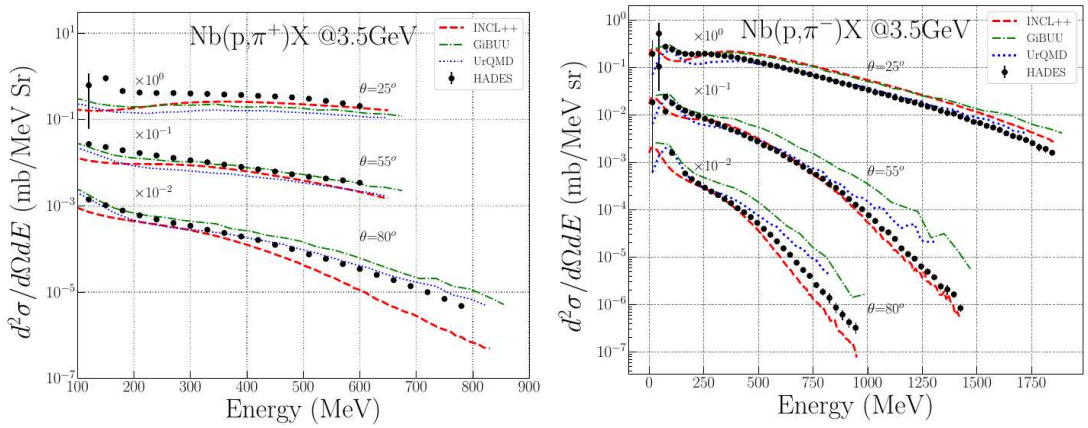

Figure 1.9: The same as in Fig. 1.8 but for π^+ (left plot) and π^- (right plot).

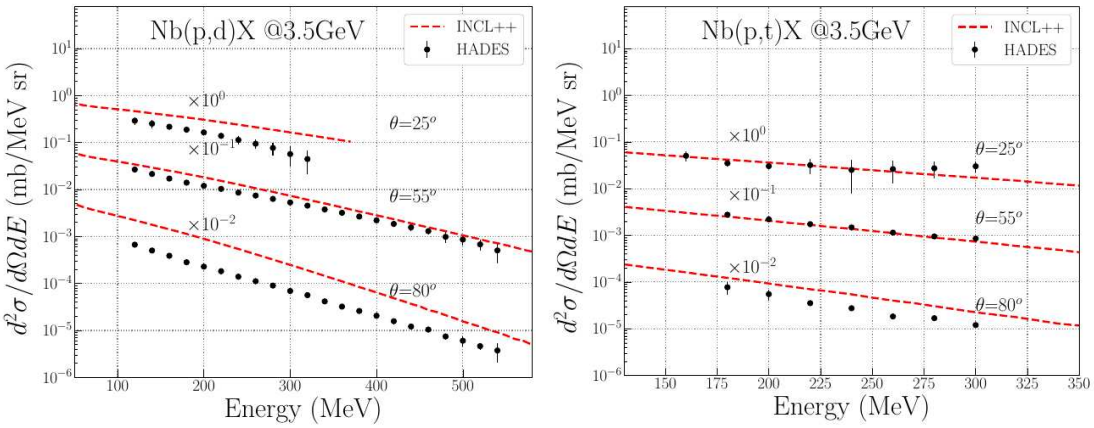

Figure 1.10: Double differential cross sections for deuterons (left plot) and tritons (right plot) measured with HADES in the p+^{93}Nb reaction at 3.5 GeV (full circles). Cross sections are shown for three laboratory emission angles of $\theta = 25°$, $\theta = 55°$ (multiply by factor 10^{-1}) and $\theta = 80°$ (multiply by factor 10^{-2}). The experimental distributions are compared to the INCL++ model (dashed lines). Figure adopted from [6].

Large differences between the two model predictions can be observed, especially for the pion production. The deviations w.r.t. experimental yields are also largest for pion production and reach 100% for π^- produced at target

rapidities in the π^-+W reaction, while the differences stay with 30% for the carbon target. The difficulty of describing pion spectra might be related to the fact that pions are all the time regenerated via baryon resonances excitation and decay. They are produced in the final stages, but their distribution is sensitive to the description of the full collision process.

The pion production was also investigated as a function of the transverse momentum p_T, see Fig. 1.13. At the highest p_T, the description of the data is very poor and both models overshoot the data. This is the region of the quasi-elastic process, where an elastic scattering occurs between the incident pion and one of the target nucleons. In our analysis, we will investigate pion and proton spectra measured both in the inclusive and various exclusive channels of the π^--^{12}C system at 0.7 GeV/c, see Sec. 6.

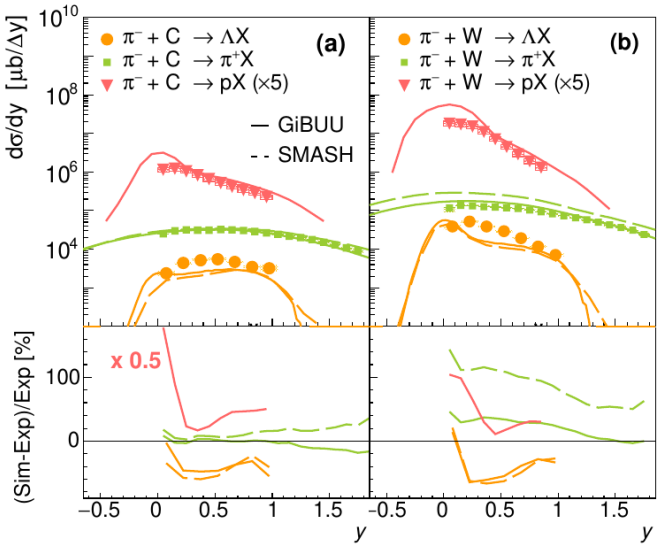

Figure 1.11: Upper panel: cross sections of Λ (orange), π^+ (green) and proton (red) as a function of rapidity in π^-+C (a) and π^-+W (b) reactions compared to the transport models, GiBUU (solid curve) and SMASH (dashed curve). Lower panel: deviations of the transport model simulations from the measured cross section as a function of rapidity. Figure adopted from [7].

1.4.5 Other applications of transport and cascade models

The transport models are unique tools for describing nucleus-nucleus, pion-nucleus, or proton-nucleus reactions, as they are able to take into account the dynamics of the reaction in detail. They are not able to describe coherent effects, but the latter can be incorporated using external inputs (e.g. modified spectral functions,..). Cascade models are more simple models, with much less sophisticated physics ingredients and less degrees of freedom. For example, INCL++ takes into account the $\Delta(1232)$ resonance, but no heavier baryon resonance. However, this is sufficient for many applications and allows for much faster calculations than transport models. This is why cascade models, and in particular INCL++ are commonly used in GEANT4 simulations for count rate estimates to prepare an experiment or for simulations of detector response in a realistic environment.

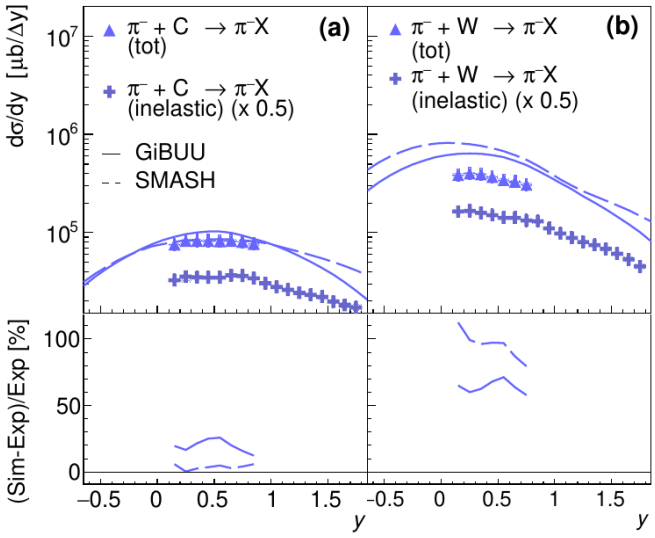

Figure 1.12: Comparison of the total (triangles) and inelastic (crosses) π^- differential cross sections as a function of rapidity with GiBUU (solid curves) and SMASH (dashed curves). Figure adopted from [7].

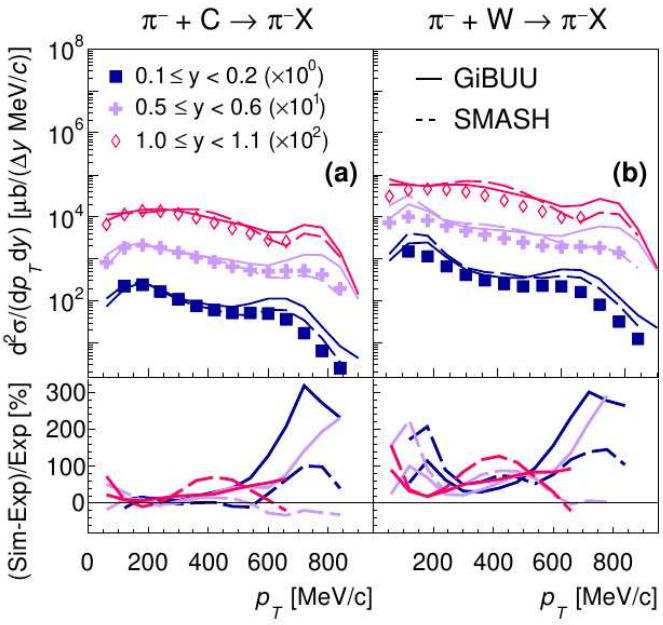

Figure 1.13: Upper panel: double-differential cross sections for π^- as a function of the transverse momentum p_T in π^-+C (a) and π^-+W (b) reactions compared to GiBUU (solid curves) and SMASH (dashed curves) for various rapidity ranges (see legend). Lower panel: Relative deviations between experimental data and the two transport model calculations. Figure adopted from [7].

A realistic description of pion interactions with nuclei is e.g. of interest for the simulation of the response of electromagnetic calorimeters, to discriminate at momenta of the order of 1 GeV or less, electrons, which lose almost all their energy in the detector material, to pions, which constitute a huge background and can also lose a big fraction of their energy by hadronic interactions. To properly describe the purity of the electron selection, the simulation needs to include an appropriate hadronic model. A limitation in these studies arises from the fact that these hadronic models could not be validated in the energy range between 500 MeV and 3 GeV, due to the lack of

data.

A good description of pion interactions with nuclei is also very important for neutrino physics. Such aspects contribute very significantly to the uncertainties on the determination of utmost important measurements, as oscillation parameters, related to the neutrino mass difference. For experiments with accelerator neutrinos, the flux of neutrinos is driven by the flux of pions and kaons which are produced by the interactions of protons on thick targets. Pions can be produced from interactions with the target, but also from secondary interactions with the material surrounding the target. They can also be rescattered or absorbed in this material before their decay. All these processes therefore influence the neutrino flux. Measurements (e.g. with the T2K replica target) are performed to measure the pion production in conditions similar to the neutrino production site and constrain neutrino flux predictions. Direct measurements of the flux are provided by detectors placed at a small distance from the accelerator facility (Near Detectors), i.e., before oscillations can impact the flux. The ν_μ energy is usually based on the detected muon, resulting from the neutrino-nucleus interaction. The energy is transferred to the nucleus via the electroweak interaction, which is of course different in the case of pion-induced reactions, but the dissipation of this energy in the nucleus can be described in a similar way, and it is dominated, in the energy range below 2 GeV, which is relevant for these neutrino experiments, by pion dynamics. As a matter of fact, the same hadronic models can, therefore be used for neutrino-induced and pion-induced reactions [54, 55, 56]. To complement existing data in the region of the $\Delta(1232)$ resonance, the DUET collaboration recently performed dedicated experiments to provide new measurements for pion charge-exchange and absorption cross sections [57], but measurements for higher energies, where no data exist, urgently need to be improved. In the next generation of near detectors, the detection of a proton in addition to the muon will be used. This should provide a better estimate of the neutrino energy but requires an even more detailed description of the processes involved. In her PhD thesis, Anna Ershova [58, 59] investigated the sensitivity of the results to two cascade models, NuWro and INCL++. By studying the emission of pions and protons in a π^-+ C experiment and providing benchmark tests of the INCL++ model, our study can therefore help reduce the uncertainties of neutrino experiments. This will be very important in view of future high precision experiments, like DUNE [60].

1.5 Pion induced reactions in the second resonance region

The De Broglie wavelength of a pion with momentum p_{beam}= 690 MeV/c is $\lambda = h/p = 2\pi\bar{h}/p = 1.8$ fm, which is smaller than the distance between two nucleons in a nucleus ($\sim$2 fm). One can therefore consider that the incident pion interacts with a single nucleon in the target nucleus. This also justifies the use of transport and cascade models, which consider a series of NN collisions. Due to the combined effects of the Fermi momentum and the binding energy of the nucleon in the carbon nucleus, the energy available for the πN reaction products is expected

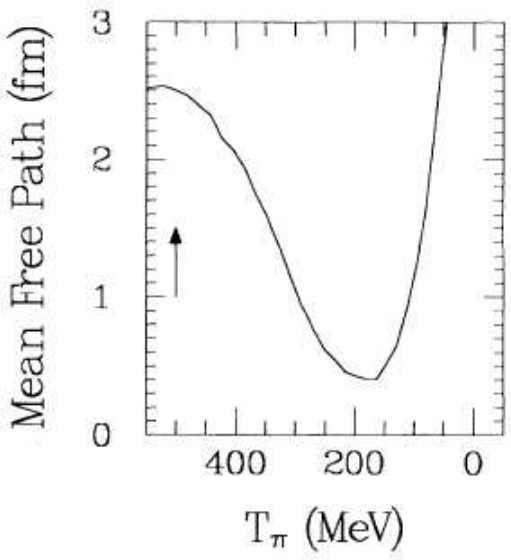

Figure 1.14: The calculated pion mean free path (mfp) as a function of kinetic energy. The calculation of the mfp is $1/\rho_0\sigma_{tot}$, where ρ_0 is the central nuclear density and and σ_{tot} is the isospin-averaged pion total cross section at a given kinetic energy [8].

to be smeared w.r.t. the π+N case. Nevertheless, it can be expected that the main characteristics of the $\pi^- + \mathrm{C}$ reaction at p^i_π= 690 MeV/c are given by the π^-+p reaction at the same incident pion momentum, corresponding to an energy in the π^-+p center-of-mass, $\sqrt{s_{\pi\mathrm{N}}}$= 1490 MeV. As will be discussed in the following, final state interaction and rescatterings modify such a quasi-free picture. However, at energies above 500 MeV, the πN cross section is lower than in the $\Delta(1232)$ region, so the rescattering effects are also expected to be reduced. This is illustrated in Fig. 1.14, which shows the pion mean free path, calculated as:

$$\lambda = \frac{1}{\rho_0 \sigma_{tot}}, \tag{1.1}$$

where ρ_0 is the central nuclear density and σ_{tot} the isospin-averaged pion total cross section at a given kinetic energy σ_{tot}. Above 500 MeV, this mean free path is of the order of 2.5 fm, i.e. somewhat similar to the carbon nucleus radius (~ 2.7 fm). This confirms that the rescattering effects should not completely distort the quasi-free picture. The information on the πN reactions is also crucial because it is used as a direct input in the calculations of the π^-+ C reaction at the same energy. We will therefore start the discussion by investigating the experimental information on the free reaction.

1.5.1 Pion-nucleon reactions

Pion-nucleon reactions have been in the past the main source of information on the baryon spectrum. Indeed, a baryon with a mass $M = \sqrt{s_{\pi\mathrm{N}}}$ can be directly excited in such reactions. The existence of a baryon is reflected in the variation of the amplitude as a function of the center-of-mass energy and the branching ratios in the various exit

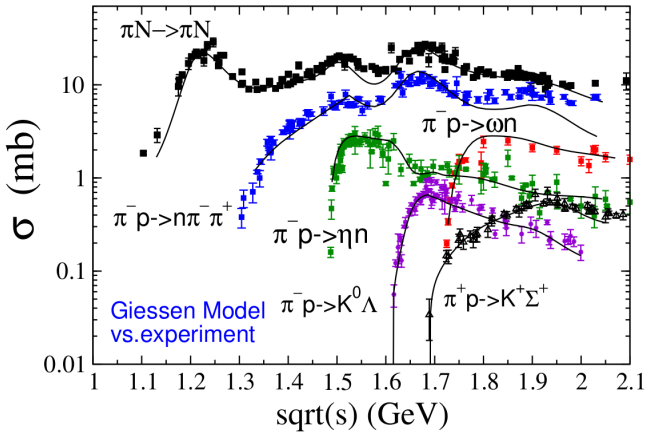

Figure 1.15: Evolution of the cross section of different channels of the π^-p reaction as a function of the center-of-mass energy. The curves show the results of coupled-channel calculations [9].

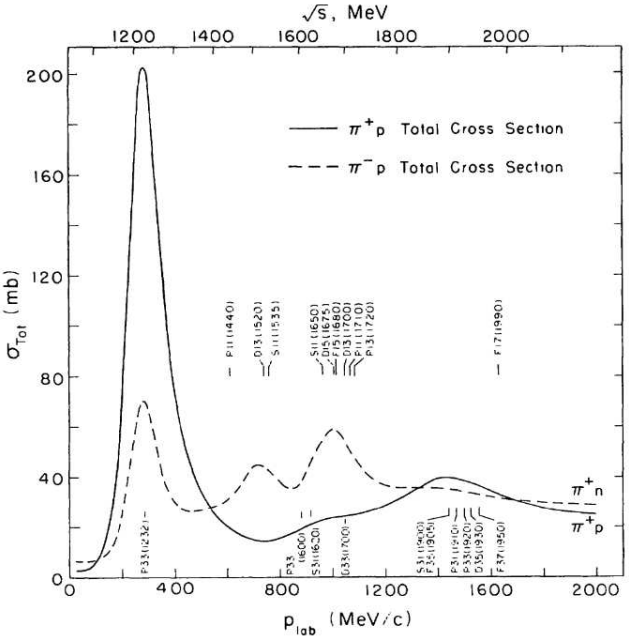

Figure 1.16: Total cross sections for the π^-p (dashed curves) and π^+p (full curves) reactions. The mass of the main baryon resonances are indicated [10].

channels can be studied by detecting the decay products. More recently, with the availability of high quality photon beams, γ N reactions have been the subject of most recent experimental efforts in the field of baryon structure. Such reactions also allow for direct excitation of a baryon, and, despite a stronger contribution of non-resonant part than in pion beam experiments, they bring complementary information, in particular due to the possibility to have polarized beams. As of today, the database for photon induced reactions is very rich, while few experiments were performed with pion beams since the bubble chamber experiments in the 80's, as will be discussed in more detail in this subsection.

To extract information on the baryon spectrum, measurements for pion and photon induced reactions are combined in Partial Wave Analysis (PWA), which perform global fits of the contributions of the various entrance and exit channels contributing in the reactions. Such a formalism is used to check the existence of a baryon resonance and to extract its decay properties. The results of PWA fits (also called solutions) are also convenient to estimate total cross sections or differential distributions for a given reaction at any given center-of-mass energy. The SAID PWA analysis [11] is often considered as a reference in the field of baryon structure and is also commonly used by experimentalists to estimate cross sections. We will therefore also discuss the comparison of the data to the SAID PWA, although it is not directly used in the present work.

In addition to the interest for baryon structure, information on πN reactions is also essential as an input for models describing heavy-ion reactions, as transport or cascade models (see Sec. 4.1.3). It is therefore interesting to investigate the existing information for πN reactions in the energy range of our experiment (i.e. p_{beam}= 0.7 GeV/c

and $\sqrt{s_{\pi N}}$= 1490 MeV).

Figure 1.15 shows the evolution with the π+N center of mass energy of the cross sections measured for various reaction channels of the π^-+p reaction. It can be observed that, at $\sqrt{s_{\pi N}}$ = 1490 MeV, the elastic cross section dominates and the main inelastic channel is the two-pion production channel. In Figure 1.16, the cross sections for the π^-+ p and π^++ p reactions are compared. The prominent peak of the $\Delta(1232)$ resonance can be clearly seen for p_{beam} lower than 400 MeV/c. This work focuses to the region of the second resonance, where N(1440), N(1520) and N(1535) contribute. It can be observed that the cross sections are smaller than in the $\Delta(1232)$ region. No resonant structure appears for the π^++ p case and the cross section is smaller, as expected due to the absence of spin 3/2 baryon resonances in this region.

Elastic and charge exchange channels

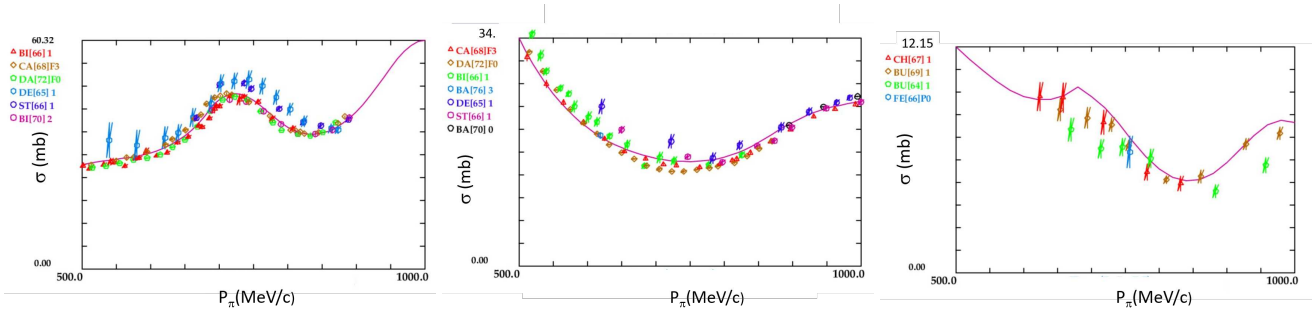

Figure 1.17: The data points show the existing measurements for cross sections for the elastic π^-+p $\rightarrow$ π^-+p (left), elastic π^+ p $\rightarrow$ π^+ p (equivalent to π^- n $\rightarrow$ π^- n) (middle) and charge exchange π^-+p$\rightarrow$ π^0 p (right) reactions in the range of incident pion momentum between 500 and 1000 MeV/c. The curves show the result of the SAID PWA. Crossed out data points are not considered in the SAID fits. Picture extracted from the SAID platform [11].

Data exist for the reactions $\pi^- + p \rightarrow \pi^- + p$ (a), π^+ + p $\rightarrow$ π^+ + p (b) and π^-+p$\rightarrow$ π^0 + n (c). The respective cross sections (f_-, f_+ and f_{chex}) of these channels fulfill, within the precision of the data the relation $f_{chex} = (f_+ - f_-)/\sqrt{2}$, which can be derived using isospin invariance ([61]). The various πN reactions differ indeed only by the isospin and can all be related to the I=1/2 and I=3/2 amplitudes. As an example, the π^+p and π^-n elastic reactions, which are symmetric under isospin transformation and both correspond to a pure I=3/2 system have the same cross sections.

Reactions (a), (b) and (c) have been measured at various facilities. Figure 1.17 shows the experimental total cross sections as a function of pion momentum for these channels in comparison to the SAID Partial Wave Analysis solution WI08 [11]. Except the recent Crystal Ball data measured at BNL for the charge-exchange reaction (denoted by [St05]), the SAID PWA is mostly based on experiments performed before 1990. More recent cross section measurements have been provided for π^-p and π^+p elastic scattering by the EPECUR experiment [12] showing discrepancies with respect to the WI08 SAID solution at the level of a few $\%$.

The HADES collaboration also measured angular distributions for the π^-p elastic scattering reaction at four different pion beam momenta. The shapes of the distributions were found in good agreement with the world data which

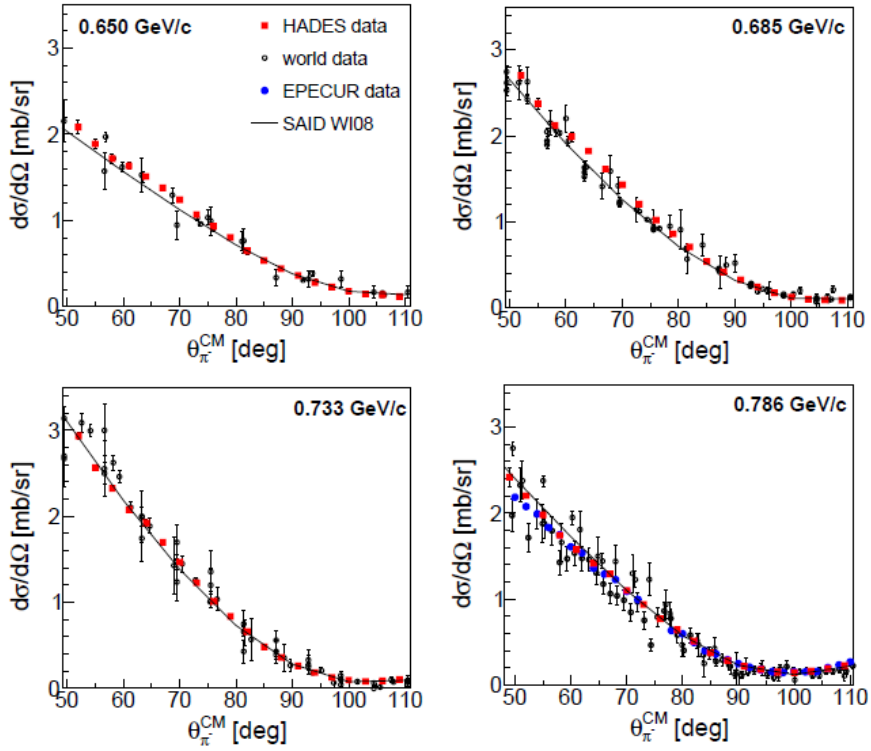

Figure 1.18: π^-+p elastic-scattering angular distributions measured by the HADES collaboration at four pion beam momenta 0.650, 0.685, 0.733 and 0.786 GeV/c (red squares) are compared to the EPECUR data (blue dots) [12] available at the highest beam momentum and to other world data (open disks). The WI08 SAID solutions is shown as a black curve [13]

.

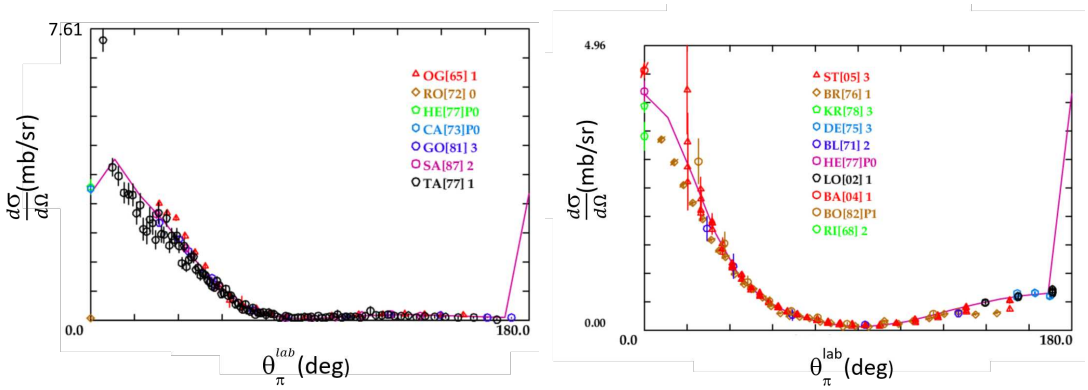

Figure 1.19: Same as Fig. 1.17 for differential cross sections as a function of the center-of-mass angle for the π^+p elastic scattering and π^-p $\rightarrow \pi^0$n charge exchange reaction. Data points measured for pion beam momenta p_{beam} between 670 and 710 MeV/c are shown. The curve shows the result of the SAID PWA for p_{beam}= 690 MeV/c.

were used for the normalization of the HADES experiment. This is illustrated in Fig. 1.18, where the comparison to the SAID PWA result is also shown. EPECUR data [12], which can be compared only for the highest incident pion momentum measurement are also in good agreement.

Figure 1.19 displays the pion angular distributions for the elastic π^+p and charge-exchange π^-p$\rightarrow \pi^0$n reactions at p_{beam}= 0.7 $\pm$ 20 MeV/c). One can notice that SAID can not describe the distribution at the most forward angles

for the π^+p reaction. For the charge-exchange case, Crystal Ball data have a good precision for angles larger than 20°, but do not help for more forward angles.

1.5.2 $\pi\pi$ N channels

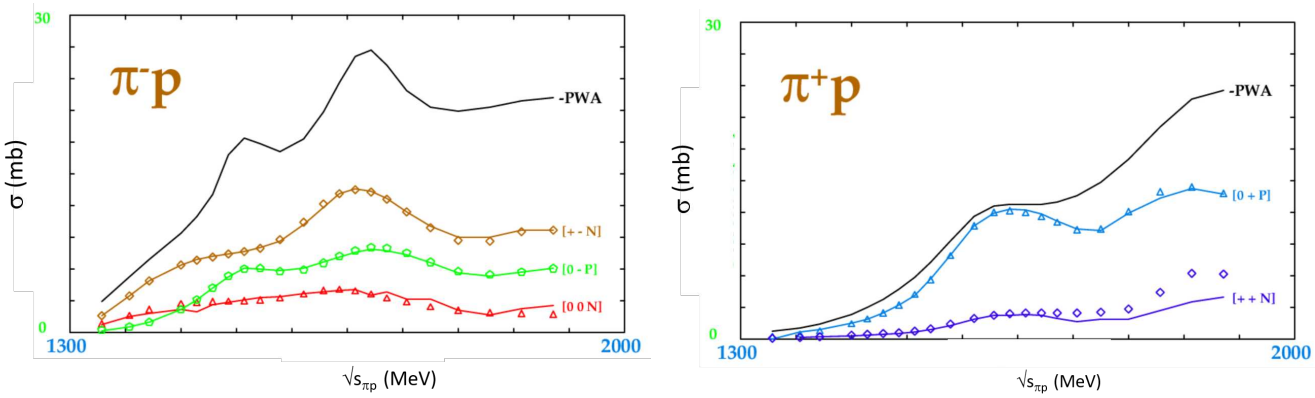

Figure 1.20: Cross sections for the various channels of the π^-p $\rightarrow \pi\pi$ N (left) and π^+p$\rightarrow \pi\pi$ N (right) reactions.

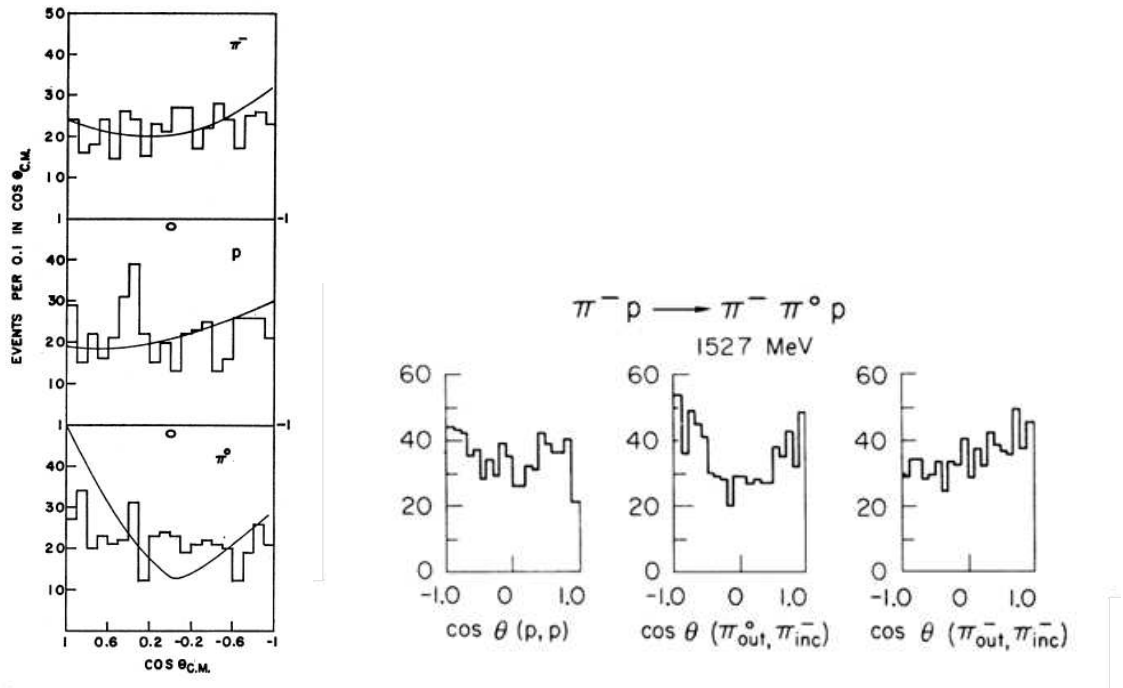

Figure 1.21: Angular distributions measured in the center-of-mass for the reaction π^-+p$\rightarrow\pi^0\pi^-$+p at an incident energy E = 558 MeV at BNL [14] (left) and E = 573 MeV at Berkeley [15] (right).

The cross-sections for the two-pion production channels in π^-+ p and π^++ p reactions obtained by the SAID analysis are shown in Fig. 1.20 as a function of the center-of-mass energy. The database used in SAID is much more scarce for these two-pion channels than for the elastic or charge exchange. This is illustrated in Fig. 1.21 which displays angular distributions measured for the π^-+p$\rightarrow\pi^0$+π^-+p reaction in our energy range. However, the π^-+p$\rightarrow$ π^0+ π^0 + n reaction has been measured very precisely by the Crystal Ball collaboration between the

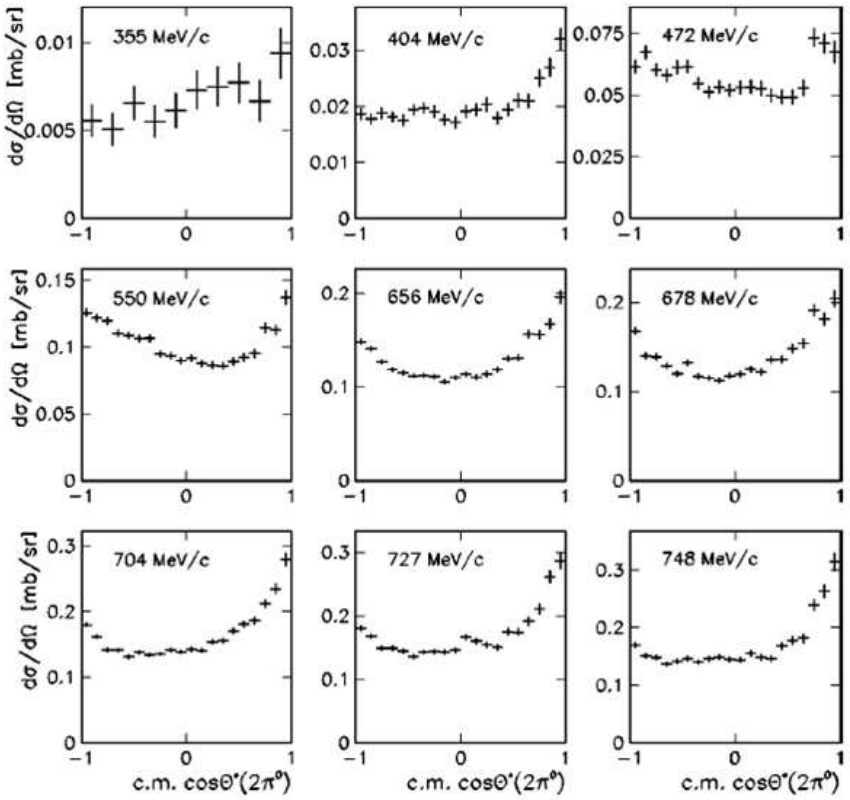

Figure 1.22: Differential cross sections as a function of the center-of-mass angle of the $2\pi^0$ system produced in the reaction π^-+p$\rightarrow\pi^0\pi^0\ n$ at different π^-momenta [16].

threshold and 770 MeV/c [16], as shown in Fig. 1.22. In addition, the HADES collaboration has recently provided precise differential distributions for the reactions $\pi^- + p \rightarrow \pi^+ + \pi^- + n$ and $\pi^- + p \rightarrow \pi^- + \pi^0 + p$ [13] (Fig. 1.23 and 1.24). The cross sections measured by the HADES collaboration are compatible with the SAID fits for the $\pi^-\pi^+$n channel and lower by 15 % for the $\pi^+\pi^0$p channel. The new HADES and Crystal Ball data were added to the Bonn-Gatchina PWA, together with other world data on single and double pion production in photon, pion and electron induced reactions and new values for the coupling of the N(1440), N(1520) and N(1535) to the $\Delta(1232)\pi$, Nσ and Nρ channels were obtained [62]. Figure 1.23 clearly demonstrates the dominance of N(1520) baryon resonance in the p $\pi^0\pi^-$channel, while N(1440) also strongly contributes in the n $\pi^+\pi^-$channel.

3π channel and η production

The threshold for three pion production is at $\sqrt{s} = 1.357$ GeV for $3\pi^0$ (p_π=0.482 GeV/c) and $\sqrt{s} = 1.352$ GeV (p_π=0.474 GeV/c) for $\pi^-\pi^+\pi^0$, which is well below the energy of our experiment. However, the few existing measurements report small cross sections: Burnstein et al. [14] have measured an upper limit of 40 μb for the multipion cross section for p = 683 MeV/c, i.e. below the η threshold, which is at p_π=0.6854 GeV/c. Considering the pion beam momentum distribution, but above all the Fermi momentum smearing in the carbon nucleus, both the regions

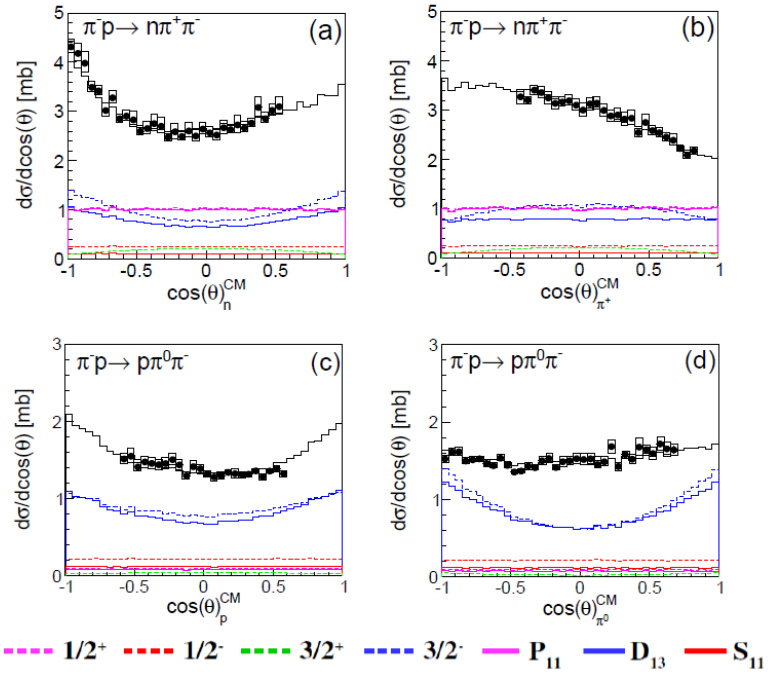

Figure 1.23: Differential cross sections as a function of the center-of-mass angle of the nucleons (left column) and pions (right column) in the CM frame for the π^-+p→ n $\pi^+\pi^-$(upper row) and π^-+p→ p$\pi^+\pi^0$(lower row) reaction channels for p_{beam}= 0.685 GeV/c. The curves display the contribution of the various partial waves in terms of spin and parity (dashed curves) and of angular momentum and isospin (full curves) in the Bonn-Gatchina PWA [13].

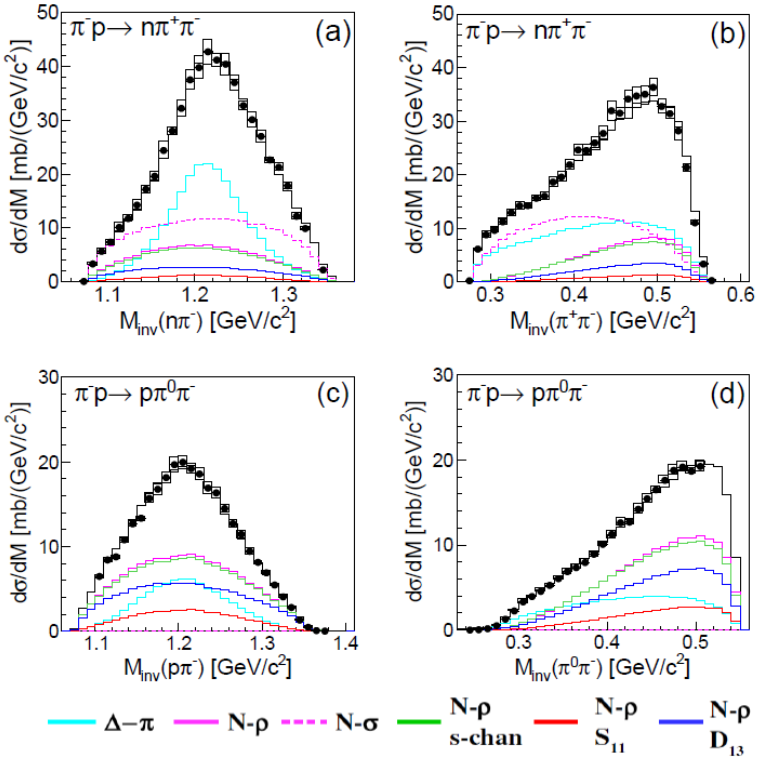

Figure 1.24: Same as Fig. 1.23 for the invariant mass of the nucleon-π^- (left column) and two-pion (right column) systems. Here the curves display the contribution of the different decay channels [13].

below and above the threshold will be probed in $\pi^- + C$ reactions at p_{beam}=0.690 GeV/c (see Sec. 6.1.3). Above the η threshold, the dominant 3-pion channel is the $\pi^+\pi^-\pi^0$, which is fed by the η decay. A few experiments have measured directly the three pion production above the η threshold [63, 64, 65, 66] in the momentum range up to 0.8 GeV/c. More precise constraints for the $\pi^-\pi^+\pi^0$ cross section can however be obtained using the known branching ratio (23%) to the $\pi^-\pi^+\pi^0$ channel and η production cross section which was measured mostly using the $\gamma\gamma$ decay [67, 68, 69, 70].

Combining these results, it can be concluded that the cross section for the η production is roughly of the order of 1 mb for $\sqrt{s_{\pi N}}$= 1.5 GeV (p_{beam}= 0.705 GeV/c) and 2.5 mb for $\sqrt{s_{\pi N}}$= 1.55 GeV (p_{beam}= 0.79 GeV/c) i.e, the 3π cross section ranges from about 0.23 to 0.6 mb in this energy range. As a summary, despite some discrepancies between the different measurements, the data base seems to be precise enough to constrain most channels of the πN reactions around p_{beam}= 0.7 GeV/c. The situation is much worse for the pion-nucleus case, as described in the next section.

1.5.3 Pion-nucleus reactions

While previous research has extensively studied the $\Delta(1232)$ resonance [71], there is a scarcity of experimental measurements at higher energies, particularly in the second resonance region involving other resonances like N(1440), N(1520), N(1535), and more. Gaining knowledge about these resonances at higher energies is crucial for understanding the behavior of dense hadronic matter, particularly in heavy-ion reactions at a few GeV.

Early experimental investigations have focused on measuring the total cross sections of pion-induced reactions. Notably, at Brookhaven National Laboratory (BNL), experiments were carried out to analyze the absorption and diffraction cross sections of π^--induced reactions on various nuclei such as Be, C, Al, Ca, and Pb. These experiments covered a range of energies from 0.6 GeV/c to 1.4 GeV/c [72]. Similarly, at the SATURNE facility, researchers examined the total cross sections of incident pions on different targets including Be, C, and Al. The measurement technique employed in these experiments involved attenuation measurements for an angle denoted as θ_m. This method entailed counting the number of particles absorbed or scattered out of a cone with an aperture angle of θ_m by the target. By extrapolating the collected data to approach zero for θ_m, the total effective cross section (σ_t) could be determined.

The Brookhaven National Laboratory (BNL) experiment was the first investigating the pion scattering ($\pi^- \& \pi^+$) on a nucleus target (C and Ca) above the Δ resonance region (800 MeV/c) [10]. The KEK experiments also delved into studying elastic scattering experiments involving the collision of $\pi^- + ^{12}C$ at various momenta: 610, 710, 790, and 895 MeV/c [73].

More closely related to our study are the measurements of emitted pions and protons from pion-induced reac-

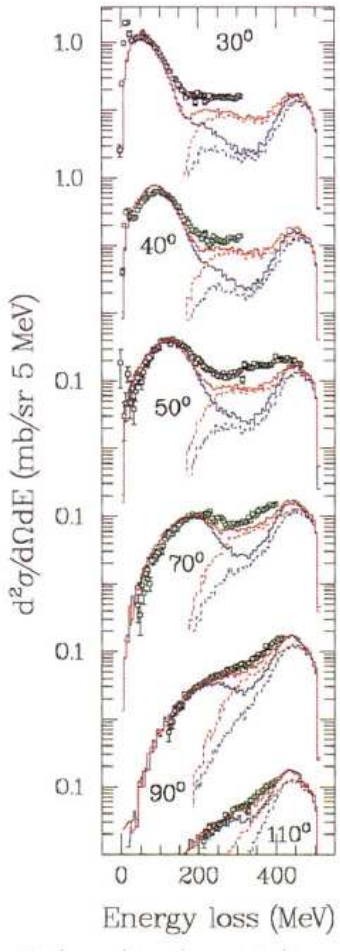

Figure 1.25: Results from ^{12}C(π^-,π^-) experiments at LAMPF. The data (open circles) is compared with two diferent intranuclear cascade calculations. The blue histograms are for the standard calculation. For the red ones, the time for $(\pi, 2\pi)$ reactions to occur is delayed by 2 fm/c. The dashed histograms indicate the portion of the respective INC calculations that are due to $(\pi, 2\pi)$ reactions [8].

tions on nuclei. The experiments conducted at the Los Alamos Meson Physics Facility (LAMPF) involved negatively charged pion beams with an energy of 475 MeV to investigate $\Delta(1232)$ production through pion charge exchange in various target nuclei, including hydrogen (^1H), deuterium (^2H), carbon (C), and zirconium-90 (^{90}Zr) [74]. Other charge exchange studies aimed at investigating the effective number of participating protons in quasi-free interactions by comparing the yields of reactions on proton and nuclei at LAMPF [75] or KEK [76]. The LAMPF experiments also investigated pion scattering on nuclei at 500 MeV [77, 8] and provided double differential cross sections for π^+ and π^- as a function of energy and angles (Fig. 1.25). The quasi-elastic peak, due to elastic pion scattering on a nucleon in the target nucleus is clearly identified and the yield at larger energy losses is attributed to the inelastic πN$\rightarrow \pi\pi$N process. In the calculations, the yields for energy losses in the region of the Δ resonance are too strongly suppressed. A better description was achieved by forbidding interactions in a certain time lapse [8].

These interesting studies of differential cross sections remained however rather scarce and limited to pion beam momenta of 625 MeV/c, at maximum. Our measurements of the reaction π^-+C at an incident pion momentum of

0.69 GeV/c will therefore fill an important gap. In addition, we will provide high statistics measurements for various exclusive channels, which allow to test rescatterings effects in different configurations, and allow to investigate both nucleon and pion rescatterings.

1.6 Summary

To summarize, the motivations of studying the pion and proton spectra in the π^-+ C at 0.7 GeV/c are as follows:

- investigating the pion dynamics in the region above the $\Delta(1232)$ resonance, which will be of utmost importance for future heavy-ion experiments, e.g at the FAIR facility.
- test transport and cascade models which are used to describe hadronic collisions in a detailed way, by looking at different exclusive channels.
- provide a data base for pion-nucleus reactions in an energy range which is extremely poorly explored and which is of interest, not only for hadronic physics, but also for detector studies, neutrino physics,...

Chapter 2

The HADES experimental set-up

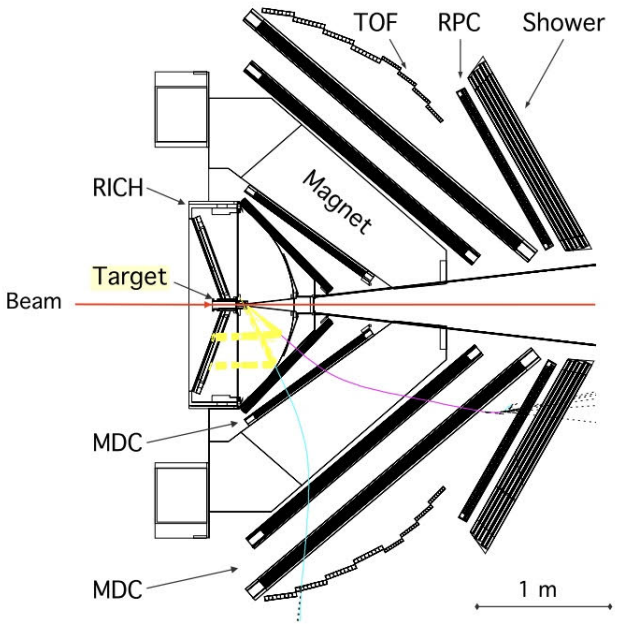

Figure 2.1: Side view of the HADES setup with the different sub-detectors.

The High Acceptance Di-Electron Spectrometer (HADES) [20] is a fixed target experiment operating at the heavy ion synchrotron SIS18 of the GSI Helmholtzzentrum für Schwerionenforschung in Darmstadt, Germany. The latter provides proton, light and heavy (up to Uranium) ion beams in the energy range of up to 4.5 GeV for protons and 1.25 AGeV for Au. A secondary pion beam is also available in the momentum range between 0.6 and 2 GeV/c. The physics program was initially mainly focused on the investigation of the spectral properties of the light vector mesons ρ, ω and φ and their modification in the nuclear medium, by measuring the dielectron radiation (e^+e^- pairs) originating from their decay. Thus, the spectrometer was specifically designed to measure the production of e^+e^- pairs. It has been equipped with the following specialized sub-detectors :

1. Hadron-blind Ring Imaging CHerenkov (RICH) detector to identify the e^+ & e^-.

2. Mini-Drift Chambers (MDC) to reconstruct the momenta of charged particles by measuring the deflection angle of the particle trajectories in a magnetic field.

3. Multiplicity and Electron Trigger Array (META) consisting of time-of-flight (tof) walls (TOF/RPC) which provide the flight time of the particles, using the information given by the START detector,. It also consists of electromagnetic shower detectors (Pre-Shower) to improve e^+e^- identification and provides another coordinate of the particle trajectory as supplement information for tracking and momentum reconstruction.

By combining the information of the MDC tracking system and tof walls, and due to its good momentum resolution, HADES proved to be very well suitable for the detection and characterization of hadrons, in addition to e^+e^- reconstruction. This makes HADES an excellent tool for the investigation of hadron properties in both elementary and heavy ion collisions.

A sixfold azimuthal geometry presents the architecture of the detector, consisting of 6 identical sectors around the beam line axis, each covering almost 60°, except for the dead zones due to the narrow frames of the sector modules. Thus, almost full geometrical coverage is achieved in the azimuth plane (85%). The polar angle acceptance covers from 18° to 85°. A detailed description of the detector in its 2009 configuration is provided in [20]. The forward angle scintillator has then been replaced by Resistive Plate Counters (see Sec. 2.3.2) which were used in the experiment described in this PhD. Further modifications have been introduced since then, but we describe here the configuration used for the 2014 pion beam experiment.

2.1 Ring Imaging CHerenkov detector

The RICH detector (see Fig. 2.2) is designed for identifying electrons and positrons with momenta 0.1 GeV/c $\leq p \leq 1.5$ GeV/c [20]. It constitutes the innermost part of the spectrometer and is sensitive only to relativistic particles which emit Cherenkov radiation in the C_4F_{10} gas radiator. The latter has a refractive index of $n = 1.00151$, corresponding to a phase speed of light of $c/n = 0.9985$ (Lorentz factor $\gamma = 1/\sqrt{1-(c/n)^2} = 18$). Each charged particle traveling in the radiator medium with a velocity β faster than light interacts with the molecules which respond by releasing photons under the angle θ_C w.r.t their trajectory. The latter is defined through the relation :

$$\cos(\theta_C) = \frac{1}{\beta n}. \tag{2.1}$$

This creates a blueish cone shape of overlapping light waves, which start at the electron and keep expanding, called Cherenkov radiation. The minimum particle momenta needed to emit Cherenkov light in the C_4F_{10} medium are $P^e \sim 10$ MeV/c, $P^\mu \sim 1800$ MeV/c and $P^\pi \sim 2400$ MeV/c for electrons, muons and pions, respectively. Therefore,

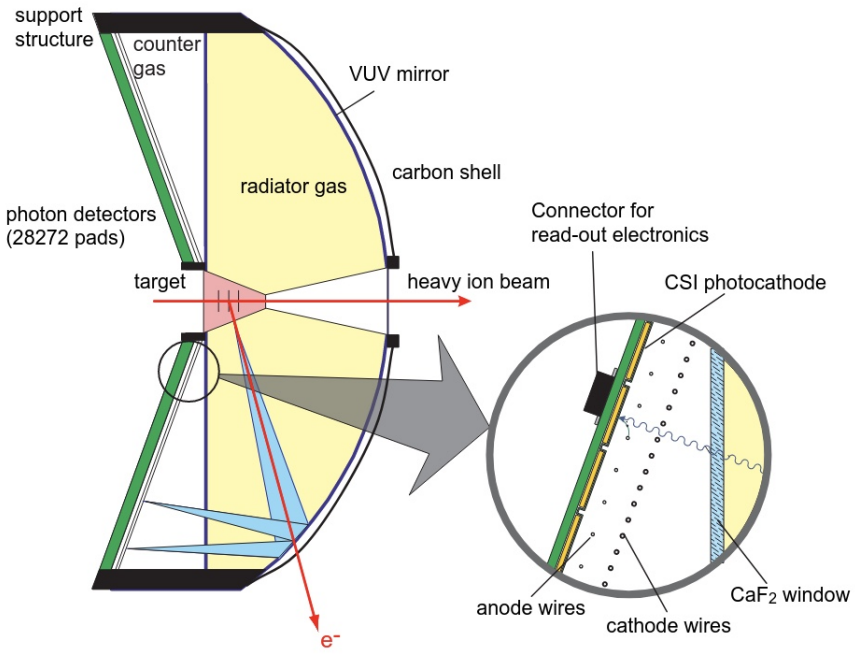

Figure 2.2: Schematic layout of the RICH, with detail on the photon detector.

the detector is not sensitive to muons and pions in the SIS18 energy range $(\gamma_{max} \sim 10)$ and is practically hadron-blind.

The gas is surrounded by :

- Carbon shell mirror (Vacuum Ultra Violet - VUV) downstream of the target, with a curvature radius R=872 mm. It reflects the light cone to the photon detectors.
- CaF_2 window which separates the C_4F_{10} gas from the CH_4 operation gas of the photon detector, while ensuring a high VUV transmission.
- Multi-Wire Proportional Chamber (MDC) with its photosensitive CsI cathode where photo-electrons are generated, then amplified and recorded as a ring pattern. It is placed upstream of the target to reduce the amount of material in the electron path. This element was replaced in 2019 by a photodetector plane.

2.2 Tracking system

2.2.1 The Superconducting Magnet

The superconducting magnet ILSE (Iron-Less Superconducting Electron magnet) is an essential component for the momentum reconstruction of charged particles. The main concept is based on providing the charged particles a momentum kick in the transverse plane, which leads to a deflection of the track polar angle, and measuring the

direction of the track before and after the deflection in the MDCs (see Sec. 3.2.2). In order to obtain momenta with sufficient resolution ($\sigma_p = 1.5 - 2\%$ for electrons), this magnet has to fulfill several conditions [20]:

- Free of materials in the particle path in order to avoid unwanted multiple rescattering.
- Covers the momentum range p=0.1 - 2 GeV/c and the spectrometer geometrical acceptance.
- No magnetic field in both the target and active area of RICH (provided by the toroidal geometry of the magnet).

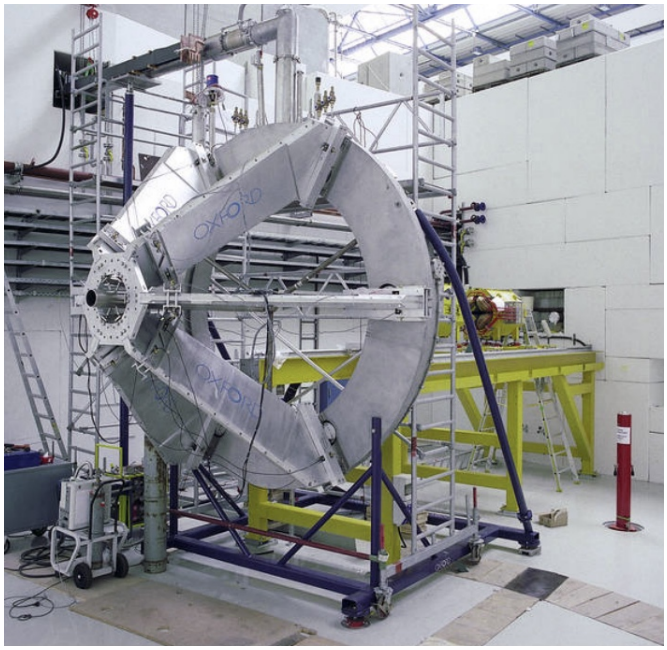

Figure 2.3: Photography of the HADES superconducting magnet during the mounting.

With its six superconducting coils (Nb-Ti), the magnet respects the 6-sector geometry of the spectrometer. An inhomogeneous toroidal magnetic field is generated around the beam axis, with a maximum value of 3.6 T on the edges of the coils and in the azimuth plane (for a current I = 3500 A) and 0.9 T in the acceptance region. In order to maintain the coils in the superconducting state, the Helium and Nitrogen liquids are used to cool down, respectively, the current leads at 4.7 K and the coil shielding at 85 K.

2.2.2 The Multi-Wire Drift Chambers

Architecture

As discussed above, the momentum of the charged particle is determined by the reconstructed curvature of the trajectory, which requires at least two positions before and two after the track deflection. For this aim, the multi-wire drift chambers are divided into 4 tracking planes of increasing size: Two of them are placed before the toroidal magnetic field magnet (I and II) and the two others are placed behind (III and IV). Each plane includes six low-mass, trapezoidal, multi-layer drift chambers symmetrically arranged into six sectors around the beam axis, see Fig.

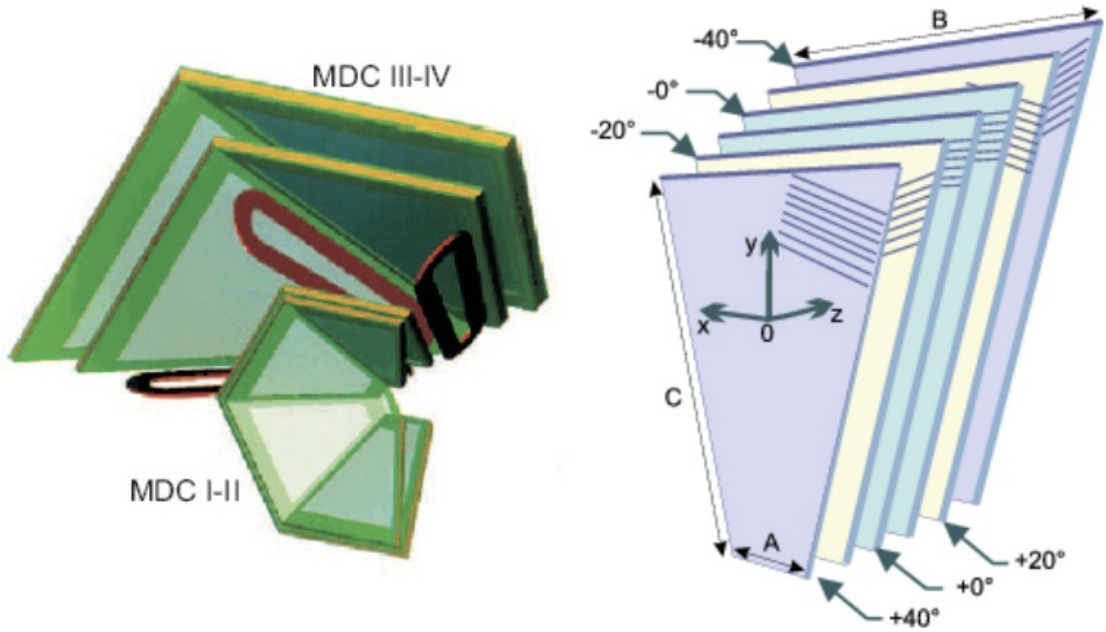

Figure 2.4: Left: Schematic view of a section of one sector including the RICH detector, four MDCs and coil of the superconducting magnet. Right: Arrangement of the HADES MDCs and the coils of the superconducting magnet.

2.4. The active area of these chambers ranges from 0.35m² for plane I to 3.2 m² for plane IV, covering the same acceptance in solid angle (polar angles between 18° and 85°). An important feature of the MDC sub-detector is that it has to be very well adapted for track reconstruction in high multiplicity environments such as heavy ion collisions, and therefore achieve an optimum spatial resolution in polar angles ($> 150\ \mu m$) to sustain the granularity and double hit resolution. In order to fulfill these conditions, all chambers are made up of 6 anode sens wire layers, oriented in 5 different angles (0°, $\pm 20^\circ$ and $\pm 40^\circ$) see the left side of Fig. 2.4, where each wire is placed between two cathode planes, leading to a total number of drift cells of 1100/plane of sizes ranging from 5x5 mm² for the plane I to 14x10 mm² for plane IV. The chambers attain a position resolution in the y direction about $60 - 100\ \mu m$ and in the x and z directions around $120 - 200\ \mu m$.

Materials

All chambers are covered with a very thin aluminized Mylar foil ($12\ \mu m$). For the cathode and field wire, bare aluminum (planes I-III) and gold-plated aluminum (plane IV) are used, with diameters of $80\ \mu m$ and $100\ \mu m$. These wires are stained with tensions between 80 and 120 cN. The choice of such low-mass materials for different components of the sub-detector was strongly related to the minimization of unwanted scatterings in the path of charged particles. For the sense wires, thick Gold-plated Tungsten with $20\ \mu m$ (planes I-III) and $30\ \mu m$ (plane IV) were used and strained respectively with a tension of 40 and 110 cN. A mixture of Ar/CO_2 (in a ratio of $70\%/30\%$) was used to fill the chambers of planes I and II, while Ar/C_4H_{10} (in a ratio of $84\%/16\%$) was used to fill the chambers

III and IV.

Electronics

The signals originate from the ionization of atoms within the gas-filled chamber. Following ionization and influenced by the applied electric potential along the wires, the ions and free electrons begin to drift toward their respective electrodes. As these electrons traverse, they trigger further ionizations in neighboring atoms, leading to an avalanche effect. This avalanche is then captured and read out. Specially designed boards mounted on the frames of the drift chamber while avoiding extension into the active area are responsible for processing the drift chamber signals. The front-end electronics are integrated through analog boards (16 channels), which are mounted on digitization boards (64 or 96 channels). Flexible printed circuits are used to connect the four sense wires to the analog boards, which contain ASD8-B chips (8 channels). These chips carry out differential amplification, shaping, and discrimination and generate logical signals with variable width as the latter represents the time the shaped signal exceeds the given threshold. The logical signals are processed to TDC (Time-to-Digital Converter) chips (mounted on the digitization board). By measuring the time over threshold (ToT) which corresponds to the width of the signal, it is possible to determine the energy loss dE/dx of the particle based on the Bethe-Bloch formula [20]. This information is useful to enhance the Particle Identification (see Sec. 3.3).

2.3 META Detectors

The Multiplicity Electron Trigger Array (META) is integrated into the HADES spectrometer. Positioned after the outermost MDC plane, it acts as a trigger due to its fast detection capabilities. It is covered by Resistive Plate Chambers (RPC) in the inner section (18°-45°) and a scintillator wall in the outer region (45°-85°). To enhance lepton identification in the area where the discrimination of electrons and pions is inadequate, an electromagnetic shower detector is employed behind the RPC. The impact point in the META detector provides another coordinate of the particle trajectory addition to the location information of the drift chambers and is therefore used as a supplement in the track reconstruction.

2.3.1 TOF

The TOF detector consists of 384 BC408 plastic scintillator rods that are divided into sectors. Within each sector, there are 64 rods that increase in size from $1\ m$ to $2\ m$ as the polar angle increases, as shown in Fig. 2.5. As a charged particle passes through the scintillators, it stimulates the material leading to the emission of light. The light is then detected by photomultipliers (PMTs) situated at both ends of each rod, which are connected by means of a 2.5 mm thick silicone disc. By measuring the times of both PMT signals on each side of the rod (t_{right} and t_{left}),

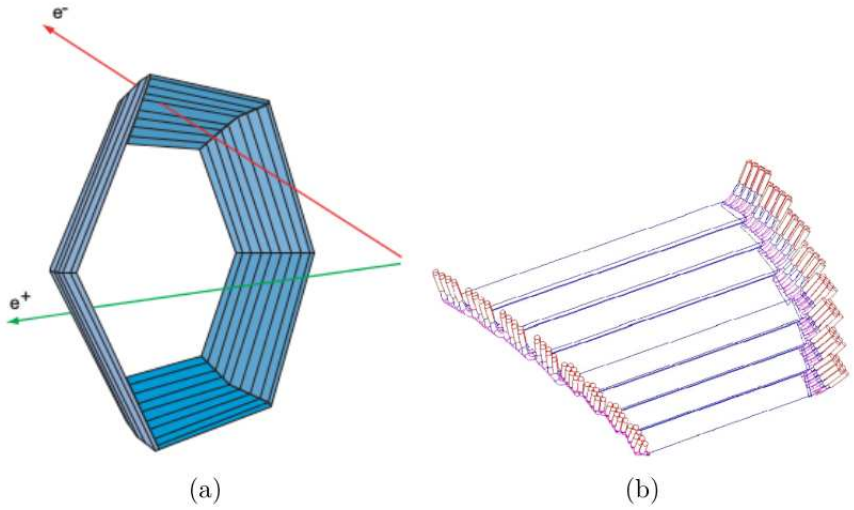

Figure 2.5: (a) Schematic layout of the TOF detector with an example of the registration electron and positron. (b) Technical drawing of one sector. Taken from [17].

the particle's time of flight (tof) and hit position (x) on the rod can be calculated. The relationship between these quantities can be expressed using the following equations:

$$x = \frac{1}{2}(t_{right} - t_{left})V_g, \tag{2.2}$$

$$tof = \frac{1}{2}(t_{right} + t_{left} - \frac{L}{V_g}) - t_0, \tag{2.3}$$

The group velocity in the rod, which is the average velocity of light in the rod, is denoted as V_g. The length of the rod is given by L. The time measured by the START detector (see Sec. 2.4) is referred to as t_0. TOF provides a time resolution of approximately $150\ ps$ and hit position resolution $\sigma_x \sim 25\ mm$. One can also extract information about the energy loss ΔE of a particle in the scintillator using the Eq.2.4, making TOF valuable for the particle identification process, where a_{right} and a_{left} are respectively the amplitudes of right and left PMT signals, λ_{at} is the attenuation length of light in the scintillator, and k is constant. TOF is also used for triggering; see Sec. 2.5.

$$\Delta E = k\sqrt{a_{right} \times a_{left} \times e^{L/\lambda_{at}}} \tag{2.4}$$

2.3.2 RPC

As discussed above, the inner TOF wall has to deal with high multiplicity events coming from heavy ion collisions. For this reason, the RPC is constructed using 1116 individual cells that are arranged into two layers. Each layer consists of 31 rows and 3 columns (Fig. 2.6). The width of the cells increases with the polar angles within the range of 2.2 to $5\ cm$. Each cell is composed of three aluminum electrodes separated by two glass plates, and

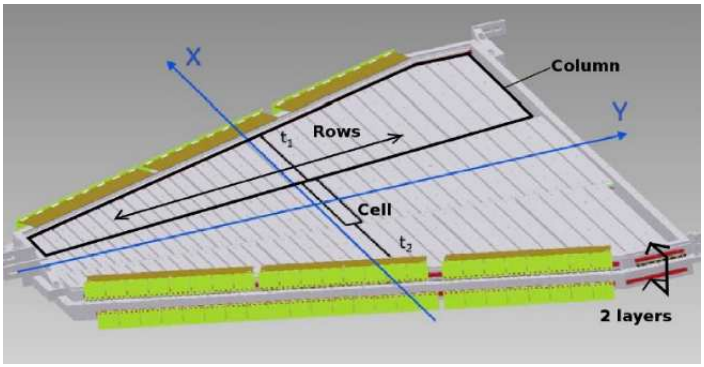

Figure 2.6: Arrangement of the RPC cells within one module.

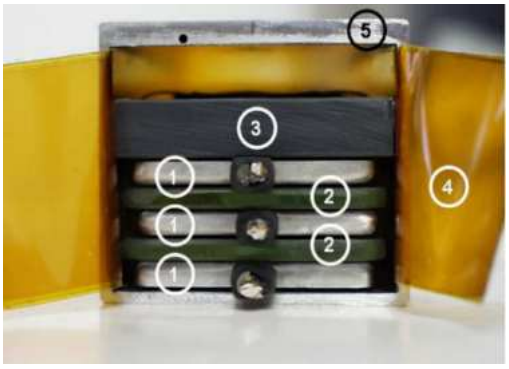

Figure 2.7: Internal layout of one RPC cell. On the left picture: 1 - Al electrodes, 2 - glass electrodes, 3 - pressure plate, 4 - kapton insulation and 5 - Al shielding. Taken from [17].

enclosed in kapton insulation and aluminum shielding (Fig 2.7). The four gas gaps located between the plates are a characteristic feature of each cell, as they induce a signal in the RPC based on the avalanche effect that occurs whenever a charged particle passes through. This effect is triggered by the high voltage applied to the cathodes, typically around $6\ kV$, which accelerates the electrons generated by the initial ionization of the gas. This, in turn, initiates a chain reaction of ionizations, leading to further electron generation and ultimately to the discharge of the gas. The detector demonstrated remarkable features, including a good time resolution ($\sigma_t < 100\ ps$), a remarkable rate capability of up to 1 kHz/cm^2 in the innermost region, and a single-hit efficiency exceeding 95% [78]. The transverse position resolution varies depending on the cell's location, with the innermost cells having a resolution of $22\ mm$, and the outer cells having a resolution of 42 mm due to their varying widths.

2.3.3 Pre-shower

The Pre-Shower detector is a crucial component of the spectrometer and is primarily used for electron identification in the low polar angle region. This area presents challenges for distinguishing electrons from hadrons due to higher hadron momenta and more significant hit densities in the detector. The detector is situated behind the RPC and comprises three Multi Wire Proportional Chambers (MWPCs), forming a trapezoidal shape, namely the pre-chamber, post1-chamber, and post2-chamber, see Fig. 2.8. Two lead converter plates separate these chambers, with a thickness of around two radiation lengths ($X_0 = 0.56\ cm$). The MWPC is filled with an isobutane-based gas mixture with alternate anodes and cathodes, placed at a distance of 4 mm from two flat cathode planes. The underlying principle of the Pre-Shower detector involves charge induction through matter interaction, whereby electrons and positrons generate a much higher charge compared to hadrons. This process starts with electrons/positrons being decelerated when passing through the lead converter and producing light through the bremsstrahlung effect. The resulting photons create high-energy e^+e^- pairs that will be multiplied in the other lead converter, leading to an electromagnetic shower. As a result, the wire chambers experience significantly higher energy deposition compared

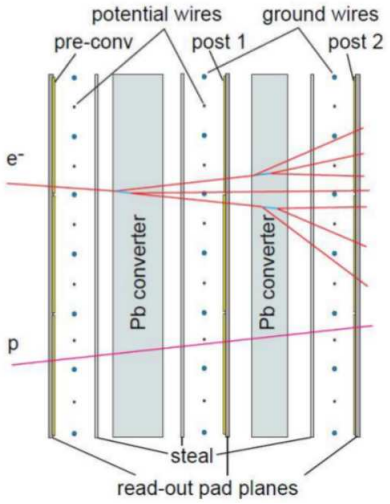

Figure 2.8: The Pre-Shower detector is made up of three gas chambers (pre-, post1-, and post2-chamber) separated by lead converters.

to hadrons, for which the measured energy corresponds to the energy loss due to the gas ionization process in the chamber. To distinguish between electromagnetic showers and hadronic tracks, the integrated charge of the particle in the three layers is measured, with a higher charge expected for electrons in the Post1- and Post2-Chamber compared to the Pre-Chamber. The Pre-Shower detector has been a critical tool in identifying and differentiating particle species in the HADES experiment. However, it has recently been replaced by a lead glass calorimeter (ECAL) that offers improved electron-to-hadron discrimination and enables the detection of real photons. The Pre-Shower detector played an essential role in our experiment, as we did not have the ECAL at the time of data acquisition.

2.4 Start detector

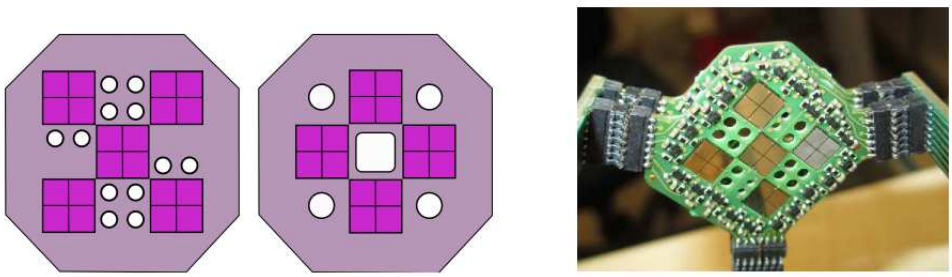

Figure 2.9: Left: Top view of five and four diamond sensor plates with fourfold segmentation on the diamond support Printed Circuit Boards (PCBs). Right: The nine diamond sensor plates are mounted on two printed circuit boards of the Start detector.

To optimize the beam profile and provide a fast timing signal that serves for both triggering purposes and a reference for time-of-flight measurements in the pion beam experiment, a T0 detector is used. Located $17\ cm$ upstream of the target center, the START detector consists of nine diamond element sensor arrays arranged on two support PCBs (Printed circuit boards) with 5 and 4 sensors [79], see Fig. 2.9. Each diamond sensor is segmented

into four quadrants and features a $4.3 \times 4.3\ mm^2$ area and a thickness of $300\ \mu m$. The four-fold segmentation ensures a reasonable position resolution and low detector capacitance. The detector achieves a time resolution lower than $100\ ps$ for particle identification via time of flight and a position resolution of $0.7\ mm$ horizontally and vertically for tracking and vertex reconstruction. The use of mono-crystalline diamond material produced with the Chemical Vapor Deposition (CVD) was intended to obtain these features in addition to having a low material budget and providing good operation stability for fluxes of about $10^7\ cm^{-2}s^{-1}$ [79].

2.5 Trigger and data acquisition system

Different triggers are used depending on the type of system and the channels of interest. For experiments with pion beams, we used a trigger based on particle multiplicity. It requires a coincidence between one hit in the START detector and at least two hits in the META detector (RPC or TOF). The information provided by each detector is stored in specific files (HLD files), see Sec.3.1.

2.6 Target

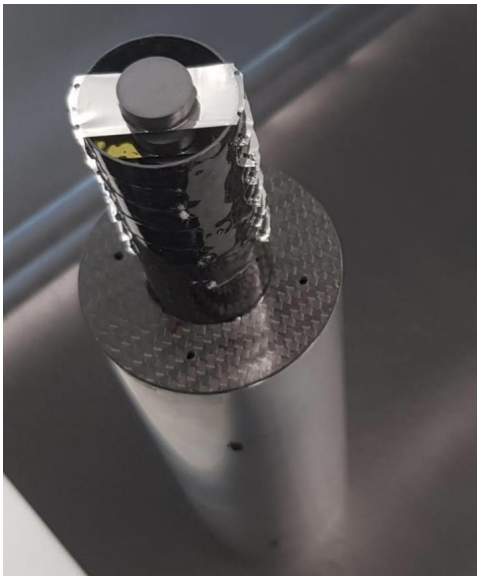

Figure 2.10: Photo of the segmented high purity carbon target used during the pion beam time.

In the pion beam experiment, two targets were involved: the carbon and the polyethylene (PE) targets. The former consists of high-purity isostatically pressed carbon material called Sigrafine type R6650, with $\rho = 1.85\ g/cm^3$. It has been developed by SGL Carbon SE based in Germany [80]. The carbon material has a cylindrical shape and is divided into seven equal segments, each having a diameter of 12 mm and a thickness of 3.6 mm. The distance between each pair equals 3.55 mm (or 7.1 mm between two centers). The target is held by a carbon fiber

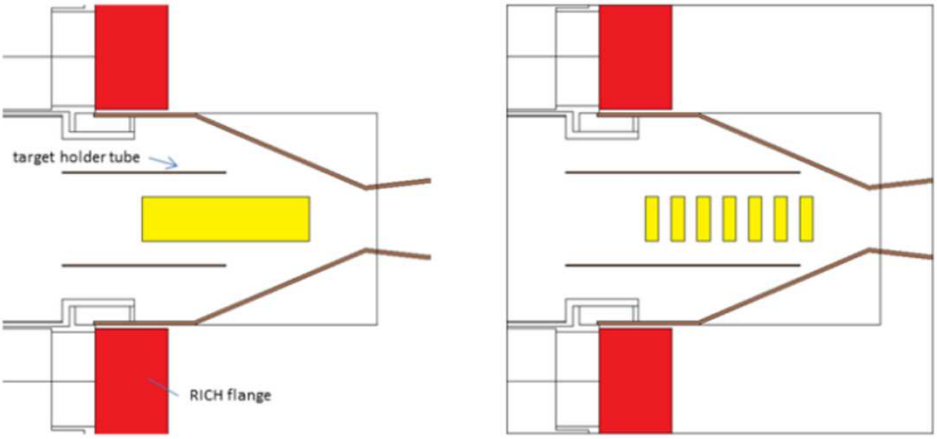

Figure 2.11: Schematic view of the polyethylene $(CH_2)n$ (left) and carbon (right) target systems.

material tube (RICH tube) with an outer diameter of 26 mm and thickness of 0.5 mm. All segments are attached to the tube by kapton foils mounted in one direction, see Figs. 2.10 and 2.11. The polyethylene target (PE) is a

Target	PE	C
Diameter (cm)	1.2	1.2
Length (cm)	4.6	2.52 + 2.13
M (g/mol)	28	12
Density (g/cm^3)	0.93	1.85
Number of carbon atoms	$18.4 * 10^{22}$	$23.4 * 10^{22}$

Table 2.1: Targets properties [35]

.

homogeneous cylinder, depicted in Fig. 2.11 (left). Just like the carbon target, it spans 46 mm in length and 12 mm in diameter. The target holder used for both targets is a carbon-fiber tube with an outer diameter of 26 mm and a wall thickness of 0.5 mm. Further information regarding the properties of the targets can be found in table 2.1. Both targets were positioned with their centers situated 3.2 cm upstream from the center of the HADES detector. It should be noted that, for our analysis, we only used data collected on the carbon target, see table 2.2.

Target	p(MeV/c)	Sum of events (10^6)	Data (h)
PE	690	774.7	175.56
PE	748	76.5	11.61
PE	656	42.4	14.08
PE	800	52.4	7.48
C	690	115.7	13.06
C	800	41.2	6.27
C	748	42.2	6.8
C	656	41.9	14.75

Table 2.2: Summary of the collected statistics [35] in the pion beam experiment.

2.7 Pion beam line

In this experiment, we have used the secondary pion beam and dedicated beam line to guide and focus the beam on the HADES target. More details about this facility can be found in [18]. In order to generate the pions, a primary

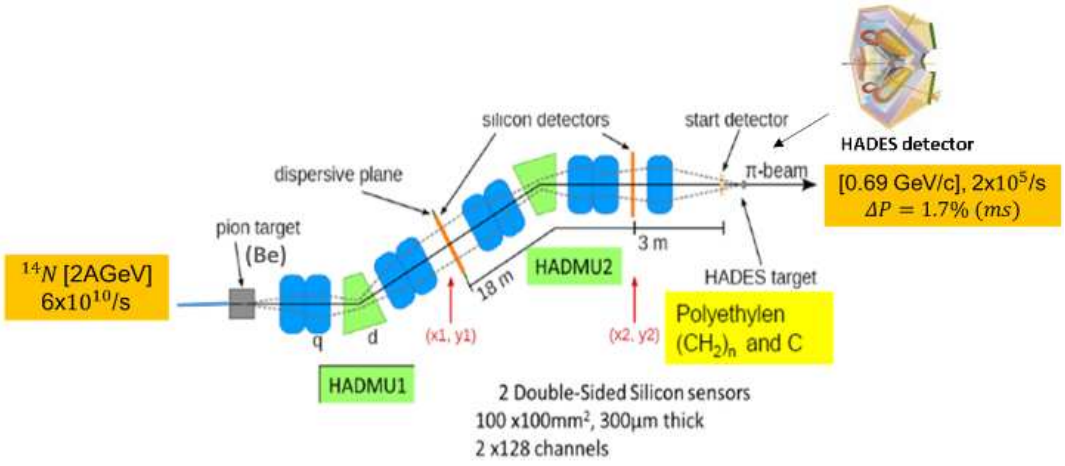

Figure 2.12: Pion beam line facility at GSI [18].

beam consisting of ^{14}N originating from the SIS18 synchrotron was used. This beam operated at energy of 2A GeV, and an average intensity of approximately $6 * 10^{10}$ ions per spill. The primary beam was directed onto a Beryllium target (Be) with a thickness of 10 cm. The HADES target was positioned downstream at a distance of 33 meters from the production point. The path was established by a beam line featuring a sequence of 9 quadrupole and two dipole magnets as illustrated in Fig.2.12. Notably, the magnetic field strength in the dipoles, and consequently the current, could be adjusted to select distinct momenta as needed. In the pion beam line, two silicon detectors were strategically positioned near the horizontal and vertical focal planes. The detectors are collectively known as the CERBEROS system [19], designed specifically for tracking beam particles. Pion trajectories have been reconstructed and pions momenta have been measured event-by-event. Fig. 2.13 shows the reconstructed momentum

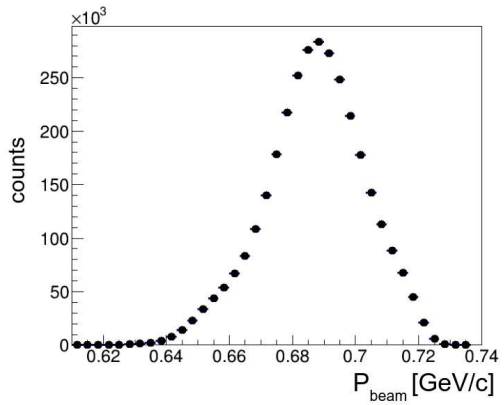

Figure 2.13: Pion beam momentum distribution measured with the in-beam tracking system CERBEROS [19, 18].

with CERBEROS momentum dispersion of the pion beam, which presents a width of about 1.7$\%$ (FWHM). Each detector is 300 µm thick and has a detection area of 10x10 cm^2, which allows for the detection of the majority of pions that strike the HADES target. The detectors are divided into 128 parallel strips, each with a width of 700 μm, and the rear and front sides of the strips are positioned perpendicular to one another. To minimize electronic noise that can result from material alterations under high particle load, as well as to prevent overheating due to vacuum operation, the detectors are cooled to -5°. Additionally, pulse height measurements are utilized to eliminate noise and to match hits on both sides of the detectors. In our experiment, only the information of the pion beam momentum distribution has been used in the analysis and simulations, but we have not used the event-by-event reconstruction of the momentum of the beam particle as it is not needed for our analysis.

Chapter 3

Experimental data analysis

This Chapter contains the description of all procedures used in the data analysis process and finally the evaluation of the observables of interest. Initially, we'll provide an overview of the pion beam experiment conducted at GSI. Subsequently, we will detail each stage of the analysis, starting with the detection of hits in the detector (raw data), particle trajectory reconstruction to the extraction of physical information about each individual particle.

3.1 Data processing

The pion beam experiment took place during the summer of 2014, spanning a 15-day period of data taking (between the end of August and the beginning of September). As already explained in chapter 2, this experiment involved two distinct targets: polyethylene $(CH_2)n$ and carbon. Both targets are described in Sec. 2.6, see Fig.2.11. The measurement has been performed at four pion beam nominal momenta: $p_{\pi^-} =$ 656 MeV/c, 690 MeV/c, 748 MeV/c, 800 MeV/c. The primary focus was on the momentum of $p_{\pi^-} =$ 690 MeV/c and took the longest period. The collected statistics with both targets are detailed in Tab. 2.2. Another experiment using the pion beam took place earlier in July 2014 at the pion momentum of 1.7 GeV/c in order to study the strangeness production on carbon and tungsten nuclei.

An overview of the essential stages of the data and simulation preparation (Fig. 3.1) is presented in this section and is listed below:

1. DAQ, trigger and HLD files: In every experiment, the Data Acquisition (DAQ) system and triggering play an important role in the data collection and reduction. The raw data - signals from Time-to-Digital Converters (TDCs) and the Amplitude-to-Digital Converters (ADCs) are obtained from read-out electronics of each sub-detector such as the RICH, MDC, TOF/RPC and Pre-Shower. The trigger is based on the multiplicity of hits in

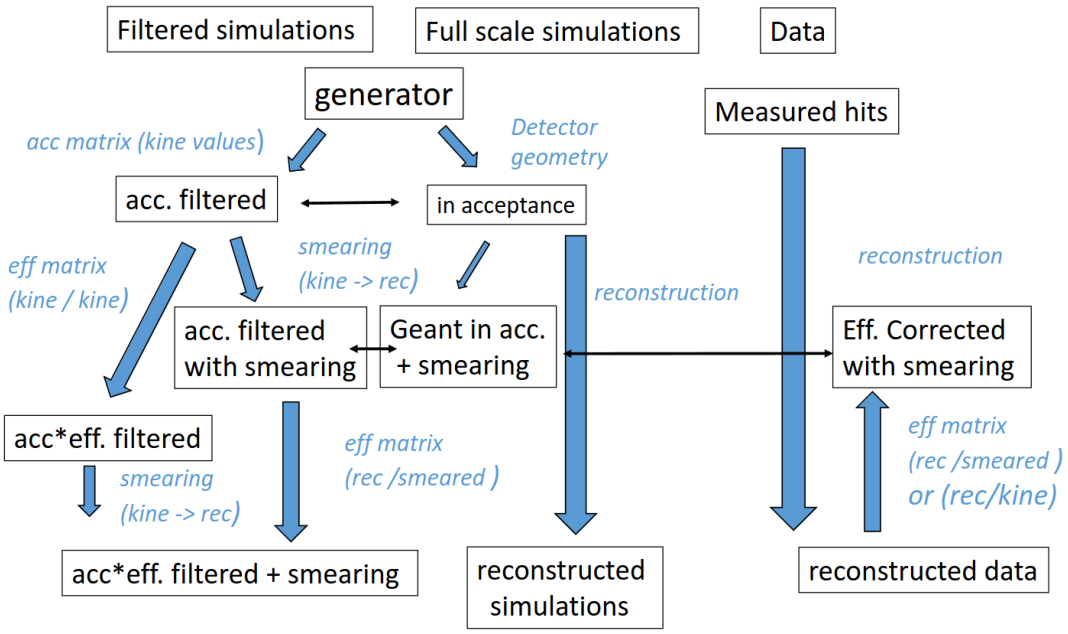

Figure 3.1: Schematic diagram representing the event processing for the data and simulations. See text for details.

the META detectors (TOF and RPC). These information are stored in specialized Hades List Data (HLD) files.

2. Data calibration and track reconstruction (DST): The second phase involves the conversion of values stored in HLD files to physical information as hit coordinates, TOF, energy loss, and also reconstructed tracks in MDCs etc... These tracks are then stored in the so-called Data Summary Tape (DST), as described in Sec. 3.2. To obtain the final DST, parameters related to the detector's geometrical setup, mapping of electronic channels and calibration are needed together with the tracking algorithm. These parameters are stored in the ORACLE database.

   To create DST files and analyze them, the HADES Collaboration has developed a common software for all kinds of analysis, which is based on the open-source data analysis framework ROOT provided by CERN. This framework is known as the Hades sYstem for Data Reduction and Analysis (HYDRA). Using the HYDRA environment, the analysis of the data is performed. The particle trajectories are reconstructed in the magnetic field using the Runge-Kutta algorithm and are matched with the META detectors. Finally, the data are written to the DST files as an object called *particle candidates*. These DST files include a lot of physical information such as TOF, energy loss measured in MDCs, along with the reconstructed momentum and angles. Moreover, DST includes the time information from the START detector and the momenta of the beam particles measured by the Cerberos system. Additionally, information concerning track quality factors is also written. More details can be found in the subsequent sections.

3. PostDST analysis: The DST files are input to a PAT (PostDST Analysis Tool) framework. This software is based on the NTuple Root structure and is dedicated to the analysis of the exclusive channels. One can easily

study hypotheses of various particle coincidences, e.g. 2-, 3-particle combinations. One needs to provide the PID cuts for each particle species: protons, pions, electrons, and positrons. More details about the PID method are given in Sec. 3.3).

4. Simulations: To compare the model predictions (simulated events) with the experimental data in the most reliable way, two methods are used: *full-scale simulations* and *filtered simulations*. For more detail, see Chapter 5.

3.2 Track and momentum reconstruction

As explained in section 2.2.2, the main role of the MDC sub-detectors is to reconstruct the charged particle trajectories. This is done using the hit positions within the chambers. In the following, we will show a small overview of the track reconstruction procedure.

3.2.1 Track path

Along the path, charged particles generate signals across various layers within each chamber. Given the different orientations of wires in each layer, it is possible to overlay the ”fired wires” [1] across the diverse layers of each chamber. This allows for estimating the particle’s hit positions within the chamber and finally reconstructing the particle trajectory. The procedure is based on the ”track candidate search”. Each track candidate is composed of two straight-line segments: an inner segment between MDC planes I and II (before the magnetic field), and an outer segment between MDC planes III and IV (after the magnetic field). This approximation is allowed due to the design of the superconducting coils, which results in an effectively negligible magnetic field between MDC I and II, and between MDC III and IV. The procedure is depicted in Fig.3.2.

Inner segment

The procedure starts with the Cluster Finder Algorithm, which aims at identifying hits belonging to the same track. First, only the inner MDCs (I and II) are considered. A set of fifteen equidistant points is designated within the target area, serving as anticipated event vertices (Fig. 3.3). For each cell with an associating signal, the volume delimited by the hit cell is projected from one of these fifteen points onto a virtual plane positioned between the two chambers. This plane is chosen to be perpendicular to the connection point of one of the 15 target segments. This iterative cluster identification procedure is repeated to all fifteen points along the z-axis, and the vertex corresponding to the cluster characterized by the highest amount of fired wires (with the greatest cell count) is designated as the ”cluster vertex.”

[1] Fired wires is a frequently employed expression within the HADES Collaboration to denote the wires that have emitted signals within the MDC chambers.

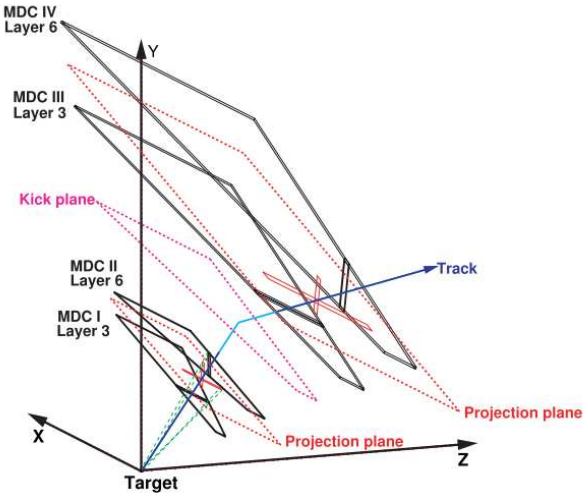

Figure 3.2: Schematic view of the four MDCs, each represented by only one of the six layers, and position of two projection planes, one between MDC-I and MDC-II and the other between MDC-III and MDC-IV. Also presented is kick plane between MDC-II and MDC-III [20].

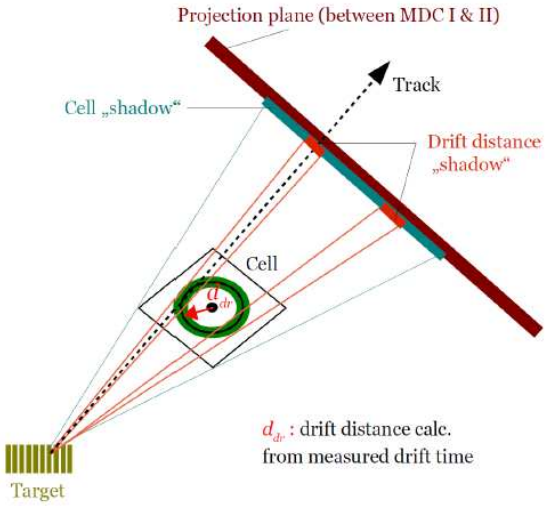

Figure 3.3: Illustration of procedure which utilizes the drift time to reduce the size of the projected area corresponding to a hit cell. The *drift distance shadow* can be compared to the *cell shadow*. The drift distance d_{dr} and the corresponding error, displayed as a green area are calculated from the measured time using GARFIELD simulations [20].

Outer segment

The effect of the magnetic field produced by the toroidal magnet on the path of a charged particle can be simplified as a modification in momentum. This adjustment takes place on a virtual flat plane known as the ”kick plane”, which is defined in simulations. This plane serves as an approximation of how charged particles are deflected inside the magnetic field, resembling a sudden change or ”kick” in their trajectory. Consequently, the track segments from the inner and outer MDC are projected and aligned onto this kick plane.

In the case of the outer drift chambers, a similar approach is employed as with the inner chambers, but, instead of utilizing the target position, the point of intersection between an inner segment and the virtual momentum kick

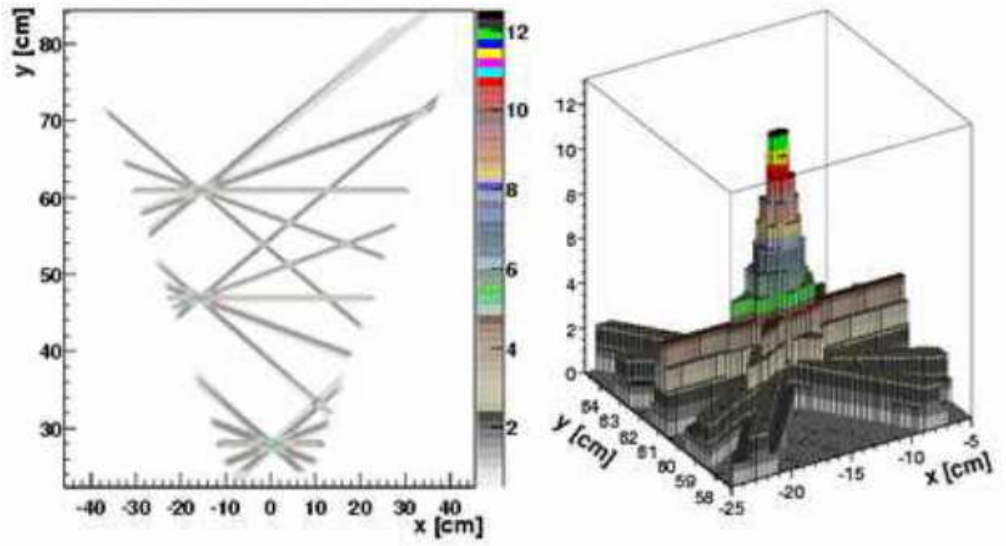

Figure 3.4: Left: Projection of drift cells on x-y detector coordinate space for an event with four tracks. Right: 2-dimensional histogram with a peak at the location where the drift cell projections have maximum overlap. In this example, the z axis indicates the peak height, corresponding here to a track with 12 hit in layers in the inner drift chambers [20].

plane is employed.

3.2.2 Momentum reconstruction

The momenta of the charged particles are reconstructed using the tracking system information. When charged particles like electrons or protons move through a magnetic field, the Lorentz force causes their paths to curve. This force is described by the equation:

$$\vec{F_L} = q(\vec{v} \times \vec{B}) \tag{3.1}$$

In this equation, q represents the particle charge, $\vec{v}$ its velocity, and $\vec{B}$ the magnetic field strength.

The net effect of this magnetic field on the particle's path leads to a change in the direction of its momentum. This momentum kick can be expressed as an integral involving the Lorentz force along the particle's path:

$$\Delta\vec{p} = \vec{p_f} - \vec{p_i} = \int_{\vec{p_i}}^{\vec{p_f}} d\vec{p} = \int_{t_0}^{t_1} \vec{F_L} dt = -q \int_{path} \vec{B} \times d\vec{s} \tag{3.2}$$

This integral can be interpreted as a sequence of successive slight "kicks" that the magnetic field gives to the particle as it travels along its curved path. This virtual kick causes the particle's direction to shift slightly, ultimately changing its momentum. To determine the momentum of the particle accurately, the Runge-Kutta method is implemented in HYDRA. This numerical approach is used to solve the equations of motion in the magnetic field region. It considers the momentum value derived from the spline method (alongside initial coordinates and direction) which is interpolated between the inner and outer segments and is based on connecting close points with a fifth-order spline

function. To fine-tune the momentum, the trajectory derived from the Runge-Kutta's solution must be adjusted. This solution provides expected hit positions across the four MDC planes. These positions are then compared to the real hits positions obtained in the measurement. The process involves iterating through parameters, with adjustments made each time to align with measurements (real hits). This alignment is achieved using the least squares minimization and the final χ^2_{RK} is stored alongside momentum and direction outcomes in analysis files. Momentum resolution is estimated to be approximately 1-2% for electrons and 2-3% for pions and protons.

3.2.3 META matching

The META matching serves as a supportive element in the track reconstruction process carried out by the tracking system (MDC), helping it with information extracted from TOF measurements (META). This procedure involves projecting the outer segments to the META detector using straight lines to establish an intersection point, effectively generating a META hit. This generated META hit is then matched with the fired META hits which are the measured signals in the META detectors, see Fig.3.5. This matching process is guided by evaluating the difference in the y-direction between the two, with a maximum difference a momentum-dependent value of up to 4 mm for high-momentum tracks. The quality factor is estimated by:

$$MetaQa = \sqrt{(\frac{x_{tof} - x_{int} - x_{offset}}{\sigma x})^2 + (\frac{y_{tof} - y_{int} - y_{offset}}{\sigma x})^2} \tag{3.3}$$

Here, x_{tof} and y_{tof} represent the extrapolation of the Runge-Kutta track in the TOF and RPC detectors. x_{int} and y_{int} represent the META hits detected in the TOF and RPC components. The terms x_{offset} and y_{offset} are chosen strategically to align the residuals around zero. The values σx and σy correspond to the resolutions along the two directions, and these are fine-tuned using simulations. All combinations of tracks and META hits that have the lowest MetaQa value are preserved at the DST level.

3.3 Charged Particle identification

The identification of charged particles in HADES can be done using two methods. The first method relies on the momentum-velocity correlation. In this approach, the particle's momentum is determined by its deflection in the magnetic field, using Runge-Kutta's method, as it was explained before. The particle's velocity is determined from the time-of-flight measured in the TOF and RPC sub-detectors, as described in Sec. 2.3.1. The velocity is calculated using the following formula $\beta = v/c = \frac{d}{c\Delta t}$, where d stands for the track length and Δt is the time of flight from the START detector to the TOF/RPC wall.

The momentum-velocity correlation is expressed as $p = m\beta\gamma c$, where m is the particle's mass, β is the velocity,

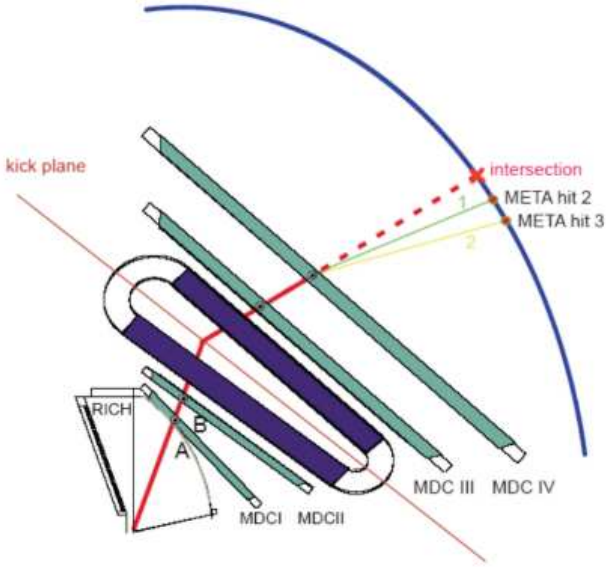

Figure 3.5: Principle of the matching procedure between the track and META information [17].

and $\gamma = \frac{1}{\sqrt{1-\beta^2}}$ denotes the Lorentz factor. Fig. 3.6 presents the typical identification spectrum for charged particles originating from the pion-carbon collisions. The second method is based on the energy loss measured in MDC and

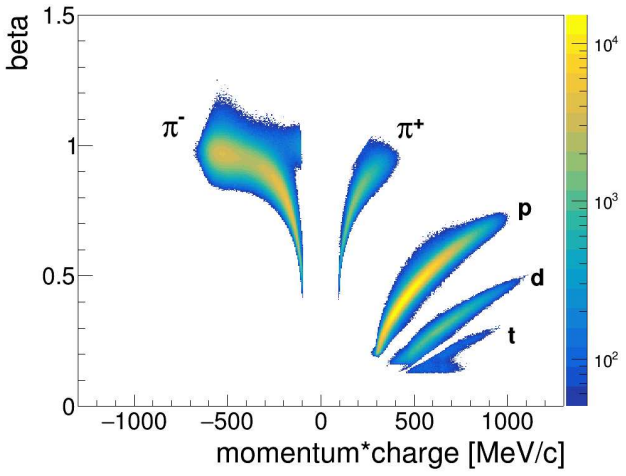

Figure 3.6: Particle identification of charged particles using beta vs. momentum∗charge correlation and plotted after imposing graphical cuts.

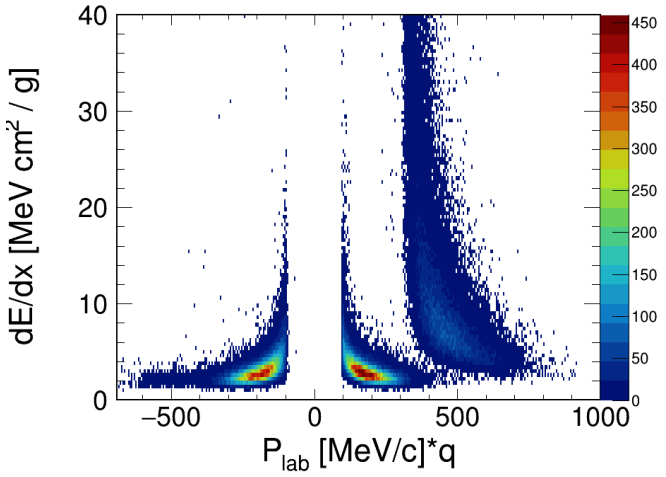

Figure 3.7: Particle identification of hadrons using dE/dx energy loss in MDC vs. momentum∗charge correlation.

the momentum correlation. The Bethe equation, which describes the dependence between the energy loss per unit of distance of a charged particle and its momentum when traversing matter ($MeV\ g^{-1}\ cm^2$) is given by:

$$-\frac{dE}{dx} = Kz^2\frac{Z}{A}\frac{1}{\beta^2}\left[\frac{1}{2}\ln\left(\frac{2m_e c^2\beta^2\gamma^2 T_{\max}}{I^2}\right) - \beta^2 - \frac{\delta(\beta\gamma)}{2}\right]. \tag{3.4}$$

Where:

- $\frac{dE}{dx}$ is the rate of energy loss per unit length (stopping power) of the particle.
- K is a constant. $K = 4\pi N_A r_e^2 m_e c^2 = 0.307\,\text{mol}^{-1}\text{cm}^2$:

  r_e is the classical electron radius, $r_e = 2.818\,\text{fm}$.

  m_e is the rest mass of the electron, $m_e = 0.511\,\text{MeV}$.

  N_A is Avogadro's number, $N_A = 6.022 \times 10^{23}\,\text{mol}^{-1}$.
- z is the charge of the particle.
- Z is the atomic number of the nucleus.
- A is the atomic mass of the nucleus.
- β is the velocity of the particle in units of the speed of light, c.
- γ is the Lorentz factor, $\gamma = \frac{1}{\sqrt{1-\beta^2}}$.
- m_e is the rest mass of the electron.
- T_{max} is the maximum energy transferable to electrons in a single collision.
- I is the average ionization energy of the material.
- δ is a density effect correction term accounting for the stopping power increase at lower velocities.

The Bethe equation gives accurate predictions within the range of momenta that are accepted by the HADES spectrometer and for the masses of charged particles formed in heavy-ion collisions at SIS18 energy. The energy loss and momentum correlation in MDC are illustrated in Fig. 3.7. This figure shows the effective differentiation and separation of the three charged particles: protons, π^-, and π^+.

The HADES detector has no specific neutron detector. However, we could check, using simulations, that neutrons can interact in the TOF detector with a probability of about 2%. One could therefore, in principle, identify neutrons using hits in the META which are not correlated with a track. We spent some time on such an analysis, in particular in view of reconstructing (p,n) SRC pairs (see Chapter 7) , but the results were not very promising, due to the large amount of secondary neutrons, which can hardly be distinguished from primaries.

3.4 Data normalization

The absolute normalization factor for the data measured on the carbon target is based on the relative normalization between measurements on the carbon and polyethylene targets. Then the measurements on the polyethylene target are normalized using the known $\pi^- - p$ elastic-scattering cross section. This procedure was used for the analysis

of the π^-p reaction, where it was necessary to subtract interactions with carbon nuclei from the measurements in the polyethylene target (see [13] for details).

The procedure was based on analyzing the missing mass spectrum of the $\pi^- + p \to \pi^- + p + X$ channel within both targets. Figure 3.8 illustrates a comparison of the missing mass spectrum. For the CH_2 target, the narrow peak near zero, corresponds to elastic pion-proton interactions. Conversely, the extended tail in the negative region corresponds to the interactions involving a proton bound in the carbon nucleus. These quasi-free interactions have indeed missing masses shifted towards negative values due to the proton's Fermi momentum distribution, as will be discussed in Sec. 6.3. In order to have a good overlap of the carbon and polyethylene spectra in the tail region, the carbon measurements need to be multiplied by an extra factor F_{C/CH_2}. This relative normalization has been obtained in a dedicated procedure of finding the most optimal value of F_{C/CH_2} by an event-by-event matching of the carbon signal derived from the CH_2 target to the events from the carbon target, for details see [13].

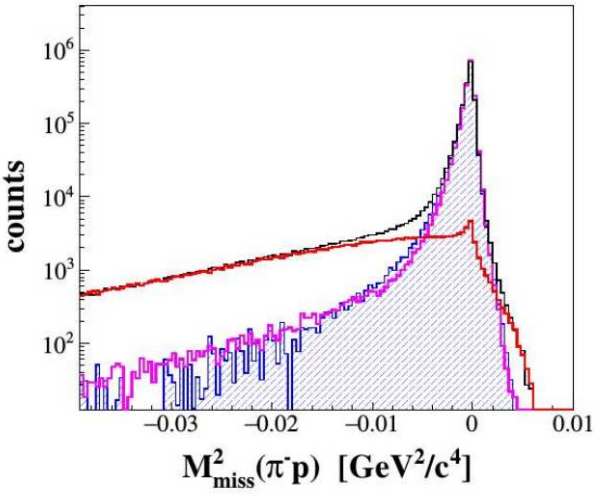

Figure 3.8: Squared $\pi^- p$ missing mass from the pion-proton system measured at 0.7 GeV/c after elastic-scattering selection. Black and red histograms present events from the polyethylene target and contribution of pion reactions on carbon nuclei in the polyethylene target, respectively. Their difference, hatched blue area, corresponds to $\pi^- p$ reactions. Simulations of the $\pi^- p$ elastic scattering are shown by the magenta histogram.

After this normalization, one can subtract the carbon contribution from the CH_2 yields. This subtraction yields the distribution of the elastic pion-proton interactions (in blue). To further select the $\pi^- + p$ elastic scattering, angular selections based on the kinematics of elastic scattering are applied. The number of selected events after correction for acceptance and efficiency in the range of CM polar angles $\theta^{CM}_{\pi^-}$ of 59.5°- 110.5° (see also [13]) is denoted as N_{el}. Knowing the cross section for elastic scattering within the same solid angle, σ_{el},we can normalize the yields on the CH_2 using the factor $\frac{\sigma_{el}}{N_{el}}$.

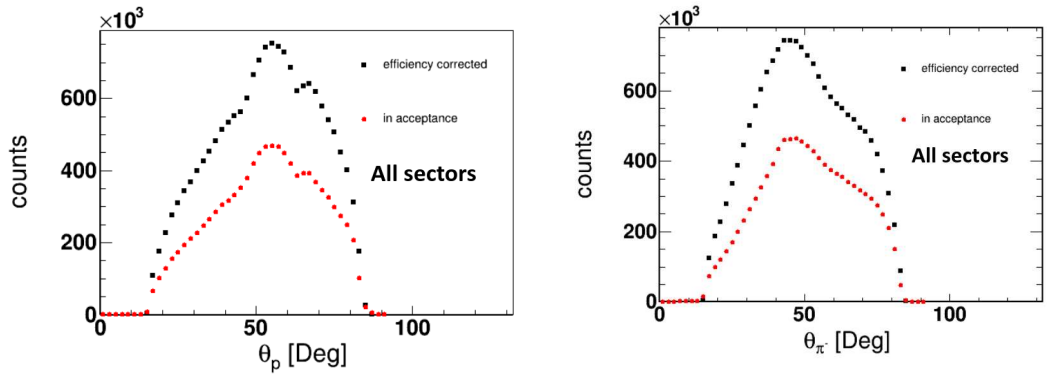

Figure 3.9: Comparison between distributions of θ polar angles plotted in the HADES acceptance with (black) and without (red) efficiency correction for protons (left plot) and π^- (right plot).

3.5 Systematic errors estimation

Efficiency correction

All our analysis plots are generated using the raw data in the HADES acceptance. The detector efficiency makes an important contribution to the uncertainties. The estimate of systematic errors involves the application of efficiency corrections to the distributions. This process is performed using the acceptance and efficiency matrices explained in Sec.5.2. To correct the yields for efficiency, the number of counts in each angle bin is divided by the weight of efficiency taken from the 3D efficiency matrices. Fig. 3.9 displays the detector's efficiency effect on proton and π^- angles, respectively.

Estimation of point-to-point systematic errors

All experimental spectra presented in the Chapter 6 will take into account statistical and point-to-point uncertainties in the error bars. The statistical errors are negligible in most of the bins. One way to estimate possible systematic errors related to detector efficiency is to cross-check the cylindrical symmetry of our results. Indeed, as the beam is not polarized, there is no preferred direction in the transverse plane. In particular, the six sectors should give a similar result, within error bars and our results should not depend on the azimuthal angle φ. To estimate the point-to-point systematic errors, we plotted for each bin (i) of the size of 2° in the polar angle of the proton and the π^- the ratios of efficiency corrected counts of each sector ($\Delta\varphi = 60^\circ$) to the mean counts per sector (Sector-to-Mean ratio-SM) defined as :

$$SM(i) = \frac{6 \times N_{s,i}}{\sum_{s=1}^{s=6} N_s} \tag{3.5}$$

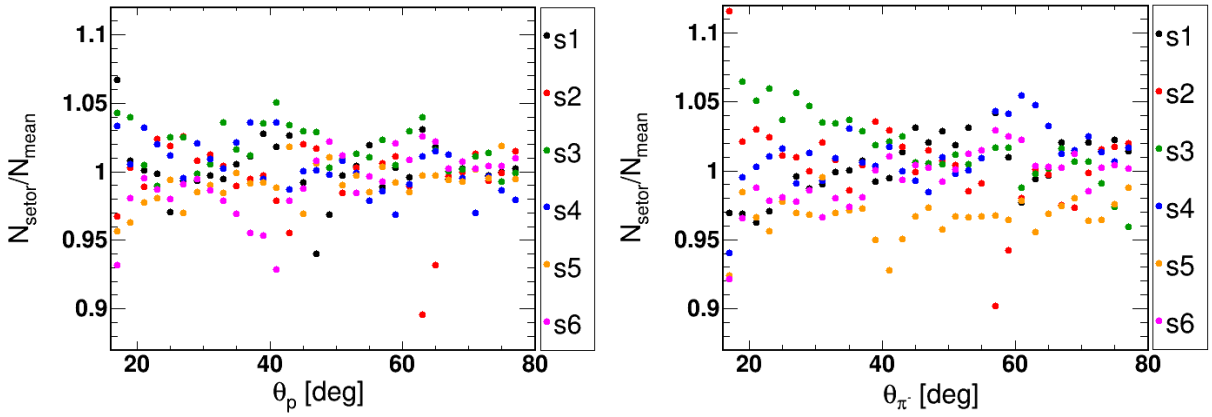

Figure 3.10: The count ratios for each sector with respect to the average count along θ, after applying efficiency correction using the INCL++ model. Left: protons. Right: π^-. Each sector is represented by a distinct color.

where $N_{s,i}$ is the number of counts for sector (s) and bin (i). Assuming a detector efficiency of 100%, we would expect an equal distribution of events across the azimuthal angle. In simpler terms, each sector, spanning 60°, would ideally contain an equal number of counts. Fig. 3.10 represent the ratios calculated for the proton and the π^- after applying the efficiency corrections. The differences between the sectors vary between $\pm$ 5% for all angle bins. All our results discussed in chapter 6 are integrated over sectors, which reduces the effect of the fluctuations by a factor of $\sqrt{6}$, i.e. point-to-point errors are estimated to be 2.5%.

The global effect can be estimated as :

$$\epsilon = \sqrt{\frac{1}{N_{tot}} \sum_{i \in bins} \sum_{s \in sectors} N_{i,s} \sigma_{i,s}^2} \tag{3.6}$$

where $\sigma_{i,s}$ is the deviation of the Sector-to-Mean ratio from the expected value of 1, and N_{tot} is the sum of the counts over all sectors and bins. The resulting global systematic errors are found to be 2.1% for proton measurements and 2.6% for pion measurements, which are considered small values. However, this does not exclude possible global systematic effects on efficiency, which would then affect all sectors in the same way.

Part of this effect is corrected by the normalization procedure. Indeed, the normalization factor $\frac{\sigma_{el}}{N_{el}}$ compensates for a possible error in the number of counts after efficiency corrections. However, such an error on efficiency correction could also depend on the momentum or on the channel (e.g. be different for pions and protons). In light of this uncertainty, we adopt a conservative approach and assign a systematic point-to-point error of 5% to account for potential efficiency variations.

The normalization error has been calculated for the analysis of the π^-p reaction using both carbon and polyethylene targets [13]. The carbon data normalization uncertainty was estimated to be 4.1%.

Chapter 4

Transport and cascade models

Theoretical hadronic models are powerful tools for studying the behavior of hadrons in nuclear matter, and are widely used in a variety of fields, including nuclear physics, astrophysics, and cosmology. In contrast to static models, which assume a fixed distribution of particles, dynamical models allow for the evolution of the momentum and spatial distributions over time, making them more accurate and versatile for studying complex systems such as nuclear collisions. In Chapter 1, a few examples of applications of transport or cascade models were discussed. In this chapter, we will provide a short description of the transport models that are commonly used to describe the interactions between hadrons and nuclear matter in the energy range up to a few AGeV. We will focus on the features that are most important for our study and on the specific models (SMASH, GiBUU, RQMD.RMF) which have been used in the present analysis.

Then, we will discuss the cascade models, and more especially the INCL++ code, which are used in the same energy range as powerful tools for fast simulations, but are less sophisticated in terms of physics processes. Moreover, we will introduce the PLUTO event generator, which will be used for the simulations of the quasi-elastic process. Finally, we will explain how the simulations for the transport and cascade models are performed, filtered, normalized, and finally compared to the data.

4.1 Transport models

Transport models are typically used to study the time evolution of the momentum distribution of hadrons in the medium, taking into account the interactions between the hadrons and the surrounding nucleons. Several generations of transport models have been developed since 1980, see Fig. 4.1. The main families of transport models used in nuclear and hadronic physics in the SIS energy range are: The Boltzmann-Uehling-Uhlenbeck (BUU) model and the Quantum Molecular Dynamics (QMD) model. In our analysis, we are using the SMASH, GiBUU, and

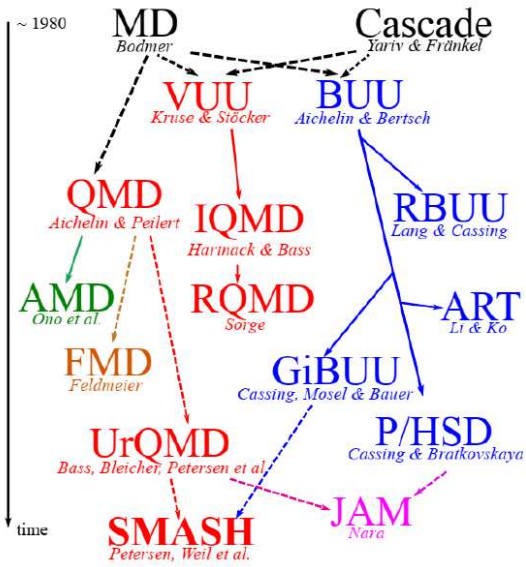

Figure 4.1: Schematic plot of various families of the transport codes and their evolution in time.

RQMD.RMF (originating from JAM transport code) transport models.

4.1.1 BUU and QMD approaches

BUU approach

In the BUU approaches, the particles are described by the function f(r,p,t) (single-particle density) which is initialized for each collision as:

$$f(r,p,t) = \sum_{i=1}^{A_{beam}+A_{target}} \delta(r-r_i)\delta(p-p_i) \tag{4.1}$$

BUU is a mean-field approach, which means that a hadron approaching the nucleus sees an average field (no granulation into nucleons).

The basic idea behind is to solve the Boltzmann equation 4.2, which describes the time evolution of the single-particle distribution function f(p,r,t), where *p* is the momentum of the particle, *r* is its position, and *t* is time. The Boltzmann equation is a partial differential equation that takes into account the collisional and transport processes that can change the momentum distribution of the particles and it is given as:

$$\frac{df}{dt} = \frac{\partial f}{\partial t} + \vec{\nabla}_r f \cdot \vec{v} - \vec{\nabla}_p f \cdot \vec{\nabla}_r U, \qquad \vec{v} = d\vec{r}/dt, \tag{4.2}$$

where U is the mean field potential, which depends on the model. The BUU equation not only includes terms that account for the mean-field effects of surrounding nucleons on the motion of particles but also might encompass various other components, such as collisional and transport processes occurring within the medium. It is a first-order differential equation in time that describes the time evolution of the one-particle phase-space distribution function of

particles interacting through binary collisions. The BUU equation describing collisions can be written as:

$$\frac{df}{dt} = I_{coll}, \tag{4.3}$$

where

$$I_{coll} = \sum_{reaction\ \ channels} \int \frac{d^3p_2 d^3p_3 d^3p_4}{(2\pi)^6} \frac{d\sigma_{12\to34}}{(d\Omega')} \left[(1-f_1)(1-f_2)f_3f_4 - f_1f_2(1-f_3)(1-f_4)\right] \delta\left(p_1+p_2-p_3-p_4\right) \tag{4.4}$$

and p_1, p_2, p_3 and p_4 are respectively momenta cells of particles in a two body process $(1,2) \to (3,4)$. $f(r,p,t)$ is a probability of occupation of momentum cell *p*. $1-f(r,p,t)$ is a probability that momentum cell *p* is free. Usually in BUU calculations the first step is a preparation of the phase-space density of the nuclear ground state. The coordinates of neutrons and protons are sampled according to density profiles, either taken from empirical Woods-Saxon (see next Section) or harmonic oscillator distributions or determined from relativistic Thomas-Fermi (RTF) calculations with the same mean-fields as those used in the dynamical propagation afterwards. The first method is used in the transport calculations with non-relativistic Skyrme-type potentials, whereas the second method is used in transport simulations with relativistic mean fields.

The most commonly used BUU-like transport codes are GiBUU and SMASH.

The **Giessen Boltzmann-Uehling-Uhlenbeck (GiBUU)** [81] model is a transport model that was developed in the 1990s as an extension of the BUU approach to include the effects of mesonic and quark-gluon plasma phases. The model was developed by the nuclear theory group at the University of Giessen in Germany and has undergone continuous development and improvement since its inception in the early 1990s. Its feature is to describe heavy-ion collisions (AA) and other hadronic collisions (pA, πA, $\bar{p}$A) and also elementary reactions on nuclei (γA, eA, νA). In this framework two different mean-field potentials are available: non-relativistic Skyrme potentials and relativistic mean fields, RMF. At higher energies, the Pythia string-fragmentation model is used. The model is based on hadronic degrees of freedom and currently contains 61 baryon and 22 meson states. The resonance parameters are taken from the analysis of Manley and Saleski [82]. Within the hadronic channels, a $2 \to 3$ particle production scheme is realized by GiBUU only.

SMASH (Simulating Many Accelerated Strongly Interacting Hadrons) is a Monte Carlo transport model based on the BUU approach. It is a quite recent model developed at the Frankfurt Institute for Advanced Studies, created for simulating heavy-ion collisions and other hadronic interactions. Details of the model can be found in [21]. In SMASH the Skyrme-like potential depends only on coordinates, not on the momentum of particles, and is calculated as a function of the local density. The potential acts only on baryons. In SMASH two degrees of freedom are taken into account: hadrons and strings. The list of hadrons includes all hadrons with 3- and 4-stars status in Particle Data Group[83], while string fragmentation is performed in Pythia 8 [84] event generator. Hadronic reactions

include $2 \rightarrow 1$ resonance formation, $1 \rightarrow 2$ decays and $2 \rightarrow 2$ reactions: NN→NN*, NN→NΔ as well as strangeness exchange reactions.

QMD approach

The QMD approach [85], an n-body theory, uses a more fundamental approach based on quantum mechanics principles. Each nucleon in the coherent state of the QMD model is represented by six time-dependent parameters, r_i and p_i, along with a fixed parameter *L* that determines the extension of the wave packet in phase space:

$$\phi_i(x_i, r_i, p_i, t) = \left(\frac{2}{L\pi}\right)^{3/4} \exp\left[\frac{-2}{L}\left(x_i - r_i(t)\right)^2 + \frac{1}{\hbar} i p_i(t) x_i\right], \tag{4.5}$$

where r_i and p_i are respectively the centroids in position and momentum of the wave packets. The total n-body wave function is obtained by taking the direct product of these coherent states:

$$\Phi = \prod_i \phi_i(x_i, r_i, p_i, t). \tag{4.6}$$

The equations of motion in QMD consist of the Schrödinger equation for the nuclear wave function and classical equations of motion for the centroids based on classical laws of motion. These equations describe the time evolution of the system and are used to simulate the dynamics of nuclear reactions and other phenomena in atomic nuclei. The equations of motions derived from the Hamiltonian are the following :

$$\dot{p_i} = -\frac{\partial \langle H \rangle}{\partial r_i} \quad , \quad \dot{r_i} = \frac{\partial \langle H \rangle}{\partial p_i} \tag{4.7}$$

The Hamiltonian *H* of the global system is given as:

$$H = \sum_i T_i + \frac{1}{2} \sum_{ij} V_{ij} \tag{4.8}$$

where T_i is the kinetic energy and V_{ij} is the potential energy. Contrary to the BUU approach, the potential is built from a sum of nucleon-nucleon potentials from surrounding nucleons.

The most commonly used QMD transport codes are UrQMD and RQMD.

RQMD stands for **Relativistic Quantum Molecular dynamics** [86, 87] and is a covariant extension of QMD. RQMD.RMF [88] is a newer version of RQMD where relativistic scalar and vector meson mean-field interactions are implemented into the microscopic transport code JAM (Jet AA Microscopic transport model) [89]. In JAM/RQMD.RMF, hadrons and their excited states are explicitly propagated in space-time by the cascade method. This approach combines elements of BUU and QMD. The treatment of the potential is similar to relativistic mean field potentials in BUU

models, while hadrons are represented as Gaussian wave packets, like in QMD models. Above the resonance region, soft-string excitation is implemented.

The ultra-relativistic quantum molecular dynamics (UrQMD) model [85] was developed in the middle of 1990s at Frankfurt. It can be used to study collisions of pp, pA, and AA over the vast energy range from GSI-SIS to CERN. The UrQMD model is widely applied for simulating heavy-ion collisions at relativistic energies. The Pythia generator is also implemented to perform the initial hard collisions and also a hydrodynamic evolution for the hot and dense stage of heavy-ion collision is possible.

In the following, we will discuss the common ingredients of these models.

4.1.2 Nucleus description

The positions are initialized using, except for RQMD.RMF, the Woods-Saxon distribution with parameters based on experimental charge distributions :

$$\frac{d^3N}{dr^3} = \frac{\rho_0}{exp\left(\frac{r-r_O}{d}\right)+1} \tag{4.9}$$

where $r_0 = 1.1\ A^{1/3}$, $d = 0.535$ fm and ρ_0 is the central density, i.e., the density at $r = 0$. GIBUU uses a harmonic oscillator for light nuclei like ^{12}C or ^{16}O.

In RQMD.RMF, the density at each nucleon position is computed using Gaussian, more details can be found in [88].

A Fermi gas description of the nucleus is used for the momentum distributions. The momenta *p* for particles are pulled randomly from a sphere of radius of $p_{_{Fermi}}(\vec{r})$ according to Local Thomas Fermi (LTF) approximations. The Fermi momentum writes:

$$p_{Fermi}(\vec{r}) = \hbar\left[\frac{3}{2}\pi^2\rho(\vec{r})\right]^{1/3} \tag{4.10}$$

where $\vec{r}$ is the nucleon position relative to the center of the nucleus.

The kinetic terms of single-particle Hamiltonians are always relativistic, i.e., they are expressed as $H \approx \sqrt{(p^2+m^2)}$, but potential terms can differ. The latter includes both Coulomb and strong interaction effects. "Non-relativistic potential" denotes a Hamiltonian of the form $H = \sqrt{(p^2+m^2)}+U$, where U refers to the potential. On the other hand, "relativistic" Hamiltonians are expanded to consider relativistic covariance and take on a more general form such as $H = \sqrt{(\vec{p}-\vec{U})^2+(m-V)^2}+U(0)$, where U and V are respectively vector and scalar potentials and U(0) is the 0_{th} component of the four-vector $(\vec{U}, U(0))$. These potentials can be momentum-dependent.

The GiBUU transport model allows for the selection between non-relativistic and relativistic potentials. The first kind of potential is the non-relativistic Skyrme-type nucleon potential with an (optional) momentum dependence. The second type of interaction is the Walecka model in the relativistic mean-field approximation.

RQMD.RMF uses momentum-dependent relativistic potentials only. By default, SMASH is using the non-relativistic nuclear Skyrme potential which is calculated during the particle propagation as a function of the local density. The potential is only exerted on baryons. No Coulomb or momentum-dependent potentials are implemented and hadrons are propagated in straight lines.

4.1.3 Collisions

Particles are moving in a potential field until a collision occurs, i.e., when the distance between two particles fulfills the following condition: $d < \sqrt{\frac{\sigma_{tot}}{\Pi}}$, where σ_{tot} is the total interaction cross-section between the two particles.

These collisions are binary reactions (of the type $a+b \rightarrow c+d$) and can be either elastic or inelastic. It has to be noted that particles are considered on-shell in the transport models. In our energy range, meson production occurs in these models via baryon resonance excitation. The SMASH model incorporates all established hadrons listed in the Review Of Particle Physics of [62] [83] up to a mass of $M = 2.35\ GeV$ as its degrees of freedom. RQMD.RMF also takes into account a lot of PDG hadrons. In GIBUU, the properties (masses, widths, and branching ratios) of all the resonances are taken from the partial-wave analysis of Manley. The treatment of unstable particles is usually done using the relativistic Breit-Wigner spectral function, as in Eq. (4.11).

$$\mathcal{A}(m) = \frac{2\mathcal{N}}{\pi} \frac{m^2 \Gamma(m)}{(m^2 - M_0^2)^2 + \Gamma(m)^2}. \tag{4.11}$$

Here, $\mathcal{N}$ is the normalization factor and is chosen such that $\int_0^\infty dm \mathcal{A}(m) = 1$, M_0 is the particle's pole mass, *m* is its current mass, and $\Gamma(m)$ is the total decay width, which is the sum of all the partial decay widths to different decay channels. A parameterization of all these decay widths is necessary, e.g., in GIBUU, the $\Delta \rightarrow \pi$N and $\rho \rightarrow \pi\pi$ are parameterized according to the following equation:

$$\Gamma(m) = \Gamma_0 \frac{M_0}{m} \left(\frac{q}{q_0} \right)^3 \frac{q_0^2 + \Lambda^2}{q^2 + \Lambda^2}, \tag{4.12}$$

where *q* denotes the final-state center-of-mass momentum for mass *m*, while q_0 is the same quantity for mass M_0, and $\Lambda = 1/R = 1 fm^{-1}$ can be viewed as a cutoff-parameter. The detailed treatment of the other decay channels can be found in chapter 3 (Sec. 3.3.1) of [81]. Such parameterization can slightly differ from one model to another. In SMASH, particles are considered stable if their decay width is less than 10 keV. Examples of such stable particles include π, ω, η, K, and others.

The probability of a given exit channel following a collision is related to its cross section and the kinematic variables of the emitted particles are sampled according to specific distributions, which in most cases follow phase space. Each model takes into account existing data in various channels to establish parameterizations of baryon

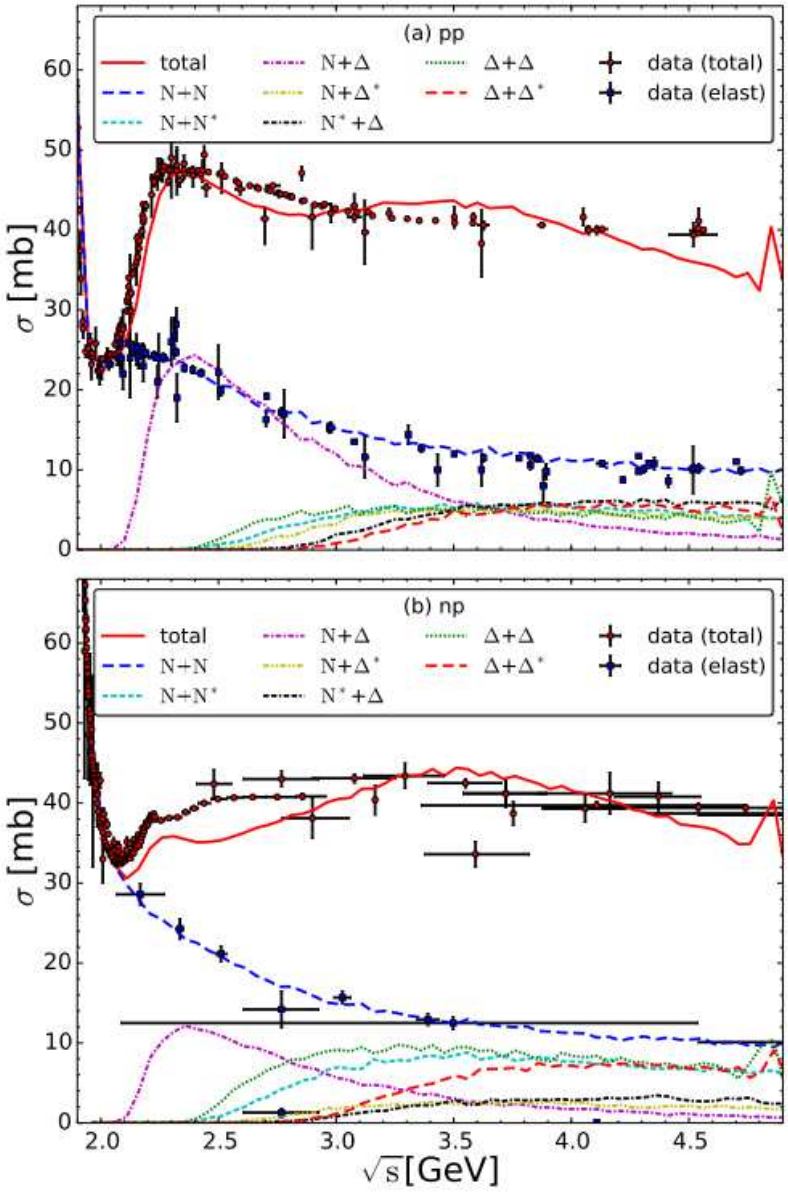

Figure 4.2: Proton-proton (a) and proton-neutron (b) cross sections from SMASH calculations compared to existing data. The contribution of single and double excitation of baryon resonances with isospin 1/2 (N*) and 3/2 (Δ) is shown [21].

resonance production cross sections or of isospin-dependent matrix elements $|\mathcal{M}|^2$ as a function of the center-of-mass energy ($\sqrt{s}$). For example, in GiBUU, the low-energy part of the nucleon-nucleon collision term is given by a resonance model based on the Teis analysis [90]. The information on differential distribution is more scarce which explains that in most cases, phase-space distributions are used. However, in some specific cases, as e.g. NN$\rightarrow$ N$\Delta(1232)$, information on the angular dependence of the reaction is also taken into account. Examples of the contributions of various types of baryonic resonance excitation in the SMASH model are shown in Fig. 4.2 for the pp and pn reactions, and the contributions from various pion production channels in pπ^-reaction are shown in Fig.4.3. Moreover, the exclusive cross sections for single-pion production in proton-proton collisions are shown in comparison to experimental data in Fig. 4.4.

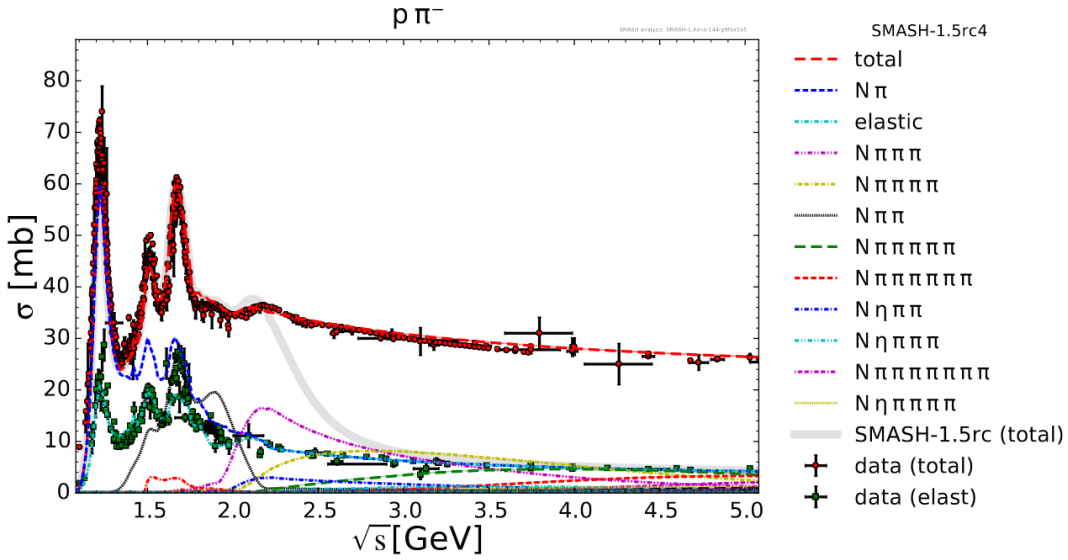

Figure 4.3: Proton-pion cross sections from SMASH calculations compared to existing data.

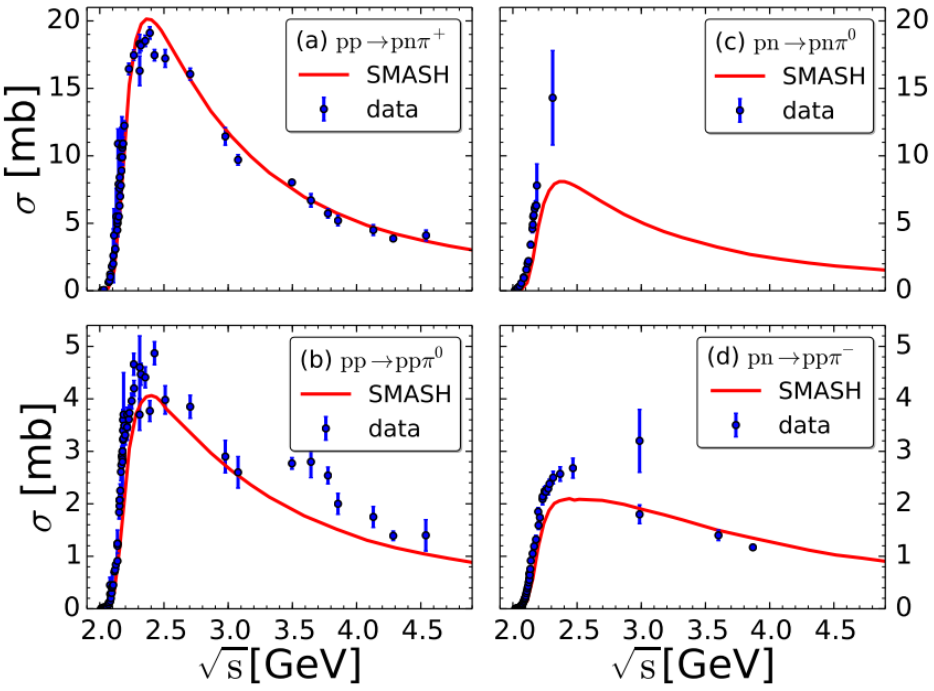

Figure 4.4: Cross sections for single pion production from proton-proton (left) and proton-neutron (right) collisions in the SMASH calculations compared to data [21].

All models consider Pauli blocking, which means that the outgoing nucleons should not be too close to other nucleons in phase space, otherwise the collision is forbidden. This is done by checking the phase-space distributions of particles in the case of BUU models and the extension of the wave packets in QMD models.

4.2 The Intranuclear Cascade Model (INCL++)

The Intranuclear Cascade was developed to study spallation reactions [91]. In such reactions, a light projectile (proton, neutron, etc.) hits a nucleus at an energy where the structure of the nucleus is not very important (typically above 50 MeV) and light particles are emitted, together with residual nuclei, which might be far from the stability. Spallation reaction was initially described as a two-step process by Seaborg in 1937 [92]: the first, very fast, during which the incident nucleon transfers part of its energy to the target nucleus. The second, slower, during which the residual nucleus evacuates its excitation energy through the emission of low-energy light particles. Spallation reactions are utilized in nuclear waste transmutation in Accelerator Driven Systems (ADS) [93]. They are also important for understanding the role of nuclear spallation in nucleosynthesis [94] or the creation of extensive air showers generated by high-energetic cosmic rays [95]. As mentioned in Secs. 1.4.3 and 1.4.4, the HADES collaboration has studied spallation reactions, leading to the emission of protons, pions and light fragments in the p+Nb reaction at 3.5 GeV [6].

INCL++ is a versatile code used in multiple applications that involve particle transport in matter. In particular, INCL++ is one of the hadronic models available in the Geant4 physics lists [96]. It uses the Monte Carlo method to solve the transport equation described in Eq. 4.3.

The nuclear cascade process involves a series of interactions between various particles within a static and constant potential well (dependent on their energies and isospins) that describes the nuclear mean field.

Nucleus description

The description of the nucleus is similar to transport models with Wood Saxon distributions for the positions of the nucleons (see [97] for details), but a global ansatz for the momentum distribution is employed, where a constant Fermi momentum ($p_F = 270\ MeV/c$) is used, see Eqs. 4.15 and 4.16, instead of a density-dependent one (Eq. 4.10).

In the global Fermi gas model, nucleons are treated as non-interacting nucleons (fermions) confined in a nucleus of volume V. Following the Fermi statistics, the Z protons and N neutrons fill up the available states in the position and momentum space, up to maximum values $k_{F,Z}$ and $k_{F,N}$ in such a way that

$$Z = \frac{4\pi k_{F,Z}^2}{3h^3} V, \tag{4.13}$$

$$\text{and } N = \frac{4\pi k_{F,N}^2}{3h^3} V. \tag{4.14}$$

The nucleus volume can be written as $V = A\frac{4\pi}{3} r_0^3$, where $r_0 = 1.1$ fm is the nucleon radius.

Then, the Fermi momentum is given by the following equation:

$$k_F = \frac{\hbar}{r_0}\sqrt[3]{\frac{9\pi}{4}\frac{Z}{A}} \quad \text{for protons,} \tag{4.15}$$

$$k_F = \frac{\hbar}{r_0}\sqrt[3]{\frac{9\pi}{4}\frac{N}{A}} \quad \text{for neutrons,} \tag{4.16}$$

where N is the number of neutrons and Z is the number of protons.

Then, the Fermi momentum for nuclei with Z=N is given by:

$$k_F = \frac{\hbar}{r_0}\sqrt[3]{\frac{9\pi}{8}} = 270\ MeV/c. \tag{4.17}$$

It should be noted that, in INCL++, one can use a value of the Fermi momentum, which is dependent on the mass of the nucleus; for more details, see Ref.[98]. Then, for the carbon nucleus $p_F(^{12}C) \approx 210\ MeV/c$, which is in better agreement with electron scattering measurements [23]. In the global Fermi gas model, the momentum probability density $\rho(p)$ is constant, and the momentum distribution follows a probability proportional to $p^2\rho(p) \sim p^2$ (where *p* represents the nucleon momentum). Fig. 4.5 from [25] illustrates the nucleon momentum distribution in the carbon

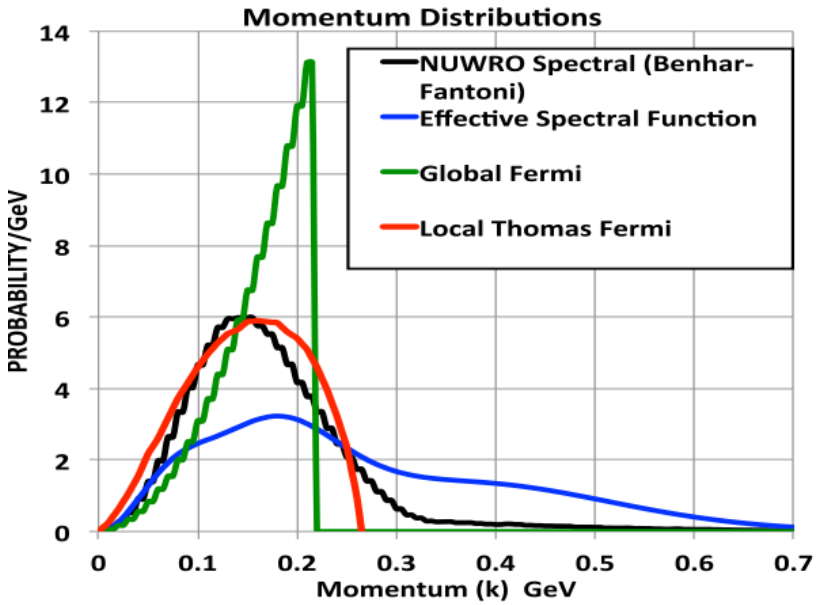

Figure 4.5: Nucleon momentum distributions in the carbon nucleus following various models: the Benhar-Fantoni 2D spectral function [22] (black), the Global Fermi model[23] (green), the Local-Thomas-Fermi gas model [24] (red) and the effective spectral function [25] (blue).

nucleus, where different spectral functions are being compared. The Global Fermi (green line) [23] clearly shows the probability proportional to k^2 until k_F, beyond which it becomes zero. On the other hand, alternative functions, like the Local-Thomas-Fermi gas (LTF) model [24] used in transport models (see Sec. 4.1.2), and the Benhar-Fantoni 2D spectral function [22], where dependence of the momentum distribution w.r.t. the position is added display broader

distributions extending beyond k_F with observable tails. The blue curve representing an effective spectral function developed in [25] and based on measurements, demonstrates an even broader distribution with an extended tail reaching up to 0.7 GeV/c.

The momentum and positions are sampled independently following distributions, as described above. However, the maximum position from the origin R_{max} that the particle can reach is correlated to its momentum *p*. This correlation is shown in Fig. 4.6, which presents the kinetic energy of a particle as a function of radial position from the origin.

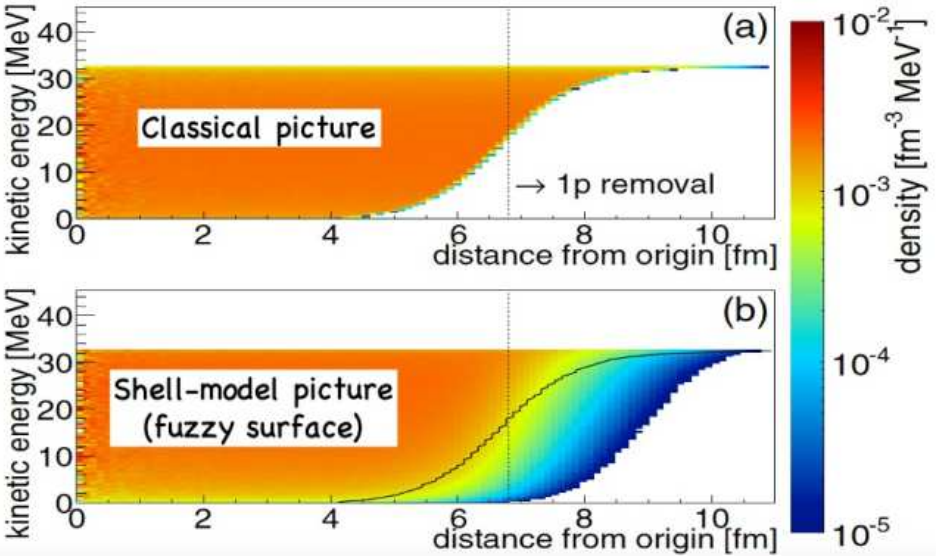

Figure 4.6: Kinetic energy and position correlations in the classical picture (top) and the fuzzy surface picture (bottom). The latter is used in INCL++ to describe the nucleus.

In this representation, the probability of occupying a distance r remains constant for each kinetic energy until the particle reaches $R_{\text{max}} = R_p$ and it is not allowed to occupy further distances. This implies that high momenta particles go further than low momenta. A classical picture was used until 2017, with a sudden fall of the probability at R_{max} then replaced by a picture with a gradual decrease in the probability of occupancy as a function of the position, following shell-model calculations [99].

Collisions

Particles move in straight lines between collisions with constant momenta. In our energy range, INCL++ takes into account only nucleons, pions, and $\Delta(1232)$ resonance. During the cascade process, binary collisions occur between nucleons, pions, and $\Delta(1232)$ resonances, which can be transmitted or reflected by the square-well potential they experience. In INCL++, these collisions are considered independent since the nucleon-nucleon distance is much greater than the mean free path λ of the incident particle in the target nucleus.

Additionally, the first collision undergoes a unique procedure known as ”local E” [97], which will be further dis-

cussed in Sec. 6.3.3. Different mechanisms are considered that take place at slower timescales and on a larger scale, encompassing the entire nuclear system, due to the relatively weak energy exchange. These mechanisms, which can include models of evaporation, Fermi fission, and break-up, are added to the cascade as de-excitation processes. ABLA07 [100] is one example of a de-excitation model that has been coupled with INCL++ and was used in the present study.

4.3 The PLUTO event generator

PLUTO is a Monte Carlo event generator developed by the HADES collaboration, built on the ROOT framework, often used in combination with the Geant4 toolkit. The main function of PLUTO is to simulate particle emission resulting from hadronic reactions, which includes the production and decay of particles in both elementary and heavy-ion-induced reactions. By representing each physics process as a set of objects created from specialized classes, each user can implement weights based on kinematical variables to take into account model predictions or data-based distributions, or experimental differential distributions. The classes in PLUTO include the `PParticle` class which describes the objects of particle type, the `PChannel` class which describes the decay of a primary particle to secondary particles, the `PReaction` class which describes a succession of channels as a chain of `PChannel`s, the `PDecayManager` class which allows the creation of reaction cocktails, and the `PData` class which lists all the different particles and their properties like mass, width, decay channels, and branching ratios.

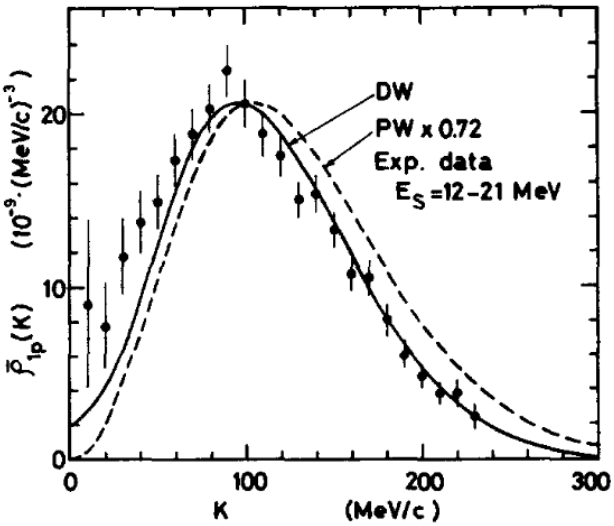

Figure 4.7: Momentum distributions measured in electron scattering on ^{12}C compared to shell-model calculations[26].

In the following analysis, we used PLUTO for simulations of the free $\pi^- p$ reaction and the corresponding quasi-free reaction on the carbon nucleus, see section 6.3. In this case, the angular distribution of emitted particles is parameterized based on the experimental data (see Fig. 1.18).

To treat interactions within the carbon nucleus, the Participant-Spectator model is used, where the nucleus is described as an off-shell participant nucleon N and on-shell spectator A-1 nucleus (see Sec. 6.1.3). The π^- interacts with a nucleon moving with a momentum distribution taken from [26], which is based directly on electron scattering on carbon data, see Fig.4.7.

Additionally, to make our predictions more realistic, we have implemented the pion beam momentum smearing measured in the experiment (see Fig. 2.13). .

Chapter 5

Simulation framework

Simulations are very crucial not only for the data interpretation, but also are used to correct the data for acceptance losses and detector effects.

In order to compare our data to simulations, one has to take into account the acceptance and the inefficiency of the detector. Usually the simulated events are generated in the full phase space while the experimental data are only available in the limited detector acceptance.

Two methods are utilized: the first one is called *Full-Scale Simulations* and involves a chain of event generation, processing it via detector acceptance and reconstruction procedure, and finally the applied analysis. This procedure is exactly the same as for the experimental data processing. The second method: *Filtered Simulations* consists of generating efficiency and acceptance matrices. They store the probabilities of particle detection inside the HADES acceptance. A simple view of the simulation processing scheme can be seen in Fig.3.1. In both cases, an accurate description of the detector's performance is crucial: precise alignment of the spectrometer, including steps like photogrammetry, measuring cosmic rays, and conducting measurements without a magnetic field. This alignment process is executed before and after each experiment, ensuring a precise description of the detector's behavior.

5.1 Full-scale simulations

In this method, the simulated particles are converted into the DST format, similar to the data and readout electronics (TDC, ADC). This method proceeds in a few steps:

- **Event Generation:** The first step is to generate the events. In this thesis, we use the following event generators: the INCL++ cascade and transport models such as SMASH, GIBUU, and RQMD.RMF. It has to be noted that each of these simulations yields distinct output formats. Therefore, a preliminary task is to convert these

outputs into EVT format, which is understood and read by HGeant.

- **Simulation with HGeant:** The Geant software toolkit originated at CERN with the purpose of simulating particle interactions in matter and their radiations. The HADES Collaboration developed a dedicated Geant simulation toolkit (HGeant) based on the GEANT3 package [101]. The detailed HADES geometry, active and passive detector elements, were implemented together with the magnetic field map. HGeant processes the propagation of particles, generated by the event generators, through the virtual spectrometer producing the map of hits in each active detector layer. The output is stored in ROOT files.
- **Event digitization:** The output from the HGeant is an input for the digitization and reconstruction processes. For consistency with the real data, all essential parameters for the digitization procedures are used and downloaded from the ORACLE database. Finally, DST files are produced which contain reconstructed trajectories (*Particle Candidates*), momenta, and other physical variables.
- **PID and final analysis:** Particle identification is implemented in the same way as in the data. The final analysis is performed using PAT, see 3.1.

5.2 Filtered simulations

The second approach relies on the preparation of the acceptance and efficiency matrices based on the HGEANT and DST. The acceptance matrices are generated based on HGEANT events in the full phase space and the HADES acceptance. The efficiency matrices are produced based on events detected in the HADES acceptance (HGEANT) and the reconstructed ones (DST). The matrices can be used to filter the simulated events in a very fast way. Filtered simulations were particularly useful for this thesis when conducting tests involving INCL++ parameters and investigating short-range correlations within the INCL++ model. Additionally, this method was also applied to filter PLUTO simulations for the quasi-elastic process.

Acceptance and efficiency matrices

The alternative method to the *Full-Scale Simulations* is to produce acceptance and efficiency matrices based on exactly the same conditions as used in the analysis and using so-called *white particles*. The *white particles* are generated using HGeant with uniform distributions in momentum (in the range between 0 and 1500 MeV/c), θ polar and φ azimuthal angles.

The detector acceptance matrix is calculated for each particle species using the HGeant output and corresponds to particles detected in the HADES geometrical acceptance (at least four MDC layers per chamber and one hit in the RPC detector or in the TOF detector). The efficiency matrices take into account the detector response and

tracking algorithm and are obtained based on DST outputs. The matrices are three dimensional and depend on the particle's momentum, θ and ϕ angles.

The matrices are then used to filter the events simulated with the INCL++ cascade model or with the transport codes. This method is very efficient. Once generated, matrices can be used for various purposes, to filter calculations or model predictions in a very quick way.

Acceptance matrices

In the initial phase, the acceptance matrices are created, assuming a perfect efficiency of 100% for the spectrometer.

The event generator produces six independent *white* particles, one per each sector, which are generated uniformly from the target volume. After processing the events in HGeant, we have information about the number of particles that successfully traverse the active volume of the detector, characterized by a specific momentum p, polar angle θ, and azimuthal angle ϕ: $N_{acc}(p, \theta, \Phi)$, and also the total number of counts of particles that were initially generated, $N_{tot}(p, \theta, \Phi)$. Then, the acceptance matrix is calculated as follows:

$$F_{acc}(p, \theta, \Phi) = \frac{N_{acc}(p, \theta, \Phi)}{N_{tot}(p, \theta, \Phi)} \tag{5.1}$$

In Fig. 5.1, 2D projections (θ vs. momentum and θ vs. Φ) of the acceptance matrices for protons, π^+ and π^- are presented.

Efficiency matrices

As already mentioned, the output files from HGeant are input for the DST where particle reconstruction takes place. In the same way as for the acceptance matrix, the efficiency matrix is calculated by the ratio of the reconstructed particles over the particles that successfully traverse the active volume of the detector, as given in the following formula:

$$F_{eff}(p, \theta, \Phi) = \frac{N_{reco}(p, \theta, \Phi)}{N_{acc}(p, \theta, \Phi)} \tag{5.2}$$

In Fig. 5.2, 2D projections (θ vs. momentum and θ vs. Φ) of the efficiency matrices for protons, π^+ and π^- are presented.

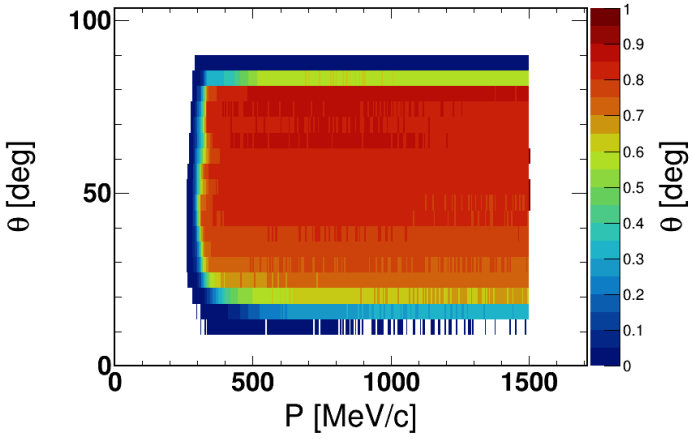

(a) The 2-dimensional projection on θ-momentum plane from the 3-dimensional acceptance matrix for protons. See text for details.

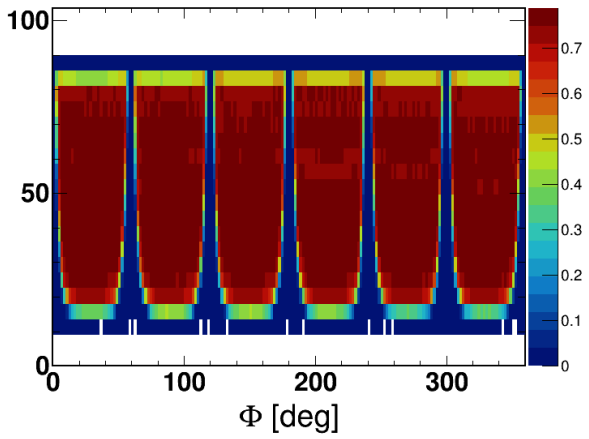

(b) The 2-dimensional projection on θ-ϕ plane from the 3-dimensional acceptance matrix for protons. See text for details.

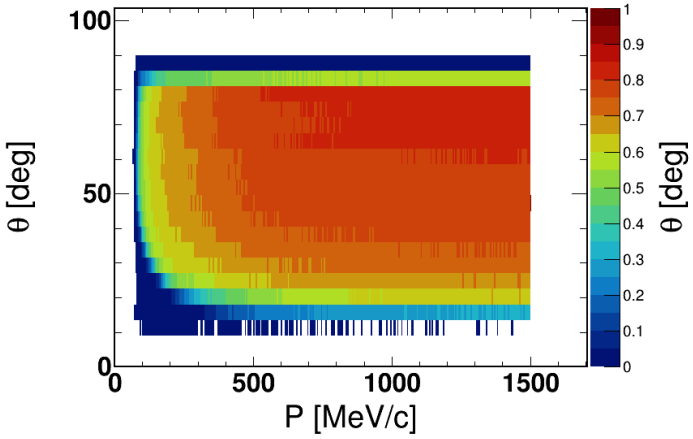

(c) Same as for 5.1a, but for π^+.

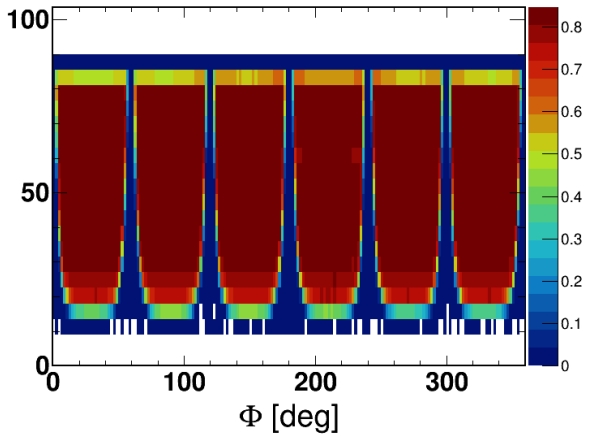

(d) Same as for 5.1b, but for π^+.

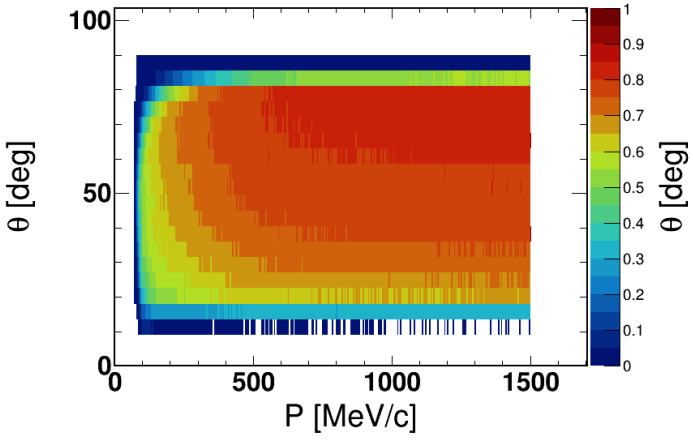

(e) Same as for 5.1a, but for π^-.

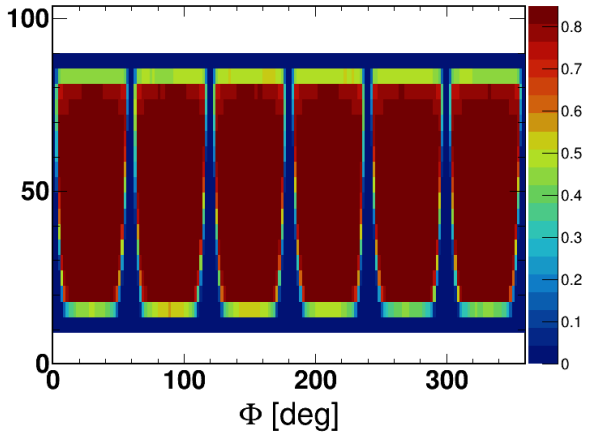

(f) Same as for 5.1b, but for π^-.

Figure 5.1: Set of acceptance matrices for protons, π^+ and π^-.

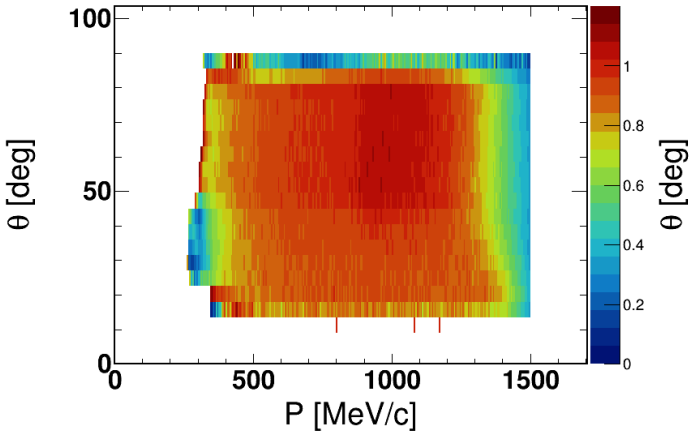

(a) The 2-dimensional projection on θ-momentum plane from the 3-dimensional efficiency matrix for protons. See text for details.

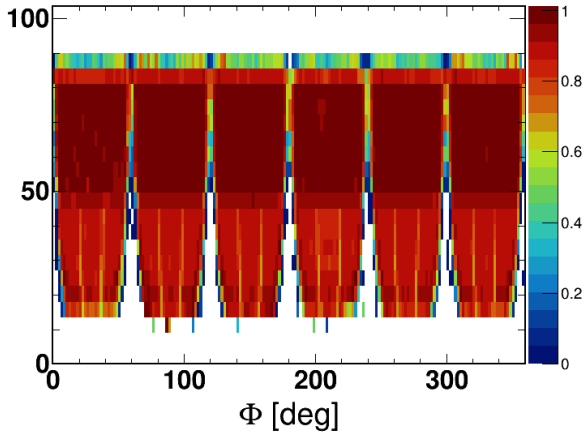

(b) The 2-dimensional projection on θ-ϕ plane from the 3-dimensional efficiency matrix for protons. See text for details.

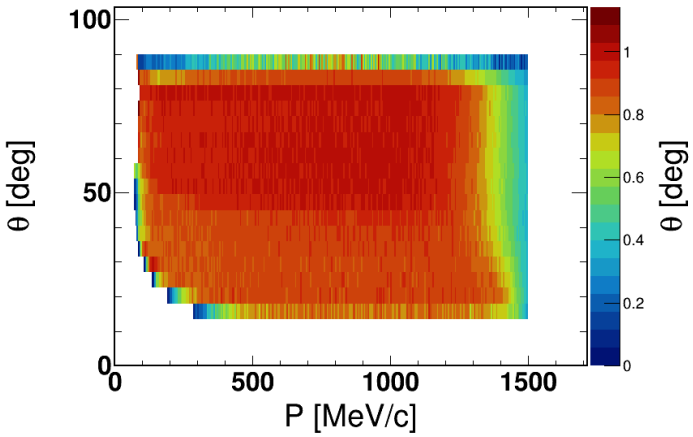

(c) Same as for 5.2a, but for π^+.

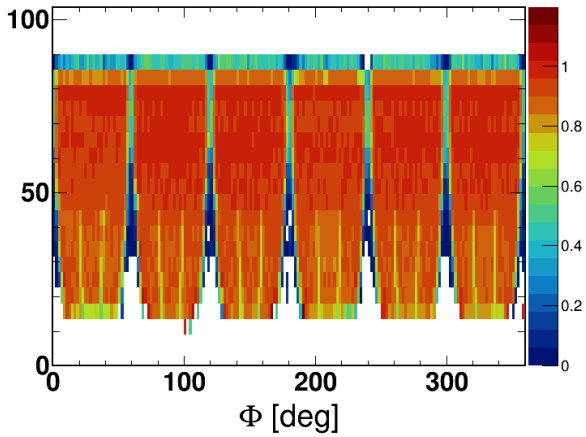

(d) Same as for 5.2b, but for π^+.

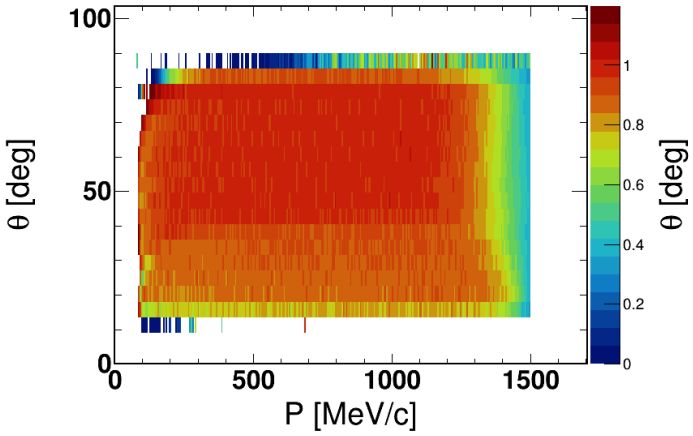

(e) Same as for 5.2a, but for π^-.

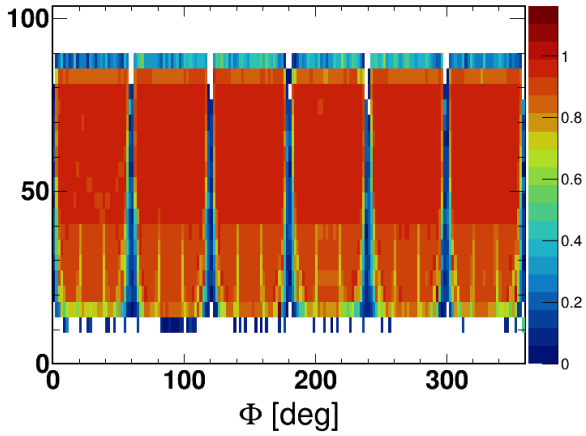

(f) Same as for 5.2b, but for π^-.

Figure 5.2: Set of efficiency matrices for protons, π^+ and π^-.

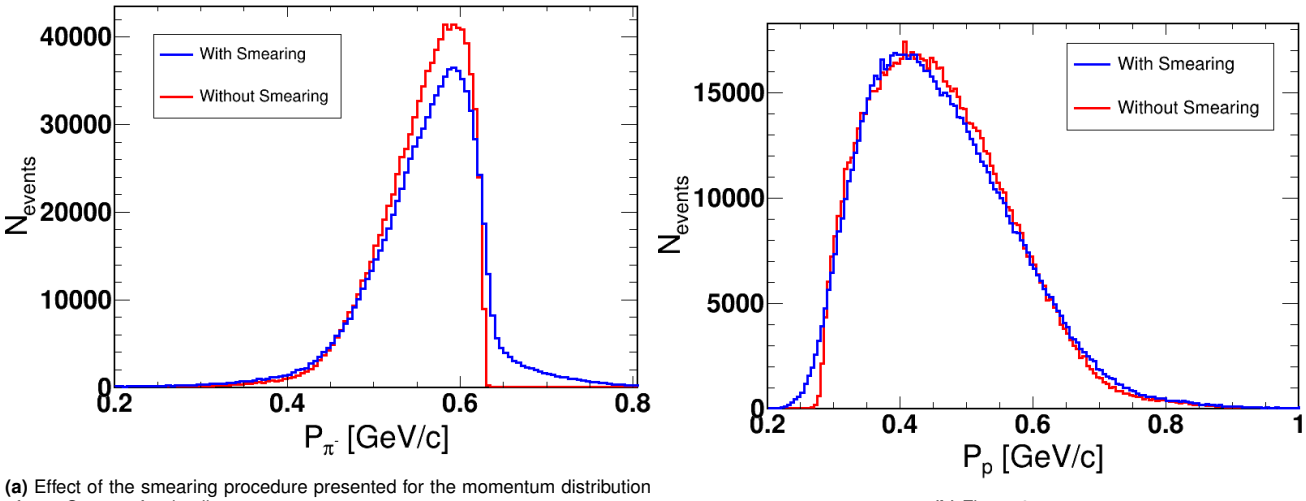

(a) Effect of the smearing procedure presented for the momentum distribution of π^-. See text for details.

(b) Figure 2

Figure 5.3: Effect of the smearing procedure presented for the momentum distribution of protons. See text for details.

Momentum smearing

The final phase of the filtered simulations involves substituting the ideal momentum derived from the simulations with the value of the reconstructed momentum (using the Runge-Kutta algorithm). Parameterization of the momentum smearing is derived based on the *white particles* and DST. For each 10 MeV bin in the ideal momentum and 2 degree bin in θ, the distribution of reconstructed momentum is plotted. Having such, the ideal momentum is replaced with the smeared value.

In Fig. 5.3 we present the smearing effects on the momenta of protons and π^- particles generated in PLUTO. The effect is not large but still should be taken into account.

5.3 Simulations Normalization

Each model has its own normalization based on a geometrical reaction cross-section $\sigma_{reaction}$, which is given in the output of the calculation, and the number of simulated events N_{shots}, which is chosen by the user. The yields have to be multiplied by $\frac{\sigma_{reaction}}{N_{shots}}$.

Chapter 6

Discussion of results

This chapter presents our analysis of the proton and pion spectra in different hadronic final states measured in the $\pi^- + ^{12} C$ reaction at an incident pion momentum of 0.69 GeV/c, with a focus on comparing our experimental data to theoretical models. In particular, we compare our data to predictions from the INCL++, SMASH, GiBUU, and RQMD.RMF models presented in chapter 4, and investigate different mechanisms within each model such as quasi-elastic, two-pion production, pion absorption and rescattering. A specific study of the quasi-elastic channel aiming at investigating short-range correlations (SRCs) is presented in chapter 7.

6.1 Overview of the various exit channels

6.1.1 Pion-Nucleon reactions

Table 6.1: List of cross sections for various final states in π^-N collisions at $\sqrt{s_{\pi N}}$= 1490 MeV from the SAID analysis (solution WI08).

Reaction	σ [mb]
$\pi^- + p \rightarrow \pi^- + p$	17.8
$\pi^- + n \rightarrow \pi^- + n$	12
$\pi^- + p \rightarrow \pi^0 + n$	10
$\pi^- + p \rightarrow \pi^+ + \pi^- + n$	5.9
$\pi^- + p \rightarrow \pi^0 + \pi^0 + n$	2.2
$\pi^- + p \rightarrow \pi^- + \pi^0 + p$	3.77
$\pi^- + n \rightarrow \pi^- + \pi^- + p$	2.1
$\pi^- + n \rightarrow \pi^- + \pi^0 + n$	0.39

As discussed in Sec. 6.1.3, following a quasi-free picture, the main characteristics of the $\pi^- + \mathrm{C}$ reactions are driven by an initial πN reaction. It is therefore interesting to have in mind the cross sections of the main reaction channels in the π^-p and π^-n reactions at $\sqrt{s_{\pi N}}$= 1.49 GeV/c, i.e. the elastic, charge exchange and $\pi\pi$ N channels, which are listed in Table 6.1. As already discussed in Sec. 1.5.1, it can be observed that the most probable pro-

cesses are the elastic and charge-exchange channels and that the π^-p interactions are more likely than the π^-n interactions.

No precise number exists for the 3 pion production cross section but the order of magnitude is at least ten times lower than the two pion production cross section, (Sec. 1.5.2 and Fig. 4.3). In addition, as mentioned in Sec. 1.5.2, the threshold for the production of the η meson is $\sqrt{s_{\pi N}}$= 1.487 GeV and the η production cross section increases very rapidly above this threshold. The η production could therefore contribute to the three pion production via the decay $\eta \rightarrow \pi^-\pi^-\pi^0$, with a branching ratio of 23%. Taking into account the pion beam momentum spread, an average cross section for the η production in the π^-+p reaction was estimated to be 0.6 mb using Pluto simulations [102]. The contribution of the η production channel to the three-pion production is therefore expected to be small.

Elastic and charge exchange channels

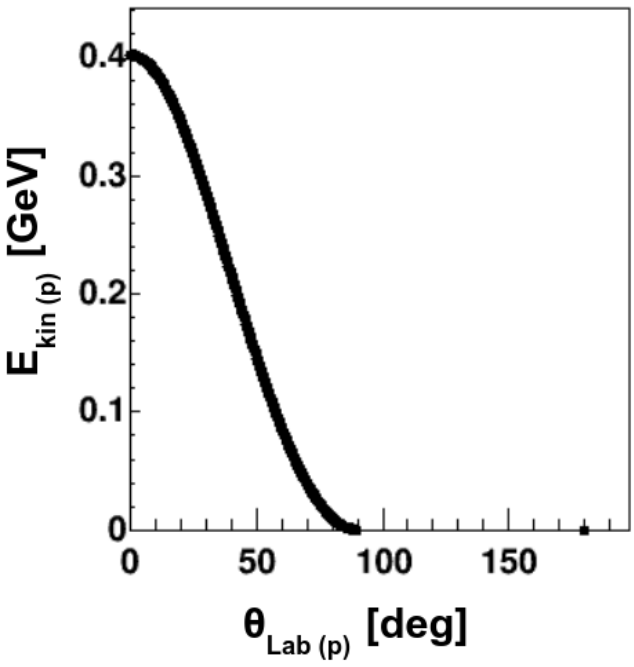

Figure 6.1: Correlation between the kinetic energy and the polar angle in the laboratory for the proton in the π N $\rightarrow$ π N process.

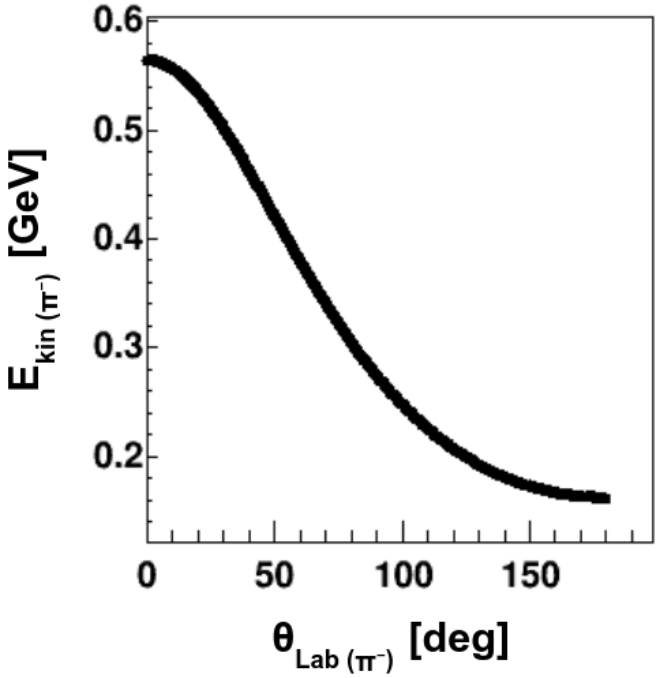

Figure 6.2: Same for the correlation between the proton and pion polar angles in the laboratory.

The elastic and charge exchange channels are characterized by the conservation of the kinetic energy between the entrance and exit channels, which implies that particles in the entrance channels are just scattered and no new particle is generated. In the charge-exchange process $\pi^- + p \rightarrow \pi^0 + n$, the isospin of the nucleon and pion changes, while in the elastic processes ($\pi^- + p \rightarrow \pi^- + p$ or $\pi^- + n \rightarrow \pi^- + n$), they do not, but the kinematics of both channels is very close, the difference being just due to the difference in the mass of nucleon and pions in the different isospin states. The momentum and energy conservation can be written in the case of the elastic and

charge-exchange reactions as:

$$\vec{p}_{beam} = \vec{p}_{\pi} + \vec{p}_{N'} \tag{6.1}$$

$$W_{beam} + M_N = W_{\pi} + W_{N'} \tag{6.2}$$

where $\vec{p}_{beam}, \vec{p}_{\pi}$ and $\vec{p}_{N'}$ are the momenta of the incident pion, exit pion and exit nucleon, respectively. W_{beam}, W_{π} and $W_{N'}$ are the incident pion, exit pion and nucleon total energies and M_N is the hit nucleon mass. In the case of charge-exchange, the nucleon and pion masses are slightly different in the entrance and exit channels. The kinematics of the elastic or charge-exchange process is characterized by the momentum of the two particles in the center-of-mass, which is equal to p_{cm} = 432 MeV/c for the π^-+p reaction at $\sqrt{s_{\pi^-\mathrm{p}}}$= 1490 MeV. As the particles are not polarized, the azimuthal angle distribution has to be isotropic and only one independent variable is left. For example, Figures 6.1 and 6.2 display the correlations between the nucleon polar angle in the laboratory and the kinetic energy (respectively polar angle of the pion in the laboratory), which is important for acceptance considerations, as will be discussed later. The nucleon is emitted below a maximum angle of about 90°, while there is no limit for the pion angle. However, it can be observed in figs 1.18 and 1.19 that the cross section decreases rather fast with the pion angle.

Pion production channels (inelastic)

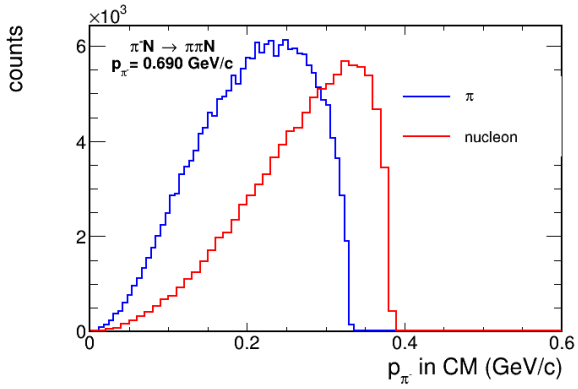

Figure 6.3: Center-of-mass momentum of pions and protons in the π N $\rightarrow \pi\pi$ N reaction at 0.69 GeV/c.

The kinematics of the two-pion channel is quite different from the elastic or charge-exchange. To illustrate this, we performed simple simulations of the π N $\rightarrow \pi\pi$ N reaction using the PLUTO event generator (see Sec. 4.3), where the particles are produced following phase space distributions. As shown in Fig. 6.3, the center-of-mass momenta of pions and protons are smaller than the elastic case value (p^{π}_{cm}=0.432 GeV/c) and have a broad distribution. The correlations between pion and proton momenta in the laboratory for the elastic and inelastic case are shown in Fig. 6.4. Although these correlations are expected to be significantly broadened due to the Fermi momentum in the

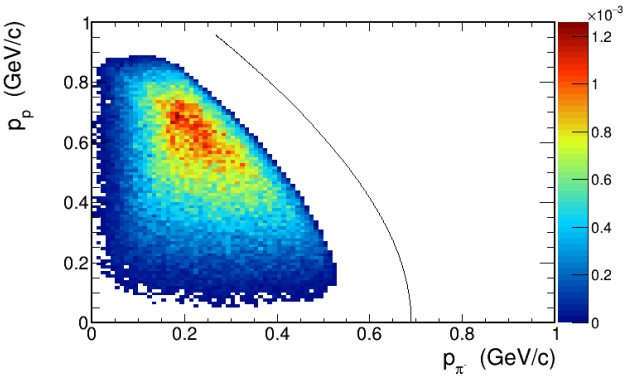

Figure 6.4: Correlation between proton and pion momenta in the laboratory in the π N $\rightarrow \pi\pi$ N reaction at 0.69 GeV/c.

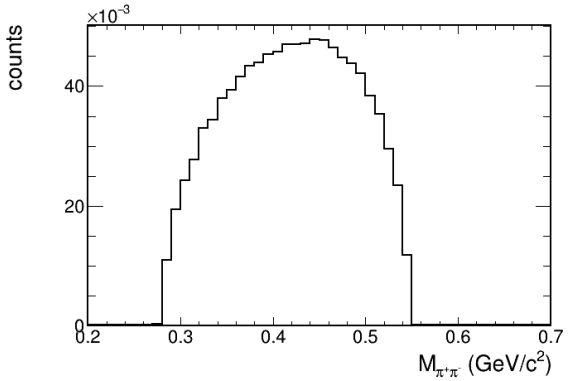

Figure 6.5: Results of PLUTO simulations for the πN$\rightarrow \pi\pi$N reaction: $\pi\pi$ invariant mass distribution.

carbon nucleus, as discussed below, they can therefore be useful to distinguish elastic and inelastic processes. The $\pi\pi$ invariant mass distribution for the πN$\rightarrow \pi\pi$N process is displayed in Fig. 6.5 as it will be useful for the discussion of channels with two detected pions.

6.1.2 Pion-Nucleus reactions

In a nucleus target, the incoming pion can interact with the nucleons in the carbon nucleus through the same reactions as in the free case. However, there is a significant distinction: the available energy for the reaction is different compared to the scenario involving a free nucleon. This modification arises due to two main factors. First, the motion of the nucleon within the nucleus affects the energy available for the pion-nucleus reaction. Second, the energy required to extract a nucleon from the nucleus, which is related to the nuclear potential seen by the nucleon in the carbon nucleus must be considered.

6.1.3 Kinematics of the quasi-free reaction

In a quasi-free picture, one can therefore consider that the pion interacts with a nucleon with a momentum $\vec{p}_N$ and a total energy: $W_N = Ek_N + M_N + U_N$, where $Ek_N = \sqrt{\vec{p}_N^2 + M_N^2} - M_N$ is the kinetic energy of the hit nucleon in the carbon nucleus and U_N the nuclear potential. The energy and momentum conservation relations write:

$$\vec{p}_{beam} + \vec{p}_N = \sum_f \vec{p^f} \tag{6.3}$$

$$W_{beam} + Ek_N + M_N + U_N = \sum_f W^f \tag{6.4}$$

Where the sum runs over the momenta $\vec{p^f}$ and energies W^f of the final detected products. Note that this equation is valid, only if the detected products did not undergo further final state interaction.

The new terms w.r.t. to the free case (see Eq. 6.2) are the nucleon momentum in the carbon nucleus $\vec{p}_N$, which is related to the kinetic energy by $Ek_N + M_N = \sqrt{\vec{p}_N^2 + M_N^2}$, and the potential energy U_N which are expected to broaden the kinematical correlations existing in the free case.

The squared center-of-mass energy can be deduced :

$$s_{\pi N} = (W_{beam} + W_N)^2 - (\vec{p}_{beam} + \vec{p}_N)^2. \tag{6.5}$$

It is assumed that the cross section is the same as the one for the reaction on a free nucleon at the same center-of-mass energy. One can note that in the general case, the hit proton is off-shell. One can define the proton effective mass $M_N^\star$ by the relation

$$W_N = \sqrt{\vec{p}_N^2 + {M_N^\star}^2}. \tag{6.6}$$

One can also write the total energy-momentum conservation:

$$\vec{p}_{beam} = \sum_f \vec{p^f} + \vec{p}_R, \tag{6.7}$$

$$W_{beam} + M_{^{12}C} = \sum_f W^f + W_R, \tag{6.8}$$

where $\vec{p}_R$ and W_R are the momentum and energy of the system of undetected particles, respectively.

One can introduce the missing momentum $\vec{p}_{miss}$:

$$\vec{p}_{\text{miss}} = \sum_f \vec{p^f} - \vec{p}_{\text{beam}} = -\vec{p}_{\text{R}} \tag{6.9}$$

which is nothing else but the momentum of the system of undetected particles.

Depending on the nature of the detected particles, the recoiling systems consists in a fixed number of nucleons and a variable number of pions, with a mass

$$M_R = \sqrt{{W_R}^2 - \vec{p_R}^2}. \tag{6.10}$$

For example, in the case of the detection of one π^- and one proton, the recoiling system has 11 nucleons, if no further pion is emitted, M_R will be expected to be close to the mass of the ^{11}B nucleus, with some possible excitation energy. If a pion is emitted, the mass of M_R should be larger than the sum of the ^{11}B and π^0 mass or ^{11}C plus π^- mass.

In the case of the π^-+ p quasi-free scattering and in the absence of rescatterings (or Final State Interaction), the system of 11 nucleons keeps its intial momentum:

$$\vec{p}_{\mathrm{R}} = \vec{p}_{\mathrm{N}} = -\vec{p}_{\mathrm{miss}}, \tag{6.11}$$

which gives access to the nucleon momentum in the target nucleus (see Sec. 6.3 and Chap. 7).

Participant-spectator model

In the case of the participant-spectator model used in Pluto, it is assumed that the carbon nucleus consists of an on-shell ^{11}B and an off-shell nucleon which do not interact and have opposite momenta ($\vec{p}_N = -\vec{p}_{^{11}B}$) in the carbon nucleus. The energies of the hit nucleon and spectator ^{11}B are related by

$$M_{^{12}C} = W_N + W_{^{11}B}, \tag{6.12}$$

where $M_{^{12}C}$ is the ^{12}C mass. Since the ^{11}B is on-shell, on can further write:

$$W^2_{^{11}B} = \vec{p}^{\,2}_N + M^2_{^{11}B}, \tag{6.13}$$

where $M_{^{11}B}$ is the ^{11}B mass. These equations allow to deduce the nucleon energy, the nucleon effective mass and the center-of-mass energy from $\vec{p}_N$.

The $\sqrt{s_{\pi \mathrm{N}}}$ distribution obtained in simulations of the $\pi^- + \mathrm{C}$ reaction using PLUTO is shown in Fig. 6.6 in comparison to the π^-+p reaction where the width of the distribution is only due to the beam momentum spread. It can be observed that the center-of-mass energy distribution obtained for the $\pi^- + \mathrm{C}$ reaction is much broader than in the π^-+p case, which means that the effect of proton momentum distribution in carbon is much larger than the spread of pion beam momentum. In addition, the $\pi^- + \mathrm{C}$ distribution is shifted to lower values, due to the effect of the binding energy. This is reflected in the effective mass which has a strongly asymmetric distribution ranging up to a maximum value which is smaller than the proton mass, as can be observed in Fig. 6.7. These features are characteristic from the quasi-elastic process, while the exact shape of the distribution reflects the hypothesis of the participant-spectator model and might be different in other models.

6.1.4 Multi-step processes

Also, multi-step processes occur in the nucleus target where the pions and/or nucleons from the final state can re-interact with other nucleons before being emitted. The multi-step process can consist of different possible combinations of the single-step processes, including possible nucleon-nucleon rescattering ($NN \rightarrow NN$). The cross

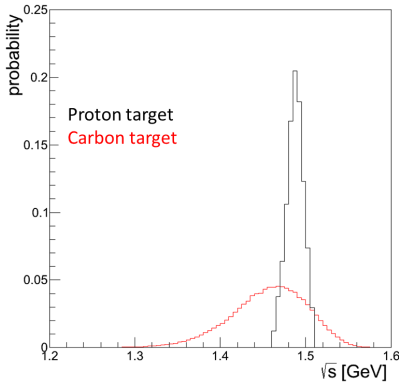

Figure 6.6: Comparison of the energy in the π^-p center-of-mass in the quasi-free π^-p reaction on ^{12}C (red) and in the free reaction (black) in PLUTO simulations.

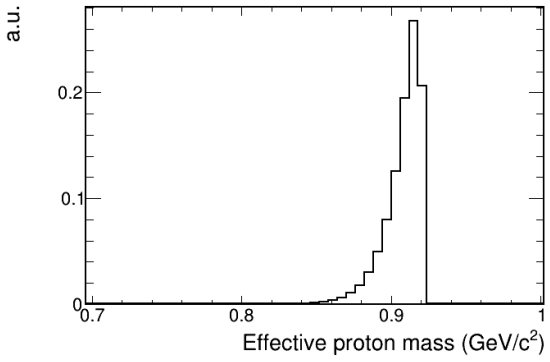

Figure 6.7: Effective proton mass in the quasi-free π^-p reaction on ^{12}C in PLUTO simulations.

sections for the further steps strongly depend on the energies of the pion and nucleons from the first step, in particular for protons, the elastic scattering cross sections rises very fast when the energy decreases (Figs. 4.2, 4.3).

Elastic or charge exchange processes can occur at different collisions steps. This is different for the pion production, which needs an energy in the πN or NN collision system above the pion production threshold. It is therefore expected that pion production will be suppressed in the later steps of the nuclear cascade. To check this, we investigated the most favorable case, where the first step is an elastic or charge exchange scattering. Nucleons emitted in the forward direction might indeed have enough energy to produce a pion in a second collision.

The minimum nucleon energy for $NN \rightarrow NN\pi$ is given by :

$$E_{kin}^{min}(N_2) = \frac{(2 \cdot m_{N_2} + m_\pi)^2 - 2 \cdot m_{N_2}^2}{2 \cdot m_{N_2}} - m_{N_2} = 288\ MeV \tag{6.14}$$

Fig.6.1 displays the kinematic relation between the kinetic energy E_{kin_N} and the polar angle θ for a scattered nucleon N in the elastic scattering ($\pi^- + N \rightarrow \pi^- + N$) on a nucleon at rest. It can be observed that, when $\theta_N < 30°$, $E_{kin_N} > 288MeV$. However, the yield in this region is very small. As a result, the production of the two pions mainly occurs in the same step.

6.1.5 Invariant and Missing masses

For each channel, we can define the following invariant and missing mass variables, which we will be using in the following analysis. The invariant mass variable : $M_{inv} = \sqrt{(\sum_i E_i)^2 - (\sum_i \vec{P}_i)^2}$. The missing mass variable: $M_{miss} = \sqrt{(E_{inc} - \sum_i E_i)^2 - (\vec{p}_{beam} - \sum_i \vec{p}_i)^2}$, where the sums run over the detected particles. These particles are characterized by their momentum represented as $\vec{P}_i$ and their total energy denoted as E_i. The term E_{inc} corresponds to the initial energy, which is the sum of the energy of the incident beam and the target (either a

nucleon or carbon). The incident momentum of the beam is represented as $\vec{p}_{inc}$.

6.1.6 Hadronic channels in INCL++

We will start the presentation of model predictions by general information on the type of exit channels obtained with INCL++. This model is chosen, as more detailed information than in other models is available, as e.g. the number of collisions, the type of the first collision (elastic or not),...

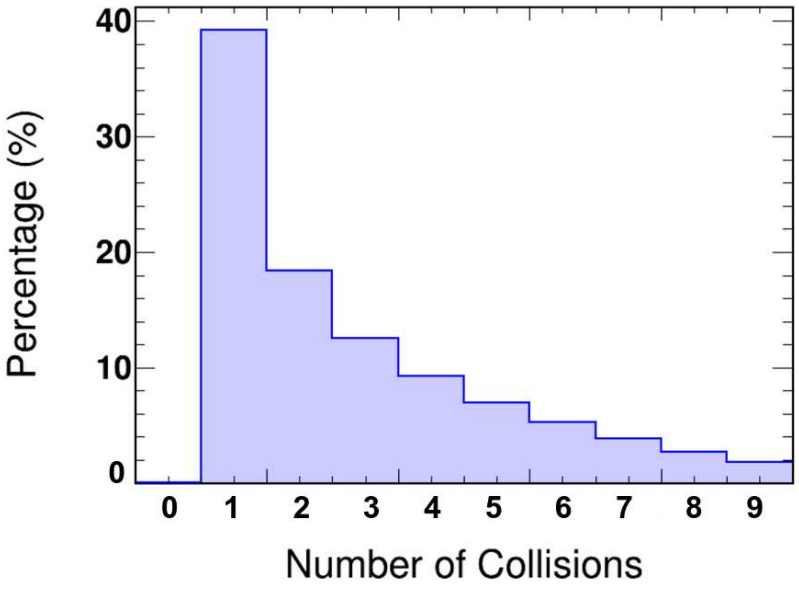

Figure 6.8: Predictions of INCL++ for the $\pi^- + C$ reaction at 0.685 GeV/c.

First, the distribution of the number of collisions is displayed in Fig. 6.8. The most probable value is one, but it presents a rather long tail. This suggests that in our energy both the first chance elementary collision and the rescatterings play an important role in the distribution of the exit channels. This specificity will be exploited in the following and we will try, as much as possible, to disentangle both types of effects.

As discussed above, due to the kinematics of the reaction, no nucleon-nucleon inelastic collision can occur in the course of the reaction. We can expect at maximum one pion-induced inelastic collision, producing two pions and other collisions in the same event will be either π+N or NN elastic collisions. The respective role of πN and NN secondary collisions is difficult to predict, as the cross sections depend a lot on the energy (Fig. 4.2).

The multiplicity of pions in the exit channel is presented in Fig. 6.9. According to the model, the single pion channel constitutes approximately 67.7% of the total, while the double pion channel accounts for around 21.5%, which is roughly in agreement with the elementary cross sections. It can also be checked that the three π production is completely negligible (less than 0.1 $\%$). One can also observe that the probability of emitting a π^+ is very small, as expected due to the fewer channels involving π^+ than π^0or π^+in π^-N reactions (see Table 6.1). As more than 50$\%$ of the events contain a π^- and, as π^0 can not be detected in our experiment, we will focus on events with a π^-.

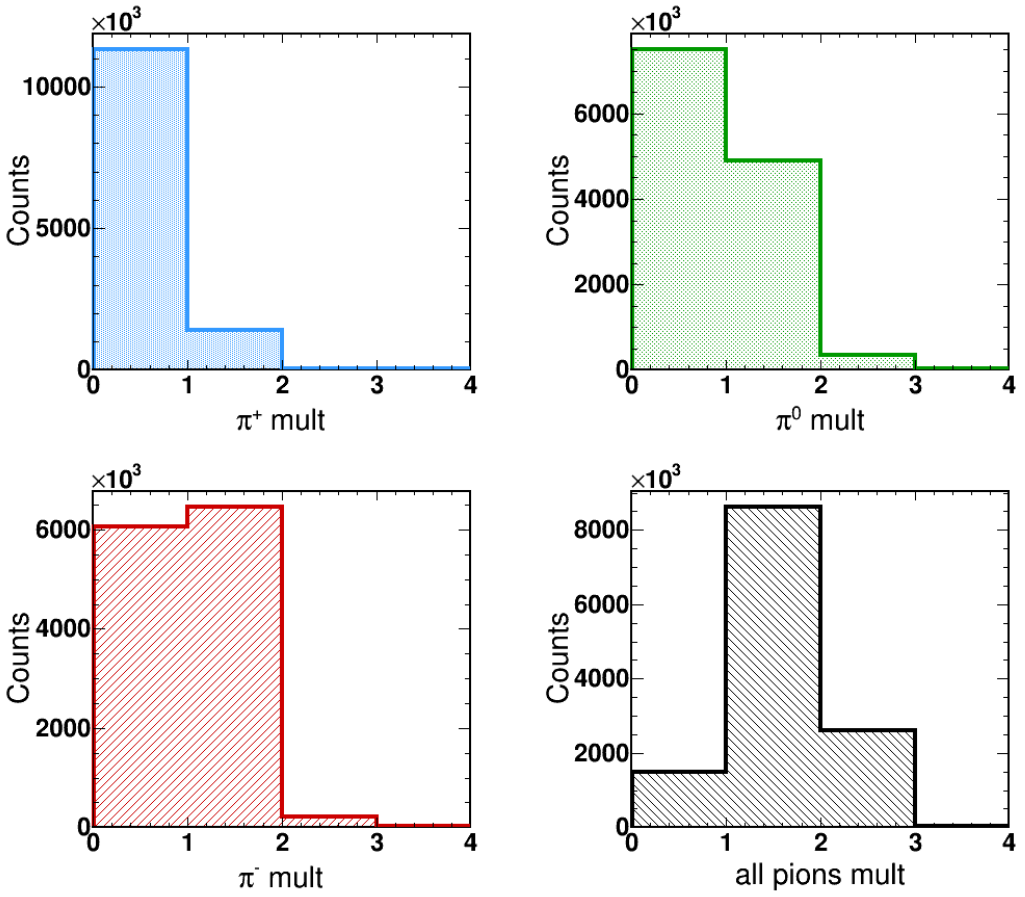

Figure 6.9: Predictions of INCL++ for the $\pi^- + C$ reaction at 0.685 GeV/c. Distribution of the multiplicities of π^+,π^-, $\pi^0$and of all pions.

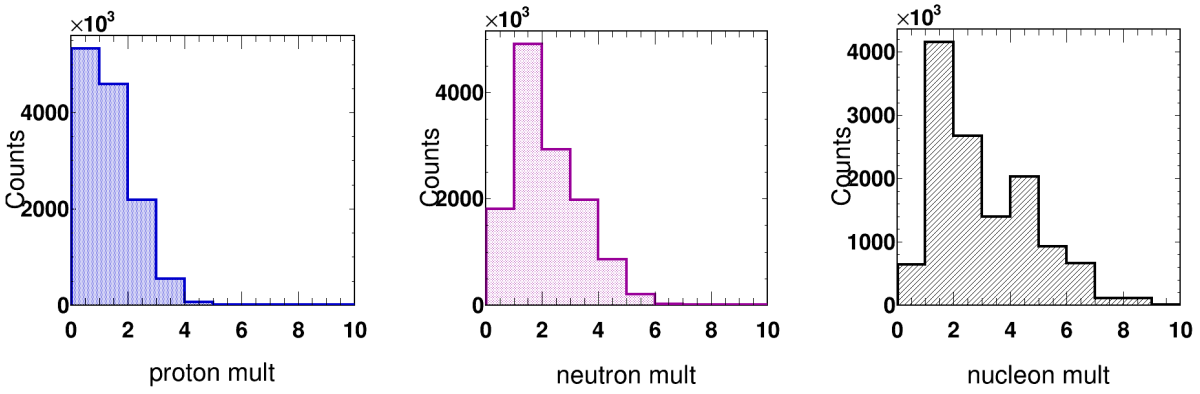

Figure 6.10: Predictions of INCL++ for the $\pi^- + C$ reaction at 0.685 GeV/c. Distribution of the multiplicities of the protons, neutrons and all nucleons.

The multiplicity of nucleons is presented in Fig. 6.10. One can observe that more neutrons are emitted than protons. This can be understood as in the evaporation step, the excited residual nucleus is more likely to emit a proton than a neutron.

In Fig. 6.11 , we present in an overview of the distribution of different exit channels containing a π^-. The categories are labeled by the type of particles requested to be present in the exit channel, but not exclusively, e.g.

π^-p means "at least one proton and one π^-emitted". This shows in more detail than Fig. 6.9 that the exit channels

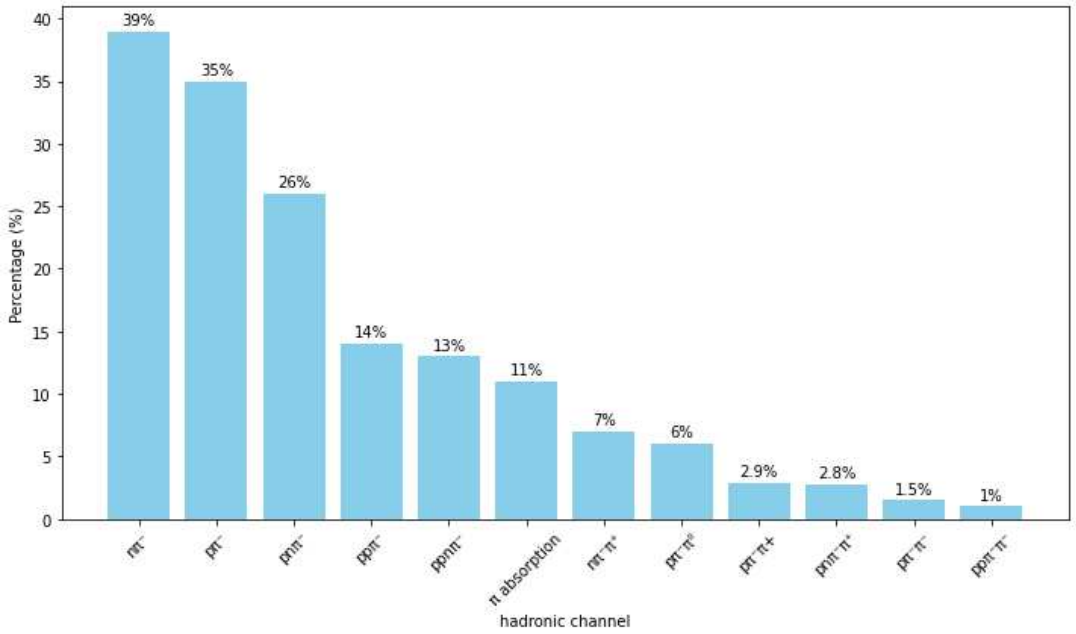

Figure 6.11: Distribution of the different categories of events, as predicted by INCL++ for the $\pi^- + C$ reaction at 0.685 GeV/c. The height of each bin is roughly proportional to the probability of the corresponding category.

with two pions are less probable than those with one pion. In each of the first two categories, the proportion of events with two emitted pions is of the order of 20%. Asking for additional nucleons to be emitted further reduces the occurrence probability, but still, it is clear that for an important fraction of events, more than one nucleon is emitted, due to subsequent elastic collisions and evaporation steps. Most of the categories with two or three charged particles will be studied in more detail in Sec. 6.2, 6.3 and 6.4, but we can already make some remarks. The $p\pi^-\pi^+$ category is an interesting case, as it can not be produced from a single π^-n or π^-p interaction but requires a scattering step (see the list of channels in Table 6.1). Indeed, we have almost the same proportion of p$\pi^-\pi^+$ and pn$\pi^-\pi^+$ events, so, this category consists in fact mostly of events containing a neutron, as a result of two consequent reactions, e.g. π^-p $\rightarrow$ n$\pi^+\pi^-$ followed by np$\rightarrow$np or by a neutron emitted in an evaporation step. It can be surprising at first glance to have a cross section smaller by a factor of 2 for $p\pi^-\pi^-$ events , which can be produced in a single step, but the elementary π^-n $\rightarrow$ p $\pi^-\pi^-$ cross sections is a factor of 3 lower than π^-p $\rightarrow$ n$\pi^+\pi^-$ which makes the first channel more favorable, although it needs at least two collisions. Both categories, $p\pi^-\pi^-$ and p$\pi^-\pi^+$ will be investigated in the following, see Secs. 6.5.4 and 6.4.2. The proportion of events without a pion, accounting for 11.6%, quantifies the role of absorption in the case of elastic processes. In the case of two pion production, one of the two pions might in addition be absorbed. More details about the absorption process will be given in Sec. 6.5.6. In these general considerations based on studies with the INCL++ generator, we disregarded constraints of our measurement, we will now start the comparison of the data to the different models. As explained in chapter 3, we will use raw data measured in the HADES acceptance and simulated events which were propagated

using GEANT simulations (see Sec. 5) and reconstructed using the same analysis chain as real data. Unless explicitly mentioned, the comparison is shown for data and models with their own absolute normalization, see Sec. 3.4 for data and Sec. 5.3 for the simulations. In this way, the yields are given in mb, which should be understood as a cross section integrated over the HADES acceptance. The error bars on the plots include both statistics and point-to-point systematic errors. We will investigate various exit channels, containing at least two or three charged particles.

6.2 $p\pi^-$ channel

We start with the π^-p channel, which, as discussed in Sec.6.1.3 , can give information on the quasi-elastic process π^-p $\rightarrow \pi^-$p. In this case, the kinematics are expected to be close to the free elastic scattering, for which one of the characteristics is the center of mass momentum p_{CM}=0.432 GeV/c.

In Figure 6.12, we show the distributions of the detected pion momentum calculated in the center-of-mass of the initial pion and a nucleon at rest. The momentum distribution shows two distinct contributions, the first one close to the theoretical value of the free elastic process ($\pi^- + p \rightarrow \pi^- + p$) corresponding to the quasi-elastic channel, and the second one at lower momenta, due to inelastic $p\pi^-$ channels such as π^-p $\rightarrow p\pi^-\pi^0$. It can be observed that the models differ significantly in describing the yields in these two regions.

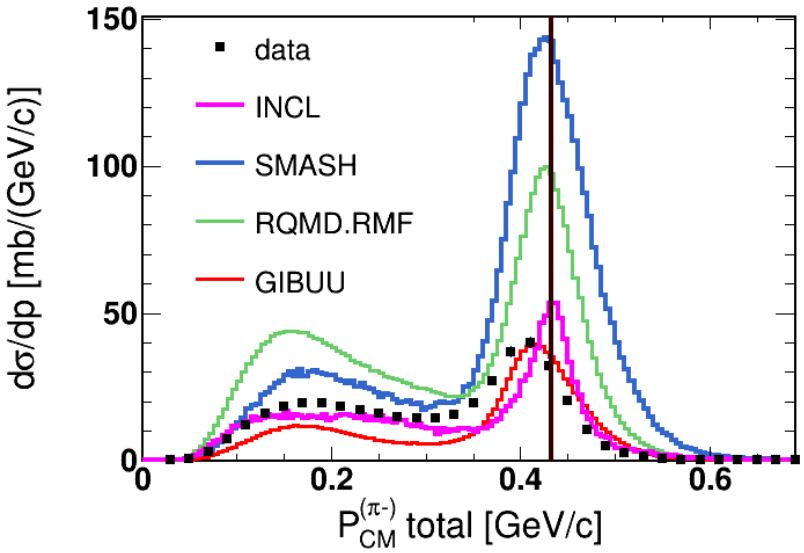

Figure 6.12: Comparison of experimental results and theoretical predictions for the $\pi^- + ^{12}C \rightarrow \pi^- + p + X$ reaction. The black line represents the theoretical center-of-mass momentum of the free elastic $\pi^- + p$ process = 0.432 GeV/c.

RQMD.RMF overestimates the π^-p yields by factors more than two, both in the quasi-elastic and inelastic regions. SMASH predictions also overestimate both regions, but are closer to the data in the inelastic region, and, in the elastic region are even larger than for RQMD.RMF. INCL and GiBUU both underestimate by respectively 12$\%$ and 36 $\%$ the inelastic region. The predictions of both models differ a bit more in the quasi-elastic region. GiBUU

gives the best description of the quasi-elastic peak, while INCL predictions are lower by about 25% and shifted towards high pion momenta.

To investigate more deeply how the models describe the data, a detailed analysis of the exclusive hadronic channels will be provided in the following, beginning with the quasi-elastic channel ($p\pi^-$) (Sec. 6.3), followed by an analysis of various inelastic channels such as $p\pi^-\pi^-$, $p\pi^-\pi^+$, $p\pi^+$, $pp\pi^-$, etc. (Sec. 6.4).

6.3 $p\pi^-$ quasi-elastic

6.3.1 Selection of quasi-elastic channel

To select the quasi-elastic channel (QE), a graphical cut is applied to the momentum correlation between the π^- and proton as shown in Fig.6.13 left. We also investigated the azimuthal angle difference between both particles in order to enhance the selection, see Fig.6.13 right. We add a cut for the coplanarity condition as follows: $150 < \delta\phi < 210°$ to further suppress inelastic contributions which are expected to produce events with large $\delta\phi$ values. One can notice that INCL strongly underestimates the width of the $\delta\phi$ distribution, while the other models better reproduce the data.

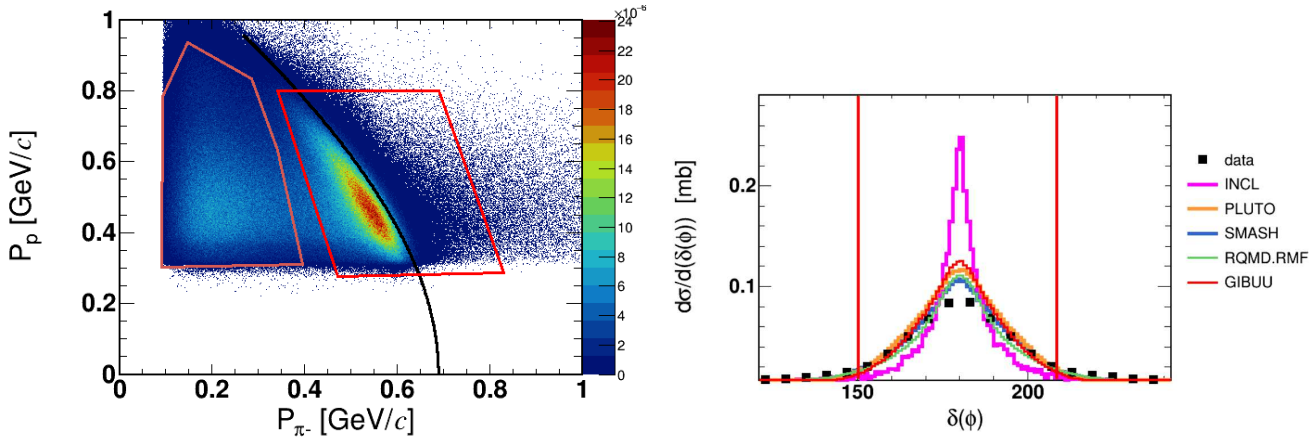

Figure 6.13: Left: Momentum correlation between the detected protons and negative pions showing two well-separated contributions (inelastic on the left and QE on the right). The black line corresponds to the momentum correlation for the free binary reaction $p + \pi^- \rightarrow p + \pi^-$. The red line shows the selections used for quasi-elastic and inelastic $p\pi^-$ events. Right: azimuthal angle difference between the detected proton and π^-, after applying the graphical cut shown on the left.

6.3.2 Comparison with models

As noted above, there is a considerable variation in yields across the different models which makes it challenging to compare the normalized spectra and draw meaningful conclusions about the differences in physics between the models and the experimental data. Therefore, to simplify the comparison process, all spectra are normalized to the area. Moreover, to achieve a more accurate and realistic comparison, the same ”QE” cuts, which consist of a

combination of the momentum correlation and the coplanarity condition, are also applied to the simulations as the experimental data.

Fig.6.14 shows the angle distribution of detected pions in the center of mass frame of the $\pi^- + p \rightarrow \pi^- + p$ reaction after applying "QE" cuts. The comparison of data obtained from the "QE" process on a carbon target ($\pi^- + ^{12}C$) represented by black dots and the data from the elastic process on a free proton target ($\pi^- + p$) represented by cyan triangles, reveals a shifted distribution in the former compared to the latter. This effect could be due to the Fermi motion of the proton which can alter the momentum transfer, eventually leading to a modified angular distribution of the emitted pion. This concurs with the approach employed in the PLUTO simulation file where a weight is applied for the quasi-free reaction based on the well-known $\pi^- + p$ angular distribution. However, it can be observed that the broadening of the angular distribution caused by the Fermi motion is not able to describe the measured angular distribution. Indeed, the other calculations, which include rescatterings predict an angular distribution shifted to

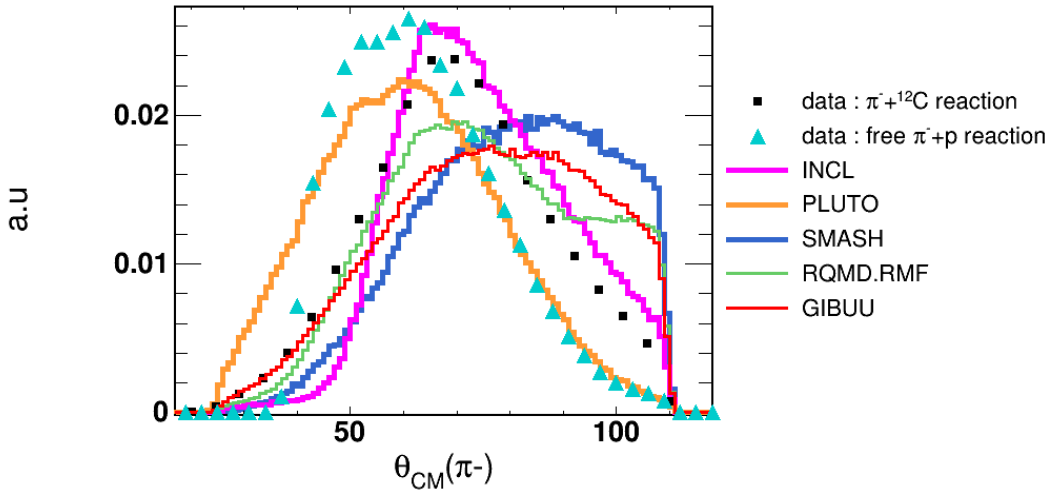

Figure 6.14: Angular distribution of the π^- for the quasi-elastic events. The distribution is shown in the center-of-mass frame of a $\pi^- + p$ reaction with a proton at rest.

larger polar angles. However, only INCL++ gives a reasonable description of the data, the other models predict a too broad angular distribution. Obviously, this distribution is sensitive to both nucleon momentum distributions and rescattering effects. Then, we investigate the missing mass variable, M^2_{miss}, calculated for a π^-p $\rightarrow \pi^-$p +X reaction with a nucleon at rest

$$M^2_{\text{miss}} = (E_{p1} + E_\pi - E_{\text{beam}} - m_p)^2 - (\vec{p}_{p1} + \vec{p}_\pi - \vec{p}_{\text{beam}})^2, \tag{6.15}$$

where E_{beam} and $\vec{p}_{\text{beam}}$ are respectively the energy and the momentum of the incident pion, m_p is the mass of the proton, E_{p1} and E_π are the energies of the detected proton and pion, respectively, and $\vec{p}_{p1}$ and $\vec{p}_\pi$ are their respective momenta. The distribution is shown in Fig.6.15.

In a free process where a pion interacts with a free proton, the missing mass is expected to be close to zero.

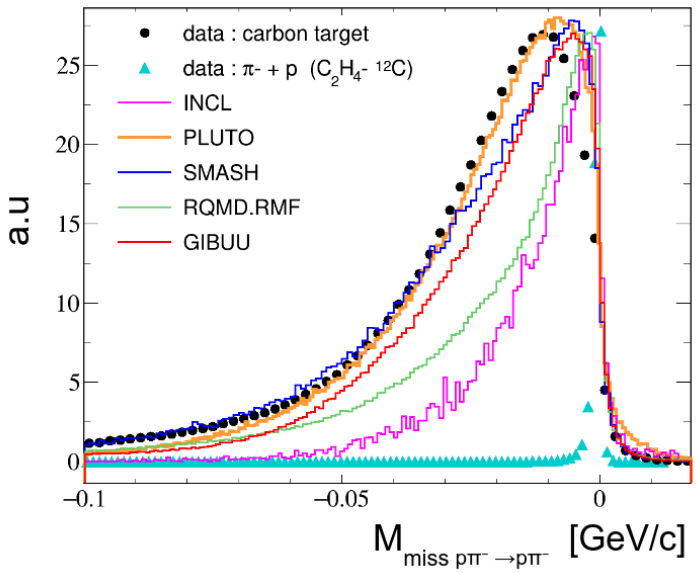

Figure 6.15: Distribution of the missing mass M_{miss} for π^-+p events measured in the free π^-p reaction (cyan triangles), for selected quasi-elastic events measured on the carbon target (black dots) and for model calculations of the $\pi^- + C$ reaction using the same selection as data (colored curves).

This is indeed the case for the data obtained on the free proton target (cyan triangles in Fig.6.15). In this case, the width of the distribution is only due to the resolution of our measurement and to the beam momentum dispersion. However, when a bound proton is involved, as in the case of a carbon target, the variable is found to be distributed towards negative values, as seen in the black dots in the same figure. For a pure quasi-elastic process, where no further rescatterings occur, the effect is due only to the proton momentum distribution and its binding energy in the carbon nucleus. In addition, the distribution is expected to be modified by rescatterings. INCL and RQMD.RMF models tend to have narrower distributions that are closer to the free proton hypothesis than the bound proton scenario, while the GIBUU model tends to have a broader distribution. On the other hand, the SMASH and PLUTO models are closer to the experimental data.

We can also investigate the total missing mass, as defined in Eq. 6.15 and shown in Fig. 6.16. The distribution is peaked close to the ^{11}B mass ($M_{^{11}B} = 10.25$ GeV/c^2). We can observe that all models describe this distribution satisfactorily, except INCL++, which predicts a distribution shifted by about 20 MeV towards higher values. Following Eq.(6.9), the missing momentum variable, denoted as $\vec{P}_{\text{miss}}$, is defined for the pπ^- case as :

$$\vec{P}_{\text{miss}} = \vec{p}_p + \vec{p}_\pi - \vec{p}_{\text{beam}}. \tag{6.16}$$

and in a pure quasi-elastic process,

$$\vec{P}_{\text{miss}} = \vec{P}_N, \tag{6.17}$$

where $\vec{P}_N$ is the momentum of the proton in the nucleus. The missing momentum distribution in Fig. 6.17 is found

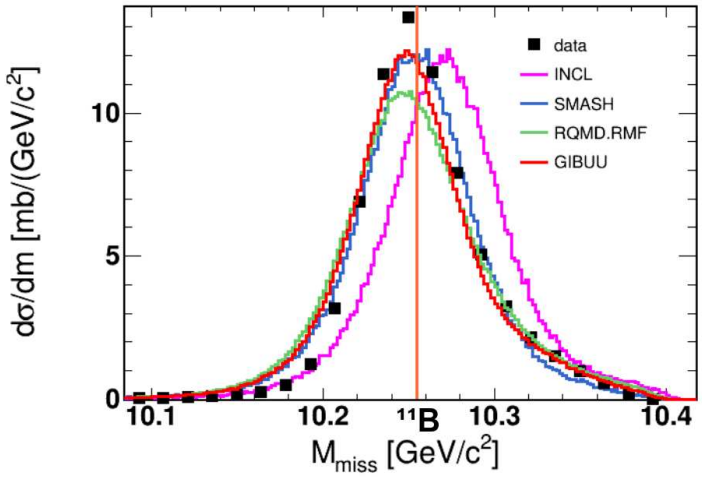

Figure 6.16: Missing mass for the quasi-elastic process, calculated on the carbon target: $\pi^- + ^{12}C \rightarrow \pi^- + p + X$.

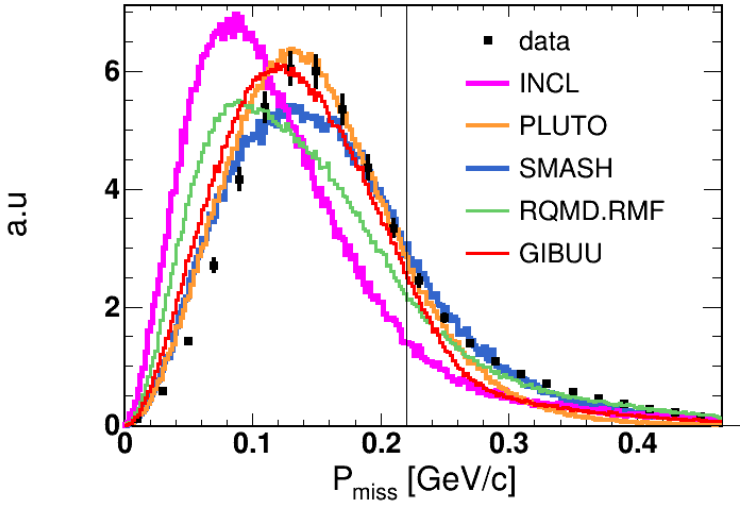

Figure 6.17: Distribution of the missing momentum $\vec{P}$miss. The Black line represents the Fermi momentum (0.21 GeV/c) taken from [23].

to vary across the simulations. In particular, RQMD.RMF displays a broader and lower-shifted missing momentum distribution, while SMASH shows a broader distribution. PLUTO reproduces the missing momentum distribution well, whereas GIBUU displays a slight shift towards lower values, and INCL is narrower and shifted towards lower values. These differences can be partly explained by the different inputs of the models: INCL uses a global Fermi momentum distribution (Sec. 4.1.2), while GiBUU, SMASH and RQMD.RMF use a local Thomas-Fermi assumption, where the Fermi momentum depends on the density. The p_{miss} distributions in GiBUU and SMASH are indeed peaked at similar values. RQMD.RMF uses different density profiles (Sec. 4.1.2), which could explain why the distribution peaks at a lower value.

The missing momentum distribution in the observed data and in the model predictions is found to extend significantly further than the expected Fermi momentum value in the nucleus, represented by the black line. Here the experimental value p_F= 221 MeV/c from [23]. This is not anticipated in a pure quasi-elastic process, and is a hint

that the measured events are affected by the effect of potential or rescatterings. The high P_{miss} tail in the experimental distribution might also be partially due to SRC effects. However, to pin down such effects, the rescatterings need to be suppressed. This aspect will be discussed in detail in Chapter 7.

6.3.3 Tests of INCL parameters

To investigate the influence of some parameters on the kinematics and physical variables such as the missing mass and momentum, we conducted tests using INCL, such tests could be useful to improve the model. Some interesting options with INCL :

1. Considering only the emission of 1 pion, removing the emission of multipions.
2. Possibility to remove the local energy (a process used to correct the nucleon energy to get the right cross section) or to reduce its value.
3. Changing the value of the Fermi momentum (for light nucleus the default option in INCL is maybe not the best one).
4. The de-excitation phase (by default, INCL uses Fermi Breakup for mass below 16).

Remove multipions

Removing the multipion production in INCL++ will in practice suppress all the inelastic steps in the collision. In our experimental approach, we are selecting events with the characteristics of the quasi-elastic process. However, it is interesting to investigate if there is still an influence from inelastic channels. The resulting angular distributions of both the pion and proton in the incident π^-p center-of-mass become distorted and broadened. However, the shapes of the missing mass and missing momentum are less sensitive (lower row in Fig. 6.18). Moreover, the cross section of the channel experiences an increase, which means that we often have an inelastic step following the QE step. This second step changes the kinematics and a big fraction of these cases are not selected due to our graphical cut. When this step is suppressed, these events keep the QE kinematics and are then selected. In summary, the yield and kinematics of the detected pion and protons are quite sensitive to this multipion production and its implementation in INCL++ is crucial for a good description of our data.

Fermi momentum

The Fermi momentum value in the nucleus was changed to 210.632 MeV/c which is the Fermi momentum for the carbon target in INCL++ (in the default simulations it is 270 MeV/c), resulting in potential modifications to the interaction cross section due to changes in the proton's momentum, thus in the center-of-mass energy of the reaction.

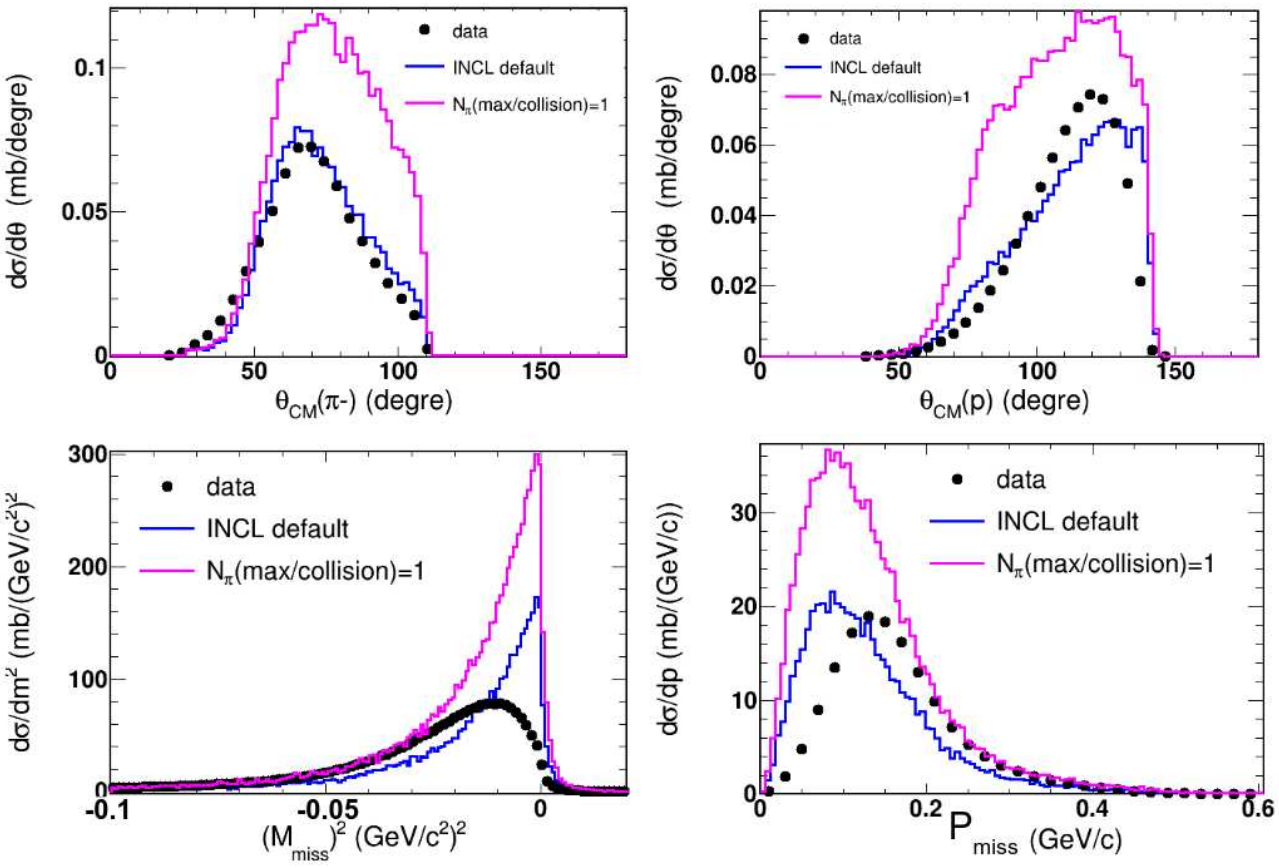

Figure 6.18: Impact of suppressing the multipion production in one step in INCL++ on the quasi-elastic observables.

The results presented in Fig.6.19 indicate a slight increase in the cross section for the quasi-elastic channel, accompanied by moderate changes in all distributions. Specifically, when the Fermi momentum is smaller, the missing mass distribution gets narrower and shifted toward the data. The missing momentum is shifted to lower values, which is expected because the reaction gets then a bit closer to the free kinematics. However, this trend increases the difference w.r.t. the data. These findings imply that the standard value in INCL may be more appropriate.

Local energy correction

Nucleons inside the nucleus are submitted to constant square-well potentials and are, therefore, moving along straight lines with constant momentum between two collisions. However, taking into account a smoothly varying potential, the nucleons' momenta should decrease close to the surface. The constant momentum approximation has an impact on processes with cross sections varying fast with momentum. In particular, it was found to underestimate the cross sections for proton-nucleus reactions below 200 MeV [97]. The 'local E' procedure, was introduced to correct for this effect, first for proton-nuclei reaction in INCL 4.6 and then for pion-nucleus reactions in INCL++ [98]. To calculate the cross section of the first collision, the local energy is removed from the nucleon energy. In this way, the cross section is calculated at a smaller center-of-mass energy. The kinematics of the reactions is unchanged.

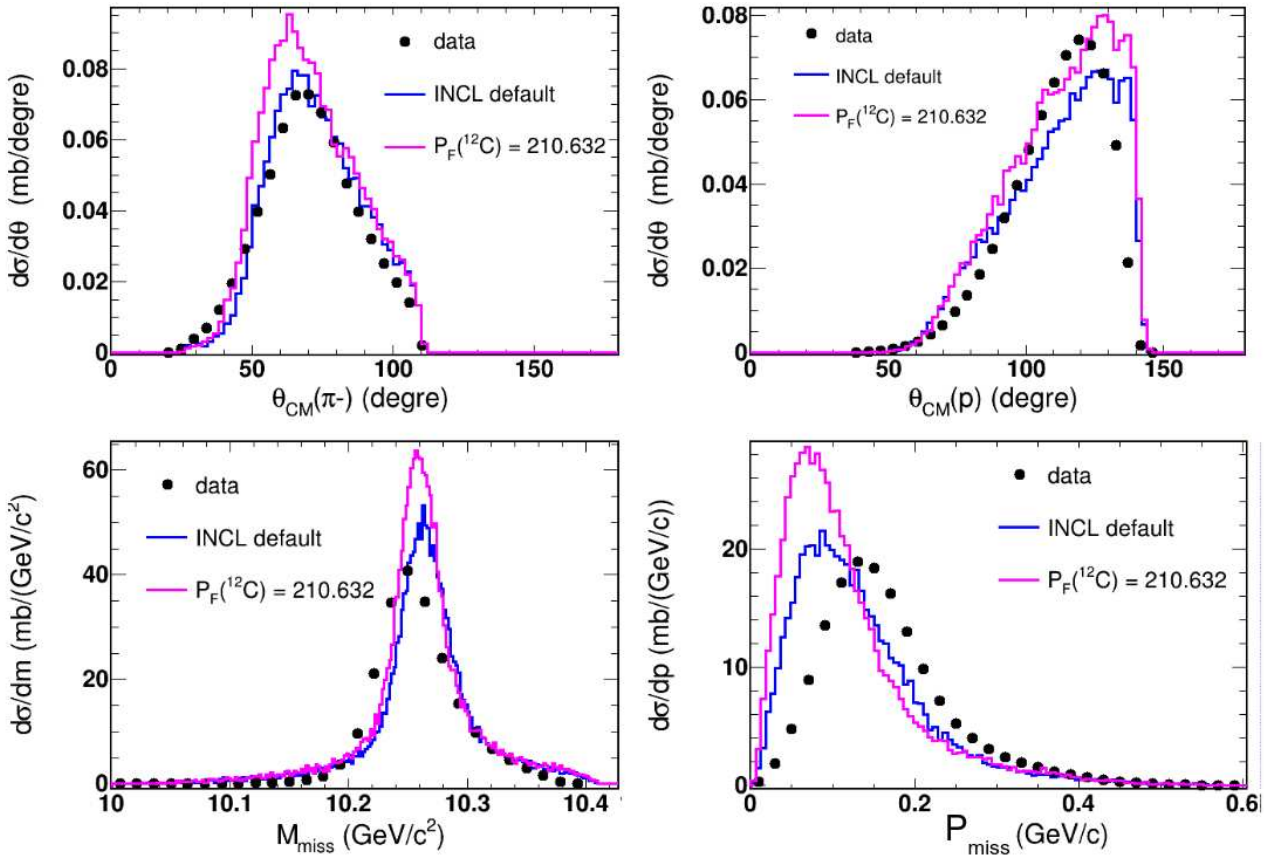

Figure 6.19: Impact of using a mass-dependent Fermi momentum in INCL++ on the quasi-elastic observables. The default value in INCL++ for all nuclei is 270 MeV/c (blue). The mass-dependent value for Carbon is 210.632 MeV/c (magenta).

However, the weights of the collisions occurring at different π N center-of-mass energies are changed when applying the local energy correction, resulting in different kinematical distributions.

To estimate the local energy value in the interaction of the incident pion with a target nucleon with a momentum *p* at a position *r*, one considers the correlation between the momentum and position distributions (see Fig. 4.6) . This allows to define the minimum momentum p_{min} to reach the distance r from the center. In the center of the nucleus, nucleons are distributed in the full range of momenta, between 0 and p_F, but at the surface, p_{min} differs from 0. The corresponding kinetic energy E_{min} is taken as local energy to be subtracted from the nucleon energy. The idea behind this procedure is that, at the distance r from the center, a particle with kinetic energy E_{min} should have no more kinetic energy but just potential energy.

The impact of eliminating the local E parameter, applied for the initial pion-nucleon collision in INCL, is illustrated in Fig. 6.20. The analysis reveals a significant impact on the missing mass and missing momentum variables. Although the missing momentum and missing mass distributions are shifted in the right direction, the amplitude of the shift is too large. Moreover, the cross section decreases by a factor of approximately 2 w.r.t to the standard INCL simulation and also w.r.t data, which confirms that the local E parameter in INCL plays an important role

in correcting the cross section. The pion angular distribution is displaced towards larger angles, while the proton one gets broader towards smaller angles. Such large effects are a bit surprising as the πN cross sections are not changing so much in the range of $\sqrt{s_{\pi N}}$ probed by the quasi-free reaction at 0.685 GeV/c.

As the local energy procedure affects mostly nucleons at the nuclear surface, the large impact of removing this correction indicates that most of the pπ^-events in our selection are produced in a first collision occurring at the surface. Indeed, when the quasi-elastic reaction occurs in the center of the nucleus, the emitted pion might be absorbed, or either the pion or proton can have further collisions, preventing them, from either to exit the nucleus or appearing in the QE correlation. The probability of detecting a proton and a pion within the QE selection is therefore higher when the reaction occurs at the surface.

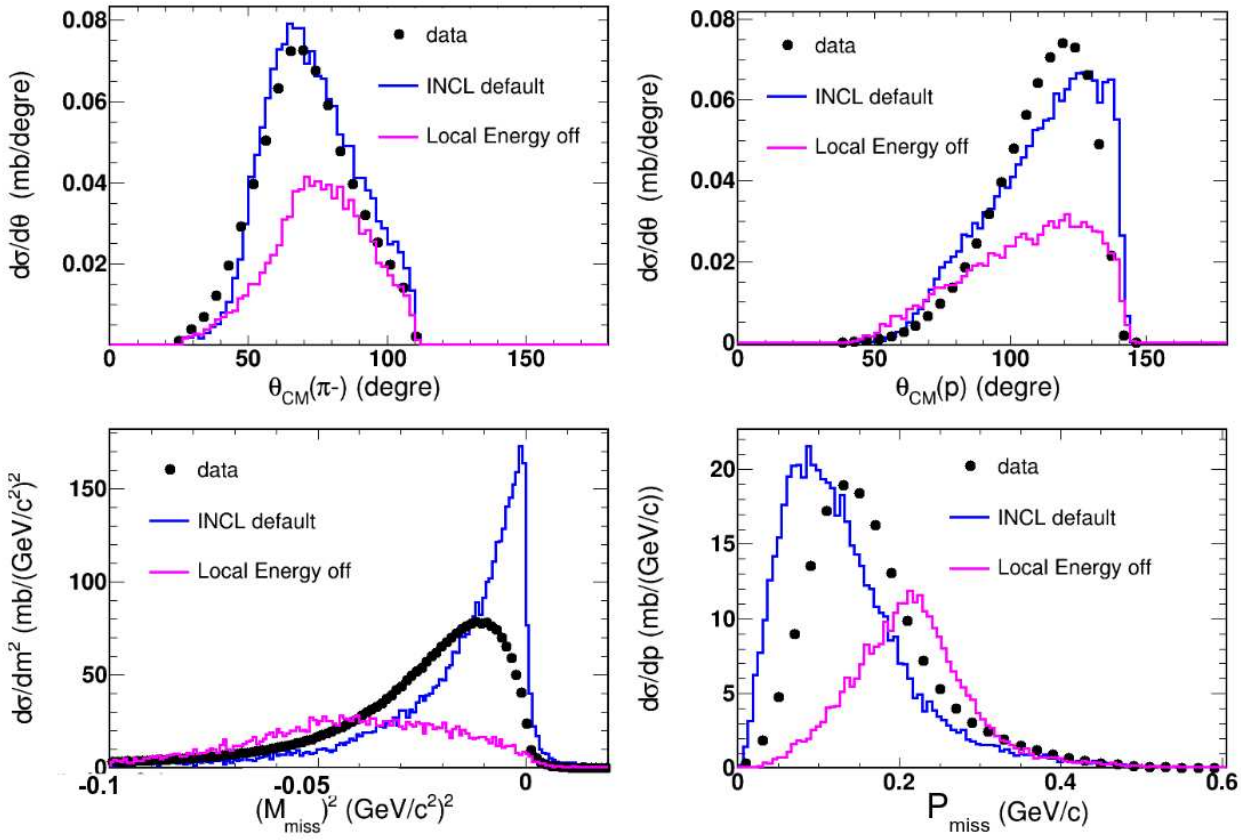

Figure 6.20: Impact of removing the local energy procedure in INCL++ on the quasi-elastic observables.

Fermi Breakup

The ”Fermi Breakup” option consists in using the ABLA07 de-excitation model for the evaporation phase instead of the usual Fermi Breakup process which is the standard option for masses below 16 as in our case. However, we checked that this alternative model has no discernible effect on the distributions. This is due to the fact that the protons emitted during the evaporation process have low energies (low momenta), which are below the HADES

detection threshold. This is shown in Fig.6.21, which presents the momentum distributions for the proton in 4π (left) and in acceptance (right) for all pπ^-events (black curve) in 4π and for pπ^-events (red colored area) corresponding to protons emitted during the cascade phase. The difference between the two distributions represents the protons emitted during the evaporation phase. In acceptance, there is no difference between both plots, thus we detect only cascade particles, see the bottom right plot, which means that we are not sensitive to the evaporation process. This statement holds significance in our study of short-range correlations (SRCs) in chapter 7 as it ensures preventing the inclusion of nucleons from the evaporation phase.

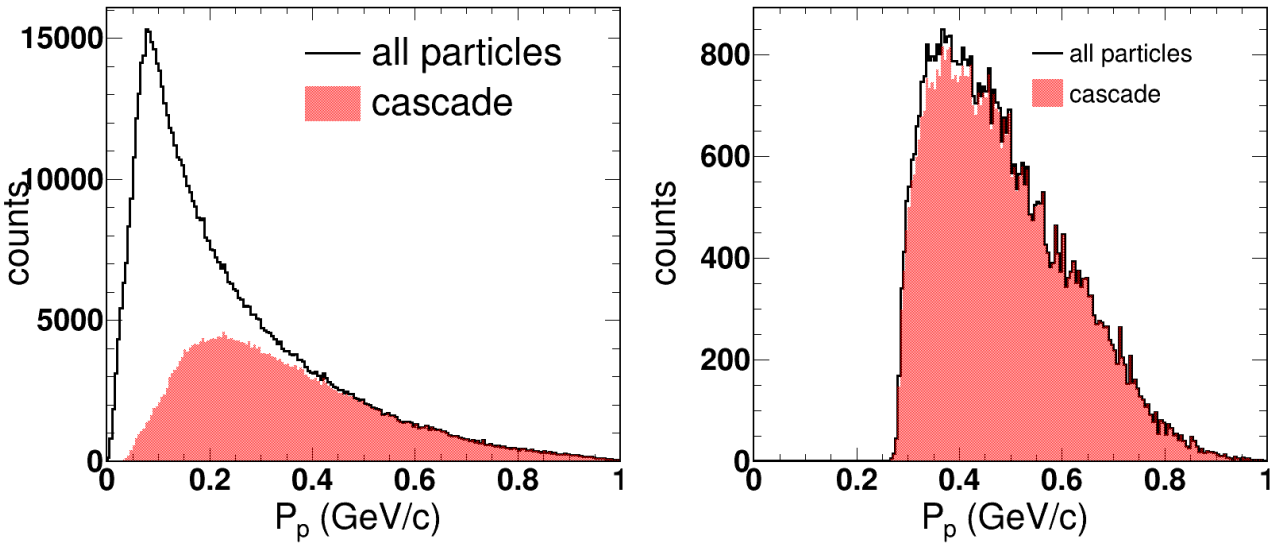

Figure 6.21: Comparison using INCL++, of protons momenta in the $p\pi^-$ channel, distinguishing between events where all protons are included (black curve) and events with only cascade protons (red colored area). Left: full solid angle (4π). Right: HADES acceptance.

6.4 Discussion of experimental distributions of inelastic channels

The analysis of π^-p events corresponding to the quasi-elastic process shows a large dispersion of model predictions. We will now investigate other channels to bring more constraints on these models. Inelastic channels correspond to the presence of at least two pions in the final state. They can be studied, rather directly, by analyzing exit channels with at least two detected pions (e.g. $\pi^+\pi^-$, $\pi^-\pi^-$, $\pi^+\pi^+$, p$\pi^+\pi^-$,...) . In addition, valuable information can also be obtained from events with one charged pion and at least one proton (e.g. π^-p, π^+p, π^-pp,...) or two protons (e.g. pp, ppπ^-,..) as one or two pions might have been missed, either in the case of π^0, or because of the HADES acceptance. However, if the two pions are not present in the final state, most of the yields will probably be due to sequential elastic collisions. We first discuss some experimental distributions, before showing the comparison with model predictions. The first part pertains to two distinct inelastic channels that require the presence of one pion and a proton, namely $p\pi^-$ and $p\pi^+$.

6.4.1 $p\pi^-$ and $p\pi^+$ channels

The emission of a proton and a π^- in an inelastic reaction can occur as a single-step process in the interaction of a pion with either a proton or a neutron, as :

1. $\pi^- + \mathrm{p} \rightarrow \boldsymbol{\pi^-} + \pi^0 + \mathbf{p}$, ($\sigma$=3.8 mb)
2. $\pi^- + \mathrm{n} \rightarrow \pi^- + \boldsymbol{\pi^-} + \mathbf{p}$, ($\sigma$=2.1 mb) [1]

For the p π^+channel, at least two steps are needed :

3. $\pi^- + \mathrm{p} \rightarrow \pi^- + \mathbf{p}$, ($\sigma$=17.8 mb) ; $\pi^- + \mathrm{p} \rightarrow \boldsymbol{\pi^+} + \pi^- + \mathrm{n}$
4. $\pi^- + \mathrm{p} \rightarrow \pi^0 + \mathrm{n}$, ($\sigma$=10 mb) ; $\pi^0 + \mathrm{p} \rightarrow \boldsymbol{\pi^+} + \pi^- + \mathbf{p}$
5. $\pi^- + \mathrm{p} \rightarrow \pi^- + \pi^0 + \mathbf{p}$, ($\sigma$=3.8 mb) ; $\pi^0 + \mathrm{p} \rightarrow \boldsymbol{\pi^+} + \mathrm{n}$

As mentioned in Sec. 6.1.4, the reactions of the type

6. $\pi^- + \mathrm{N} \rightarrow \pi + \mathrm{N}$; $\mathrm{N} + \mathrm{N} \rightarrow \pi + \mathrm{N} + \mathrm{N}$

are expected to be kinematically suppressed. This was checked using INCL++ simulations in 4π where the multipion production in one step was suppressed. In this case, the remaining fraction of events with two emitted pions is 4.7% for $\pi^-\pi^-$ and 1.1% for $\pi^-\pi^+$. This confirms that when two pions are emitted, they originate most of the time from the same step.

Among all these reactions which allow for the production of a proton and a π^+, reaction (3) is expected to be the most probable due to the larger cross sections of both steps. One can also already notice that the sequence of reactions producing a π^+ and a proton, also produce a π^-, so the study of the p$\pi^-\pi^+$ events (Sec. 6.4.2) will give further information on these processes.

To isolate pπ^- events from inelastic reactions, the contribution from the quasi-elastic process needs to be suppressed. As mentioned in Sec. 6.3, the correlation between the π^- and proton momenta, shown in Fig. 6.13, presents, in addition to the region corresponding to the quasi-elastic process, a second region which has characteristics similar to the π N $\rightarrow \pi\pi$ N process (see Sec. 6.4.2). To isolate those events, a graphical cut is applied, represented by the left red line in Fig.6.13.

As expected, in the case of the pπ^+ events, only the contribution from inelastic events is present (Fig. 6.22). The difference between the pπ^- (inelastic) and pπ^+ channels is first clearly demonstrated by the experimental yields which are about a factor 11 lower for the pπ^+ case than for the pπ^- case. This is qualitatively expected since, as discussed above, the emission of a π^+ is always simultaneous to the emission of a π^-. A further illustration can be obtained by comparing the missing mass (MM) in the $\pi^- + C \rightarrow \pi + p + X$ reaction and the invariant mass spectra

[1] Throughout the document, the detected particles will be indicated with a bold font.

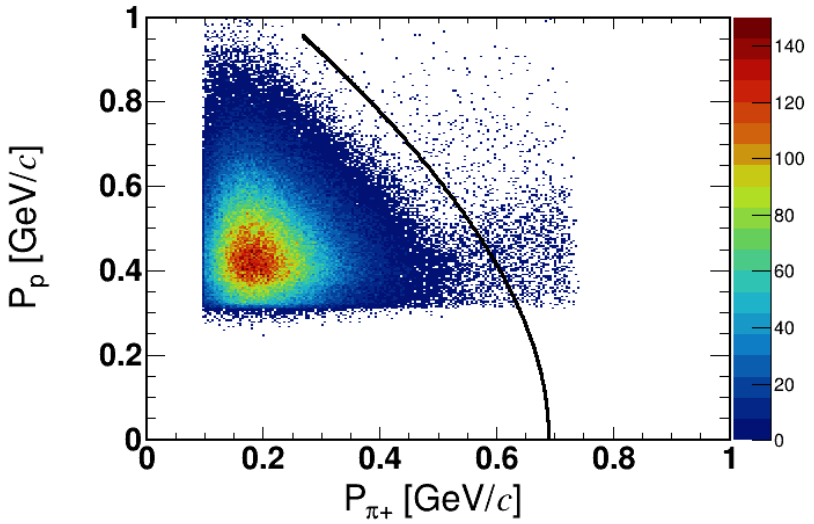

Figure 6.22: p and π^+momentum correlation, for the pπ^+channel. The black line represents the elastic scattering p+π kinematics.

of detected particles, as shown in Figs. 6.23 and 6.24. For observables definitions, please refer to Sec.6.1.5. The MM mass for the pπ^- channel starts at values close to the threshold given by the sum of the masses of the pion and the ^{11}B nucleus. This is expected, as in the single step reactions (1) and (2) only one pion is emitted in addition to pπ^-pair. On the contrary, in the pπ^+ case, at least one nucleon and a pion are emitted, with some relative energy, which implies a larger missing mass. This effect also explains why the invariant masses are larger in the case of the pπ^-pair, as less energy is dissipated among other particles than for the pπ^+ case.

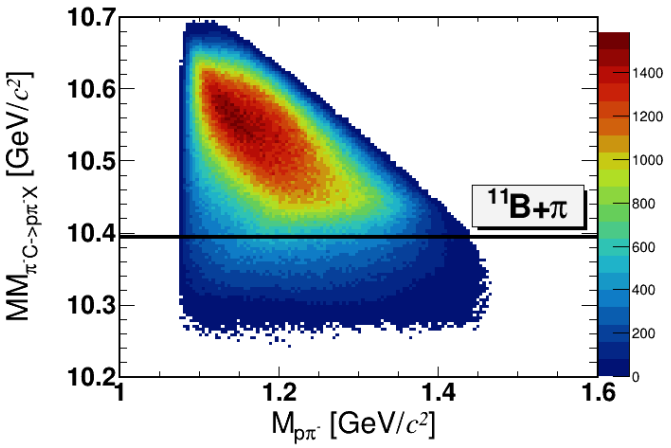

Figure 6.23: Analysis of the $\pi^- + C \rightarrow \pi^- + p + X$ reaction after selection of inelastic events: missing mass as a function of invariant mass.

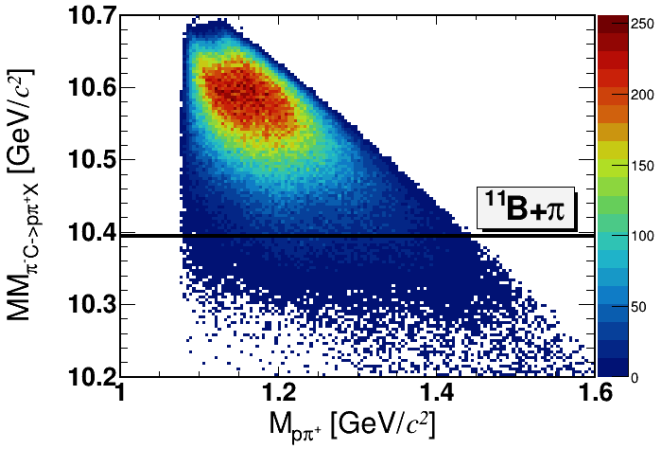

Figure 6.24: Analysis of the pπ^+ channel in the π^- + C $\rightarrow$ π^+ + p + X reaction: missing mass as a function of invariant mass.

6.4.2 $p\pi^-\pi^+$ and $p\pi^-\pi^-$ channels

To provide a more comprehensive study of the two-pion production channels, we investigate the $p\pi^-\pi^+$ and $p\pi^-\pi^-$ channels. The first channel, $p\pi^-\pi^+$, as mentioned above, is produced through the same multi-step processes as the $p\pi^+$ channel. The second channel, which involves the emission of a proton and two negative pions ($p\pi^-\pi^-$), can be produced in a single step, i.e., reaction (2), or multi-step processes (7-10), see Sec.6.5.4.

Again, the correlation between missing mass and invariant masses for both event categories (as shown in the top rows of Fig. 6.25 and Fig. 6.26) is very striking and the observed difference can be explained in a similar way as for the pπ^- and pπ^+ case. In the case of p$\pi^-\pi^-$, the missing mass distribution starts close to the ^{11}B mass and the invariant mass is peaked at large values, close to the kinematical limit, which is consistent with the dominance of reaction (2), where the three particles carry most of the available energy in the collision. For the p$\pi^-\pi^+$channel, the lower invariant mass and larger missing mass are due to the emission of at least one nucleon in addition to the three detected particles. To investigate the presence of π^-+p elastic scattering steps in both cases, one can study the correlation between the proton momentum and angle, as shown in the bottom rows of Figs. 6.25 and 6.26. It can be observed that a correlation similar, albeit shifted, w.r.t the free kinematics curve is present in both cases, which signals the presence of reaction (3), with a πN elastic step, but it is much more significant for the $p\pi^+\pi^-$ than for the $p\pi^-\pi^-$ events, as expected due to the dominance of reaction (2) in the $p\pi^-\pi^-$ case. We can notice that the energy of these protons is smaller than in the simulations of the πN $\rightarrow \pi\pi$ N reaction (see Fig. 6.4). This is expected as this reaction occurs at a different energy due to the first πN elastic step. As a consequence, a big fraction of these events is cut by the acceptance cuts. On the other hand, events corresponding to reaction (3) are more likely to be detected.

In conclusion, the distributions are qualitatively consistent with a dominance of reaction (2) in the data for the $p\pi^-\pi^-$ channel. Additionally, they indicate a significant π^-p elastic collision step for the p$\pi^+\pi^-$channel in the data.

6.5 Comparison of inelastic channels with simulations

6.5.1 channels: $p\pi^-$ & $p\pi^+$

To determine if the dominance of single-step processes in the $p\pi^-$ channel is predicted by the models, we compare the missing mass and invariant mass distributions, as presented in Fig.6.27. As already discussed in Sec. 6.3, there is a large scatter in the predictions of yields. Except for GiBUU, all model predictions extend to too large masses. It can also be observed that some yield is present below the pion emission threshold, which means that our selection, based on the correlation between proton and pion momenta (see Fig. 6.13) does not fully suppress the quasi-elastic pπ^-events, where no pion is emitted. This contribution is probably highly sensitive to the rescattering steps. Such

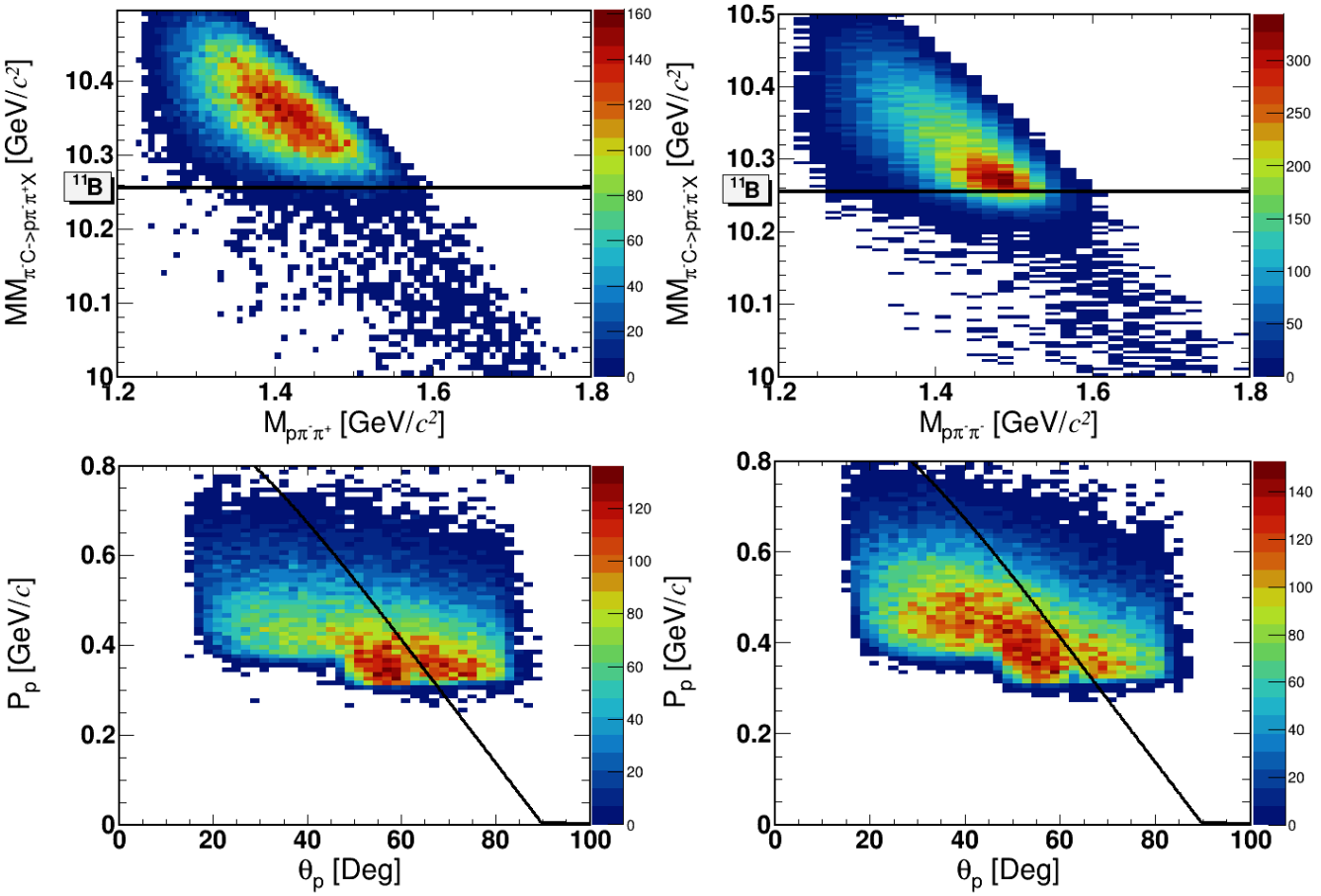

Figure 6.25: Analysis of the $\pi^- + C \rightarrow \pi^- + \pi^+ + p + X$ reaction. Top: missing mass as a function of invariant mass. Bottom: momentum as a function of the angle of the proton.

Figure 6.26: Analysis of the $\pi^- + C \rightarrow \pi^- + \pi^- + p + X$ reaction. Top: missing mass as a function of invariant mass. Bottom: momentum as a function of the angle of the proton.

a contribution represents in the different models a variable fraction of the events. The invariant mass distribution presents a weak but visible broad structure a bit below the $\Delta(1232)$ mass. The analysis of $\pi^- p$ reactions has indeed shown that the process π N $\rightarrow \pi\pi$ N has a strong contribution from a $\Delta\pi$ intermediate step Fig.1.24. The $\Delta^0(1232)$ might also be excited in π^-p rescattering steps. In any case, the structure is expected to be smeared due to potential and rescattering effects.

The corresponding distributions are shown for the pπ^+ events in Fig. 6.28. RQMD.RMF and SMASH overestimate the pπ^+yields by a larger factor than for pπ^-. GIBUU model has similar predictions for pπ^-, which is, same as INCL++, too low by about a factor of two w.r.t. data. But, INCL++ satisfactorily describes the pπ^+ channel. These differences between the two channels indicate a different probability of sequential collisions in the various models. However, there are also common features: the theoretical missing mass distributions, except for GiBUU, indeed extend to too large values and the invariant masses display in the case of GiBUU and SMASH a weak structure below the $\Delta^0(1232)$ mass.

Additionally, the momentum of the detected proton in the π^-+p center of mass for pπ^+events is presented in

Fig. 6.29. A clear structure is present below 0.4 GeV/c in the proton p_{cm} distribution in the data and in all models, which is clearly due to protons from an initial π^-p quasi-elastic step, following reaction (3). INCL reproduces very well the kinematics of the proton.

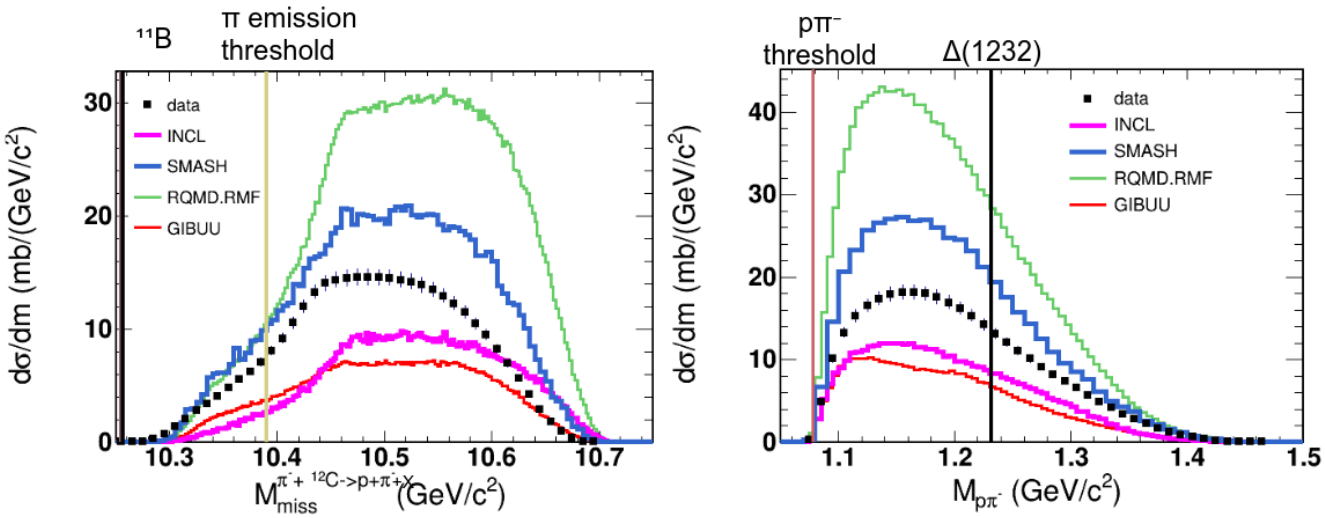

Figure 6.27: Invariant mass (right) and missing mass distributions (left) for pπ^- events with the inelastic selection.

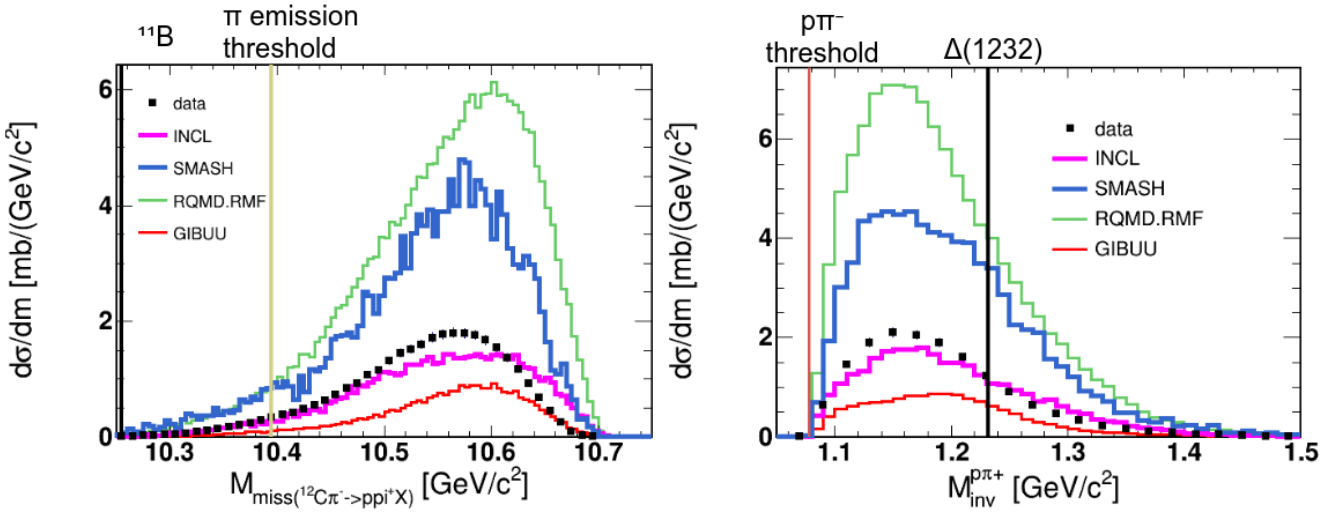

Figure 6.28: Same Fig. 6.27 for the pπ^+ channel.

6.5.2 channel: $p\pi^-\pi^+$

As mentioned above, as reactions (3), (4), and (5), which were identified as the main processes to produce pπ^+ events imply the emission of a π^-, the study of p$\pi^+\pi^-$events will allow to study the same processes but with more detailed observables. Figure 6.30 shows the momentum of the detected pions in the π^-+p center of mass. The description of the yields by the different models is similar to the pπ^+ channel and seems not to be affected by

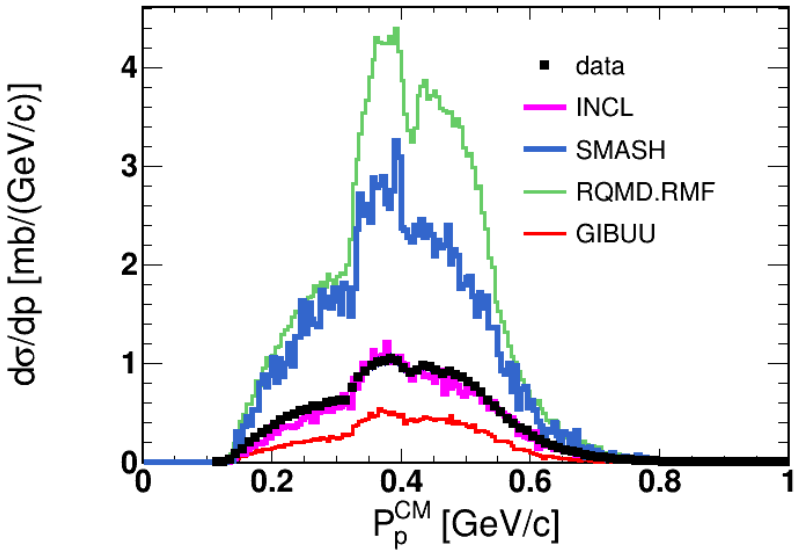

Figure 6.29: Proton momentum in the CM for pπ^+events.

acceptance effects due to the detection of the π^-. It has to be noted that INCL provides a very accurate description of this distribution. The experimental distributions of center-of-mass momentum are peaked at slightly smaller values for π^+ than for π^-. The two charged pions play symmetrical roles in processes (3) and (4), except if the $\Delta(1232)$ resonance is excited in a process πN$\rightarrow \Delta\pi$, with subsequent decay of the Δ into πN. In this case, the kinematics might indeed be different for the pion emitted from the Δ and the other pion. Differences between π^+ and π^- momentum distributions are also expected from reaction (5), as the pions from an inelastic step and the π^- from a rescattering step have different kinematics. The shape of these distributions for both π^+ and π^- is very well captured by INCL++ while the predictions for the other models are generally shifted to too large values.

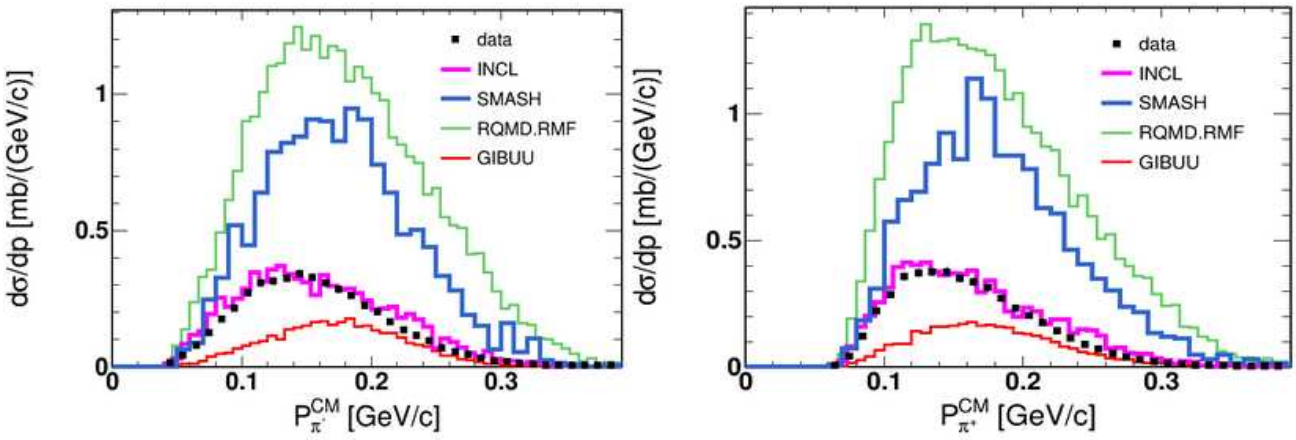

Figure 6.30: Center-of-mass momenta of the π^-(left plot) and π^+(right plot) in the p$\pi^-\pi^+$channel.

We also show invariant and missing mass distributions of the p$\pi^-\pi^+$in Fig.6.31.

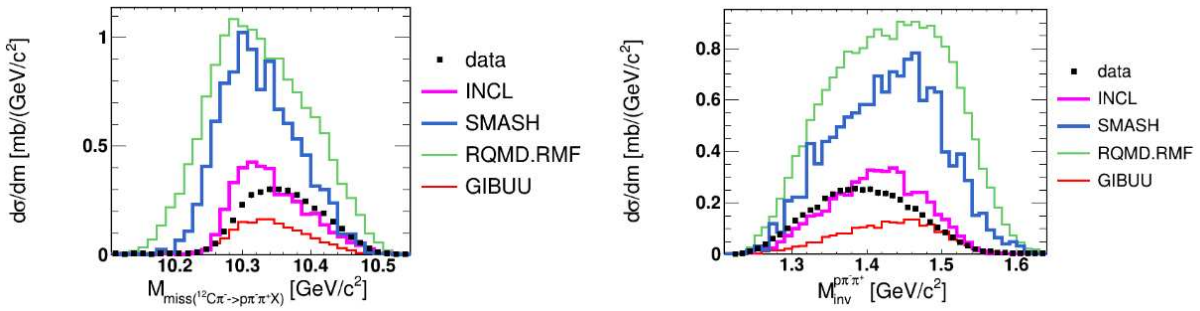

Figure 6.31: Missing mass and invariant mass of the π^-p $\rightarrow$ p $\pi^-\pi^+$+X channel.

6.5.3 channel: $\pi^-\pi^+$

A $\pi^+\pi^-$pair can be produced, either in reactions (3-5), which all imply an inelastic π +n reaction, as mentioned for the analysis of the p$\pi^+\pi^-$channel or in the process (7): π^-+ p $\rightarrow$ $\pi^+\pi^-$n. So, the study of the $\pi^-\pi^+$channel allows us to look at inelastic channels in a complementary way to p$\pi^-\pi^+$ channels.

As mentioned in the introduction (Sec. 1.3.4), the HADES collaboration has measured $\pi^- + p$ collisions at four values of the incident pion momentum in the second resonance region ($P_{\text{beam}} = 0.685$, GeV/c, ...), some results are presented in Fig.1.24 (a), [13]. These figures display curves representing the contributions of various final states to the total yield (depicted as black solid line histograms), as indicated in the legend. The predictions of INCL for the $\pi^+\pi^-$ invariant mass distributions in the carbon case present a similar shape as the HADES measurements for the π^-p reaction, which probably reflects a dominance of two-pion production in the first step of the reaction, see Fig.6.32. On the other hand, the data and the other models present a much broader distribution, with a stronger contribution at low invariant masses than in INCL++. This is in agreement with a stronger contribution from a two-step process with an elastic scattering collision before the two-pion production. We had such a situation in the case of the p$\pi^-\pi^+$ events, where, indeed, the invariant mass distribution was shifted closer to the threshold. In the case of RQMD.RMF this low invariant mass contribution is strongly overestimated. On the other hand, GIBUU and SMASH models provide a good description of the shape of the distributions but SMASH overestimates the cross section by roughly a factor 2, while GIBUU underestimates it by a factor 2. The INCL overestimates by a factor 1.4 and is concentrated in the region of the first collision production.

It has also to be noted that the processes for two-pion production are very different in the transport models and in INCL. In the transport models, the two pion production proceeds via resonance production and deexcitation, i.e. πN $\rightarrow$ N* $\rightarrow$ $\pi\pi$N, where branching ratios taken from the PDG are used for the decay into σN or ρN. In INCL, the production of two-pion is parameterized, based on the elementary cross sections. These differences might influence the kinematics of the two-pion production processes.

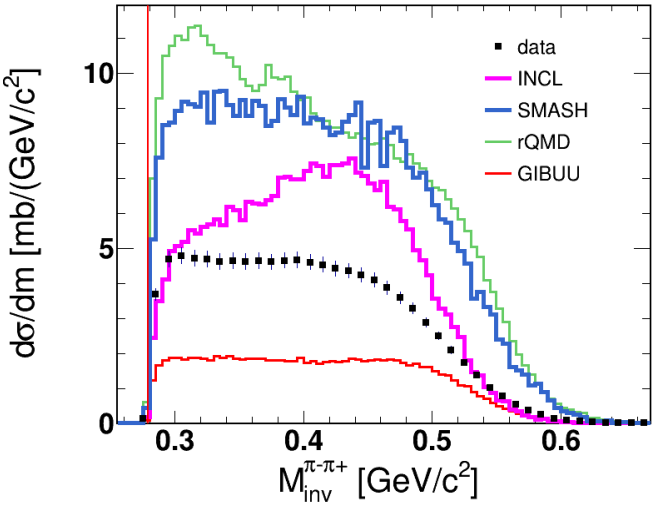

Figure 6.32: Invariant mass of the $\pi^-\pi^+$system in the $\pi^-\pi^+$channel.

6.5.4 channel: $p\pi^-\pi^-$

In this channel, the three particles can come from the same step as in (2). We remind :

2. $\pi^- + n \rightarrow \mathbf{p} + \boldsymbol{\pi}^- + \boldsymbol{\pi}^-$ (2.1 mb),

or from at least two different steps, with various options, as :

7. $\pi^- + \mathrm{p} \rightarrow \pi^- + \mathbf{p}$ (17.8 mb); $\pi^- + \mathrm{n} \rightarrow \mathbf{p} + \boldsymbol{\pi}^- + \boldsymbol{\pi}^-$

8. $\pi^- + \mathrm{p} \rightarrow \boldsymbol{\pi}^- + \pi^0 + \mathbf{p}$ (3.3 mb); $\pi^0 +$ n $\rightarrow \boldsymbol{\pi}^- + \mathbf{p}$

9. $\pi^- + \mathrm{n} \rightarrow \boldsymbol{\pi}^- + \pi^0 +$ n (0.4 mb); $\pi^0 +$ n $\rightarrow \boldsymbol{\pi}^- + \mathbf{p}$

where the detected particles are indicated with a bold font. As mentioned in Sec.6.1.4, the production of two pions in our reaction can indeed occur only via a πN$\rightarrow \pi\pi$N collision. In reactions (8) and (9), the proton can be detected either from the first or the second step.

As the two types of reactions involve different elementary mechanisms, it will be interesting to try to disentangle them experimentally. For this, one can notice that there is a notable difference in the energy balance. In the case of reaction (2), most of the energy available in the collision is indeed expected to be transferred to the p$\pi^-\pi^-$ system, if no further collision occurs. So, the recoiling ^{11}C might have a small excitation energy, i.e., the missing mass should be close to the ^{11}C mass. In the other cases, energy is carried away by other emitted particles, so the invariant mass of the three-particle system should be smaller and the missing mass larger. For RQMD.RMF, a narrow structure is indeed visible for missing masses close to the ^{11}C mass and for invariant masses close to $\sqrt{s_{\pi\mathrm{N}}}$ (Fig. 6.33), while the broader structure at larger missing masses and lower invariant masses could be due to particles coming from distinct steps (like in reactions 7, 8 or 9) or from further rescatterings.

Such structures are much less visible in INCL and GiBUU predictions and completely absent in the experimental

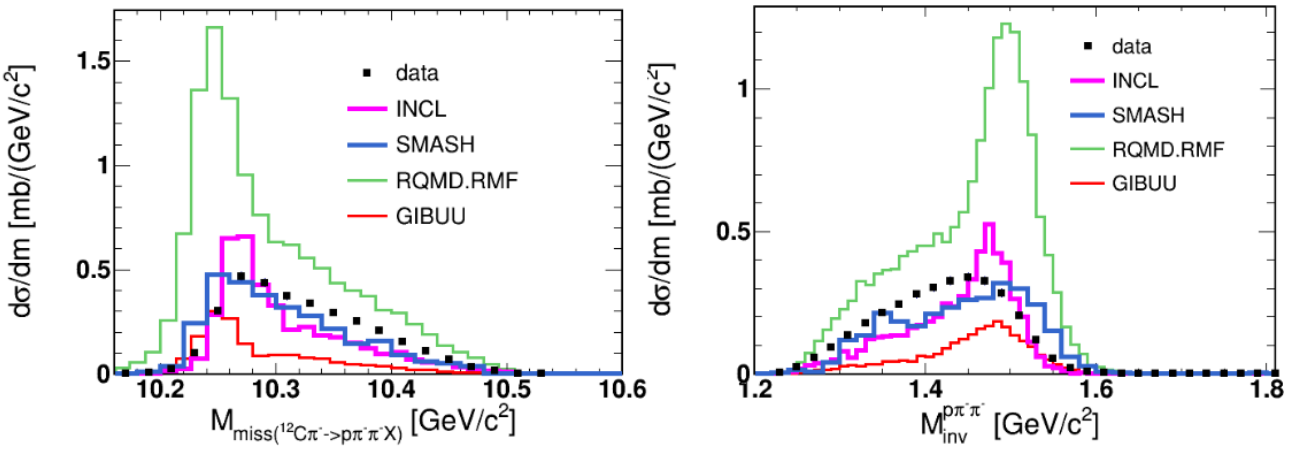

Figure 6.33: Invariant (right) and missing (left) masses for p$\pi^-\pi^-$channel.

distributions as well in SMASH, which are smoother and broader than other theoretical predictions. This means that the production of the three detected particles in the same single step is disfavored by our data, SMASH satisfactorily describes this channel.

It is also interesting to notice that, for RQMD.RMF and INCL, the proton momentum distribution in the π+N center-of-mass, which is displayed in Fig.6.34 presents a structure close to 0.432 GeV/c , which is the value expected for the quasi-elastic scattering. We explain this result by a strong contribution of reaction (7), where one of the protons comes for the quasi-elastic reaction. The experimental distributions and the ones from SMASH and GiBUU are peaked around the same value, but with no clear structure, which probably indicates a strong effect of further rescatterings.

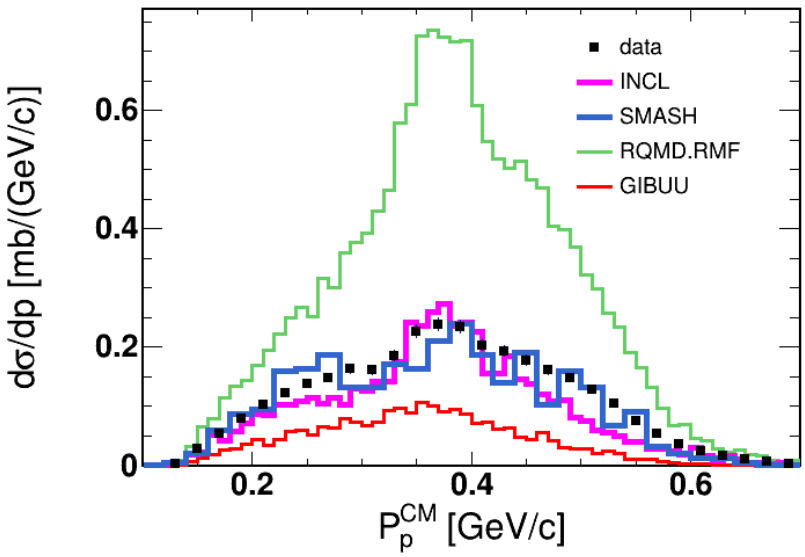

Figure 6.34: Center-of-mass momentum of the proton in the p$\pi^-\pi^-$channel.

The $\pi^-\pi^-$invariant mass distribution presented in Fig. 6.35 is peaked at values that are much smaller than

expected from the free πN$\rightarrow \pi\pi$N (see Sec. 6.5), which is also consistent with the fact that the dominant process is not a pure quasi-free π^-n $\rightarrow$ $\pi^-\pi^-$p reaction, but that further rescatterings occur.

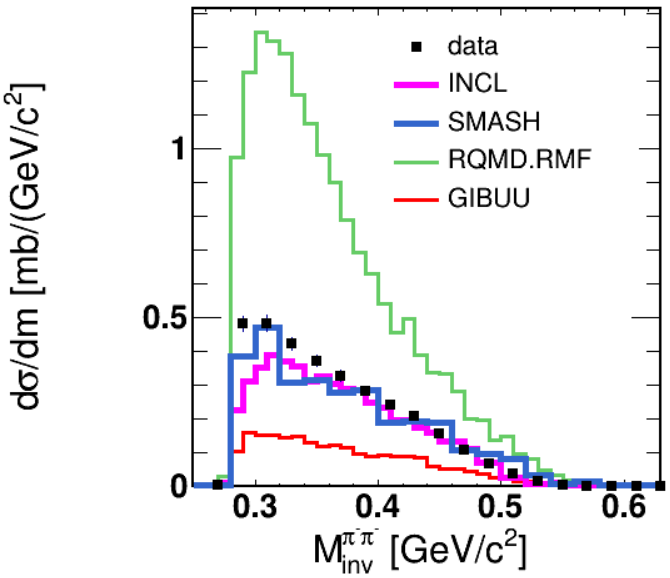

Figure 6.35: $\pi^-\pi^-$invariant mass in the p$\pi^-\pi^-$channel.

As observed already for the other channels, RQMD.RMF yields are way too large, while the order of magnitude of the predictions of the other models is quite reasonable. This comes as a surprise in the case of SMASH which overestimated the yields for the other types of channels studied so far. It can indeed be concluded that SMASH gives the best description for this channel. We were expecting a significant difference between the p$\pi^+\pi^-$ and p$\pi^-\pi^-$channels, due to the possibility of producing the latter channel in a single step. However, due to the dominance of processes with a rescattering step in the p$\pi^-\pi^-$ channel, there is indeed a difference in the experimental distributions, e.g. in invariant masses and missing masses for both channels, Figs.6.31 , 6.33, 6.32 and 6.35, albeit not as pronounced as observed in RQMD. All models, except SMASH, predict a too large proportion of single step channels, where the three particles carry most of the energy in the collision.

The analysis of INCL++ results in 4π (see Sec. 6.1.6) demonstrated that most of the events with two π^- in the final state are accompanied by the emission of a proton. This means that $\pi^-\pi^-$events are produced, similarly to p$\pi^-\pi^-$events, by reactions (1-4). The kinematics of the pions in both types of events is therefore expected to be similar. However, by comparing the two-pion invariant mass in the case of $\pi^-\pi^-$and p$\pi^-\pi^-$events, as shown in Fig. 6.36, one can observe that they have different shapes, due to the proton acceptance. The fact that SMASH better describes the two-pion channels than the channels with a proton may point to some problems with the nucleon potential. To do so, a test of the nucleon potential is presented in Sec.6.7.

6.5.5 channel : $pp\pi^-$

The $pp\pi^-$ channel can be obtained through multi-step processes consisting of at least two steps. These processes can be categorized into two groups:

10. Two-step processes with 2π production (inelastic): e.g.

    (a) $\pi^- + p \rightarrow \boldsymbol{\pi^-} + \pi^0 + \mathrm{p}\ (3.8\ mb);\ \mathrm{p} + \mathrm{p} \rightarrow \mathbf{p} + \mathbf{p}$ (proton rescattering)

    (b) $\pi^- + \mathrm{p} \rightarrow \pi^- + \mathbf{p}\ (17.8\ mb);\ \pi^- + \mathrm{p} \rightarrow \boldsymbol{\pi^-} + \pi^0 + \mathbf{p}$ (π rescattering)

    (c) $\pi^- + p \rightarrow \pi^- + \pi^0 + \mathbf{p}\ (3.8\ mb);\ \pi^- + \mathrm{p} \rightarrow \boldsymbol{\pi^-} + \mathbf{p}$ (π rescattering)

    (d) $\pi^- + p \rightarrow \boldsymbol{\pi^-} + \pi^0 + \mathbf{p}\ (3.8\ mb);\ \pi^0 + \mathrm{p} \rightarrow \pi^0 + \mathbf{p}$ (π rescattering)

    (e) $\pi^- + p \rightarrow \boldsymbol{\pi^-} + \pi^0 + \mathbf{p}\ (3.8\ mb);\ \pi^0 + \mathrm{n} \rightarrow \boldsymbol{\pi^-} + \mathbf{p}$ (π rescattering)

11. Two-step processes with 1π production (elastic): e.g.

    (a) $\pi^- + p \rightarrow \boldsymbol{\pi^-} + \mathrm{p}\ (17.8\ mb)$; p + p $\rightarrow$ **p + p** (proton rescattering)

    (b) $\pi^- + p \rightarrow \pi^- + \mathbf{p}\ (17.8\ mb)$; $\pi^- + \mathrm{p} \rightarrow \boldsymbol{\pi^-} + \mathbf{p}$ (π rescattering)

Following the same kind of reasoning as for the p$\pi^-\pi^-$ case, we can notice that in the case of reaction (10), energy is taken away by the undetected π^0 , while in the case of reaction (11) all the particles in the final state are detected. The distribution of the measured invariant mass is shown in Figs. 6.37 for the ppπ^- channel in comparison with the model predictions. Two distinct structures are clearly visible for RQMD.RMF, SMASH, and GIBUU models. As discussed above, the one at invariant masses close to $\sqrt{s_{\pi NN}}$ can be attributed to a reaction of type (11), i.e. a sequence of elastic collisions, while the one at lower values could be due to a reaction of type (10), involving one inelastic step, with a missing pion. However, further elastic collisions (more than two), with additional emitted

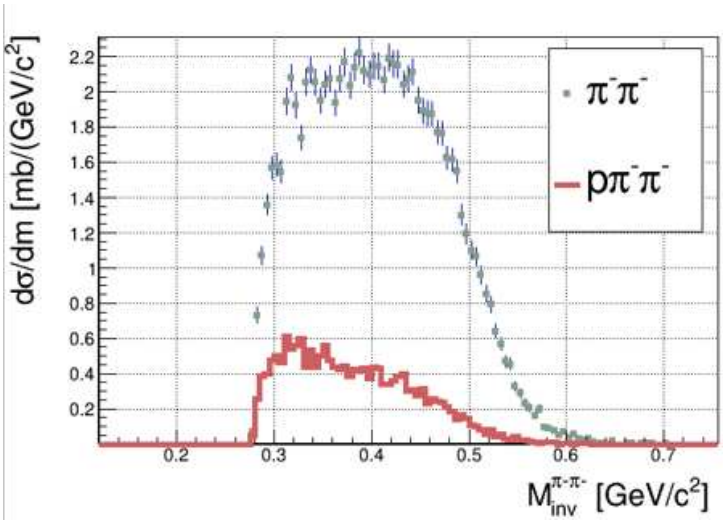

Figure 6.36: $\pi^-\pi^-$ invariant mass distributions measured for $\pi^-\pi^-$(grey dots) and p$\pi^-\pi^-$events (red histogram)

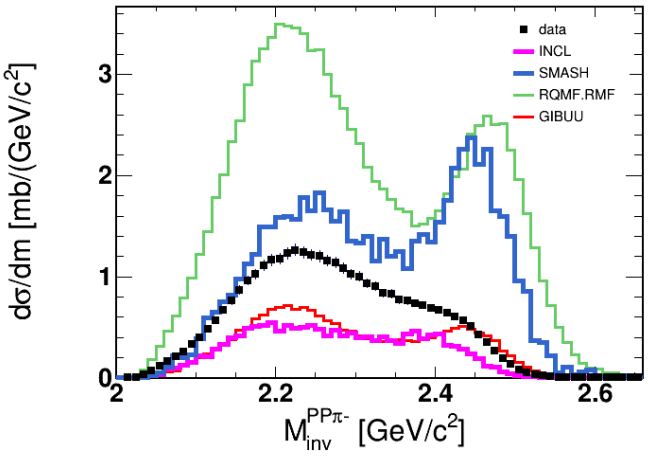

Figure 6.37: Invariant mass of the ppπ^-system in the ppπ^-channel.

particles can also shift the invariant masses to lower values. In a similar way as for the p$\pi^-\pi^-$case, the size of these structures varies a lot from one model to another. The presence of a narrow structure in RQMD.RMF, SMASH and GiBUU is fully consistent with two sequential elastic collisions. On the contrary, for the data and for INCL++, the contribution at large invariant masses is just visible as a shoulder and not as a well separated structure, which indicates that elastic processes have a smaller contribution to this ppπ^- channel than inelastic channels and involve more collisions. The kinematics of the pion and proton can be used to further distinguish the different reactions contributing to the ppπ^- channel. It can be noticed that the ppπ^- channel is in fact a sub-channel from the pπ^-case, where at least two steps are needed: an elastic or inelastic π^-p reaction and an elastic π^-p or pp reaction. One can probably expect reactions (10a) and (11a) to be more likely. Indeed, as already mentioned earlier, cross sections for elastic nucleon-nucleon scatterings are much larger than for pion-nucleon reactions. In the case of reactions (10.a) and (11.a), the pion should have the characteristics of the πN elastic or inelastic reactions. Indeed, Fig. 6.38 , which shows the pion momentum in the incident πN center-of-mass has a similar structure as Fig. 6.12, with two distinct regions corresponding to inelastic and elastic πN reactions at low and high pion momenta respectively, in agreement with the dominance of reactions 11a and 10a. In comparison to Fig. 6.12, the size of the high momentum structure is largely reduced for all models, albeit in different proportions (e.g. the quasi-elastic peak is now lower for SMASH than for RQMD.RMF). This clearly points to a lower probability of rescattering following reactions 11a in SMASH than in RQMD.RMF. For other models and for the data, these channels are strongly suppressed w.r.t. the inelastic case. As mentioned for the π^-p case, RQMD.RMF overestimates the yields in both the inelastic and quasi-elastic regions, while for SMASH, the overestimate is smaller in the inelastic region. One can also notice that the structures in the pion momenta and invariant mass distributions are a bit different, which can be due to the contributions of reactions (10b-e, 11b).

If we now investigate the proton momentum distribution in the center-of-mass, we can observe the characteristic structure close to the elastic scattering value. It is much weaker than in the case of the pion, but still signals the

contribution of reaction 10b or 11b. To conclude on the study of this quite interesting channel, we can say that the data favor the contribution of inelastic processes, while GiBUU and INCL++ give the best agreement for this channel, but still underestimate by about a factor 2 the contribution of inelastic processes, while RQMD.RMF and SMASH obviously overestimate the contribution of elastic processes.

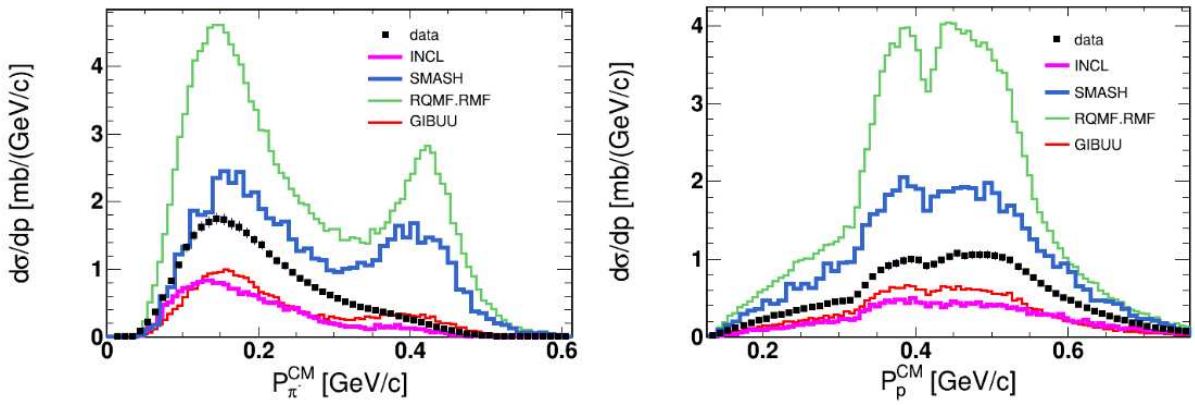

Figure 6.38: Center-of-mass momenta of the pion (left) and the proton (right) for the ppπ^-channel.

6.5.6 Pion absorption

The pion absorption of the incident π^- involves at least two protons, $\pi^- + p + p \rightarrow p + n$. As we can detect only protons, we could expect to see a contribution of pion absorption in a sequence as: $\pi^- + p \rightarrow \pi^0 + n$, and then by $\pi^0 + p + p \rightarrow$ **p + p**. Using the INCL model, comparing events with and without detected pions is possible.

Figs. 6.39 and 6.40 present a comparison of the pp channel, where at least two protons are detected, and the same channel without any detected pions (representing pion absorption). The different yields indicate approximately 30% of pion absorption is within the pp channel. There is no significant difference in the shape of the missing mass, invariant mass, or proton center-of-mass momentum distributions, which adds to the challenge of studying this phenomenon. We investigated the comparison of the pp and ppp channels, both of which may involve pion absorption, as well as the ppπ^-channel, where pion detection occurs. We examined the invariant mass of the two protons in these three scenarios and observed strikingly similar distribution shapes across all cases, see Fig.6.41. This similarity again demonstrates that it is difficult to identify pion absorption in our events. A better sensitivity could be maybe expected from the investigation of channels with neutrons. Indeed, the simplest channel where pion absorption occurs is π^-+ ^{12}C$\rightarrow$ nn^{10}B.

Fig.6.42 represents the nucleon multiplicities in the case of the pion absorption in INCL++. Compared to Fig.6.10, the pion absorption consists of at least one neutron emission in the final state, thus a detailed investigation requires neutron detection.

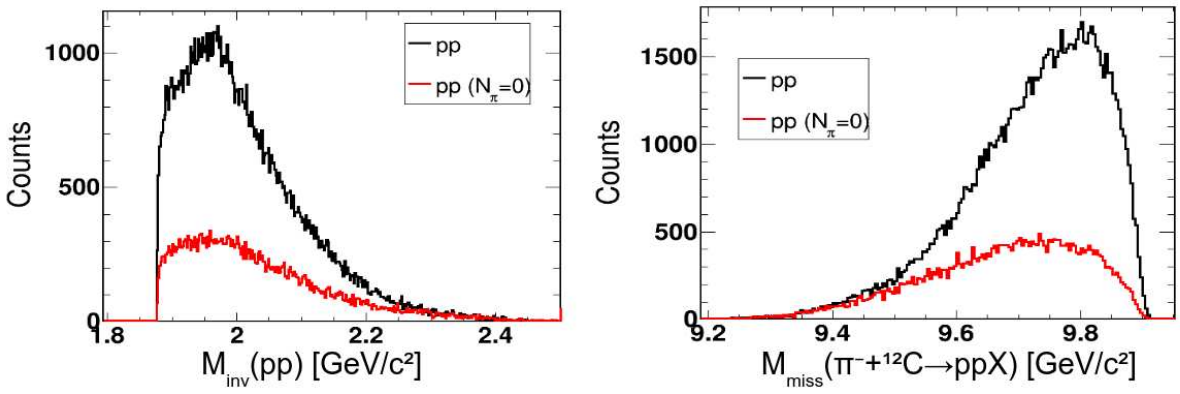

Figure 6.39: Invariant mass and missing mass for the pp channel in INCL++, compared to the case of the pp channel where no pion is emitted (absorbed).

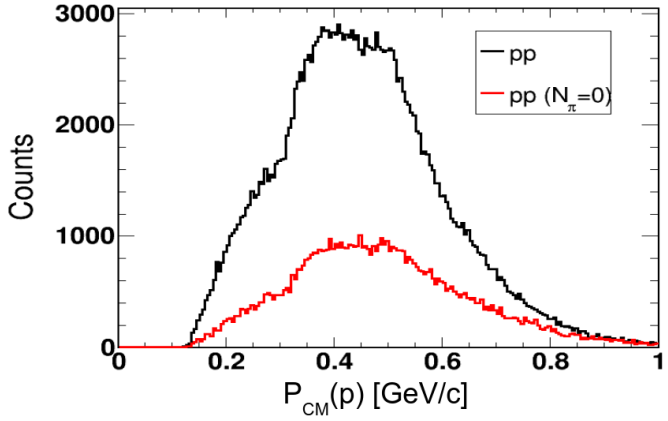

Figure 6.40: Same as Fig.6.39, but for the center-of-mass distribution of the emitted proton.

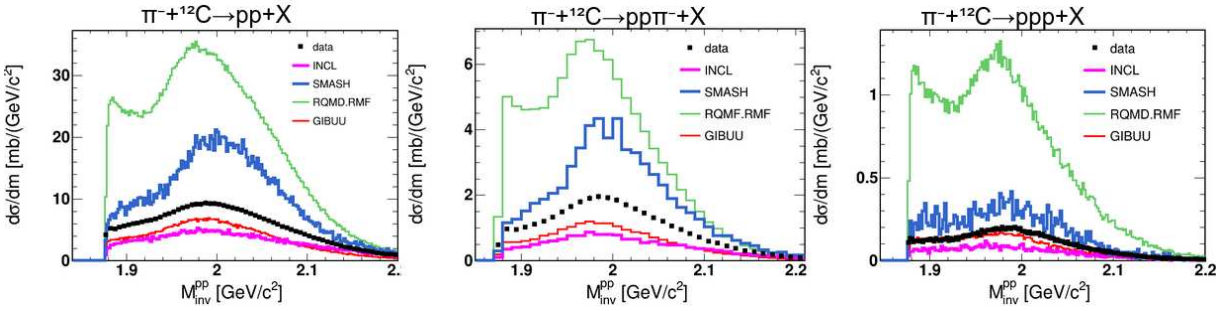

Figure 6.41: Comparison of the invariant mass of the two emitted proton in three channels: pp, ppπ^- and ppp.

6.6 Cross section summary table

The significant disparities between the data and model predictions for the cross sections of various hadronic channels, with protons and pions emitted within the HADES acceptance, are illustrated in Table.6.2.

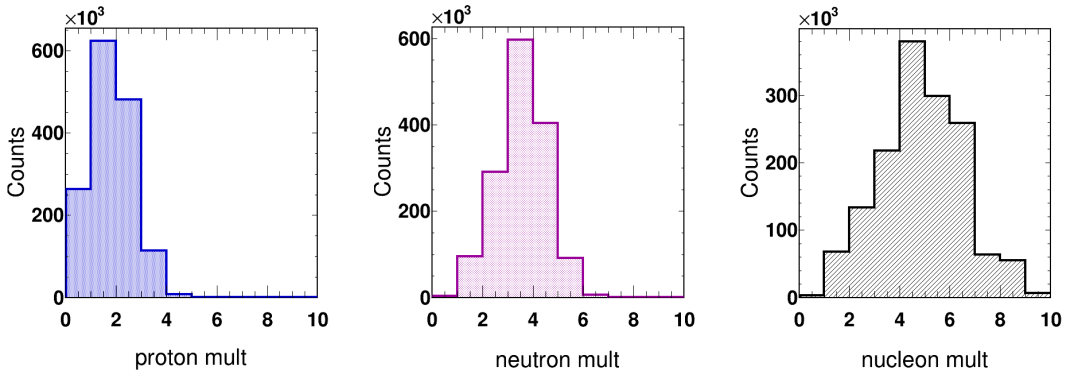

Figure 6.42: Predictions of INCL++ for the pion absorption in the $\pi^- + C$ reaction at 0.685 GeV/c. Distributions of the multiplicities of the protons, neutrons, and all nucleons.

Process	$\sigma^{acc}_{data} \pm \sigma_{err}$ [mb]	σ^{acc}_{INCL} [mb]	σ^{acc}_{SMASH} [mb]	$\sigma^{acc}_{RQMD.RMF}$ [mb]	σ^{acc}_{GIBUU} [mb]
pπ^-quasi-elastic	3.06 $\pm$ 0.20	1.98	12.86	6.97	3.45
pπ^-inelastic	3.36 $\pm$ 0.22	2.16	4.90	7.45	1.76
$\pi^-\pi^-$	0.230 $\pm$ 0.015	0.32	0.19	0.44	0.053
$\pi^-\pi^+$	1.06 $\pm$ 0.069	1.46	2.20	2.40	0.46
$\pi^+\pi^+$	0.0021 $\pm$ 0.0001	0.0031	0.0077	0.0064	0.00025
pπ^+	0.320 $\pm$ 0.021	0.30	0.78	1.12	0.14
pp	1.83 $\pm$ 0.12	1.067	3.35	6.35	1.19
p$\pi^-\pi^+$	0.0463 $\pm$ 0.003	0.053	0.13	0.20	0.022
p$\pi^-\pi^-$	0.065 $\pm$ 0.004	0.054	0.060	0.16	0.023
ppπ^-	0.338 $\pm$ 0.022	0.15	0.62	1.072	0.19
ppp	0.0480 $\pm$ 0.0031	0.024	0.082	0.30	0.039

Table 6.2: Table of different cross sections for experimental measurements of different hadronic exit channels consisting of two or three charged particles, compared with the models and calculated in the HADES acceptance.

6.7 SMASH potential test

As previously mentioned, SMASH provides a more accurate description of the two-pion channels compared to channels involving a proton. One possible explanation for this difference could be linked to the influence of the nucleon potential. To investigate this, we conducted a comparison of SMASH simulations with and without the inclusion of the nuclear potential across various channels. Fig. 6.43 illustrates this comparison for the quasi-elastic channel. We investigated the proton momentum since it is directly associated with the potential impact. As expected, our observations reveal that the inclusion of the nuclear potential in SMASH leads to a reduction in yields for high proton momenta. Conversely, removing the potential results in an overall increase in yields, which increases the mismatch with experimental data. This is just due to the fact that less protons are cut by the acceptance.

Similar observations were noted for the ppπ^-channel, albeit with a more pronounced effect that can be attributed to the detection of two protons instead of just one, with each proton being influenced by the nuclear potential. Figure 6.44 displays the invariant mass of the ppπ^-channel, illustrating the consequences of excluding the potential. Notably, the removal of the potential leads to elevated values at higher invariant masses. This phenomenon can be explained by the fact that, in the absence of the potential, there is more available energy in the center of mass,

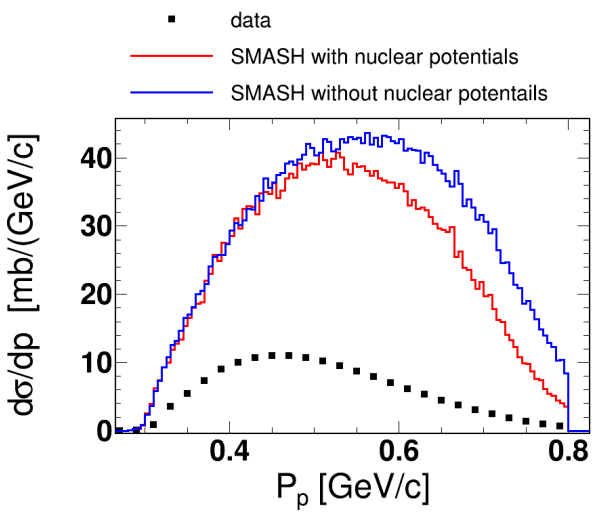

Figure 6.43: Comparison of the Proton momentum distribution for the quasi-elastic $p\pi^- \rightarrow p\pi^-$ channel, for SMASH simulation with and without nuclear potential.

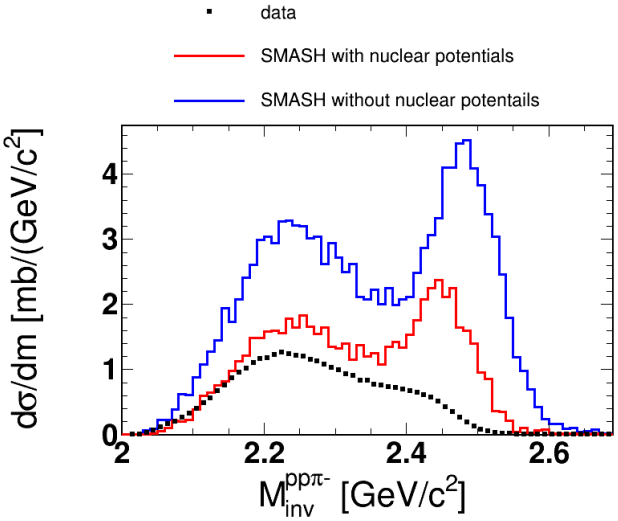

Figure 6.44: Same as in Fig. 6.43, but for invariant mass of the $pp\pi^-$ in the $pp\pi^-$ channel.

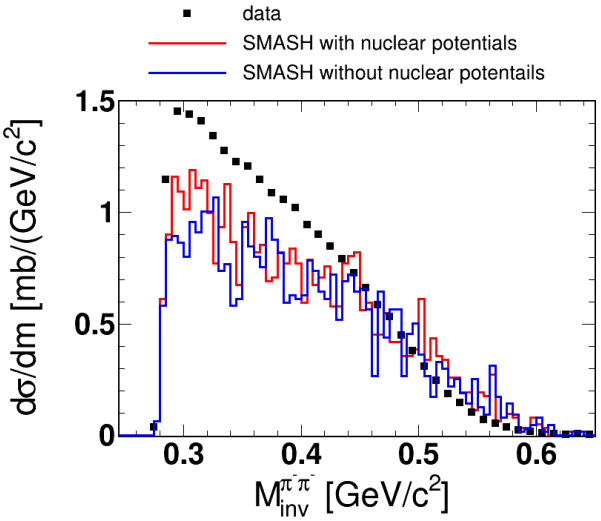

Figure 6.45: Same as in Fig. 6.43, but for the invariant mass of the $\pi^- + C \rightarrow \pi^-\pi^-$ channel.

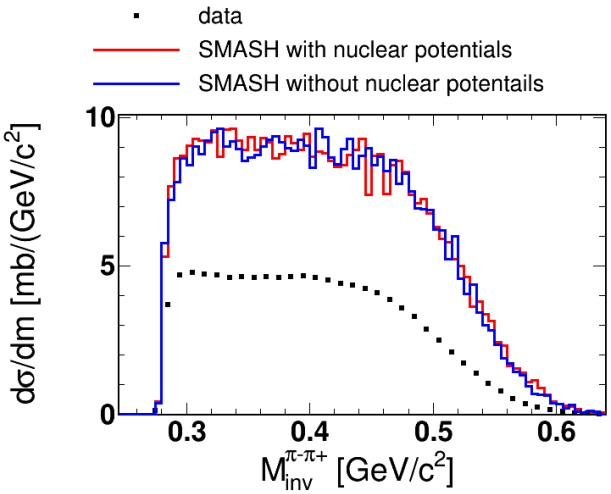

Figure 6.46: Same as in Fig. 6.43, but for invariant mass of the $\pi^- + C \rightarrow \pi^-\pi^+$ channel.

resulting in higher invariant mass values.

The impact on the two pion channels where no protons are detected is negligible, as illustrated in Figs. 6.45 and 6.46. To summarize, while the nuclear potential implemented in SMASH improves its performance, disparities still persist in the simulations.

6.8 Inclusive analysis

In this work, we have also studied the inclusive production of protons, deuterons, tritons, π^- and π^+. This analysis, however, is not fully inclusive due to the implemented trigger condition, which was defined with the META multiplicity

≥ 2 (at least 2 hits in the META detector), see also Sec. 2.5.

For each particle species, we have obtained double-differential $\frac{d^2N}{d\theta dT}$ (in polar angle θ and kinetic energy *T*) yields. These yields have not been yet corrected, neither for efficiency nor acceptance. Moreover, these distributions have not been corrected for the trigger bias. The polar angle θ changing between 20° and 80° with the step of 5°. The experimental results were integrated within the range of $\Delta\theta = 5^\circ$ ($\theta \pm 2.5^\circ$). The bin size along the energy *T* was chosen to be 10 MeV. For comparison with the HADES data we are using the same set of transport calculations: RQMD.RMF, SMASH, GiBUU and the INCL++ cascade model. Among them, only INCL++ has implemented a mechanism of surface coalescence responsible for clustering. The coalescence is included for the formation and emission of lighter composite particles (A≤ 8) during the first stage of a reaction.

As was already explained before (see Sec. 5), the data and the simulations are treated in the same way and all the analysis conditions are exactly the same. In Figs. 6.47a, 6.47b and 6.47c the comparison between the data and the models for π^-, π^+ and protons is presented. For picture clarity, we have selected three θ angles: 20°, 50° and 70°. The global conclusion is that none of the models describe the data satisfactorily.

In the case of the π^- production (Fig. 6.47a), INCL++ and GiBUU seem to be the closest to the data. A striking problem is visible at the lowest angle 20°, at which the contribution from the quasi-elastic process is visible at the highest energies $\sim$ 0.5 GeV. None of the models properly reproduces the quasi-elastic peak. In this case, INCL++ is far away from the data.

In the case of the π^+ production (Fig. 6.47b), at 20° GiBUU reproduces the data satisfactorily, however at 50° and 70° SMASH and INCL++, respectively, are closer to the data.

In the case of protons (Fig. 6.47c) none of the models describe the data properly at various θ angles and in the available energy range of the protons.

These results are consistent with the analysis of $\pi^- - p$ QFS, see Fig. 6.12. Except of the lowest angle of 20° (see Fig. 6.47a), at the highest energies corresponding to the QFS regime the calculations follow the similar trend as for the $\pi^- - p$ QFS. For the lower energies, which correspond to inelastic regime (see Sec. 6.4.1) the two models INCL and GiBUU underestimate the data while SMASH and RQMD.RMF overestimate the data significantly. This pattern is visible in Figs. 6.47a- 6.47c.

In the second set of figures 6.48a-6.48e, we present the more detailed comparison between the data and the INCL++ simulations. In this case the differential distributions are presented for all available θ ranges. In general, the INCL++ describes the data for various particles quite well. The disagreement is visible at very forward θ angles $20^\circ - 40^\circ$ for π^- (Fig. 6.48a), π^+ (Fig. 6.48b) and protons (Fig. 6.48c). There are also problems for tritions (Fig. 6.48e) at the smallest available energies.

In the third set of figures 6.49a-6.49c, we present a more detailed comparison between the data and the SMASH

calculations. In this case, we have focused on studies of the effect of the nuclear potential. We have used the Skyrme and Symmetry potentials, see also Sec. 4.1.1 for more details. The Skyrme potential has the following form:

$$U_{sk} = A\frac{\rho}{\rho_0} + B(\frac{\rho}{\rho_0})^{\tau}, \tag{6.18}$$

where ρ is baryon density in the local Eckart [103] rest frame and the parameters have the following values: A$=-209.2$, B$=156.4$ and $\tau = 1.35$. In the case of the Symmetry potential, which has the form:

$$U_{Sym} = \pm 2S_{pot}\frac{I_3}{I}\frac{\rho_{I_3}}{\rho_0} + S(\rho_B)(\frac{\rho_{I_3}}{\rho_B})^2, \tag{6.19}$$

where ρ_{I_3} is the density of the relative isospin $\frac{I_3}{I}$ and ρ_B is the net baryon density and

$$S_{\rho_B} = 12.3MeV \times (\frac{\rho_B}{\rho_0})^{2/3}. \tag{6.20}$$

The parameter S_{pot} was set to be 18.0.

The differential distributions are presented for all the available θ ranges and are compared to the simulations with and without potential included. As one can notice, switching off the potential clearly worsens the data description for π^- (6.49a) and protons (6.49c) at the very forward $\theta \leq 30^\circ$ angles and at the highest energies, corresponding to the QFS region. Similar conclusions are drawn for the other studied channels, see also Sec. 6.7 for analysis of QFS and the semi-exclusive channels ($pp\pi^-$, $\pi^-\pi^-$, $\pi^-\pi^+$).

6.9 Summary

The interaction of the pion with the carbon nucleus is a quite complicated process. It involves various reactions like quasi-elastic scattering of (secondary) pions and nucleons and inelastic processes in which pions and nucleons are produced and can further (re-)interact. Such processes are described in the cascade INCL++ model and the transport codes, which utilize the already measured cross-section world database for such reactions. In HADES we detect charged particles like protons, deuterons, tritons and pions and by analysis of inclusive or semi-exclusive (double- and triple-coincidences) channels, it is possible to evaluate the model predictions.

Regarding the RQMD.RMF model, there is a consistent overestimation of yields across all channels, with some cases exceeding a factor of two. The model's kinematics, which involves the consideration of wave packets rather than individual particles, appears to approach free kinematics. This is evident in the narrowness of the missing mass squared for the quasi-elastic channel and the shifting of missing momentum values to lower ones. The shift in the missing momentum is directly linked to the model's description of nucleon density [88]. It employs a local

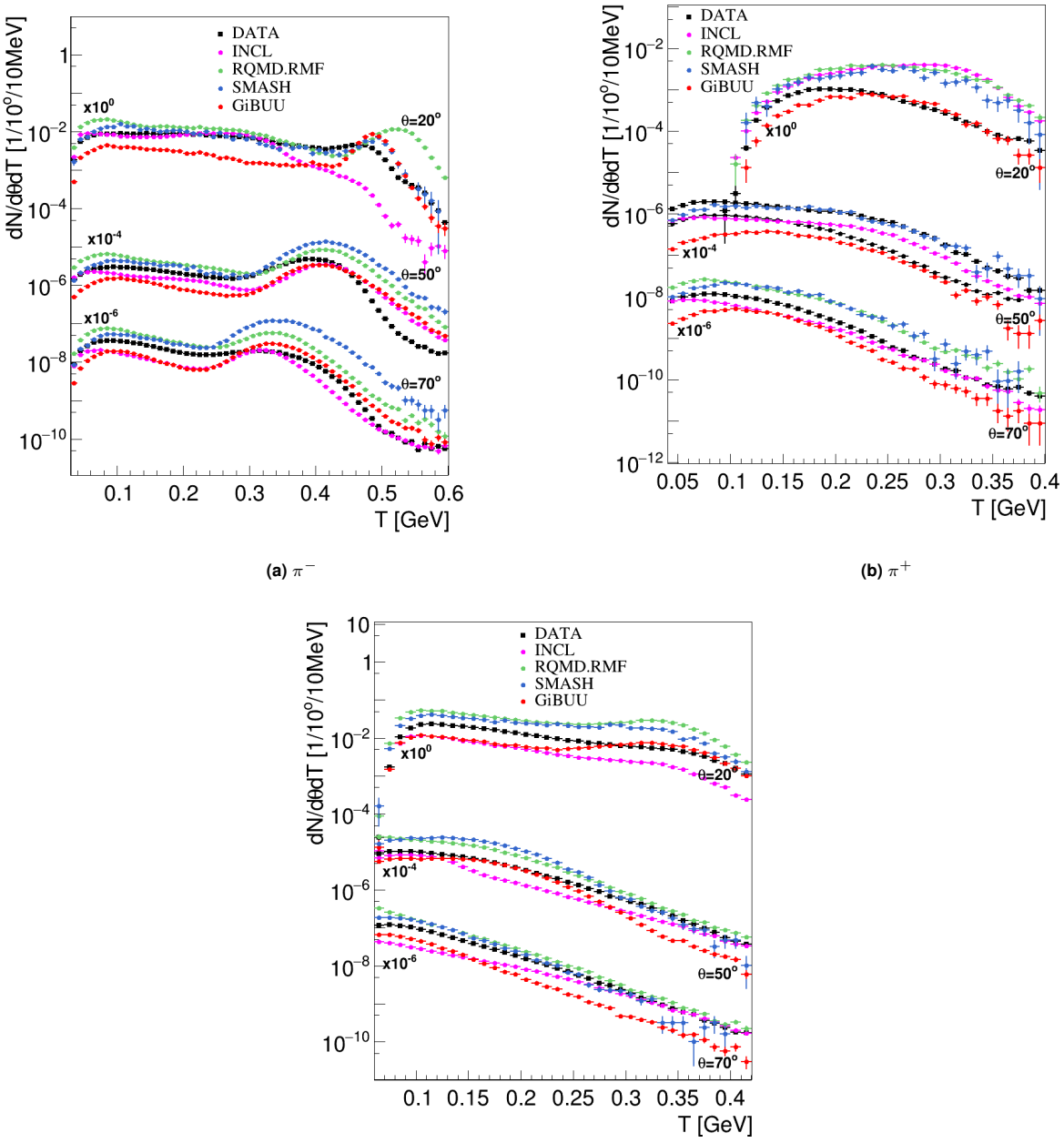

(a) π^-

(b) π^+

(c) protons

Figure 6.47: Double differential cross sections of π^- (a), π^+(b) and protons (c): measured in HADES in π^-+^{12}C reaction at 0.7 GeV/c incident pion energy. The distributions measured at emission angles of $20°$, $50°$ and $70°$ are shown. In order to facilitate the comparison each distribution at higher angle is multiplied by a factor of 10^{-2}. The experimental distributions are compared to the results of theoretical models: INCL++, RQMD.RMF, SMASH and GiBUU, see the legend for details.

Thomas-Fermi momentum distribution that is dependent on the local density. Strikingly, this model exhibits a highly peaked contribution from the (π^-p $\rightarrow$ p $\pi^-\pi^-$) process, which is inconsistent with the experimental data, see 6.33. Same case for the sequential elastic steps (quasi-elastic followed by $pp \rightarrow pp$), which do not align with the observed data. This model has been used so far for higher energies and it was probably not tuned to our case.

In comparison to RQMD.RMF, the GIBUU model demonstrates better performance. It consistently underesti-

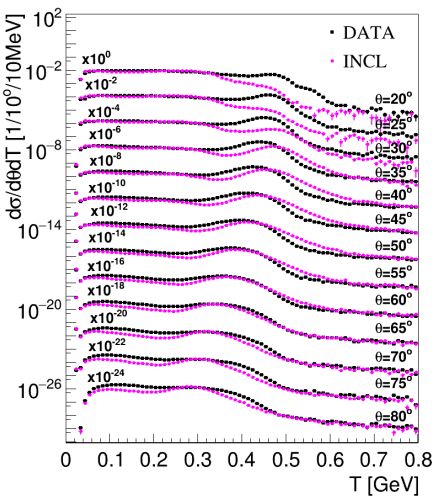

(a) π^-

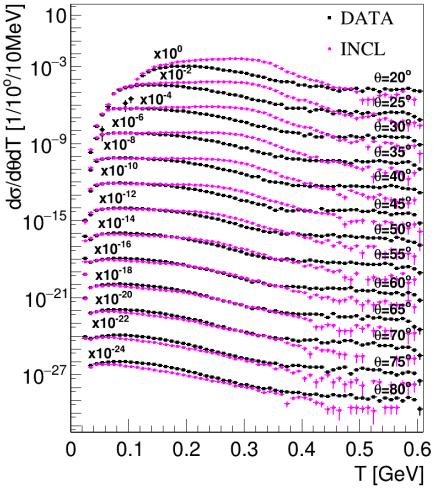

(b) π^+

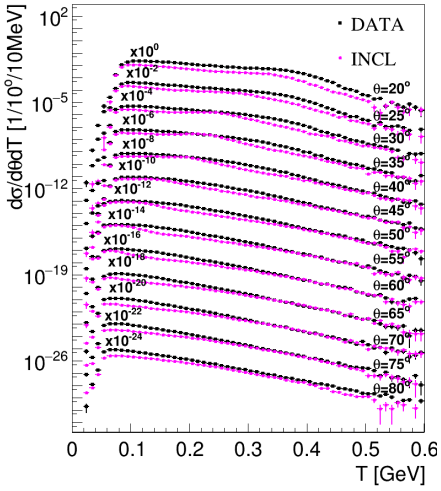

(c) protons

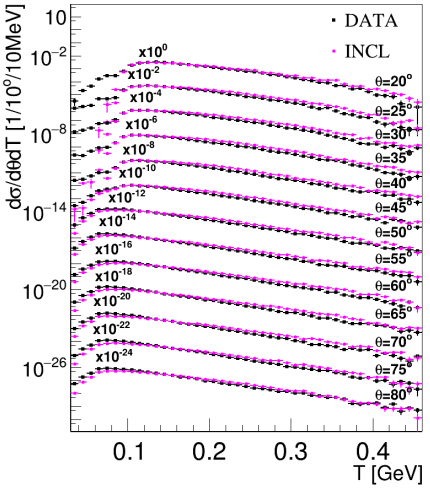

(d) deuterons

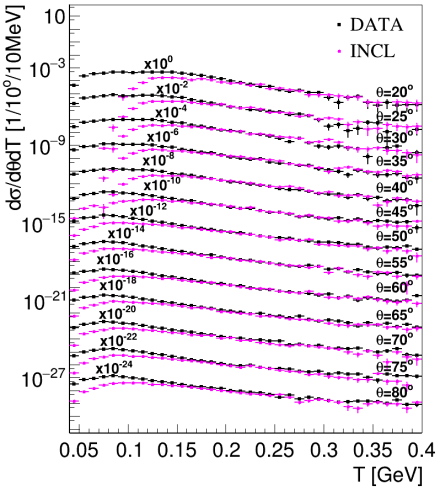

(e) tritons

Figure 6.48: Double differential cross sections of π^- (a), π^+(b), protons (c), deuterons(d) and tritons (e) : measured in HADES in π^-+^{12}C reaction at 0.7 GeV/c incident pion energy. The distributions measured at emission angles in the range $20^\circ - 80^\circ$ are shown. In order to facilitate the comparison, each distribution at higher angle is multiplied by a factor of 10^{-2}. The experimental distributions are compared to the results of the INCL++ model.

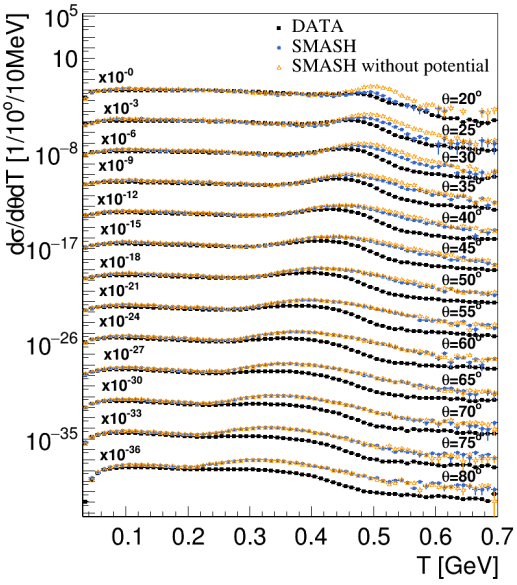

(a) π^-

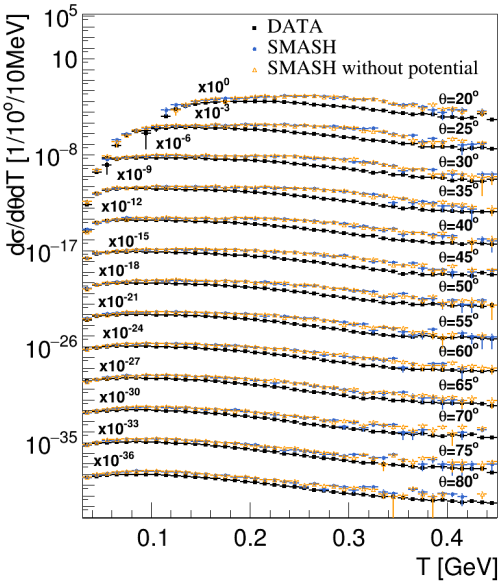

(b) π^+

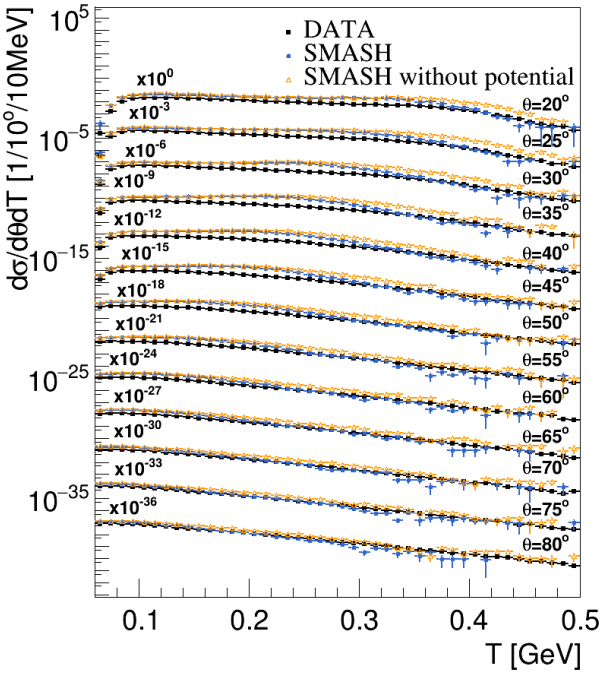

(c) protons

Figure 6.49: Double differential cross sections of π^- (a), π^+(b) and protons (c): measured in HADES in π^-+^{12}C reaction at 0.7 GeV/c incident pion energy. The distributions measured at emission angles in the range $20° - 80°$ are shown. In order to facilitate the comparison, each distribution at higher angle is multiplied by a factor of 10^{-2}. The experimental distributions are compared to the results of the SMASH model with and without nuclear potential.

mates yields, typically by a factor of two or less. Notably, we observe a strong peak for the single-step process (π^-p $\rightarrow$ p $\pi^-\pi^-$) although it is less pronounced than observed for the RQMD predictions. The GIBUU model exhibits a very small structure for the Δ(1232) resonance, which is observed in the pπ^+channel. GIBUU quite well describes the shapes of the experimental distributions and in many cases follows the INCL predictions.

SMASH usually overestimates the data. The worst case is the $p^{\pi^-}_{CM}$ distribution in the quasi-elastic region, see Fig. 6.12. However, it performs impressively well in reproducing the yields of the p$\pi^-\pi^-$channel. Similar to RQMD.RMF, its predictions reveal a narrow peak for ppπ^- channel, see Fig. 6.38, which is in disagreement with the data. Like GIBUU, it exhibits a small structure for the Δ(1232) resonance seen for the pπ^+channel (Fig. 6.29).

Studies of the nuclear (non-relativistic) potential effects in various channels have been performed with SMASH. This test revealed that switching off the potential worsens the data description, also in the inclusive analysis in the region corresponding the π^-p QFS.

The INCL++ model gives the best description of our data in most of the studied distributions. Problems are visible in missing and invariant masses of the $p\pi^-$ system (underestimation) and the $\pi^+\pi^-$ system (overestimation). There is also a problem in the $pp\pi^-$ channel in which INCL++ predicts too low yield.

The Fermi-gas model used by INCL++ generates a missing momentum distribution distinct from that reconstructed from the data. The choice of the local Fermi-Thomas momentum that is employed in the transport models appears to be the closest match to the data. The INCL++ model quite accurately predicts rescattering effects, particularly in the p$\pi^-\pi^+$and ppπ^-interactions. However, it exhibits a preference for the single-step process (p$\pi^-\rightarrow$ n $\pi^-\pi^+$), which is observed in $\pi^-\pi^+$channels, than for multi-step processes (3),(4), and (5). The use of the local energy procedure in INCL++ allows to obtain the proper yield description and in general is needed. Nevertheless, the description of the missing momentum distribution (Fig. 6.20) was not possible using the default value of the local energy used in INCL. To find the most optimal value, a more careful analysis is needed.

The pion absorption is a challenging process to study. It requires neutron detection for a better and deeper investigation.

In the case of the inclusive analysis, similar conclusions can be drawn like for the semi-exclusive one. None of the models properly describe the QFS region at very forward angles, which is visible in Fig. 6.47a. In the case of the pions production, the INCL and GiBUU models reproduce the data satisfactorily. A similar conclusion can be drawn for protons, however at higher angles (see Fig. 6.47c) and energies, SMASH and RQMD.RMF, perform better. The INCL model quite well describes yields of deuterons (Fig. 6.48d) and tritons (Fig. 6.48e) at all studied polar angles. The problems are visible at very small energies, especially for tritons. To obtain more quantitative and qualitative conclusions about the data description by the models additional analysis utilizing the χ^2-test or the so-called A-deviation factor [52, 6] is needed.

Chapter 7

Investigation of Short-Range Correlation effects

Short Range Correlations are brief fluctuations of two nucleons with high and opposite momenta, where each of them is higher than the nucleus Fermi momentum. Using the HADES $\pi^- - ^{12}$C scattering at 0.7 GeV/c we have made a try to study the SRC pairs using double ($\pi^- - p$) and triple ($\pi^- - p - p$) coincidences. Our goal was mostly to gain experience in this field, in particular in view of future dedicated experiments planned with HADES, and to check if our data reveal any sensitivity to the SRC effects. However, we cannot deliver any definite and solid conclusions on the existence of the SRC pairs in our data.

7.1 Introduction on SRC

7.1.1 Nucleon-nucleon interaction

The strong force between nucleons is an effective residual force that arises from the interaction between quarks and gluons, which are constituents of the nucleons. The stability of nuclei is an interplay between the long-range attractive force and the short-range repulsion that prevents the system from collapsing. The repulsive core is a scalar (central) part of the interaction at very short distances while at moderate and long distances the tensor force, which depends on the spin orientation and the relative angular momentum of the nucleons, dominates. The nucleon-nucleon (NN) interaction is described using semi-phenomenological potentials like Argonne V18 [104] or CDBonn [105]. They are able to predict observables for two nucleon systems with very high precision. An alternative method to model the NN interaction is the Chiral Perturbation Theory (ChPT), an effective field theory for the nuclear interaction [106]. These effective models are well constrained at typical NN distances in nuclei ($\sim$2.5 fm) [107], but

not at shorter distances (0.5-1.5 fm) at which the repulsive core exists, see Fig. 7.1. This limitation causes that the description of high-density nuclear matter, like the cores of neutron stars, is not possible and needs to be constrained based on experimental studies and dedicated effective theories. Nucleons at short distance, like in nuclei, can interact strongly and create short-range correlated (SRC) pairs with high relative (above 400 MeV/c) and low center-of-mass momenta, relatively to the Fermi momentum. SRC are a manifestation of the NN interaction at short distances and can help constraining the models, with an impact in various fields where a detailed description of the high density or high momentum components of the nucleons is needed (e.g. neutron stars structure [108], the nuclear symmetry energy or neutrino nucleus interactions[109, 110]).

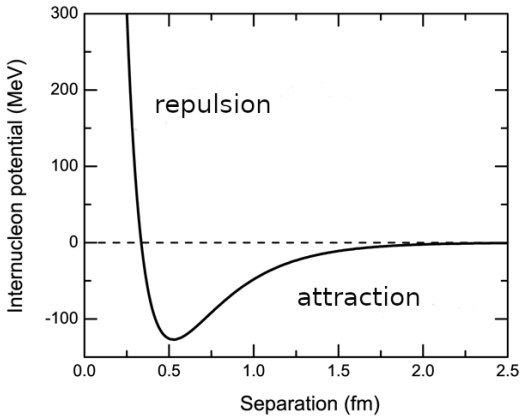

Figure 7.1: The nucleon-nucleon potential.

7.1.2 Limitations of the shell model

The shell model picture of the nucleus is very successful in predicting energy levels of nuclei including their spin and parities [111]. In this model, nucleons move independently in a potential that corresponds to an average of all nucleon-nucleon strong interactions. However, it was early found that such a single-particle model can not correctly predict the occupancy of the different energy levels [112].

Shell model calculations are also not able to explain the existence of high momentum components, with values much larger than the Fermi momentum of the nucleon momentum distribution (see Sec. 4.1.2). To explain such high momentum values, the individual interactions of the nucleon with other nucleons need to be taken into account.

7.1.3 Experimental observations

The short-distance interaction can be directly studied using the high momentum-transfer electron- and proton-scattering A(e, e'N), A(e, e'pN), A(p,pN), A(p,ppN). The electron or proton beams interact with protons or neutrons in the target nucleus, leading to the knockout of a high-momentum nucleon and the simultaneous emission of a correlated recoil nucleon, if a SRC pair is hit. Over the last decade, we have learned a lot about SRCs for selected nuclei

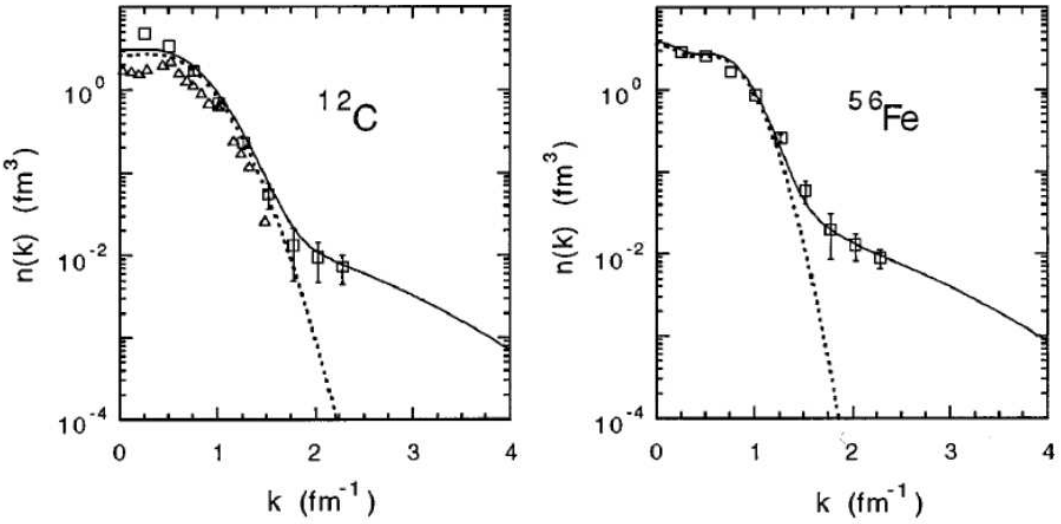

Figure 7.2: The nucleon momentum n(k) distribution (solid lines) presented for ^{12}C and ^{56}Fe nuclei. The dotted lines show the low-momentum and single-particle part of n(k), i.e., when nucleon-nucleon correlations are switched off. The data points (squares) come from SLAC inclusive measurement A(e,e') [27]. The empty triangles represent the values of n_0(k) obtained from the exclusive experiments on various nuclear targets, e.g. [28, 29]. Figure adopted from [30].

^{4}He, C, Al, Fe and Pb thanks to experiments at Brookhaven National Laboratory (BNL) and later at Jefferson-Lab (JLab).

The first high-energy, large momentum transfer and exclusive SRC studies was carried out at BNL using a 6-9 GeV/c proton beam, the EVA spectrometer, and a recoil-neutron detector [113, 114, 115]. This measurement allowed for the first direct observation of the np-SRC pairs, however, the statistics were very limited. The search for SRC was also an important part of the JLab 6 GeV science program. The next measurements, using electron beams at JLab, allowed for simultaneous direct observation of pp-SRC and np-SRC pairs, and extended the measurements to various target nuclei (^{4}He, ^{12}C, ^{27}Al, ^{56}Fe and ^{208}Pb) [113, 31, 116, 117, 118]. Recently, the ^{12}C(p,2p)^{10}B was used to unambiguously identify (pn) SRC pairs and efficiently suppress rescatterings and Final State Interaction effects [33]. This experiment consisted of detecting two protons at large angles with a coincidence of ^{10}B fragments, which are expected to be produced by SRC breakup reactions when interacting with proton-neutron (pn) pairs. Some results of this experiment will be shown in Sec. 7.5.2. Experimental studies show that short-range-correlated NN pairs account for practically all of the high-momentum ($k > k_F$) nucleons in nuclei and about 20% of all the nucleons in nuclei. This is illustrated in Fig. 7.2, where the measurements from BNL are compared to a model [30] including both a mean-field contribution at low momenta and a SRC contribution which extends up to larger momenta. Exclusive experiments demonstrated that short-range *pn* pairs dominate over *pp* pairs, with a ratio np/pp=18$\pm$5, [115, 113, 116] in any type of nuclei [119, 120]. This is due to the dominant tensor force which acts between nucleons only in spin-triplet states and at large relative momenta (tensor correlations). *np* pairs indeed include contributions from spin-singlet and spin-triplet states while *pp* pairs are only spin singlet [113, 121, 122]. Fig. 7.3 shows the experimentally extracted fractions of *np* and *pp* SRC pairs from the sum of pp and np pairs in

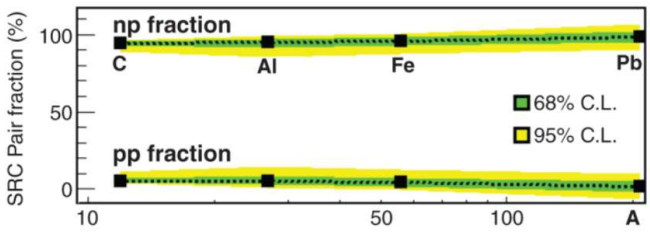

Figure 7.3: The experimental fractions of *np* (top) and *pp* (bottom) SRC pairs in nuclei. The green and yellow bands reflect 68% and 95% confidence levels, respectively. np-SRC pairs dominate over pp-SRC pairs in all measured nuclei. Figure adopted from [31].

nuclei. Thus, np-SRC pairs dominate in all measured nuclei, including neutron-rich imbalanced ones.

Plans for a dedicated SRC experiment with HADES

High energy proton beams were identified as well suited to study SRC. By carefully selecting the kinematical conditions in quasi-free reactions, the effects of rescatterings can be suppressed and SRC effects can be unambiguously identified [33]. It was proposed to use the HADES setup and the 4.5 GeV proton beam at GSI to search for SRC in the p+Ag reaction. An experimental proposal has been already submitted to the GSI PAC committee in 2020 and could take place in the next years. Neutron detectors will be installed at backward angles to detect the recoil neutrons. The backward going neutrons and protons will be detected in order to measure both A(p,ppn) and A(p,ppp) reactions as well as possible 3N-SRCs in exclusive A(p,2p2N) reactions. This measurement will be very unique since the planned statistics will be around 70 times larger than it was achieved so far with the JLab (e,e'pn) data. The goals for this measurement are to study the details of the short-range part of the NN potential.

7.1.4 Models for SRC description

Several approaches have been developed to take into account SRC in the description of nuclei. Current mean-field nuclear approaches are not able to properly describe the effects of SRCs. Ab-initio many body calculations (Variational Monte Carlo VMC methods) are successful in predicting the static properties, like momentum distributions of nucleons [123] in nuclei and nucleon-pair (nucleon-cluster) [124] momentum distributions but are limited to light nuclei (A≤ 12) and soft interactions [121, 125].

To describe the medium and heavy nuclei and account for processes at short distances, effective theories are utilized. They used various methods like the lowest-order correlation operator approximation (LCA) [126, 127], a relativistic multiple-scattering Glauber approximation (RMSGA) [128] or the model proposed in [30] to calculate the nucleon spectral function in few- and many-nucleon systems. Another approach to describe the SRCs in a Fermi system is a *contact* theory which was studied and validated experimentally for ultra-cold Fermi gases [129]. The contact theory is applicable to the systems with significant scale separation and was generalized to nuclear systems [130].

In the generalized nuclear contact formalism (GCF) the system wave-function is factorized in the following way:

$$\Psi^A \overset{p_{ij}\to 0}{\longrightarrow} \sum_\alpha \varphi_\alpha(\mathbf{p}_{ij}) A_{ij}^\alpha(\mathbf{P}_{ij}, \mathbf{p}_{k\neq ij}), \tag{7.1}$$

where $\varphi(\mathbf{p}_{ij})$ is a universal two-body function of the relative momentum of the SRC pair ($\mathbf{p}_{ij} = (\mathbf{p_i} - \mathbf{p}_j)/2$), A_{ij} is a function describing the motion of the (A-2) residual system with total pair CM motion, $\mathbf{P}_{ij} = (\mathbf{p_i} + \mathbf{p}_j)$. Index *ij* corresponds to *pn*, *pp*, *nn* pairs, α runs over all possible NN channels. The GCF assumes the scale-separation between the short-distance interactions between the SRC pairs, and the long-range interactions between the pair and the (A-2) system. To calculate the cross sections for a specific process the GCF needs to be properly adjusted (nuclear contact values, universal $\varphi(\mathbf{p}_{ij})$ functions, SRC pairs CM momentum distribution, excitation energy of the A-2 system). The GCF calculations are used to predict the SRC effects and confront them to experimental results [118, 33]. Unfortunately, simulations with GCF were not yet available and could not be compared to our experimental results in the framework of this PhD.

7.1.5 Implementation of SRC in INCL++

During the course of this thesis, a significant advancement has been made in the INCL++ model through the implementation of SRCs. SRCs were first implemented for pp elastic scattering only, but, on our request, also for π^-p elastic scattering. However, at the moment, only the most probable proton-neutron SRC pair case is treated. As discussed above, the particles in INCL move in straight lines and with constant momenta, which are shot in a hard Fermi sphere. The maximum momentum a particle can have is the Fermi momentum (210.6 MeV/c for carbon nuclei). In SRC pairs, nucleons experience strong repulsion of the nuclear interaction at short distances. INCL++ strategy is to calculate for each step of a collision the distance between the participant nucleon and the spectator one. If this distance is shorter than $d_{max} = 1.6fm$, then the pair is recognized as a SRC pair and an "extra momentum" denoted as $\vec{P}_{SRC}$ is added to the nucleon momentum, keeping the same direction. It is defined as :

$$\mid \vec{P}_{SRC} \mid = \left(\frac{d_{max} - d_{part}}{d_{max}}\right)^2 \cdot P_{SRC}^{max}, \tag{7.2}$$

where d_{part} is the distance between the nucleons in the SRC pair. P_{SRC}^{max} is the maximum momentum of the nucleons being in the SRC pair and corresponds to the situation when they overlap. In order to determine P_{SRC}^{max} the INCL++ experts used the SLAC data [27] from inclusive quasi-elastic electron scattering on a ^{56}Fe target, as illustrated in Fig. 7.4, where the nucleon momentum distributions in $[fm^{-1}]$ for various choices of P_{SRC}^{max} in INCL++ are also displayed. The results show the best agreement between INCL++ and the data for $P_{SRC}^{max} = 2 * P_F$. To validate the implementation of the SRC in INCL++, the evolution of the number of high-momentum ($k \geq k_F$) protons and

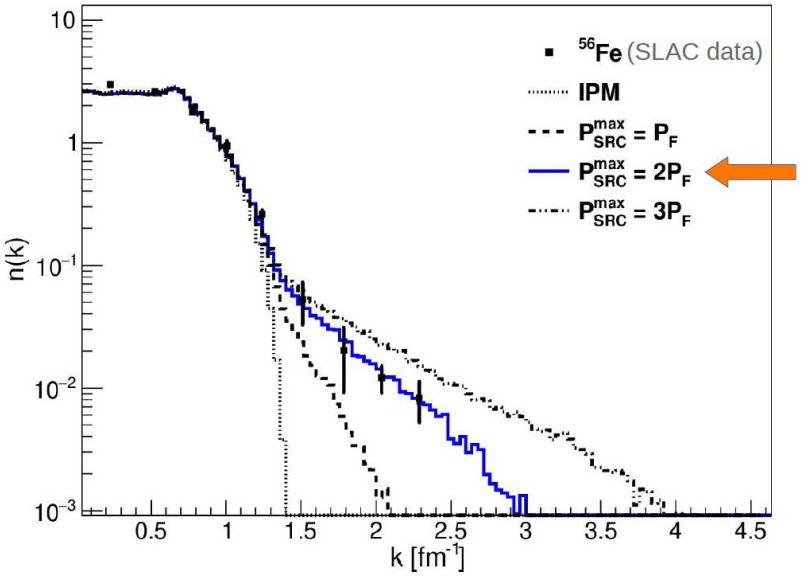

Figure 7.4: Constraints for the ”extra momentum” generated by the SRCs.

neutrons was studied as a function of the neutron excess N/Z. In this way, they could directly compare the results of the INCL simulations with existing data delivered by CLAS [32]. The CLAS data have been collected in inclusive electron scattering experiments on various nuclei (various neutron excess values), such as C (N/Z=1), Al (N/Z=1.1), Fe (N/Z=1.15), and Pb (N/Z=1.5). In these measurements, two distinct momentum regions have been investigated: the low-momentum region (below the Fermi momentum), where nucleons primarily experience the mean field, and the high-momentum region, where nucleons participate in SRC pairs. Reduced cross-section ratios (e,e'n)/(e,e'p) for both regions have been obtained, see Fig.7.5. Notably, it has been observed that the low-momentum reduced cross section increases with the N/Z ratio. This is consistent with a single particle behavior. However, the high-

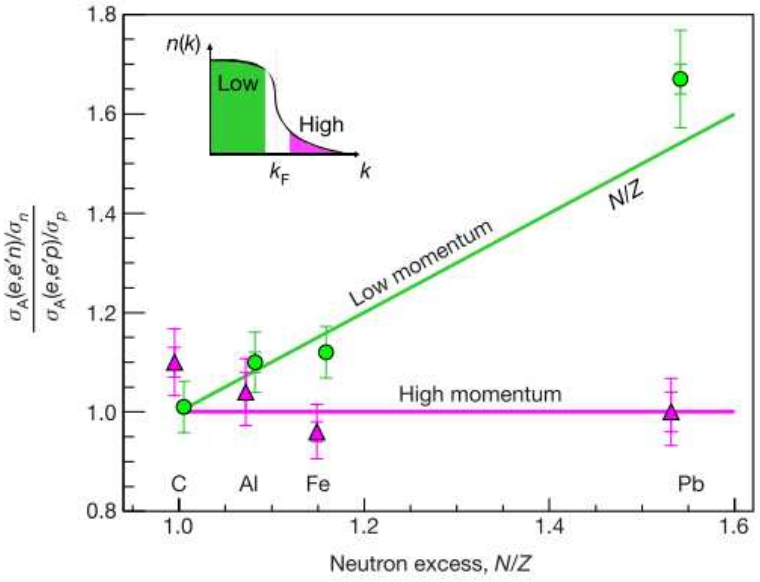

Figure 7.5: Evolution of the fraction of high and low momentum neutrons to protons with the neutron excess. Taken from [32]

momentum reduced cross section remains constant at 1 for all studied nuclei. This finding suggests that there is an equal number of high-initial-momentum protons and high-initial-momentum neutrons, implying that SRC pairs mainly consist of np pairs, as it was explained in Sec. 7.1 . This observation aligns also with previous work by [121].

The constant high-momentum ratio leads to a greater number of low-initial-momentum neutrons compared to low-momentum protons as N/Z increases. Consequently, we see the increasing reduced cross section for the low momentum region in Fig. 7.5. This indicates a higher fraction of initial high-momentum protons, which was explored in Fig. 7.6. The figure displays the ratios of high-momentum to low-momentum for both protons and neutrons. As expected from previous results, the proton fraction should increase with the neutron excess. The neutron ratios were found to decrease only slightly. INCL++ assumptions/criteria for the treatment of the SRC pairs appear to be correct, as the simulations accurately reproduce the high-momentum proportions for both neutrons and protons.

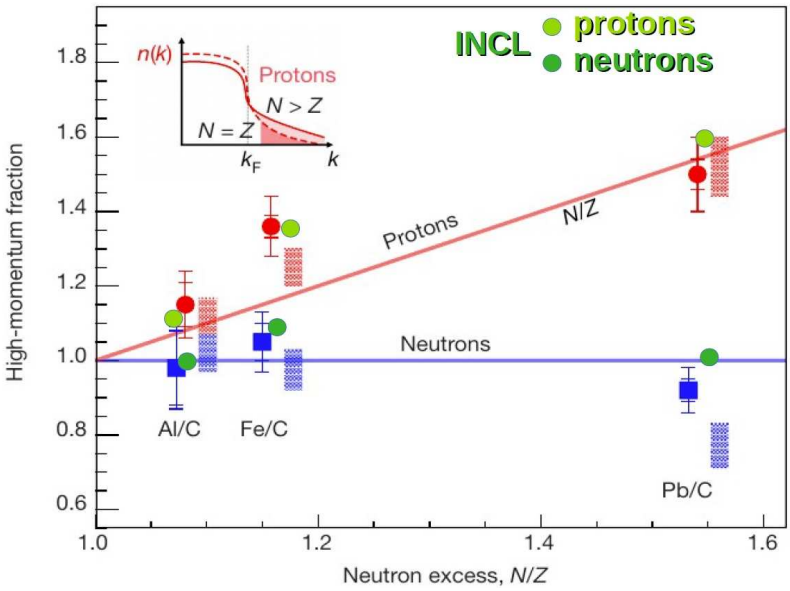

Figure 7.6: Evolution of the fraction of high to low momentum protons and neutrons with the neutron excess (N/Z).

We tried to understand the observed trend using simple assumptions: If there are mostly pn SRC pairs, and assuming a constant proportion *x* of nucleons that are in SRCs pairs, the number of protons H_p and neutrons H_n in the high momentum region can be written:

$$H_p = H_n = \frac{x}{2}A = cA,$$

where A is the mass number ($A = N + Z$) and c = x/2. Therefore,

$$H_n/H_p = 1.$$

On the other hand, the number of low momenta neutrons (L_n) and protons (L_p) are given by

$$L_n = N - cA$$

and

$$L_p = Z - cA,$$

then

$$\frac{L_n}{L_p} = \frac{N - H_n}{Z - H_p} = \frac{N - cA}{Z - cA} \approx \frac{N}{Z}$$

This is in agreement with Fig. 7.5. We can also deduce the ratios between the numbers of low and high momentum protons for a nucleus of atomic mass A:

$$(H_p/L_p)_A = \frac{cA}{Z - cA} = c\frac{1 + N/Z}{1 - c(1 + N/Z)},$$

which is an increasing function of N/Z and for neutrons:

$$(H_n/L_n)_A = \frac{cA}{N - cA} = c\frac{1 + N/Z}{N/Z - c(1 + N/Z)},$$

and for ^{12}C:

$$(H_p/L_p)_{^{12}C} = (H_n/L_n)_{^{12}C} = \frac{2c}{1 - 2c}.$$

So, the double ratios write:

$$\frac{(H_p/L_p)_A}{(H_p/L_p)_C} = \frac{1 - 2c}{2}\frac{1 + N/Z}{1 - c(1 + N/Z)}, \tag{7.3}$$

which is increasing as a function of N/Z.

$$\frac{(H_n/L_n)_A}{(H_n/L_n)_C} = \frac{1 - 2c}{2}\frac{1 + N/Z}{N/Z - c(1 + N/Z)}, \tag{7.4}$$

which is slightly decreasing as a function of N/Z.

Fig.7.7 illustrates the proton and pion momentum correlation in INCL++ for the pnπ^-channel in the full solid angle. In the left plot, all events are shown, while in the right plot, only pure quasi-elastic events due to a (pn) SRC pair are selected. More precisely, we select events with both the *number of collisions* and the *number of SRC collisions*, both equal to 1. The small contribution with a proton and pion correlation momenta characteristic to the quasi-elastic process (Sec. 6.3) is clearly due to reactions on a nucleon in a SRC pair.

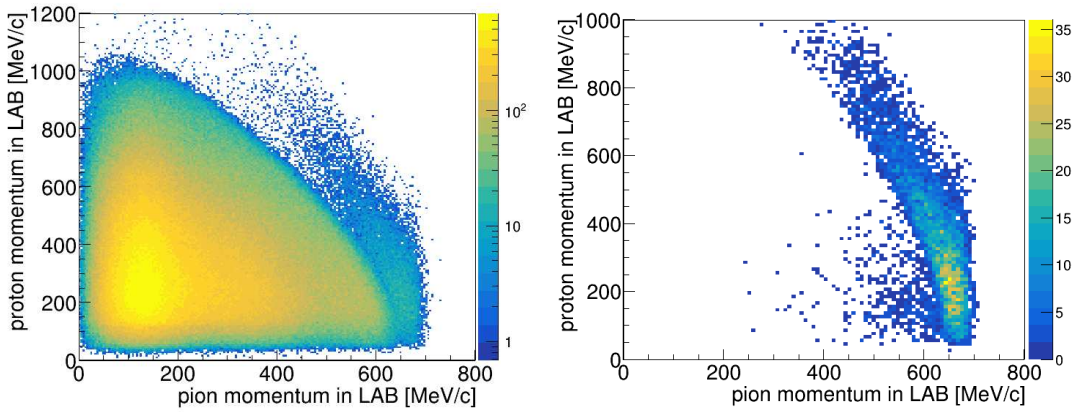

Figure 7.7: Correlation between the proton and pion momentum for the ^{12}C(π^-, π^-pn) reaction simulated with the INCL+SRC cascade model at 0.7 GeV/c. Left panel: all the simulated events. Right panel: the simulated events but with conditions on the *number of collisions* and the *number of SRC collisions*, both equal to 1.

7.2 Missing momentum distribution

In our case we consider quasi-elastic scattering of π^- on proton inside the ^{12}C nucleus. In a pure quasi-elastic scenario, where no additional scatterings occur, the momentum of the proton can be calculated as a difference in momentum between the initial and final states of the $\pi^- + p \rightarrow \pi^- + p$ reaction, see Eq. 6.16. Fig. 7.8 shows this missing momentum distribution measured in the HADES experiment. The straight line represents the Fermi momentum of the proton in the carbon target, as determined by Moniz in their study [23] utilizing the Stanford Mark III linear electron accelerator (k_F=221$\pm$5 MeV/c). This research employed quasi-elastic electron scattering on various nuclear targets, including the carbon one, and comparison to Moniz's Fermi gas model calculations [131]. It can be noticed that the distribution in Fig. 7.8 is characterized by a long tail extending beyond the Fermi momentum. The origin of this tail can have two sources: rescattering effects, which are not fully suppressed by our

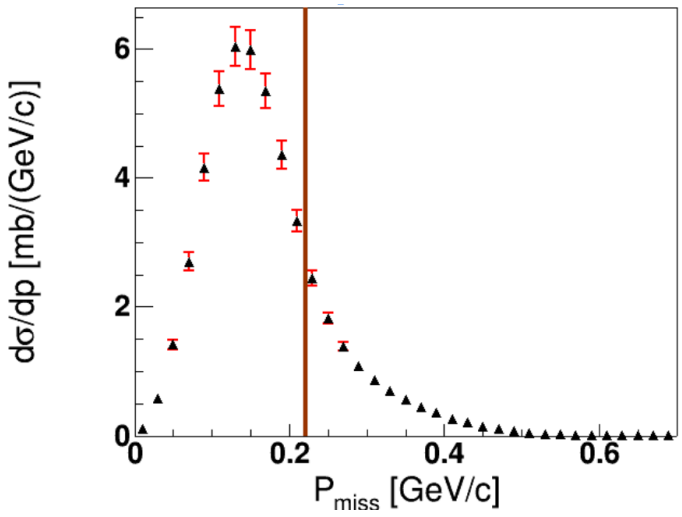

Figure 7.8: Experimental distribution of the missing momentum of the quasi-elastic pπ^-. The brown line represents the Fermi momentum value (221 MeV/c) which is taken from [23].

event selection, or short-range correlations (SRCs) explained in detail in Sec. 7.1. But it is also important to consider the resolution effect, also they are in principle taken into account in the simulations. Fig.7.9 shows the resolution of the missing momentum which was obtained in INCL++ simulations as a difference between the P_{miss} calculated using the momenta as generated by INCL++ code, and the one calculated using the reconstructed momenta (see Sec. 5.2). To study SRC it is very important to minimize effects of re-interactions, FSI, or resonance excitation,

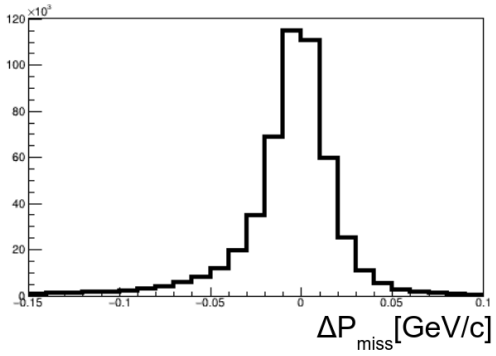

Figure 7.9: P_{miss} resolution derived from INCL++ simulations.

which contribute with various strength at various momentum transfer and the phase-space regions. These effects can be studied using e.g. GCF calculations. In our case we have used the basic INCL++ cascade model to study the rescattering effects at pion beam momentum of 0.7 GeV/c due to the fact that the GCF calculations have not been provided and available for us for the pion beam. This was a very important step to define the kinematical conditions and cuts to suppress the re-interaction effects.

Before comparing the data with INCL simulations including SRCs, we show in Fig. 7.10 a comparison of the P_{miss} distribution with all models used in Chapter 6. This is the same figure as Fig. 6.17, but with a logarithmic y-axis. One can observe that RQMD.RMF and SMASH predict a large tail above the Fermi momentum for this distribution, close to the data, but the analysis of the ppπ^- events has demonstrated that they considerably overestimated the rescattering effects following the quasi-elastic process (see Sec. 6.5.5). Therefore, we consider that we cannot rely

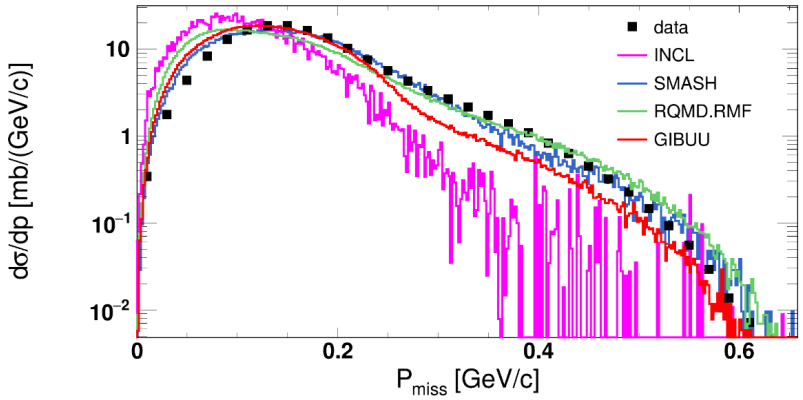

Figure 7.10: Missing momentum for the quasi-elastic pπ^-channel. Simulations are normalized to the same area as the data. The distribution is represented in the logarithmic scale for the y-axis.

on these models for the description of the quasi-elastic channel. On the other hand, INCL and GIBUU, which have a better description of these processes underpredict the yields above 300 MeV/c. This gives us some justification to investigate a dedicated study of the quasi-elastic process with the INCL++ version including SRCs. (GIBUU does not have such an option).

7.3 Minimization of rescattering effects

To test the sensitivity of our data to SRCs, it is necessary to minimize the impact of rescattering effects as much as possible in order to clearly select the SRC pairs. Achieving this separation without cleaning the presence of SRCs, if they exist, presents a challenging task. To address this challenge, we have used the INCL++ model, which allows us to explore various process options.

In Figs. 7.11 and 7.12, we investigate the missing mass and missing momentum distributions for π^-p events simulated with the INCL++ model. For the results presented in this subsection, we use the INCL++ version without implementation of the SRC. The blue curves show events wherein the first collision is elastic, and no further collisions occur (labeled as recoiling ^{11}B*). In this case, the missing mass is peaked close to the ^{11}B mass and the missing momentum does not extend much above p_F. The orange area shows events corresponding also to a first elastic collision, but with a further collision. In this case, the distributions are much broader and extend to much higher missing mass and missing momentum values. However, when comparing to the distributions for all π^-p events, we can conclude that most of the events at high missing masses and high missing momenta are due to a first inelastic collision. We also show the distributions obtained after applying our *QE experimental cut* (see Sec. 6.3). We can conclude that this cut suppresses only partly the rescatterings after a first elastic collision. Our experimental cut includes these rescattering effects until a missing mass of approximately 10.4 GeV/c. These rescattering effects

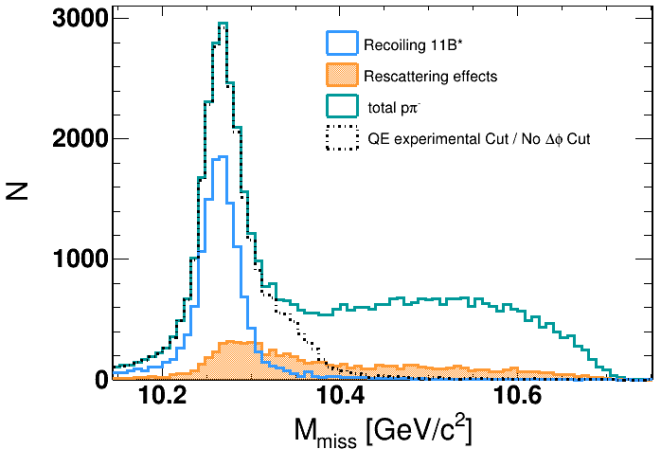

Figure 7.11: Missing mass distribution for the quasi-elastic graphical cut of the pπ^- events compared to total, pure quasi-elastic, and rescattering events in INCL++.

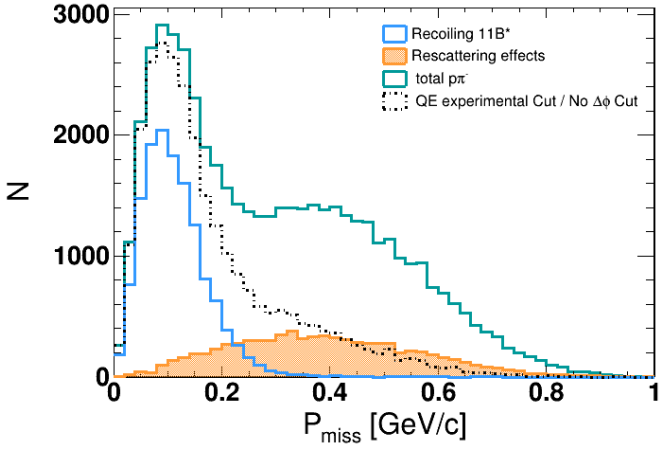

Figure 7.12: Missing momentum distribution for the quasi-elastic graphical cut of the pπ^- events compared to total, pure quasi-elastic, and rescattering events in INCL++.

account for the high missing mass values but are also present in low missing mass values.

The presence of these rescattering effects in low missing mass values, which should ideally correspond to pure quasi-elastic events only, makes it challenging to completely suppress these rescattering effects by applying a cut on the missing mass. For this, we investigated the pion and proton momenta which are presented in Figs. 7.13 and 7.14. In Fig.7.13 we present the missing mass distribution as a function of different proton momentum bins. The goal is to minimize the impact of rescattering effects and establish a selection that ensures that all events are primarily attributed to the pure quasi-elastic process. The plot reveals that at higher proton momenta, the quasi-elastic process is nearly suppressed, and instead, inelastic channels become dominant. However, at very low proton momenta, the total events tend to converge towards the pure quasi-elastic process, but rescattering effects seem to be present in all proton momentum bins. In pion momenta bins shown in Fig. 7.14 we see that the faster the pion

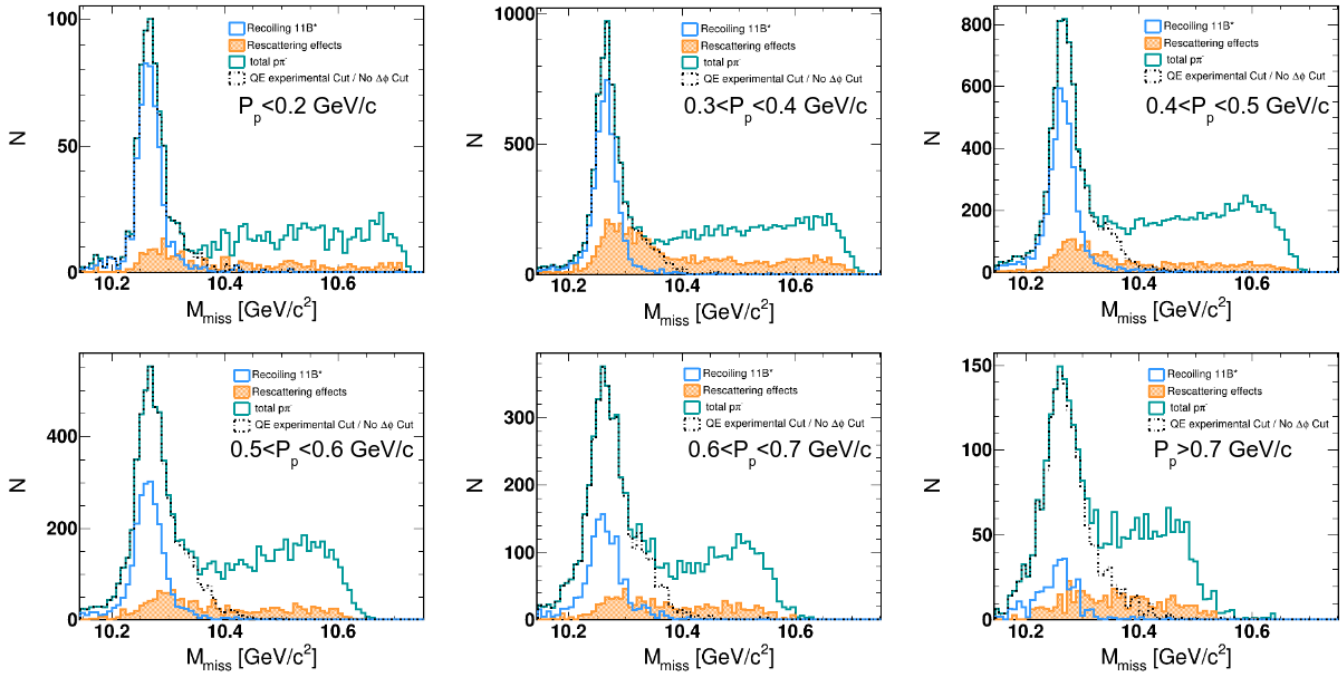

Figure 7.13: Same as Fig.7.11 but in different bins in the proton momentum.

is, the lower the rescattering effects are.

When the pion momentum exceeds 600 MeV/c, we achieve significant suppression of both rescattering effects and inelastic events, and total events converge towards a pure quasi-elastic process.

We used that pion momentum bin (with momenta exceeding 600 MeV/c) as a reference point in our experimental analysis, primarily aiming to selectively isolate the quasi-elastic process. In this regard, we compared the data obtained from the HADES experiment with INCL++ simulations. This comparison is effectively depicted in Figs. 7.15 and 7.16. To ensure consistency, the data has been scaled to match the area of the INCL++ experimental cut spectra.

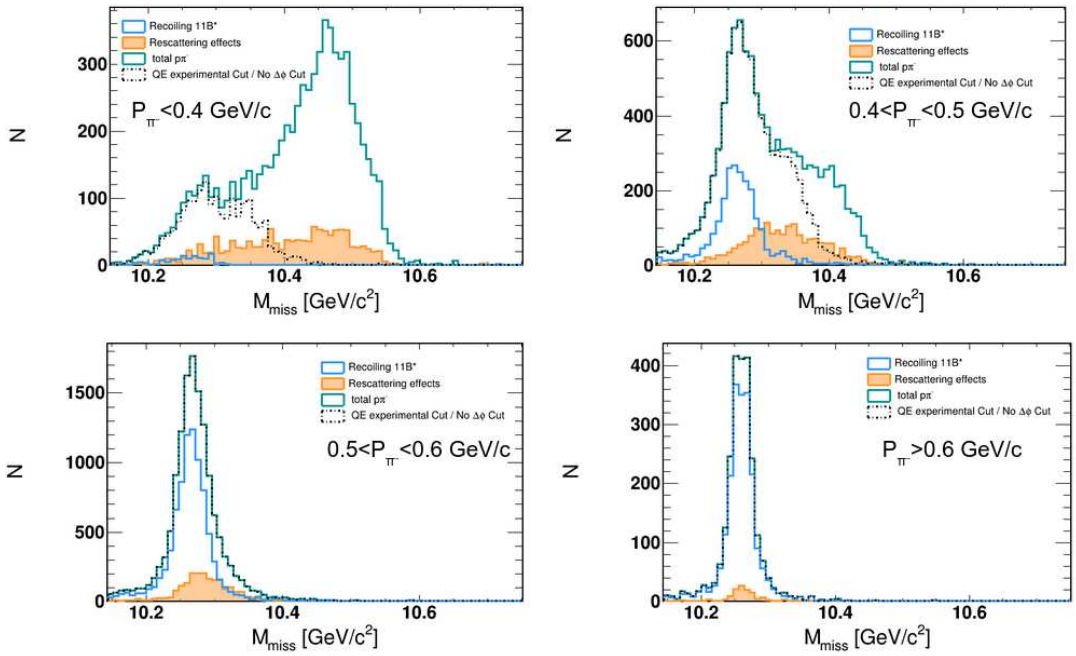

Figure 7.14: Same as Fig.7.11 but in different bins of pion momentum.

The first plot shows a slight difference in the tail region between the HADES data points (represented by stars) and the INCL++ simulated results (dotted line). The use of a logarithmic Y-axis scale (logY) allows for a clear and comprehensive comparison of all spectra. The spectrum marked in blue represents the pure quasi-elastic process selected with INCL++, extending beyond the Fermi momentum value. This extended region, beyond the expectations, is attributed to the presence of proton potentials within the nucleus, which modify its momentum and therefore affects the missing momentum (as detailed in Eq. 6.17).

Notably, the influence of rescatterings appears to be largely constrained. When focusing on rescatterings belonging above the Fermi momentum, it becomes evident that they contribute to the tail of the overall $p\pi^-$ event

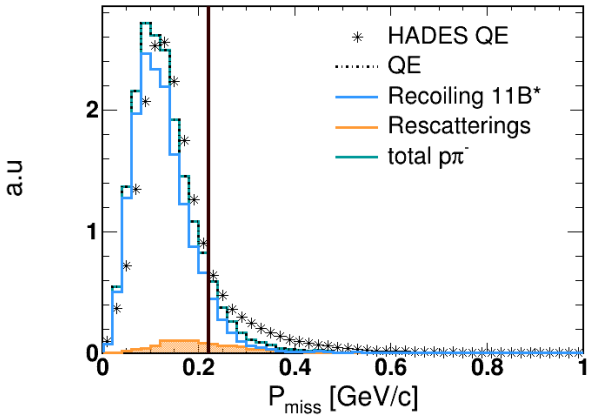

Figure 7.15: The missing momentum distribution for $P_{\pi-} > 600$ MeV/c. The different selections of $p\pi^-$ events in INCL++ are compared to the experimental data. QE means using the graphical cut shown in Fig.6.13.

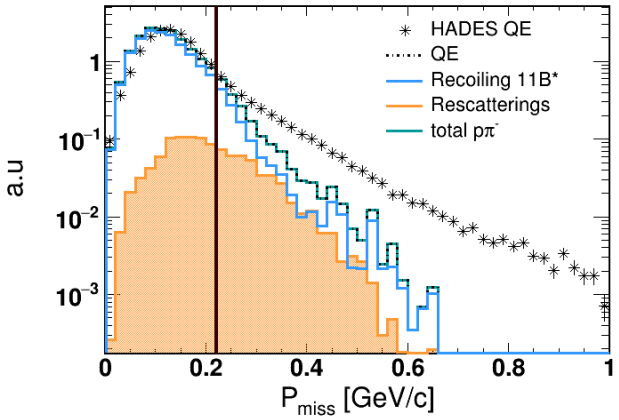

Figure 7.16: Same as Fig.7.15, but using a logarithmic scale in the y-axis.

spectrum, in addition to the tail originating from the pure quasi-elastic process. We expect the presence of both effects in the data's tail. However, in comparison to the INCL++ simulations, the tail in the data surpasses that of INCL++, suggesting the likelihood of short-range correlations in the data. This aspect was subsequently explored in section 7.1.5.

7.4 Comparison with INCL++ including SRC effects

In the next step we have investigated the distribution of the missing momentum with and without SRC included, see Fig. 7.17. The results of this comparison revealed an intriguing observation when looking at the tail of the missing momentum distribution. The INCL+SRC simulations reproduce the experimental data satisfactorily well above 0.5 GeV/c, while the calculations without the SRC included fail. This suggests the possible existence of SRCs. However, in the momentum range between the Fermi momentum and 0.5 GeV/c both predictions fail. This could be due to an underestimation of potential or rescattering effects in INCL++. However, we are also surprised by the shape of the P_{miss} distribution in the INCL++ predictions including SRC effects. We were expecting a continuous tail as in Fig. 7.17.

We can also notice that the effects of SRCs is very small. The implementation of SRCs in INCL++ is based on experimental data reporting that 20% of the nucleons in a nucleus belong to SRC pairs (Sec. 7.1.3), while the effect observed in Fig. 7.4 is much smaller.

One explanation of such a small contribution of SRC pairs in our π^-+p quasi-elastic scattering events is that, as mentioned in Sec. 6.3.3, they are mostly produced from reactions occurring at the surface. This means that the average density probed by such reactions selected by our analysis is smaller than the average nucleus density. As the SRC probability is related to the density in the nucleus, one can expect that SRCs are suppressed.

We can indeed write:

- **Probability of Finding a Nucleon in Volume dV:** $P_{nucleon} = \frac{\rho(r)dV}{A}$ where: $\rho(r)$ is the nucleon density, dV = r^2 dr dcos(θ) dϕ, and A is the number of nucleons.
- **Probability of having a nucleon close enough to form an SRC pair in the volume dV:** $P_{NN} = \frac{\rho(r)}{A} V_{correl}$ where $V_{correl} = \frac{4}{3}\pi d_{max}^3$ is the correlation volume and d_{max} is the maximum distance for the correlation.
- **Probability of having an SRC pair in the small volume dV** $P_{SRC} = P_{nucleon} * P_{NN} = (\frac{\rho(r)}{A})^2 \, V_{correl} \, dV$
- **Integration Over Angles:** $\int P_{SRC} \, dV = (\frac{\rho(r)}{A})^2 \, V_{correl} * 4\pi * r^2$

Therefore, the probability of having an SRC is proportional to $r^2 * \rho(r)^2$, while the probability of having a "mean field" nucleon is proportional to $r^2 * \rho(r)$. It is clear that SRCs are suppressed at lower densities, $e.g.$, at the nucleus

surface.

7.5 Search of SRC in ppπ^- events

In the next step we have searched for possible SRC effects in the analysis of triple coincidences in the ^{12}C(π^-, π^-pp) reaction. As it was investigated in the previous experiments (see Sec. 7.1) the short-range *np* pairs dominate over *pp* pairs with a ratio np/pp $\sim$ 20 [132], however the neutron detection in HADES is very difficult and challenging. Therefore, we have chosen the $pp\pi^-$ channel over the $pn\pi^-$ channel. By doing this study, we can also learn about the rescatterings effects in the three particle channel. The $pp\pi^-$ final state can be produced in two scenarios. In the first scenario both protons form a SRC pair and the π^- interacts with one of them, which results in the simultaneous emission of the two protons from the nucleus by the breaking of this pair and a ^{10}Be fragment produced, see Fig. 7.18. In the second scenario, the two protons do not belong to the SRC pair and the π^- interacts with one

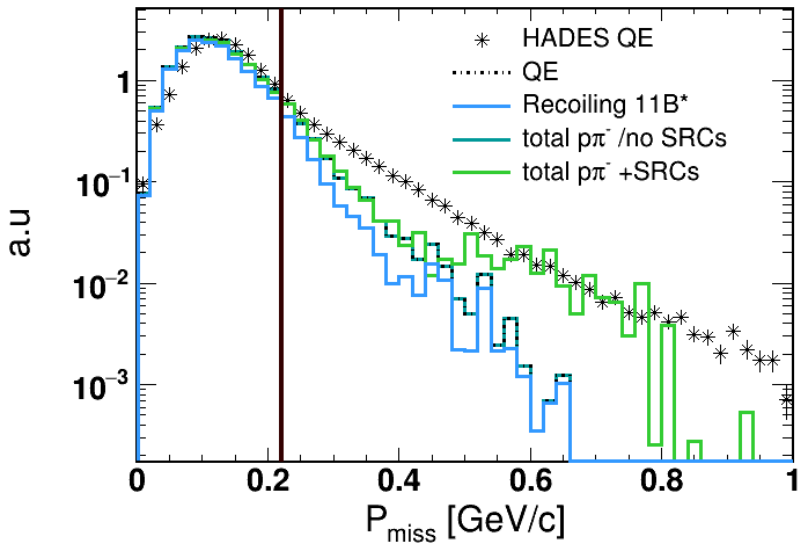

Figure 7.17: The missing momentum distribution for $P_{\pi-} > 600$ MeV/c compared between INCL++ simulations with/without SRCs with data.

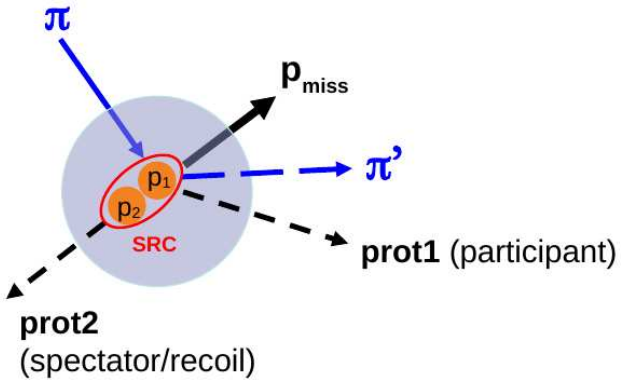

Figure 7.18: Schematic drawing of the two proton knockout A(π, $\pi^{'}$pp) reaction, within the SRC model.

of them, and subsequently, either the pion or the proton undergoes a rescattering with the other proton etc. This process is referred to as a *sequential emission*. The INCL++ model which is used by us to study the rescattering and SRC effects does not have yet implemented the short-range-correlated *pp* pairs. Only short range correlated *pn* pairs are taken into account, as it was already explained in Sec. 7.1.5. Therefore, events in the $pp\pi^-$ channel can only be produced in a sequential emission in INCL++.

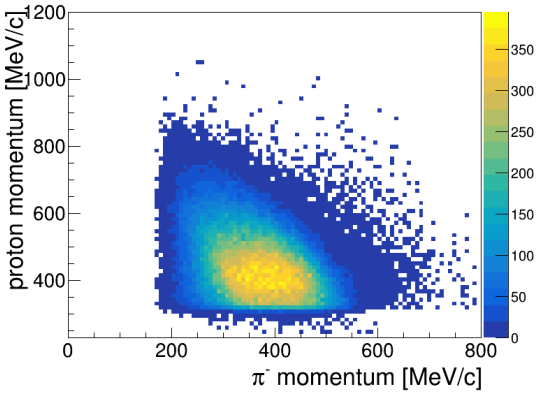

Figure 7.19: Correlation between the proton and pion momentum in the experimental data for the ^{12}C(π^-, π^-pp) reaction at 0.7 GeV/c. The correlations are plotted after deciding on which proton is a participant one and which is a spectator one.

7.5.1 Selection of events

In the case of quasi-elastic scattering on a proton in a (pp) pair, we expect the participant proton to be correlated to the pion, according to the quasi-elastic scattering kinematics (see Fig.7.7). Due to the fact that both protons are indistinguishable particles we need to decide which of them is a spectator proton and which is a participant one in the reaction. Therefore we calculate the relative $\Delta\varphi = |\varphi_{\pi^-} - \varphi_{prot}|$ azimuthal angle between the "first" proton and π^- and same for the "second" proton. The participant proton, with momentum p_{part} is the one which is closer to fulfill the coplanarity condition ($\Delta\varphi \sim 180°$). However, the experimental distributions, shown in Fig. 7.19 do not show any hint of quasi-elastic correlation. Nevertheless, we still investigate events in this region, by applying a selection similar to the one in Fig. 6.13 . The final step is to suppress the rescattering effects to have the cleanest data sample. This is accomplished by imposing a constraint on the pion momentum, which was explained in Sec. 7.3. We have used the condition $P_{\pi^-} > 500\ MeV/c$ instead of $600\ MeV/c$ due to a lack of statistics in this momentum range in the $pp\pi^-$ channel.

7.5.2 Comparison with INCL++ simulations including SRC

As explained above, in the case of scattering on a proton in a pp SRC pair, we expect a recoiling system with a mass close to ^{10}B. Indeed, the experimental distribution of the missing mass $MM(pp\pi^-)$ of the $\pi^- + ^{12}C \rightarrow \pi^- + p + p + X$ process, which is shown in Fig. 7.20 is consistent with a missing $^{10}_{4}$Be fragment ($m_{^{10}_{4}Be} = 9325.6$ MeV/c^2). However,

the INCL++ predictions, where no SRC is present have a very similar shape. In Fig. 7.20, left plot the normalized distributions are presented, while in Fig. 7.20, right plot both spectra are scaled to their area to compare their shapes. This is due to the fact that we select high pion momenta, close to the kinematical limit for the π^-+ ^{12}C $\rightarrow \pi^- pp\ ^{10}$B. Although we did not check that explicitly, it means that our selection keeps only events in INCL++ corresponding to two and only two collisions. In this case, sequential events cannot be distinguished from simultaneous emission, by the missing mass, as the recoiling system is ^{10}B in both cases. As noticed in Sec. 6.5.5, the yield predicted by the INCL++ simulations is too low in comparison to the data. This could be interpreted as a sign of (pp) SRC, but, one would have then to investigate the model dependence of the INCL prediction. INCL++ indeed gives one of the overall best descriptions of the quasi-elastic process, but this description is not perfect.

In analogy to Eq.(6.16), we can use the momentum $\vec{p}_{part}$ of the participant proton to calculate the missing momentum:

$$\vec{P}^{\pi^- p}_{\text{miss}} = \vec{p}_{part} + \vec{p}_{\pi} - \vec{p}_{\text{beam}}. \tag{7.5}$$

The corresponding distribution is shown in Fig. 7.21. It is peaked at values well above the Fermi momentum and extends up to 600 MeV/c. This is the region where SRC are expected to contribute. But, just like the missing mass distributions, the missing momentum distributions are very similar for data and INCL++ simulations. In the absence of simulations including pp SRC, it is difficult to tell what are the expectations for the $p^{\pi^- p}_{miss}$ distributions from SRC under these particular conditions. However, an important information is that the sequential emission process can produce high missing momenta.

Therefore, we can conclude that there is no clear signal indicating the presence of pp-SRC in the data.

Angular correlation between missing and spectator momenta

In the SRC picture, the quasi-free process takes place with a participant nucleon in the SRC pair, which has an initial momentum $\vec{p_N}$, and the spectator proton has a momentum:

$$\vec{p}_{spec} = -\vec{p}_N = -\vec{p}_{miss}. \tag{7.6}$$

This means that in the SRC picture, we expect the angle between $\vec{p}_{spec}$ and $\vec{p}_{miss}$ to be close to 180° (see Fig. 7.18). Such a back-to-back correlation was investigated in particular in the recent experiment studying SRCs, using the scattering of 48 GeV/c ^{12}C ions from hydrogen at Joint Institute for Nuclear Research (JINR) [33]. Fig. 7.22 shows the result which refers to the momentum of the participant proton and the reconstructed undetected recoil neutron momentum in the ^{12}C(p, 2p)^{10}B reaction. The plot displays a clear back-to-back correlation, which aligns with expectations for strongly correlated pairs of the two nucleons. Notably, these results are in good agreement with the predictions derived from the GCF calculations (see Sec. 7.1.4) [130, 34].

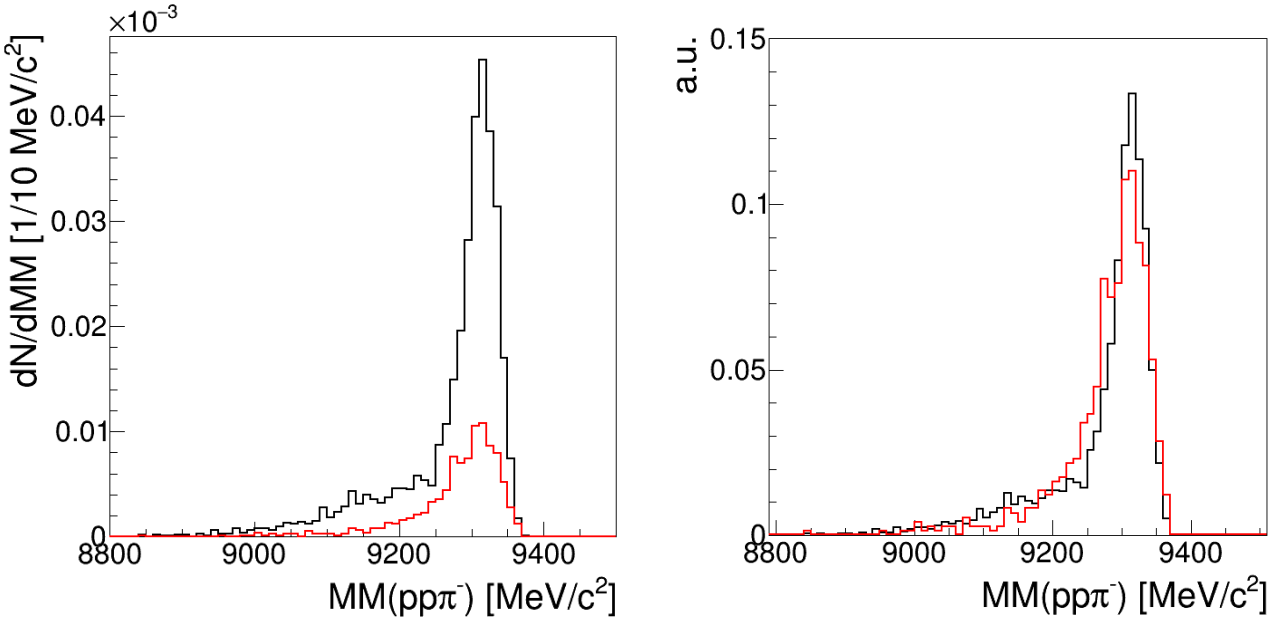

Figure 7.20: Missing mass distributions obtained for the ^{12}C(π^-, π^-pp) reaction from the data (black line) and the INCL++ simulations (red line). Left plot presents normalized yields and the right plot shows arbitrary normalized distributions to compare their shapes.

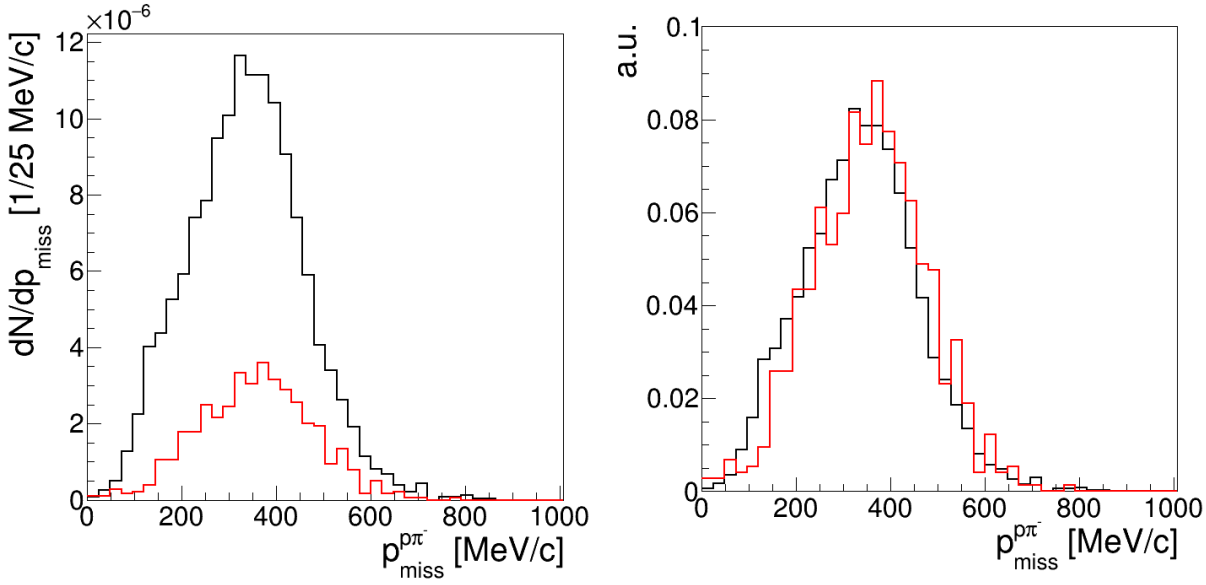

Figure 7.21: Missing momentum distributions obtained for the ^{12}C(π^-, π^-pp) reaction from the data (black line) and the INCL++ simulations (red line). Left plot presents normalized yields and the right plot shows arbitrary normalized distributions to compare their shapes.

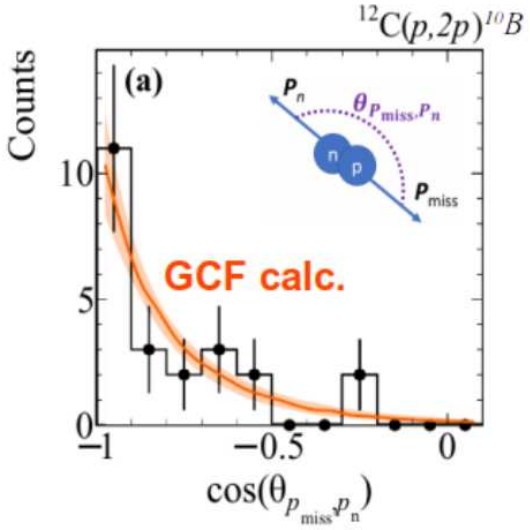

Figure 7.22: Distribution of the cosine of the angle between the recoil nucleon and missing momentum. Data measured by the BM@N collaboration for ^{12}C(p,pp)^{10}B reaction at 48 GeV/c of the ^{12}C beam are compared to GCF predictions (orange line) [33, 34].

Motivated by this study, we investigated this angular correlation in the case of the analysis of the ppπ^- in our experiment, as described above. In Fig. 7.23 the distributions of the cosine of the angle between $\vec{p}_{miss}$ and p$_{spec}$ for missing momenta $p^{\pi^- p}_{miss} \geq 300$ MeV/c are presented. A clear back-to-back correlation is visible, as expected for the correlated nucleon pairs. However, such a peaking is also observed in simulations with the INCL++ code where no SRCs are present. To understand this, we notice that such a back-to-back peaking would be naturally realized by momentum conservation in the case of a π^-+d reaction. This deuterium-like behavior is then also expected, both

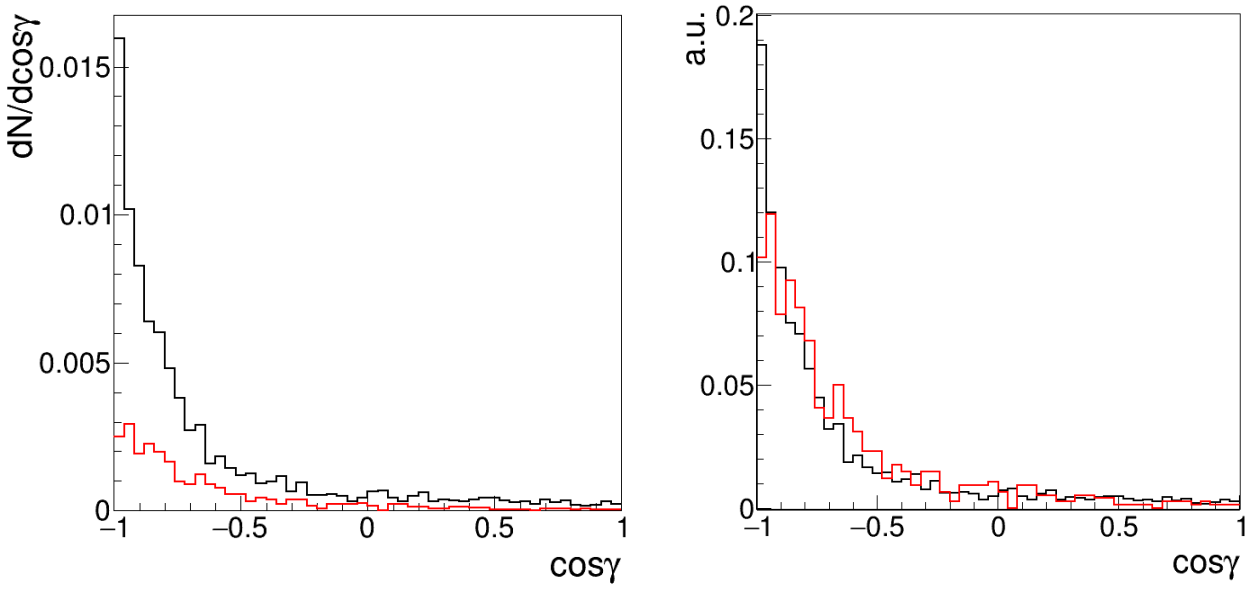

Figure 7.23: Distributions of cosine of the angle γ between the missing momentum p_{miss} and the momentum of the recoil proton p_{prot} for the ^{12}C(π^-, π^-pp) reaction obtained from the data (black line) and the INCL++ simulations (red line). Left plot presents normalized yields and the right plot shows arbitrary normalized distributions to compare their shapes.

in the case of a SRC pair moving with a low momentum in the carbon nucleus and in the case of two sequential reactions on two nucleons, with a momentum inside the Fermi sphere, leaving the nucleus with an even smaller (in average) momentum. So, this peaked distribution does not really allow to disentangle SRC form to the sequential emission of two nucleons.

To get more solid conclusions about the existence of pp-SRC in the HADES data we would need more reliable calculations based on the GCF contact formalism as well as pp-SRC implementation in the INCL cascade model.

Chapter 8

Conclusion and Outlook

8.1 Conclusion

The primary focus of HADES experiments lies in investigating the hot and dense phase produced in heavy-ion collisions at incident energies of a few GeV per nucleon, hence probing a similar region of the QCD phase diagram as neutron star mergers. In such collisions, the pion dynamics plays an essential role in the way energy is dissipated, via the coupling to baryon resonances, and finally in the way particles are produced. Pion-nucleus experiments are therefore needed to directly study such effects and validate models used for the description of heavy-ion collisions. The validation of these models with pion-nucleus data in different exclusive channels is crucial for hadronic matter studies, but also for neutrino physics, as the precise description of both nucleus-nucleus or neutrino-nucleus reactions strongly relies on pion-nucleon dynamics.

The pion beam at GSI offers a unique opportunity to directly study such effects for energies above the $\Delta(1232)$ resonance. It is a unique tool for hadronic structure and cold matter studies. The experiment realized in August 2014 aimed at investigating electromagnetic time like transition form factors and two-pion couplings in the second resonance region ($\sqrt{s} \sim$ 1.49 GeV/c) in the π^-+p reaction, using polyethylene and carbon targets. The analysis of measurements on the carbon target had been previously limited to the subtraction from the polyethylene data to access π^-+p interactions. The acquisition of a large dataset from $\pi^- +^{12} C$ scattering at 0.7 GeV/c led to a possible investigation of inclusive production, encompassing charged pions, hydrogen isotopes (protons, deuterons, tritons), as well as two- and three-particle coincident spectra, which were divided according to the exit channel topology$(1\pi^-, 1\pi^+, 1p, 2\pi^-, 2\pi^+, 2p, 3p...)$.

This PhD work was devoted to the analysis of all these channels and studied their description by transport models such as SMASH, RQMD.RMF, GiBUU, as well as the intranuclear cascade model INCL++. In these models,

the cross sections of elementary pion-nucleon or nucleon-nucleon reactions and the description of the nucleus, especially the spatial and momentum distributions of nucleons and the potential applied on each nucleon, play an important role in the dynamics of the reaction and particle production. In this energy range, rescatterings are limited, and the collision dynamics remain highly sensitive to the initial elastic or inelastic pion-nucleon interaction. Thus, the comparison of diverse observable distributions with the models predictions that we present allows for a selective testing of different processes (elastic scattering, pion production, rescattering, absorption).

The work presented in this PhD reveals significant disparities between the models. The RQMD.RMF model consistently overestimates yields, while the GIBUU model generally underestimates them, but still closer to data than RQMD.RMF and SMASH. The latter overestimates the distribution in the quasi-elastic region but performs well in reproducing yields in the p$\pi^-\pi^-$channel. SMASH and RQMD.RMF show an overestimation of the nucleon-nucleon scattering in the nucleus after a quasi-elastic step. INCL++ offers a better description than other models in most of inclusive and exclusive studied distributions, especially regarding pion production, but still has some limitations: at forward angles, it underestimates the $\pi^-$and protons in quasi-elastic peak and overestimates the π^+production. The test of the description of the quasi-elastic channels is, in particular, of the highest importance for the reconstruction of neutrino energy. Our analysis was however not sensitive to pion absorption, and further investigation, particularly with neutron detection, would be needed for a deeper insight into this process.

Among the examined reactions, the quasi-elastic process $\pi^- +^{12} C \rightarrow \pi^- + p + X$ is of particular interest. This reaction was selected based on the momentum correlation of the detected proton and π^-, in addition to the coplanarity condition. Having in hand data on quasi-elastic scattering, the natural question about SRC effects was raised. This gave us the opportunity to test the recent version of the INCL++ code including (pn) SRC pairs. In the region of very large missing momenta, the data are in agreement with the predictions of this updated model. We also looked for a possible signal of pp SRC pairs in the ppπ^-events, although the effects of (pp) SRC pairs are expected to be much smaller than the one of (pn) SRC pairs. We observed no signal of SRC in the analysis of ppπ^-events.

Some additional tasks were started but could not be finalized within the time of this work. We indeed made an attempt to add to the list, the analysis of pnπ^-, which is expected to be more sensitive to SRCs. For this, we investigated in simulations the response of the TOF detector to neutrons. The identification of neutrons was challenging, due to a large number of secondaries. We also developed a method to calibrate the pion beam energy, based on the elastic scattering on hydrogen impurities in the carbon target.

8.2 Outlook

Pion beam experiments are not ideal for SRC studies, as pions have a higher probability for elastic scattering on the surface, where SRCs are expected to be less prominent, rather than deep within the nucleus. In the upcoming future, the HADES collaboration plans to perform a dedicated measurement to study the short-range correlations using the high intensity proton beam at 4.5 GeV energy and various nuclear targets ^{12}C, ^{40,48}Ca, ^{56}Fe and ^{107}Ag [133]. Our improved understanding of short-range correlations will be beneficial for the analysis of these experiments.

Moreover, HADES will become a part of the CBM (Compressed Baryonic Matter) experiment at the FAIR facility. The main goal of this project is to study the QCD phase diagram and baryonic matter Equation of State in the region of high net-baryon densities. Therefore the extension of the current data base for pion-nucleus interactions is very crucial for the validation of the microscopic transport models used to describe heavy-ion collisions. Pion-nucleus data are very useful to validate hadronic models used in GEANT4, like INCL++, which is a guiding idea of this thesis. Moreover, the precision of many measurements, especially the ones connected to the neutrino oscillations (Super Kamiokande and in the future Hyper Kamiokande or the DUNE project) is limited by the uncertainties on pion-nucleus interactions.

In the near future, an experiment with the secondary pion beam is planned to explore the third resonance region around $\sqrt{s} = 1.7$ GeV. By using the same type of analysis as presented in this PhD, new data on inclusive and exclusive proton and pion production will be obtained. This will complete the very poor data base for pion-nucleus reaction. In addition, it will allow for a comparison of data to transport and cascade model predictions in an energy range relevant for heavy-ion experiments at a few AGeV.

Our results reveal certain discrepancies in the model ability to accurately describe the data. It is our hope that these failures in the models for describing the different processes inside the nucleus will be considered by experts in model development to enhance their performance.

This work has also led to many discussions with experts in models, SRCs, and neutrino physics. In particular, it opened up possibilities for future collaborations to use HADES data in pion-induced reactions to test models useful for neutrino physics.

Bibliography

[1] T. Galatyuk, P. M. Hohler, Ralf R., F. Seck, and J. Stroth. Thermal dileptons from Coarse-Grained transport as fireball probes at SIS energies. *Eur. Phys. J.*, A52(5):131, 2016.

[2] J. Adamczewski-Musch et al. Probing dense baryon-rich matter with virtual photons. *Nature Phys.*, 15(10):1040–1045, 2019.

[3] R. Rapp and J. Wambach. Chiral symmetry restoration and dileptons in relativistic heavy ion collisions. *Adv. Nucl. Phys.*, 25:1, 2000.

[4] Janus Weil, Hendrik van Hees, and Ulrich Mosel. Dilepton production in proton-induced reactions at SIS energies with the GiBUU transport model. *Eur. Phys. J.*, A48:111, 2012.

[5] J. Adamczewski-Musch et al. Charged-pion production in $\mathbf{Au} + \mathbf{Au}$ collisions at $\sqrt{\mathbf{s_{NN}}} = 2.4\ \mathbf{GeV}$: HADES Collaboration. *Eur. Phys. J. A*, 56(10):259, 2020.

[6] R. Abou Yassine et al. Production of hydrogen isotopes and charged pions in p (3.5 GeV) + Nb93 reactions. *Phys. Rev. C*, 108(6):064902, 2023.

[7] R. Abou Yassine et al. Hadron production and propagation in pion-induced reactions on nuclei. *arXiv:2301.03940 [nucl-ex]*, 2023.

[8] J. D. Zumbro, C. L. Morris, J. A. McGill, S. J. Seestrom, R. M. Whitton, C. M. Edwards, A. L. Williams, M. R. Braunstein, M. D. Kohler, B. J. Kriss, S. Høibråten, R. J. Peterson, J. Ouyang, J. E. Wise, and W. R. Gibbs. Inclusive scattering of 500-mev pions from carbon. *Phys. Rev. Lett.*, 71:1796–1799, Sep 1993.

[9] H. Lenske V. Shklyar and U. Mosel. 2π production in the Giessen coupled-channel model. *Phys. Rev. C*, 93(4):045206, 2016.

[10] Daniel R. Marlow et al. Pion Scattering From C and Ca at 800-MeV/c. *Phys. Rev.*, C30:1662, 1984.

[11] CNS Data Analysis Center, SAID Home Page. http://gwdac.phys.gwu.edu/.

[12] I. G. Alekseev et al. High-precision measurements of πp elastic differential cross sections in the second resonance region. *Phys. Rev. C*, 91(2):025205, 2015.

[13] J. Adamczewski-Musch et al. Two-Pion production in the second resonance region in $\pi^- p$ collisions with HADES. *Phys. Rev.*, C102(2):024001, 2020.

[14] R. A. Burnstein, G. R. Charlton, T. B. Day, G. Quareni, A. Quareni-Vignudelli, G. B. Yodh, and I. Nadelhaft. pi–p Interactions at 683 MeV/c. *Phys. Rev.*, 137:B1044–B1052, 1965.

[15] A. D. Brody et al. Experimental results on the reactions $\pi^- p \to \pi\pi N$ in the center-of-mass energy range 1400-MeV to 2000-Mev. *Phys. Rev.*, D4:2693, 1971. [Erratum: Phys. Rev.D5,2899(1972)].

[16] S. Prakhov et al. Measurement of $\pi^- p \to \pi^0\pi^0$ n from threshold to 750-MeV/c. *Phys.Rev.*, C69:045202, 2004.

[17] L.Chlad. *Study of transverse flow of kaons in Au+Au collisions at 1.23A GeV*. PhD thesis, Faculty of mathematics and physics Charles University Prague, Charles U., Prague (main), 2021.

[18] J. Adamczewski-Musch. A facility for pion-induced nuclear reaction studies with hades. *Eur. Phys. J.*, A53(9):188, 2017.

[19] R. Lalik et al. Cerberos — beam detector for pion experiments at gsi. In *2013 IEEE Nuclear Science Symposium and Medical Imaging Conference (2013 NSS/MIC)*, pages 1–6, 2013.

[20] G. Agakishiev et al. The High-Acceptance Dielectron Spectrometer HADES. *Eur. Phys. J. A*, 41:243–277, 2009.

[21] J. Weil et al. Particle production and equilibrium properties within a new hadron transport approach for heavy-ion collisions. *Phys. Rev. C*, 94(5):054905, 2016.

[22] O. Benhar, S. Fantoni, and G. I. Lykasov. Backward hadron production in neutrino nucleus interactions. *Eur. Phys. J. A*, 7:415–419, 2000.

[23] E. J. Moniz, I. Sick, R. R. Whitney, J. R. Ficenec, Robert D. Kephart, and W. P. Trower. Nuclear Fermi momenta from quasielastic electron scattering. *Phys. Rev. Lett.*, 26:445–448, 1971.

[24] T. Leitner, O. Buss, L. Alvarez-Ruso, and U. Mosel. Electron- and neutrino-nucleus scattering from the quasielastic to the resonance region. *Phys. Rev. C*, 79:034601, Mar 2009.

[25] A. Bodek, M. E. Christy, and B. Coopersmith. Effective Spectral Function for Quasielastic Scattering on Nuclei. *Eur. Phys. J. C*, 74(10):3091, 2014.

[26] K. Nakamura, S. Hiramatsu, T. Kamae, H. Muramatsu, N. Izutsu, and Y. Watase. The Reaction C-12 (e, e' p) at 700-MeV and DWIA Analysis. *Nucl. Phys. A*, 268:381–407, 1976.

[27] D. B. Day, J. S. McCarthy, Z. E. Meziani, R. Minehart, R. Sealock, S. T. Thornton, J. Jourdan, I. Sick, B. W. Filippone, R. D. McKeown, R. G. Milner, D. H. Potterveld, and Z. Szalata. y scaling in electron-nucleus scattering. *Phys. Rev. Lett.*, 59:427–430, Jul 1987.

[28] S. Frullani and J. Mougey. Single Particle Properties of Nuclei Through (e, é p) Reactions. *Adv. Nucl. Phys.*, 14:1–283, 1984.

[29] C. Marchand, M. Bernheim, P. C. Dunn, A. Gérard, J. M. Laget, A. Magnon, J. Morgenstern, J. Mougey, J. Picard, D. Reffay-Pikeroen, S. Turck-Chieze, P. Vernin, M. K. Brussel, G. P. Capitani, E. De Sanctis, S. Frullani, and F. Garibaldi. High proton momenta and nucleon-nucleon correlations in the reaction ^{3}he(e,e'p). *Phys. Rev. Lett.*, 60:1703–1706, Apr 1988.

[30] C. Ciofi degli Atti and S. Simula. Realistic model of the nucleon spectral function in few- and many-nucleon systems. *Phys. Rev. C*, 53:1689–1710, Apr 1996.

[31] O. Hen et al. Momentum sharing in imbalanced Fermi systems. *Science*, 346:614–617, 2014.

[32] M. Duer at al. Probing high-momentum protons and neutrons in neutron-rich nuclei. *Nature*, 560(7720):617–621, 2018.

[33] M. Patsyuk et al. Unperturbed inverse kinematics nucleon knockout measurements with a 48 GeV/c carbon beam. *Nature Phys.*, 17:693, 2021.

[34] R. Cruz-Torres, D. Lonardoni, R. Weiss, N. Barnea, D. W. Higinbotham, E. Piasetzky, A. Schmidt, L. B. Weinstein, R. B. Wiringa, and O. Hen. Many-body factorization and position–momentum equivalence of nuclear short-range correlations. *Nature Phys.*, 17(3):306–310, 2021.

[35] P. Rodriguez-Ramos. *Experimental results in pion induced reaction with carbon and polyethylene targets obtained by HADES-GSI*. PHD-thesis, Czech Technical University in Prague, 2021.

[36] Gerhard Ecker. Quantum chromodynamics. In *2005 European School of High-Energy Physics*, 4 2006.

[37] R. Abbott et al. Observation of Gravitational Waves from Two Neutron Star–Black Hole Coalescences. *Astrophys. J. Lett.*, 915(1):L5, 2021.

[38] Matthias Hanauske, Jan Steinheimer, Anton Motornenko, Volodymyr Vovchenko, Luke Bovard, Elias R. Most, L. Jens Papenfort, Stefan Schramm, and Horst Stöcker. Neutron Star Mergers: Probing the EoS of Hot, Dense Matter by Gravitational Waves. *Particles*, 2(1):44–56, 2019.

[39] Agnieszka Sorensen et al. Dense nuclear matter equation of state from heavy-ion collisions. *Prog. Part. Nucl. Phys.*, 41:104080, 2023.

[40] Szabolcs Borsanyi, Zoltan Fodor, Jana N. Guenther, Ruben Kara, Sandor D. Katz, Paolo Parotto, Attila Pasztor, Claudia Ratti, and Kálman K. Szabó. Qcd crossover at finite chemical potential from lattice simulations. *Phys. Rev. Lett.*, 125:052001, Jul 2020.

[41] P. Senger et al. Astrophysics with heavy-ion beams. *Phys. Scr.*, 96:054002, 2021.

[42] M Durante, P Indelicato, B Jonson, V Koch, K Langanke, Ulf-G Meißner, E Nappi, T Nilsson, Th Stöhlker, E Widmann, and M Wiescher. All the fun of the fair: fundamental physics at the facility for antiproton and ion research. *Physica Scripta*, 94(3):033001, jan 2019.

[43] G. Agakishiev et al. Study of dielectron production in C+C collisions at 1-A-GeV. *Phys. Lett. B*, 663:43–48, 2008.

[44] G. Agakishiev et al. Dielectron production in Ar+KCl collisions at 1.76A GeV. *Phys. Rev. C*, 84:014902, 2011.

[45] J. Stroth P. Salabura. Dilepton radiation from strongly interacting systems, progress in particle and nuclear physics. *Progress in Particle and Nuclear Physics*, 120:103869, 2021.

[46] G. Agakishiev et al. Study of exclusive one-pion and one-eta production using hadron and dielectron channels in pp reactions at kinetic beam energies of 1.25 GeV and 2.2 GeV with HADES. *Eur. Phys. J. A*, 48:74, 2012.

[47] G. Agakishiev et al. Baryon resonance production and dielectron decays in proton-proton collisions at 3.5 GeV. *Eur. Phys. J. A*, 50:82, 2014.

[48] G. Agakishiev et al. Baryon resonance production and dielectron decays in proton-proton collisions at 3.5 GeV. *Eur. Phys. J. A*, 50:82, 2014.

[49] J. Adamczewski-Musch et al. $\Delta(1232)$ Dalitz decay in proton-proton collisions at T=1.25 GeV measured with HADES at GSI. *Phys. Rev. C*, 95(6):065205, 2017.

[50] R. Abou Yassine et al. Inclusive e^+e^- production in collisions of pions with protons and nuclei in the second resonance region of baryons. 2023.

[51] R. Abou Yassine et al. First measurement of massive virtual photon emission from n* baryon resonances, 2022.

[52] Udai Singh. *Investigations of mechanisms of particle production in proton-induced nuclear spallation*. PHD-thesis, Institute of Physics of the Jagiellonian University, 2021.

[53] J. Adamczewski-Musch et al. Strong absorption of hadrons with hidden and open strangeness in nuclear matter. *Phys. Rev. Lett.*, 123(2):022002, 2019.

[54] Yoshinari Hayato. A neutrino interaction simulation program library NEUT. *Acta Phys. Polon. B*, 40:2477–2489, 2009.

[55] L. Alvarez-Ruso et al. Progress and open questions in the physics of neutrino cross sections at intermediate energies. *New J. Phys.*, 16:075015, 2014.

[56] U. Mosel. Neutrino interactions with nucleons and nuclei: Importance for long-baseline experiments. *Annual Review of Nuclear and Particle Science*, 66(1):171–195, 2016.

[57] E. S. Pinzon Guerra et al. Measurement of $\sigma_{\rm ABS}$ and $\sigma_{\rm CX}$ of π^+ on carbon by the Dual Use Experiment at TRIUMF (DUET). *Phys. Rev. C*, 95(4):045203, 2017.

[58] Anna Ershova. *Toward high-precision measurements of neutrino oscillations in the future long baseline experiments*. PhD thesis, AIM, Saclay, 2023.

[59] Anna Ershova. First usage of Intra-Nuclear Cascade of Liège (INCL) model for nuclear transport of protons from neutrino-nucleus scattering. *J. Phys. Conf. Ser.*, 2586(1):012131, 2023.

[60] B. Abi et al. The Single-Phase ProtoDUNE Technical Design Report. 6 2017.

[61] Sophie Pedoux. Extension of the Liége Intranuclear Cascade Model to the 2-15 GeV Incident Energy Range. PHD-thesis, University of Liége, Faculty of Sciences Department of Astrophysics, Geophysics and Oceanography Fundamental Interactions in Physics and Astrophysics, 2012.

[62] R. L. Workman et al. Review of Particle Physics. *PTEP*, 2022:083C01, 2022.

[63] John D. Oliver, I. Nadelhaft, and G. B. Yodh. pi++p Interactions at 646 MeV. *Phys. Rev.*, 147:932–938, 1966.

[64] S. Feminò, S. Jannelli, and F. Mezzanares. π- p interactions at 650 MeV. *Nuovo Cim. A*, 52(3):892–902, 1967.

[65] C. N. Vittitoe, B. R. Riley, W. J. Fickinger, V. P. Kenney, J. G. Mowat, and W. D. Shephard. pi–p Interactions at 604 MeV. *Phys. Rev.*, 135:B232–B240, 1964.

[66] M. G. Bowler and R. J. Cashmore. Single pion production in pi+ p interactions between 0.6 and 0.8 gev/c. *Nucl. Phys. B*, 17:331–358, 1970.

[67] Penner, G. Vector meson production and nucleaon resonance analysis in a coupled-channel approach. PhD, Justus Liebig University, Giessen, 2002.

[68] S. Prakhov et al. Measurement of $\pi^- p \to \eta n$ from threshold to p $_{\pi^-}$ = 747 MeV/c. *Phys. Rev.*, C72:015203, 2005.

[69] T. W. Morrison. Ph.D. dissertation, The George Washington University, 2000.

[70] R. A. Arndt, W. J. Briscoe, T. W. Morrison, I. I. Strakovsky, R. L. Workman, and A. B. Gridnev. Low-energy η N interactions: Scattering lengths and resonance parameters. *Phys. Rev.*, C72:045202, 2005.

[71] M. Hirata, F. Lenz, and M. Thies. Δ - Nucleon and Pion - Nucleus Interactions. *Phys. Rev. C*, 28:785, 1983.

[72] J. W. Cronin, R. Cool, and A. Abashian. Cross sections of nuclei for high-energy pions. *Phys. Rev.*, 107:1121–1130, Aug 1957.

[73] T. Takahashi et al. pi- - C-12 elastic scattering above the Delta resonance. *Phys. Rev. C*, 51:2542–2552, 1995.

[74] B. L. Clausen, R. A. Loveman, R. J. Peterson, R. A. Ristinen, J. L. Ullmann, and F. Irom. Delta production by pion charge exchange on complex nuclei. *Phys. Rev. C*, 35:1028–1036, Mar 1987.

[75] J. Ouyang, S. Høibråten, and R. J. Peterson. Effective number of protons for quasifree (π^-,π^0) at 500 and 400 mev. *Phys. Rev. C*, 47:2809–2811, Jun 1993.

[76] T. Kishimoto et al. Quasifree C-12 (pi+, p) reaction and the pi N amplitude in nuclei. *Phys. Rev. C*, 43:1454–1457, 1991.

[77] J. E. Wise et al. Quasifree pion scattering at 500-MeV. *Phys. Rev. C*, 48:1840–1848, 1993.

[78] D. Belver et al. The HADES RPC inner TOF wall. *Nucl. Instrum. Meth. A*, 602:687–690, 2009.

[79] J. Pietraszko et al. Diamonds as timing detectors for minimum-ionizing particles: The HADES proton-beam monitor and START signal detectors for time of flight measurements. *Nucl. Instr. and Meth.*, A 618:121, 2010.

[80] https://www.sglcarbon.com/pdf/SGL-Datasheet-SIGRAFINE-R6650-EN.pdf.

[81] O. Buss, T. Gaitanos, K. Gallmeister, H. van Hees, M. Kaskulov, O. Lalakulich, A. B. Larionov, T. Leitner, J. Weil, and U. Mosel. Transport-theoretical Description of Nuclear Reactions. *Phys. Rept.*, 512:1–124, 2012.

[82] D. M. Manley and E. M. Saleski. Multichannel resonance parametrization of pi N scattering amplitudes. *Phys. Rev. D*, 45:4002–4033, 1992.

[83] Particle Data Group. Review of Particle Physics. *Progress of Theoretical and Experimental Physics*, 2022(8):083C01, 08 2022.

[84] T. Sjöstrand et al. An introduction to pythia 8.2. *Comput. Phys. Commun.*, 191:159, 2015.

[85] S. A. Bass et al. Microscopic models for ultrarelativistic heavy ion collisions. *Prog. Part. Nucl. Phys.*, 41:255, 1998.

[86] C. Fuchs, L. Sehn, Amand Faessler, D. S. Kosov, V. S. Uma Maheswari, and Z. Wang. Treatment of baryonic resonances in the RQMD approach including scalar - vector mean fields. In *25th International Workshop on Gross Properties of Nuclei and Nuclear Excitation: QCD Phase Transitions (Hirschegg 97)*, pages 433–440, 1 1997.

[87] C. Fuchs, E. Lehmann, L. Sehn, F. Scholz, T. Kubo, J. Zipprich, and A. Faessler. Heavy ion collisions and the density dependence of the local mean field. *Nucl. Phys. A*, 603:471–485, 1996.

[88] Y. Nara et al. Momentum-dependent potential and collective flows within the relativistic quantum molecular dynamics approach based on relativistic mean-field theory. *Phys. Rev. C*, 102:024913, 2020.

[89] Y. Nara et al. Relativistic nuclear collisions at 10A GeV energies from p+Be to Au+Au with the hadronic cascade model. *Phys. Rev. C*, 61:024901, 1999.

[90] S. Teis, W. Cassing, M. Effenberger, A. Hombach, U. Mosel, and G. Wolf. Pion production in heavy ion collisions at SIS energies. *Z. Phys. A*, 356:421–435, 1997.

[91] J. Cugnon, A. Boudard, J. C. David, S. Leray, and D. Mancusi. Processes involving few degrees of freedom in the frame of Intranuclear Cascade approaches. *Eur. Phys. J. Plus*, 131(5):169, 2016.

[92] R. Serber. Nuclear Reactions at High Energies. *Phys. Rev.*, 72:1114–1115, 1947.

[93] A. Mosnier et al. Present Status and Developments of the Linear IFMIF Prototype Accelerator (LIPAc). *Proceedings of IPAC2012, New Orleans, Louisiana, USA*, THPPP075, 2012.

[94] M. Cassé E.Vangioni-Flam. Evolution of lithium–beryllium–boron and oxygen in the early Galaxy. *New Astron. Rev.*, 45:583, 2001.

[95] Ralph Engel, Dieter Heck, and Tanguy Pierog. Extensive air showers and hadronic interactions at high energy. *Ann. Rev. Nucl. Part. Sci.*, 61:467–489, 2011.

[96] A Heikkinen et al. International conference on computing in high energy and nuclear physics. *Journal of Physics*, 2008.

[97] Alain Boudard, Joseph Cugnon, Jean-Christophe David, Sylvie Leray, and Davide Mancusi. New potentialities of the Liège intranuclear cascade model for reactions induced by nucleons and light charged particles. *Phys. Rev. C*, 87(1):014606, 2013.

[98] Davide Mancusi, Alain Boudard, Joseph Cugnon, Jean-Christophe David, Pekka Kaitaniemi, and Sylvie Leray. Extension of the Liège intranuclear-cascade model to reactions induced by light nuclei. *Phys. Rev. C*, 90(5):054602, 2014.

[99] Jose Luis Rodríguez-Sánchez, Jean-Christophe David, Davide Mancusi, Alain Boudard, Joseph Cugnon, and Sylvie Leray. Improvement of one-nucleon removal and total reaction cross sections in the Liège intranuclear-cascade model using Hartree-Fock-Bogoliubov calculations. *Phys. Rev. C*, 96(5):054602, 2017.

[100] Aleksandra Kelic, M. Valentina Ricciardi, and Karl-Heinz Schmidt. ABLA07 - towards a complete description

of the decay channels of a nuclear system from spontaneous fission to multifragmentation. In *Joint ICTP-IAEA Advanced Workshop on Model Codes for Spallation Reactions*, 6 2009.

[101] R. Brun, F. Bruyant, M. Maire, A. C. McPherson, and P. Zanarini. GEANT3. 9 1987.

[102] Federico Scozzi. Studying excited states of the nucleon with the HADES detector at GSI. PHD, Paris-Sud and TU Darmstadt universities, 2018.

[103] Carl Eckart. The thermodynamics of irreversible processes. iii. relativistic theory of the simple fluid. *Phys. Rev.*, 58:919–924, Nov 1940.

[104] Robert B. Wiringa, R. A. Smith, and T. L. Ainsworth. Nucleon Nucleon Potentials with and Without Delta (1232) Degrees of Freedom. *Phys. Rev. C*, 29:1207–1221, 1984.

[105] R. Machleidt, F. Sammarruca, and Y. Song. Nonlocal nature of the nuclear force and its impact on nuclear structure. *Phys. Rev. C*, 53(4):R1483–R1487, 1996.

[106] D. R. Entem, R. Machleidt, and Y. Nosyk. High-quality two-nucleon potentials up to fifth order of the chiral expansion. *Phys. Rev. C*, 96(2):024004, 2017.

[107] Evgeny Epelbaum, Hans-Werner Hammer, and Ulf-G. Meissner. Modern Theory of Nuclear Forces. *Rev. Mod. Phys.*, 81:1773–1825, 2009.

[108] O. Hen, A. W. Steiner, E. Piasetzky, and L. B. Weinstein. Analysis of Neutron Stars Observations Using a Correlated Fermi Gas Model. 8 2016.

[109] L. Fields et al. Measurement of Muon Antineutrino Quasielastic Scattering on a Hydrocarbon Target at E$\nu\sim$3.5 GeV. *Phys. Rev. Lett.*, 111(2):022501, 2013.

[110] G. A. Fiorentini et al. Measurement of Muon Neutrino Quasielastic Scattering on a Hydrocarbon Target at $E_\nu \sim 3.5$ GeV. *Phys. Rev. Lett.*, 111:022502, 2013.

[111] E. Caurier, G. Martinez-Pinedo, F. Nowacki, A. Poves, and A. P. Zuker. The Shell Model as Unified View of Nuclear Structure. *Rev. Mod. Phys.*, 77:427–488, 2005.

[112] J. J. Kelly. Nucleon knockout by intermediate-energy electrons. *Adv. Nucl. Phys.*, 23:75–294, 1996.

[113] R. Subedi et al. Probing Cold Dense Nuclear Matter. *Science*, 320:1476–1478, 2008.

[114] A. Tang et al. n-p short range correlations from (p,2p + n) measurements. *Phys. Rev. Lett.*, 90:042301, 2003.

[115] E. Piasetzky, M. Sargsian, L. Frankfurt, M. Strikman, and J. W. Watson. Evidence for the strong dominance of proton-neutron correlations in nuclei. *Phys. Rev. Lett.*, 97:162504, 2006.

[116] I. Korover et al. Probing the Repulsive Core of the Nucleon-Nucleon Interaction via the $^4He(e, e\prime pN)$ Triple-Coincidence Reaction. *Phys. Rev. Lett.*, 113(2):022501, 2014.

[117] R. Shneor et al. Investigation of proton-proton short-range correlations via the C-12(e, e-prime pp) reaction. *Phys. Rev. Lett.*, 99:072501, 2007.

[118] A. Schmidt et al. Probing the core of the strong nuclear interaction. *Nature*, 578(7796):540–544, 2020.

[119] H. Feldmeier, W. Horiuchi, T. Neff, and Y. Suzuki. Universality of short-range nucleon-nucleon correlations. *Phys. Rev. C*, 84:054003, 2011.

[120] Massimiliano Alvioli, Claudio Ciofi Degli Atti, Leonid P. Kaptari, Chiara Benedetta Mezzetti, and Hiko Morita. Universality of nucleon-nucleon short-range correlations and nucleon momentum distributions. *Int. J. Mod. Phys. E*, 22:1330021, 2013.

[121] R. B. Wiringa, R. Schiavilla, Steven C. Pieper, and J. Carlson. Nucleon and nucleon-pair momentum distributions in $A \leq 12$ nuclei. *Phys. Rev. C*, 89(2):024305, 2014.

[122] R. Schiavilla, Robert B. Wiringa, Steven C. Pieper, and J. Carlson. Tensor Forces and the Ground-State Structure of Nuclei. *Phys. Rev. Lett.*, 98:132501, 2007.

[123] Argonne National Laboratory, Single-Nucleon Momentum Distributions. https://www.phy.anl.gov/theory/research/momenta/norfolk.html.

[124] Argonne National Laboratory, Two-Nucleon Momentum Distributions. https://www.phy.anl.gov/theory/research/momenta2/norfolk.html.

[125] M. Alvioli, C. Ciofi degli Atti, L. P. Kaptari, C. B. Mezzetti, and H. Morita. Nucleon momentum distributions, their spin-isospin dependence and short-range correlations. *Phys. Rev. C*, 87(3):034603, 2013.

[126] Jan Ryckebusch, Wim Cosyn, and Maarten Vanhalst. Stylized features of single-nucleon momentum distributions. *J. Phys. G*, 42(5):055104, 2015.

[127] W. Cosyn and J. Ryckebusch. Phase-space distributions of nuclear short-range correlations. *Phys. Lett. B*, 820:136526, 2021.

[128] C. Colle, O. Hen, W. Cosyn, I. Korover, E. Piasetzky, J. Ryckebusch, and L. B. Weinstein. Extracting the mass dependence and quantum numbers of short-range correlated pairs from A(e,e'p) and A(e,e'pp) scattering. *Phys. Rev. C*, 92(2):024604, 2015.

[129] S. Tan. Energetics of a strongly correlated fermi gas. *Ann. Phys.*, 323:2952, 2008.

[130] R. Weiss, R. Cruz-Torres, N. Barnea, E. Piasetzky, and O. Hen. The nuclear contacts and short range correlations in nuclei. *Phys. Lett. B*, 780:211–215, 2018.

[131] E. J. Moniz. Pion electroproduction from nuclei. *Phys. Rev.*, 184:1154–1161, 1969.

[132] O. Hen, L. B. Weinstein, E. Piasetzky, G. A. Miller, M. M. Sargsian, and Y. Sagi. Correlated fermions in nuclei and ultracold atomic gases. *Phys. Rev. C*, 92(4):045205, 2015.

[133] Short-Range Correlations Studies in Nuclei via the A(p,2pN) Reaction with HADES. https://www.hen-lab.com/srchades.